# PETROLOGY AND GEOCHEMISTRY OF BONINITES AND RELATED LAVAS FROM THE MATA VOLCANOES, NE LAU BASIN

A THESIS SUBMITTED TO THE GRADUATE DIVISION OF THE UNIVERSITY OF HAWAIʻI AT MĀNOA IN PARTIAL FULFILLMENT OF THE REQUIREMENTS FOR THE DEGREE OF

MASTERS OF SCIENCE

IN

GEOLOGY AND GEOPHYSICS

DECEMBER 2014

By

Sarah Elizabeth Glancy

Thesis Committee

Ken Rubin, Chairperson
Eric Hellebrand
Jeff Taylor

## ABSTRACT

The Lau Basin is an excellent location for studying suprasubduction zone processes due to numerous volcanoes spanning from the forearc, arc, reararc, to backarc settings, providing windows into different aspects of the subduction zone. The young, primarily boninitic submarine Mata Volcanoes, located between the arc and the backarc spreading center, are an important part of this picture. This thesis presents a preliminary study of the Mata Volcanoes, including XRF whole rock and glass, and mineral EPMA analysis of samples, thermometry, and crystallization modeling. Differentiation at the Mata Volcanoes occurred under oxidizing conditions, and over a temperature range of approximately 1000-1200 °C. Starting magmas had high water contents of at least 1.7- 2 wt%. Lavas preserve heterogeneities, suggesting that no well-developed magma storage system/homogenization zone is present. Complex crystal chemistry and compositions suggest that magma mixing played a role in the formation of these magmas.

## TABLE OF CONTENTS

## LIST OF TABLES

### Chapter One



### Chapter Two

**Chapter Three**



**Chapter Four**



**Chapter Five**

**Chapter Six**



**Appendix A**



**Appendix D**

## LIST OF FIGURES

### Chapter One



### Chapter Two



### Chapter Three

**Chapter Four**

**Chapter Five**



**Chapter Six**

**Appendix A**

**Appendix B**



**Appendix C**

# CHAPTER 1. INTRODUCTION

Processes affecting magmas in suprasubduction zones are an important, but still incompletely understood aspect of the global geologic picture, despite extensive literature on the topic. These processes have been suggested to include:

- Presence of depleted or enriched mantle compositions
- Depletion of the mantle wedge by prior melting events
- Dehydration of the subducting slab and sediment
- Partial melting of sediments
- Reaction of fluids from the subducted slab and sediments with the mantle wedge
- Partial melting of the mantle wedge
- Migration of the melts to the surface
- Crystallization
- Melt-crystal interaction
- Magma mixing

The greater Lau Basin and Tonga Arc region is an excellent location to study suprasubduction zone magmatism and processes due to the large amount of volcanism in the forearc, arc, reararc, and backarc settings, which provide windows into different aspects of the subduction zone. For example, analysis of samples collected along the arc or collected at varying distance from the arc can study variations in mantle source composition with location. Studies of volcanoes at varying distance away from the arc can investigate changes in subduction input further away from the arc as the slab subducts progressively deeper into the mantle, as will be discussed in this chapter. Previous work on the greater Lau basin and Tonga Arc region and on subduction zones in general will be discussed and citations will also be provided later in this chapter.

This study focuses on a series of small, active or recently active submarine volcanoes in the northeast Lau Basin between the arc and the backarc spreading center. These volcanoes became of particular interest to the geologic community when West Mata was observed in

eruption in 2009, one of the first direct observations of a submarine volcanic eruption. Additionally, these volcanoes are interesting to study because they primarily erupt boninite, a rare type of lava. Previous studies of boninite discussed herein have primarily focused on older rocks because young rocks were not available. In contrast, these boninites are very young and fresh, providing an opportunity to study boninite petrogenesis.

This chapter first presents an overview of subduction zones and backarc spreading systems. Second, it introduces the Lau Basin. It then defines boninite and summarizes previous work on this unusual lava type. Next, it introduces the study area in more detail. Finally, it provides an overview of the thesis work that will be presented in this manuscript.

## Subduction Zones

As one tectonic plate sinks under another in a subduction zone, it recycles oceanic lithosphere, oceanic sediments, and water into the mantle. As the plate sinks, dehydration reactions release water and fluid mobile elements into the mantle wedge of the overriding plate. Addition of these components, especially water, has a profound effect on the mantle wedge. Water allows for fluid fluxing of the mantle wedge, resulting in the formation of arc volcanoes on the overriding plate. While this overview is widely accepted, the details of the process are difficult to observe and thus are not well known and undoubtedly vary from place to place. Current studies of arc volcanic regions, ophiolites, and experimental studies are clarifying the subduction process.

Subduction related lavas have distinctive trace element signatures due to the processes involved in their petrogenesis, such as progressive dehydration of the subducted slab and sediments or mantle melting. Different elements are affected to varying degrees by these processes. Therefore, selective study of certain elements sensitive to a process of interest can provide valuable information about this process. For example, some elements, such as Ba, are indicative of the process of addition of fluid components being added to the to the mantle wedge (Pearce and Stern, 2006). Other elements, such as Nb, are indicative of the original concentration of the mantle wedge or the nature or conditions of melting of the mantle wedge.

By studying a suite of trace elements in samples that have been affected by a variety of processes, we can begin to unravel these processes. Many types of trace elements are important to the understanding of lavas erupted in subduction zones. Two examples of such groups will be discussed here: 1) fluid mobile elements that are introduced to the mantle wedge by subduction related fluids, and 2.) non-fluid mobile elements that are indicative of the original composition of the mantle wedge. Table 1.1 and the following section discuss these elements.

Table 1.1. An example of two types of processes/components found at subduction zones and elements and ratios that can be used to study them.

| **Process(es)/components of interest** | **Addition of subduction related fluids** | **Original mantle composition and melting processes** |
|---|---|---|
| **Element category** | Fluid mobile elements | Non-fluid mobile elements |
| **Examples of elements** | K, Rb, Cs, Sr, Ba, Pb, and U | Y, Zr, Hf, Nb, Ta, Ti and HREE |
| **Examples of ratios** | Ce/Pb, Ba/Nb | Th/Nb, La/Nb |

See text for more details (Elliott, 2003; Hawkesworth *et al.*, 1991; Pearce and Stern, 2006; Plank, 2005; Stern, 2002; Workman and Hart, 2005)

The first group of elements is fluid-mobile trace elements. These elements will travel with the fluid when dehydration of the subducting slab and sediments occurs. Aqueous fluids from the dehydrating slab enrich the mantle wedge with fluid mobile elements such as K, Rb, Cs, Sr, Ba, Pb, and U (e.g., Stern, 2002). Therefore, when compared to mid-ocean ridge basalts (MORB), arc lavas are typically more enriched in incompatible alkali and alkaline earth elements (K, Rb, Cs, Sr, and Ba) than in other incompatible elements. This reflects the enrichment of these elements in the mantle wedge due to subduction.

To study the influence of these fluids, fluid mobile trace elements and trace element ratios are used. The ratios include one element that is highly affected by addition of aqueous fluid and one that is not. Ratios are most useful when the two elements are not fractionated by other processes. For example, the elements behave similarly during melting and crystallization so that their ratio is indicative of the source not of the degree of melting or crystallization. Ce/Pb and Ba/Nb are examples of useful ratios. Ce/Pb is influenced by fluid addition from the slab (e.g. Plank, 2005 and references therein) and is not generally thought to be very sensitive to degrees of melting (eg. Sun *et al.*, 2008 and references therein and; Workman and Hart, 2005 and references therein), so it is a useful indicator of slab influence. Ba/Nb is another useful indicator of influence from slab derived fluids (e.g. Pearce and Stern, 2006). Arc lavas tend to have high ratios of large ion lithophile elements to high field strength elements, such as Ba/Nb. During melting of upper mantle material, Ba and Nb usually have similar bulk distribution coefficients, so the elevated Ba/Nb ratios of arc rocks may reflect the addition of Ba from a subducted source (e.g., Elliott, 2003 and Pearce and Stern, 2006). Only very small amounts of subduction derived fluids are necessary to cause these enrichments (Stern, 2002). These elements can shed light onto subduction related processes and tell us if lavas were influenced by subduction related processes.

Some elements such as Y, Zr, Hf, Nb, Ta, Ti and heavy rare earth elements are not mobilized by subduction derived fluids. Because these elements are not being added to the mantle wedge by subduction derived fluids, their concentrations are thought to reflect concentrations in the mantle wedge before it was influenced by the subduction zone and mantle

melting processes (Stern 2002 and Hawkesworth et al. 1991). As Nb and Ta are not added to the mantle wedge by subduction related fluids like other trace elements, Nb and Ta are found to have lower concentrations than other nearby elements on a normalized extended rare earth element diagram. For Nb, this is referred to as a "negative Nb anomaly" and can be expressed by Th/Nb and La/Nb ratios and is typical of arc lavas (Plank, 2005).

## Backarc Basins

Backarc basins are regions behind a volcanic arc often dominated by seafloor spreading and rifting. They often form first by arc rifting, then by backarc spreading. Thus, spreading first occurs close to the arc and as oceanic crust is accreted, the backarc spreading center migrates further and further away from the arc (Martinez and Taylor, 2006).

Initially, the chemical composition of backarc basin basalts (BABB) was thought to be very similar to that of mid ocean ridges (Pearce and Stern, 2006 and references therein). However, it has been discovered that there can be a variety of volcanic products in the backarc (Pearce and Stern, 2006 and references therein) and that backarc basin basalts often have different chemical compositions from mid ocean ridge basalts (MORB) (Langmuir *et al.*, 2006). For example, backarc basin basalts tend to have lower $TiO_2$ and FeO contents than mid ocean ridge basalts due to source depletion (Langmuir *et al.*, 2006 and references therein).

The chemical composition of backarc basin basalts is influenced by many factors including the nature of the mantle source, the nature of the subduction component, the interaction between these two sources, and the effects of water on melting and crystallization. The amount and location of subduction input in a given location in the basin varies due to the basin's evolution, flow in the mantle, and how close the location is to the arc volcanic front. Proximity of the backarc spreading center to the arc volcanic front can have profound effects on the magmatic productivity, morphology, and geochemistry of backarc spreading centers (Martinez and Taylor, 2006). Many spreading systems in the Lau Basin trend obliquely away from the arc and thus their compositions, characteristics and/or chemical elements vary with distance from the volcanic arc front. For example, the Central and Eastern Lau Spreading centers, which range

from ~40 to 180 km from the arc volcanic front, experience changes with distance from the arc volcanic front. As distance from the arc increases, the morphologies of the spreading centers change from thick andesitic crust with shallow axial highs to a deep, faulted axis with thinner crust than average mid ocean ridges and finally to mid ocean ridge-like crust (Escrig *et al*., 2012 and Martinez and Taylor, 2006 and references therein). These changes can often be linked with changes in melting. Decompression melting at spreading centers can be augmented by flux melting due to addition of a fluid subduction component closer to the arc (Pearce and Stern, 2006). This can cause changes in both the structure of spreading centers and the composition of erupted lavas with distance away from the arc.

## Regional geology

### The Lau Basin

The Lau Basin is located in a tectonically complicated and active region, containing a confluence of many tectonic settings in close proximity (Figure 1.1 and 1.2). The basin has a maximum width of 500 km and maximum length of 600 km (Langmuir *et al.*, 2006). The 2-3 km deep basin is in close proximity to active and remnant volcanic arcs, back arc spreading centers and a large transform boundary. The basin is bordered to the west by the 2,400 km long remnant arc called the Lau Ridge and to the east by the Tonga Ridge and Tofua Arc. The Tonga Ridge is more than 1100 km long, stretching from the transform boundary to the north to the Louisville Seamount chain to the south, where it meets the Kermadec Ridge. The Tonga Ridge includes the active, western Tofua Arc and the eastern Tonga platform. To the east lies the 10.5 km deep Tonga Trench where the Pacific Plate subducts under the basin (Hawkins, 1995). The northern part of the basin is bounded by the poorly understood Vitiez Transform, with Samoa located on the Pacific Plate north of the transform boundary. The Havre Trough is located to the south of the Lau Basin, adjacent to the Kermadec Arc.

The Lau basin formed through rifting of a volcanic arc into the Tonga Ridge and the Lau Ridge. Spreading started approximately 6 million years ago in the northern part of the basin

(Hawkins, 1995). Today, spreading in the basin is accommodated by multiple overlapping spreading centers (Figure 1.1).

Much of the basin can be considered a suprasubduction zone setting, except perhaps regions in the extreme northwest. Active arc volcanism in the adjacent Tonga Arc has occurred and currently occurs contemporaneously with primarily basaltic magmatism with a composition similar to MORB that occur at spreading centers (Hawkins, 1995). However not all volcanism in the back arc is basaltic and extreme geochemical variability can be found (e.g. Acland, 1996; Caulfield *et al.*, 2012; Escrig *et al.*, 2009, 2012; Falloon *et al.*, 2007, 2008; Keller *et al.*, 2008; Martinez and Taylor, 2006).

The tectonics of the basin is complex. Zellmer and Taylor (2001) subdivided the basin into microplates (Figure 1.3). The Lau Ridge to the west is located on the Australian Plate. The Niuafo'ou Plate comprises the middle of the basin. The Tongan arc is located on the Tongan Plate (Zellmer and Taylor, 2001). The study area is located on the Tongan plate (Figure 1.2). The study area lies between the Northeast Lau Spreading Center and the Tofua Arc, just south of the transform boundary at the northern part of the basin on the Tongan plate (Figure 1.2).

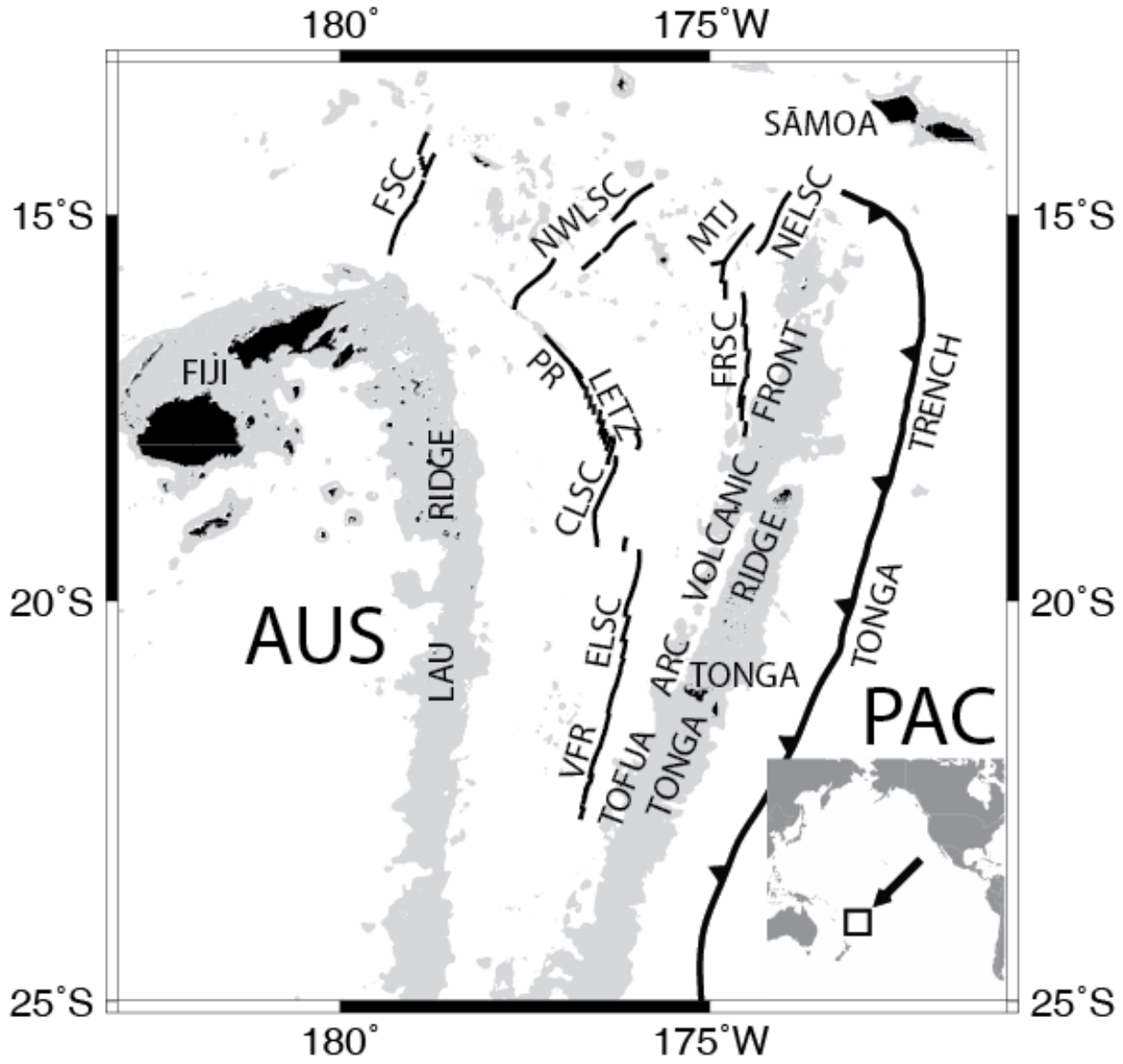


Figure 1.1. Map of the Lau Basin. From the insert showing the entire Pacific Ocean, we can see that the Lau Basin is in the Southwest Pacific Ocean, northeast of New Zealand. Islands are marked in black. Grey zones represent seamounts and other shallower areas. Remnant arc segments, the Lau Ridge and the Tonga Ridge are labeled. The Tofua Arc Volcanic Front consists of the currently active arc volcanoes. The major spreading systems and tectonic features in the basin are the Futuna Spreading Center (FSC), Northwestern Lau Spreading system (NWLSC), Peggy Ridge, Eastern Lau Spreading System (ELSC), Lau Extensional Transform Zone (LETZ), Central Lau Spreading System (CLSC), the Eastern Lau Spreading Center (ELSC), Valu Fa Ridge, Northeast Lau Spreading Center (NELSC), Mangatolu Triple Junction (MTJ), and the Fonualei Rift and Spreading Center (FRSC). Figure by Johnathan Sleeper.

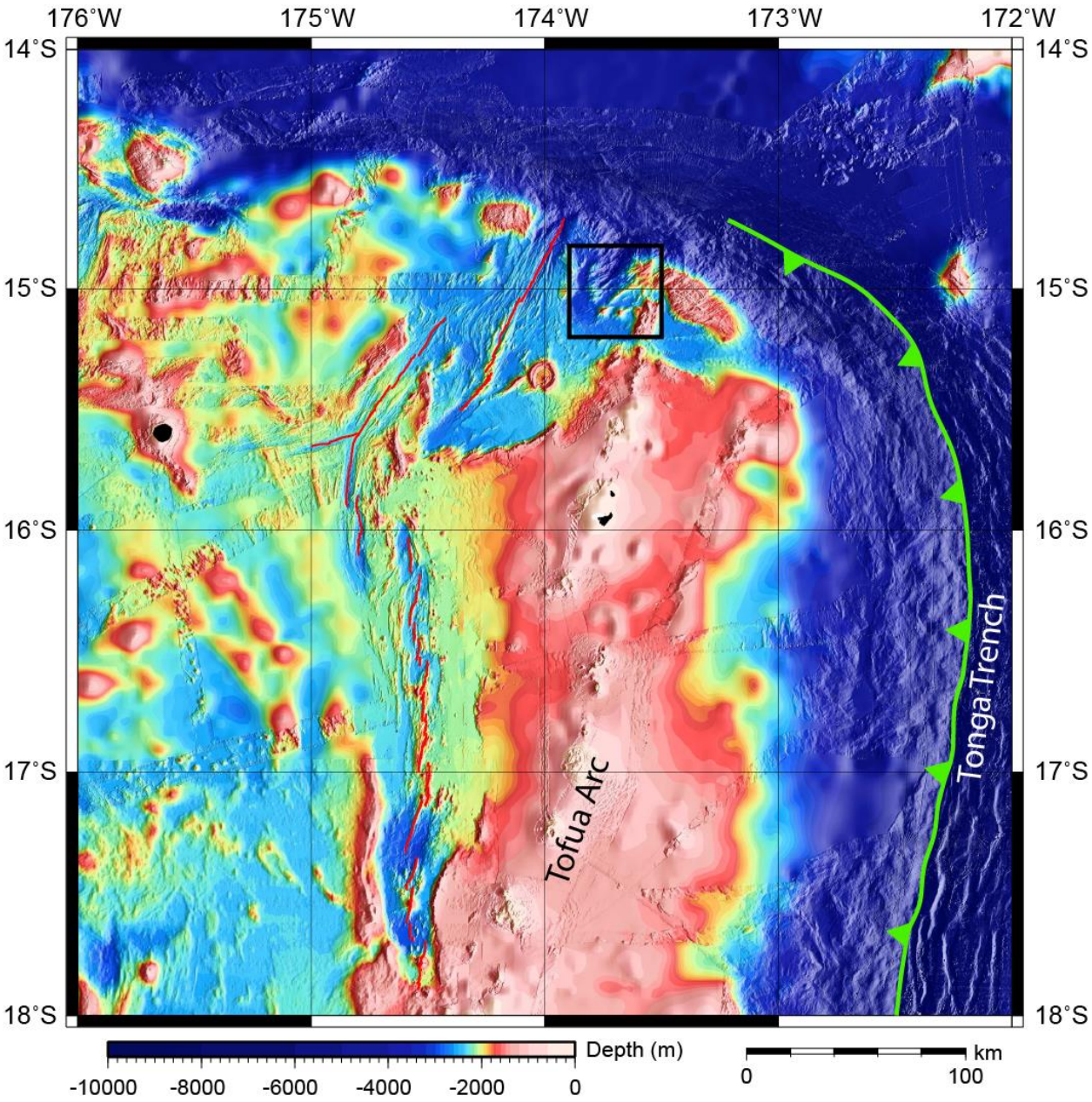


Figure 1.2. Bathymetry map of the Northeastern corner of the Lau Basin. The Tonga Trench and Tofua Arc are marked. The axis of major spreading centers are outlined in red. The black box outlines the study area, which will be shown in more detail in Figure 1.5. Figure from Jonathan Sleeper.

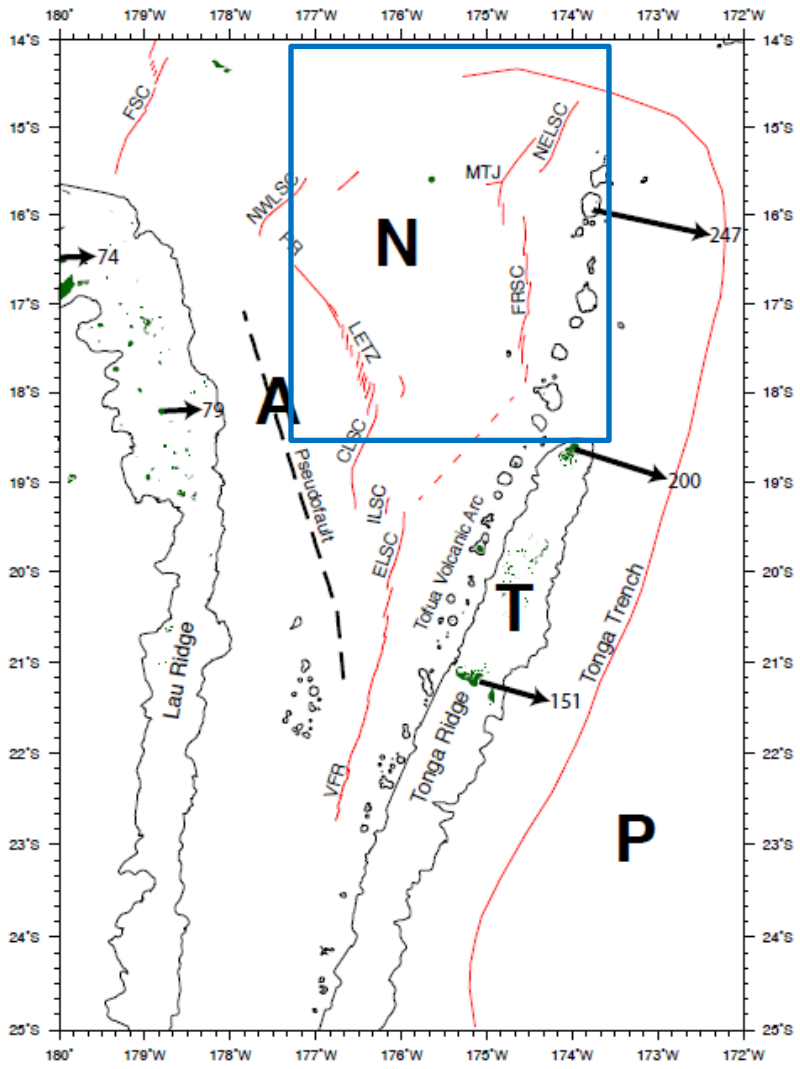


Figure 1.3. Tectonic Map of the Lau Basin showing the locations of microplates. This figure is adapted from Austin's MS thesis from UH Manoa. Austin (2012) has drawn plate boundaries identified by Zellmer and Taylor (2001) in red and pseudofault lines in a black dashed line. She used GPS-derived plate motions (in mm/yr) from Phillips, (2003). The blue box represents the region of interest in this study that is shown in detail in the Figure 1.2. The major spreading systems and tectonic features in the basin are the Futuna Spreading Center (FSC), Northwestern Lau Spreading system (NWLSC), Peggy Ridge, Eastern Lau Spreading System (ELSC), Lau Extensional Transform Zone (LETZ), Central Lau Spreading System (CLSC), the Eastern Lau Spreading Center (ELSC), Valu Fa Ridge, Northeast Lau Spreading Center (NELSC), Mangatolu Triple Junction (MTJ), and the Fonualei Rift and Spreading Center (FRSC).

## Boninite

Boninites are relatively rare volcanic rocks with MgO > 8 wt% and $TiO_2$ < 0.5 wt% (Le Bas, 2000). The type example of boninite is found in an uplifted forearc in the Bonin Islands. Taylor et al. (1993) argue that these boninites formed by subduction of young oceanic crust under a young hot plate. Boninites are thought to be the result of melting depleted mantle in the presence of water (Caulfield *et al.*, 2012; Falloon and Danyushevsky, 2000; Sobolev and Danyushevsky, 1994).

The petrogenesis of boninites is not well understood. While many researchers agree that boninites may form from subduction zone initiation, others, such as Meffre et al. (2012), point out that boninites can also form whenever extension occurs in the forearc. One suggested scenario is the propagation of backarc spreading centers into the forearc region (as in Meffre *et al*., 2012). Interactions between mantle plumes and the arc are also discussed in literature as a possible scenario for boninite formation in the Lau Basin (Falloon *et al.*, 2007, 2008). While many researchers argue that boninites generally form at high temperatures, this is still debated. More information on this debate is provided in Chapter 5, where the temperatures of crystallization of boninites determined in this study will be also be discussed.

### Previous work on boninites in the Lau Basin

Boninites can form in many tectonic settings including both fore-arcs and back-arc regimes (Escrig *et al.*, 2012; Falloon *et al.*, 2008). Multiple mechanisms and magma mixes have been proposed to explain boninite formation in the Lau Basin. Falloon and Crawford (1991) argued that lavas dredged from the Northern Tonga Ridge formed from several components. They proposed that the mantle wedge was depleted during the formation of the backarc and was later enriched with an incompatible element rich source such as hydrous fluid from the subducting slab or a carbonatite melt. Melt from this mantle wedge mixed with melt from an ocean island basalt (OIB) domain in the mantle. Sobolev and Danyushevsky (1994) suggested that boninites from the northern end of the Tonga trench had three sources: a depleted mantle component, a water rich fluid from the slab, and a melt from a plume. Danyushevsky et al.

(1995) argued that the previously melted Samoan plume melted again to form OIB melts which intruded above the subducting slab and reacted with slab derived fluids to produce primary boninite magmas. The primary boninite magmas may mix with primary OIB-like melts resulting in a variety of boninite magmas. Falloon et al. (2007) hypothesized that boninites in this region formed when hot Samoan mantle plume material intrudes above the subducting slab through the slab window and was then fluxed by water rich fluids from the subducting slab. Escrig et al. (2012), find that samples with boninitic affinity have the highest degree of melting and most refractory mantle component of the samples studied along the Fonualei Spreading Center. They also exhibit an important subduction related fluid component. Because the boninites are located behind an area of the arc that was not active, the authors proposed that the subduction input was entering into the back-arc rather than feeding volcanoes in the arc (Escrig *et al.*, 2012). Meffre et al. (2012) studied forearc eruptive products collected from a series of dredges along the length of the Tonga forearc trench walls. About half of the dredges contained boninite similar to high Ca boninites studied by Falloon and Crawford (1991) and Falloon et al. (2007 and 2008) from the northern Tongan Arc and Lau Basin. Samples from each dredge are distinct; however, those to the north tend to be more depleted in the HREE.

## Study Area

### The Mata Volcanoes

This study focuses on a series of young boninite seamounts in the northeastern corner of the Lau basin. The seamounts are located behind the main trend of the Tofua arc, south of the transform boundary that marks the northern end of the basin, and east of the Northeast Lau Spreading Center. They lie in a small extensional basin, close to the arc. Fractures in the basin trend en echelon obliquely away from the subduction trench (Figures 1.3 and 1.4). West and East Mata are the furthest south and thus closest to the arc. The North Matas have been named using Tongan numbers, from South to North: Taha (1), Ua (2), Tolu (3), Fa (4), Nima (5), Ono (6), and Fitu (7) (Figure 1.4). The Mata volcanoes are closely spaced.

Until recently, little work had been conducted on active or recently active boninite volcanoes. In 2008, a water column survey cruise identified indications of an eruption at West Mata Volcano and the nearby Northeast Lau Spreading Center (Embley *et al*., 2009 and Lupton *et al*., 2009) In May 2009, the Northeast Lau Response Cruise (NELRC) observed an active submarine eruption of boninite lava in the Lau Basin on West Mata seamount (Clague *et al.*, 2011; Resing *et al.*, 2011; Rubin *et al.*, 2009), the first time that a boninite eruption had been observed. Visual observations made by this group on several subsequent research cruises suggest that the Matas volcanoes are still active or were recently active. All of the Mata volcanoes are hydrothermally active except for Mata Nima. Lavas are young, fresh, and not covered by sediment (Rubin *et al*., 2011).

**Cruises and Sample Collection**

This project utilizes sample collections from five cruises from 2009 to 2012, as described below (Figure 1.4). Dr. Ken Rubin was a participant on each of these sampling cruises, and has provided these samples for this project.

In November 2008, an event plume was found by the *R/V T.G. Thompson* (John Lupton, Chief Scientist), indicating that an active eruption was occurring at West Mata. The plume over West Mata had a high $H_2$ concentration (> 3 uM) and a high concentration of volcanic glass chards (Merle, 2008, 2009). The Northeast Lau Basin Response Cruise, NELRC (May 2009, Resing and Embley, co-Chief Scientists), was quickly organized to study the eruption. NELRC observed the West Mata eruption over five dives with the ROV Jason-2. Two actively erupting vent areas were discovered and named Hades and Prometheus. Both explosive (fire fountaining and eruption of magma skin bubbles) and effusive activity (formation of pillows) were observed. Fresh, recently erupted samples and older samples were collected during the dives, and are part of this study (Resing *et al*., 2011).

R/V *Kilo Moana* Expedition KM1008 (April- May 2010, Joe Resing, Chief Scientist) found that six of the seven North Mata volcanoes were hydrothermally active. Matas Ua and Fitu had the largest plumes. CTD surveys detected $^3$He levels consistent with some interaction

between hydrothermal fluids and sea floor sediments or rock. However, it did not indicate that active eruptions were occurring. East Mata was actively venting, but did not appear to be currently erupting. Ongoing activity at West Mata indicated that it was still erupting. Visual imagery was collected at three North Matas using the Woods Hole Oceanographic Institution Towcam vehicle. Hydrothermal chimneys were observed in these images. Several small rock samples were also inadvertently collected by the vehicle during accidental contacts with the seabed.

NE Lau Basin Rock Dredging Expedition *R/V Kilo Moana* Expedition KM1024 (Dec. 2010, Ken Rubin, Chief Scientist) conducted twelve dredges on the Mata volcanoes. Samples were collected from all of the volcanoes except for Mata Nima. Recovered rocks appeared to be primarily boninites and were analyzed in this project. An event plume was observed above West Mata, indicating that West Mata was still erupting at the time of this cruise.

KM1129a (2011, Fernando Martinez, Chief Scientist) conducted dredges on East Mata, Mata Ua, Mata Tolu, and Niua. Rock samples from these dredges are also analyzed in this study.

Most recently, the R/V Revelle (2012, Resing and Embley, co-Chief Scientists) conducted ROV dives on West Mata, Mata Ua, Mata Tolu, Mata Fitu, and Niua using the Quest 4000 vehicle, collecting video, images, and rock samples which are part of this project. West Mata volcano was found to be no longer erupting.

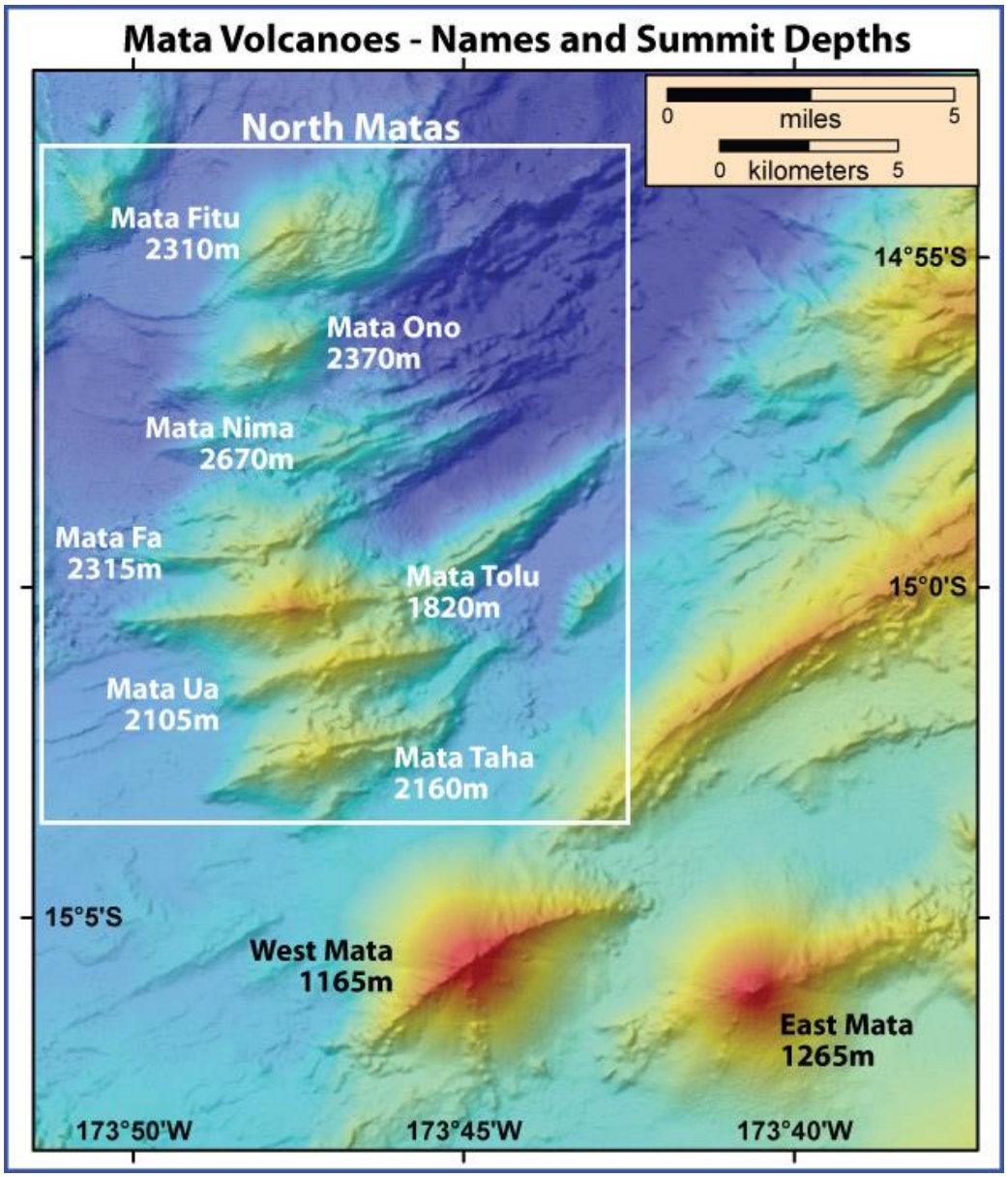


Figure 1.4. A bathymetry map of the Mata Volcanoes. The northern Mata Volcanoes are numbered from one (Taha) to seven (Fitu) in Tongan (Resing, 2010).

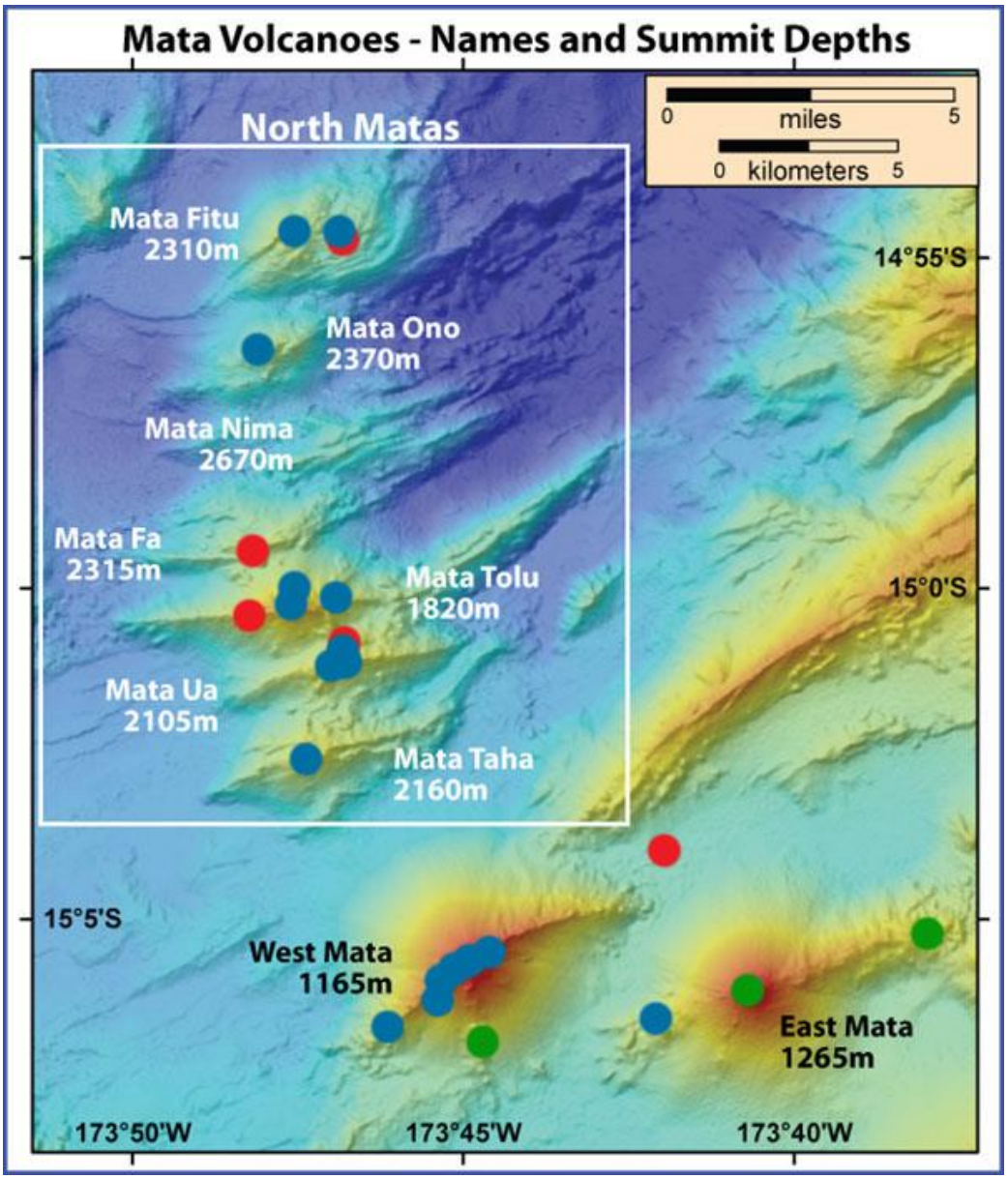


Figure 1.5. Sample locations on the Mata Volcanoes. The dots represent locations where samples were collected by a Remotely Operated Vehicle (ROV) or by dredge. The different colors represent the type of sample collected: blue for boninites, red for samples with higher $TiO_2$ contents, and green for evolved samples. Chapter 4 discusses geochemistry of collected lavas. (After Resing, 2010)

**Previous and ongoing research on the Mata volcanoes**

Findings from the cruises discussed in the previous section have led to several papers and numerous conference abstracts. Conference abstracts have been published on various aspects of study of the Mata Volcanoes: bathymetric surveying (Caress *et al.*, 2009; Embley *et al.*, 2012), monitoring (Bohnenstiehl *et al.*, 2010; Dziak *et al.*, 2009, 2010, 2013; Matsumoto *et al.*, 2010), geochemistry (eg. Arculus, 2013; Glancy *et al.*, 2012, 2014; Rubin *et al.*, 2013a, 2014, 2009; Rubin and Embley, 2012), submarine volcanology (Clague *et al.*, 2009; Embley *et al.*, 2009; Resing and Embley, 2009), and microbiology (Davis *et al.*, 2009; Huber *et al.*, 2009) to studies of hydrothermal systems (Butterfield *et al.*, 2009; Embley *et al.*, 2009, 2013; Lupton *et al.*, 2013). Most of this work focuses on West Mata volcano. This section will briefly discuss only those abstracts and papers that are closely related to this project.

Talks and posters presented in a special session at the AGU 2009 meeting presented the discovery of the eruption at West Mata volcano and initial findings following the 2009 cruise. Cruise participants observed West Mata erupting boninitic lava from two submarine vents, with fountaining and bubble burst activity at these vents. Boninite pyroclasts and lava flows were found elsewhere on the volcano as well (Caress *et al.*, 2009; Clague *et al.*, 2009; Dziak *et al.*, 2009; Lupton *et al.*, 2009; Michael *et al.*, 2009; Resing and Embley, 2009; Rubin *et al.*, 2009). Several papers also further discussed this discovery. Resing *et al*. (2011) described the eruption of molten lava as flows and also as explosions or magma bubbles that produced pyroclasts. They reported that the West Mata boninite was vesicular and crystal-rich, containing orthopyroxene, clinopyroxene, and olivine phenocrysts. They hypothesized that West Mata represents a proto-backarc system consisting of young rifted crust. Resing *et al*. (2011) reported the discovery of an eruption at West Mata when a hydrographic survey cruise in November 2008 discovered an event plume in the water column above the volcano and discuss findings from the response cruise that visited the erupting volcano in May 2009. Two active vents were observed on the summit ridge, Hades to the south and Prometheus to the NE. Both were actively erupting to produce pyroclasts. Pillow lavas and lobate flows were observed actively forming at Hades vent.

Young lava flows and pyroclastic deposits were found throughout the summit area (Resing *et al.*, 2011).

Resing *et al*. (2011) reported petrological and geochemical analysis of high Ca boninite samples from the young vesicular lavas containing pyroxene and olivine in generally glassy matrixes. Individual crystals and complicated intergrowths are present. They argued that some may be antecrysts and/or xenocrysts and are evidence that the magma is interacting with pre-existing crystals in a poorly developed magmatic system. While their geochemical analysis did not find supporting evidence of a Samoan source for the magmas, they could not conclusively rule out a Samoan source. Regardless, the Samoan plume may provide heat to the area. Because 77-95% of $CO_2$ erupted at West Mata is from the subducted slab, Resing *et al*. (2011) suggested that West Mata may be a proto-arc volcano.

Rubin *et al*. (2012) provided a review of submarine eruptions. They focused primarily on mid ocean ridge eruptions, but also make comparisons to other settings, including the West Mata Volcano. They include records of the first molten lava sampled on the ocean floor at West Mata. Rubin et al documents that the most recent eruption at West Mata is a continuous, multiyear eruption with a low magma flux rate.

Clague *et al*. (2011) discussed the volcanic morphology of West Mata Volcano. They used *Allan B.*, the MBARI mapping AUV, to map the volcano during the eruption, as well as ship-based multibeam sonar from multiple cruises. West Mata is a steep volcanic cone with a summit at 1159 m. Estimates of its volume range from ~26.6 $km^3$ (Clague *et al.*, 2011) to ~32 $km^3$ (Embley *et al.*, 2014 in press). The volcano has smooth slopes and two main rift zones. One rift zone extends west-northwest and the other extends east-northeast. The smooth steep slopes are due to clastic debris fans. Much of this is probably made of volcanic sand. They suggested that the other Mata volcanoes, which all have broadly similar shapes, could have similar structures. Pits were found on the east-northeast rift zone. At the time of this mapping, the summit was a ridge with no summit pit or caldera. However, they suggested that possible remnants of a caldera are present. (Clague *et al.*, 2011).

A recent study by Embley et al. (2014 in press) investigated the recent eruptive history of West Mata. They calculate that at least 0.115 $km^3$ of material erupted from 1996 to 2012 at West Mata. They found that eruptive activity occurred at the summit and along the rift zones.

The beginning of West Mata's most recent eruptive activity is not known. However, activity at the summit started in or before April 2007. Summit activity gradually declined from November 2008 to December 2010, ending in late 2010 or early 2011. However, more intense eruptions may have occurred in April 2010. An eruption on the west-southwest rift zone occurred between May 2009 and May 2010 at ~1400 m water depth (Embley *et al.*, 2014 in press).

About the same time of the end of the summit eruption, a small crater formed where Hades vent was located previously (Embley *et al.*, 2014, in press and Embley *et al.*, 2012). Embley *et al*. (2014, in press) note the similarities between this crater and Hawaiian pit craters caused by magma withdrawal and collapse of the magma plumbing system and conclude that the Hades crater at West Mata may have formed in a similar way. A landslide on the East of the volcano may have formed a similar way (Embley *et al.*, 2014 in press).

Further work on samples from this and additional cruises has furthered understanding of West Mata and the Mata volcanoes. Boninite and related lavas were found at other Mata Volcanoes as well. Variable trace element signatures have been found at individual volcanoes and within individual eruptions. Magmas may ascend quickly in poorly developed magmatic systems. The Mata volcanoes may be receiving some of the flux that would normally go to the arc volcanoes or may be related to the nearby arc volcanoes (Arculus, 2013; Glancy *et al.*, 2012, 2014; Rubin *et al.*, 2009. 2011. 2013a, 2014, 2013b; Rubin and Embley, 2012). These and other findings will be further discussed in this thesis.

Additional unpublished XRF work was conducted on NELRC, KM1024, and KM1129 samples from East Mata, West Mata, Taha, Ua, Tolu, Fa, Ono, and Fitu by Ken Rubin, Eric Hellebrand, and John Sinton. This thesis incorporates these data as well as analyses of additional samples. This project also incorporates Peter Michael's electron microprobe analyses of West

Mata samples from the NELRC expedition and presents additional EPMA analyses of Mata glass samples. Frances Jenner has conducted preliminary LA-ICPMS analysis of volcanic glass from the Mata Volcanoes. Others have also conducted preliminary analyses that will not be included in this thesis, including trace element analysis of samples from West Mata by Stéphane Escrig and studies of pyroclasts from West Mata by Dave Clague.

## Project overview

The freshness of the lavas and the unique setting provide an excellent opportunity to study boninite petrogenesis and could potentially lend insights into subduction zone dynamics and magma genesis at subduction settings. Because the Matas trend away from the subduction zone, they also provide a unique opportunity to analyze magmas formed at various distances from the subduction zone.

Before this project, a complete geochemical and petrologic analysis of the Mata Volcanoes' boninite samples had not been undertaken. The objective of this project is to study the petrogenesis of boninite lavas which have erupted at the Mata volcanoes in the Northeast Lau Basin and the conditions of differentiation of the samples.

To do so, the samples were characterized using a petrographic microscope, EPMA BSE images, and EPMA element maps. Quantitate EPMA spot analysis of olivine, orthopyroxene, clinopyroxene, and volcanic glass and XRF whole rock major and trace element analysis further characterized the samples. EPMA glass and mineral analysis was used to calculate temperatures of formation of crystal phases and volcanic glass. EPMA glass compositions were used as a starting composition for MELTS modeling of crystallization. MELTS modeling constrained possible conditions of crystallization of the magmas from the Mata Volcanoes.

# CHAPTER 2. METHODS

## Point Counting

Point counting is used to quantify vesicularity, crystallinity, and phase proportions of thin sections. Using a petrographic microscope, the stage moves the thin section by a set amount for each count in a grid system. The researcher identifies the phase that is under the crosshairs of the microscope and records the phase.

Nineteen thin sections (Table 2.1) were point counted at 100x magnification for the Mata volcanoes. At least one sample was point counted for each Mata Volcano. Where additional samples were available, more than one sample was used. The samples are heterogeneous. Because significant variation is visible within an individual hand sample or thin section, (Chapter Three) the portion of the sample that is being counted can affect the results. To obtain as accurate of a representation as possible, 1000 points were counted on each sample. Each point was identified as olivine, clinopyroxene, orthopyroxene, vesicle, or groundmass/glass. Crystals that were too small to identify were counted as matrix/glass.

As a test to see how much variation is possible from counting different parts of a thin section, two parts of a thin section from sample J2-413-R13 from West Mata were recounted with 250 points each. There is significant variation in this thin section, as shown by the different results from the two point counts of 250 points each. The percentage of vesicles and the phase proportions of the major mineral phases (olivine, clinopyroxene, and orthopyroxene) for both of these point counts differ from the percentages recorded in the original count of 1000 points (Tables 2.2 and 2.3). Since it consists of more points, and thus is more likely to be representative of the sample, the original point count is used for interpretation. Because the differences between the two shorter point counts represent significant variations in the sample, the results from the 1000 point count analyses should be considered carefully. Therefore, the results are used only for a general description of the samples and to group samples into general groups. Data from visual observations using a petrographic microscope and EPMA BSE images are used in conjunction with the point counting data in the following section to characterize the samples.

Table 2.1. Number of samples point counted for each Mata Volcano and samples used for point counting.

| Location | Number of Thin Sections Counted | Samples |
|---|---|---|
| East Mata | 2 | KM1024 D14-R02 |
| | | KM1024 D14-R07 |
| West Mata | 7 | J2-413-R04 |
| | | J2-413-R13a |
| | | J2-418-R01a |
| | | J2-418-R11-2 |
| | | J2-418-R18a |
| | | J2-420-R2-1 |
| | | J2-420-R17-1 |
| Mata Taha | 1 | KM1024 D16-R04 |
| Mata Ua | 2 | KM1024 D18-R01 |
| | | KM1024 D18-R02 |
| Mata Tolu | 1 | KM1024 D20-R01 |
| Mata Fa | 1 | KM1024 D21-R02 |
| Mata Ono | 3 | KM1024 D22-R01 Dark |
| | | KM1024 D22-R01 Light |
| | | KM1024 D22-R02 |
| Mata Fitu | 2 | KM1024 D23-R01 |
| | | KM1024 D23-R04 |

At least one sample was point counted for each Mata Volcano. Where additional samples were available, more than one sample was used. Note that KM1024 D22-R01 Dark (elsewhere abbreviated KM1024 D22-R01 D) and KM1024 D22-R01 Light (elsewhere abbreviated KM1024 D22-R01 L) are two thin sections from the same rock. While on the research cruise, researchers noticed that part of the rock appeared lighter than other parts. The shipboard party made two thin section billets as they were unsure if the different colors could be due to different parent magmas. Further examination of the samples suggests that the rock shares a common parent and that the difference is textural. The KM1024 D22-R01 Light thin section has fewer vesicles and more matrix (Tables 3.4 and 3.5 and Figure 3.7 in Chapter Three).

Table 2.2. Comparison of phase percentages for original point count (1000) points, and two point counts of two different parts of the thin section (250 points each) from two different parts of thin section J2-413-R13 from West Mata.

| Phase | Original Count | Count 1 | Count 2 | Average of 1 and 2 |
|---|---|---|---|---|
| Vesicle | 11 | 8 | 17 | 12 |
| Matrix | 68 | 65 | 67 | 66 |
| Olivine | 4 | 8 | 1 | 5 |
| Cpx | 12 | 12 | 3 | 7 |
| Opx | 5 | 8 | 12 | 10 |

An average of the two counts is also listed. The phase proportions vary significantly throughout the sample, as shown by differences in results of the two point counts, one and two (250 points each). Phases counted are vesicles, matrix/groundmass/glass (matrix), olivine, clinopyroxene (cpx), and orthopyroxene (opx).

Table 2.3. Comparison of percentages of crystal phases for original point count (1000) points, and two point counts from two different parts of the thin section (250 points each) for J2-413-R13 from West Mata.

| Phase | Original Count | Count 1 | Count 2 | Average of 1 and 2 |
|---|---|---|---|---|
| Olivine | 18 | 30 | 3 | 17 |
| Cpx | 57 | 42 | 13 | 27 |
| Opx | 26 | 28 | 50 | 39 |

An average of the two counts is also listed. The phase proportions vary significantly throughout the sample, as shown by differences in results of the two point counts, one and two (250 points each). Phases counted are vesicles, matrix/groundmass/glass (matrix), olivine, clinopyroxene (cpx), and orthopyroxene (opx).

## EPMA Element Mapping

The electron microprobe is capable of acquiring maps of polished rock thin sections and probe mounts. These maps show the relative concentrations of an element in the mapped region. To do this, a grid is specified and the probe analyzes each point in the grid. The relative intensities of chosen elements analyzed are not converted to absolute concentrations, but rather to relative concentrations. To obtain high precision data with the electron microprobe, much longer analyses times are required for each point. Absolute concentrations are only obtained through point analysis. (Point analysis of glass, olivine, orthopyroxene, and clinopyroxene was conducted and the methods associated with these analyses are discussed in the following sections). The intensities of identified peaks are used to color individual pixels corresponding to their relative concentration of the element of interest. The user can modify the range of intensities presented. For example, for a low concentration element, only the low intensity part of the spectrum can be examined. An example of a map is shown below (Figure 2.1).

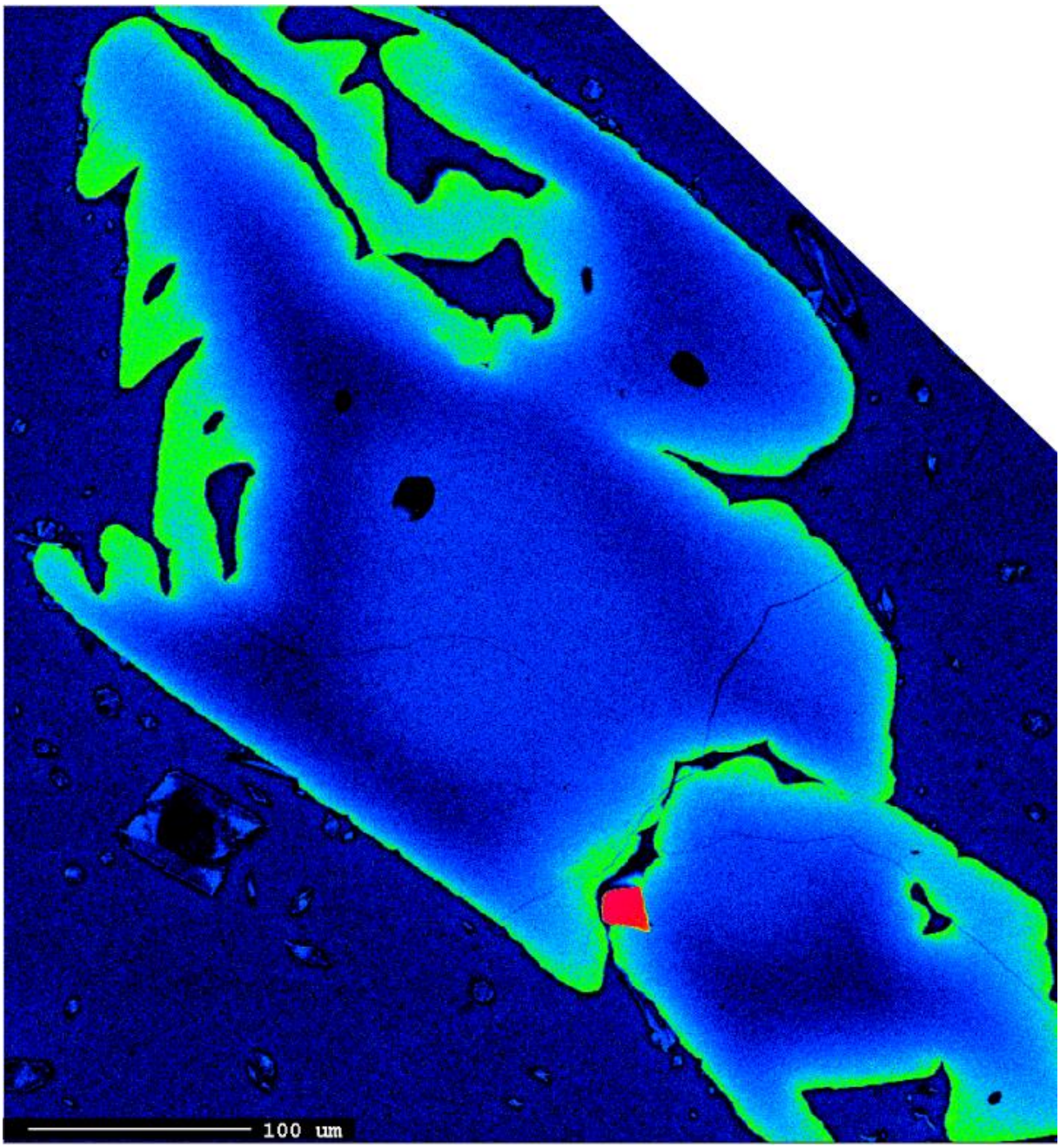


Figure 2.1. Fe map of rapidly growing olivine crystal. EPMA Fe map of an olivine from glass chip one of sample RR1211 Q331-R16 (Tolu). Black represents the lowest concentration of Fe in this map. The color scale ranges from cool colors to warm colors, with reds and pinks being the highest concentrations of Fe present in the image.

**Thin section maps**

The maps were acquired by Eric Hellebrand using the University of Hawai'i JEOL JXA-8500F five-spectrometer electron microprobe for Al, Ca, Cr, Fe, and Mg. Al and Mg were measured on TAP, Cr was measured on LiFH, Ca was measured on PETH, and Fe was measured on LiF.

Five sets of maps were acquired for the samples: J2-413-R13a, J2-413-R13b, J2-418-R18, KM1024 D20-R01, and KM1024 D23-R01. J2-413-R13a and J2-413-R13b are two thin sections made from rock sample J2-413-R13a. While both sections were mapped, all point analysis for this project is from thin section J2-413-R13a. While the elements measured and crystal assignments were the same for all of the maps acquired, analytical conditions differed.

For the West Mata samples (J2-413-R13a, J2-413-R13b, and J2-418-R18), the accelerating voltage was 15 keV, the beam current was 25 nA, and the beam diameter was 5 microns. The dwell time was 15 milliseconds per point. The grid was 1000 x 2000 points, with X and Y increments of 17 μm.

For KM1024 D20-R01 from Mata Tolu, the accelerating voltage was 20 keV, the beam current was 35 nA, and the beam diameter was 10 microns. The dwell time was 10 milliseconds per point, the two grids were 1024 x 850 points each, with X and Y increments of 20 μm. KM1024 D23-R01 from Mata Fitu was measured under the same conditions, except that two grids of 1000 by 950 points each were used, with an X and Y interval of 18 μm.

**Mineral Maps**

Four sets of maps were acquired by Eric Hellebrand using the University of Hawai'i JEOL JXA-8500F five-spectrometer electron microprobe for Al, Ca, Cr, Fe, and Mg. Al and Mg were measured on TAP, Cr was measured on LiFH, Ca was measured on PETH, and Fe was measured on LIF. The following section describes the conditions under which the maps were acquired. For convenience, an EPMA BSE image of each mineral/intergrowth is provided after the description of the conditions under which it was acquired.

For KM1024 D20-R01 Pyroxene 1 with Olivine 15 included from Mata Tolu, the accelerating voltage was 15 keV, the beam current was 25 nA, and the beam diameter was 1 microns. The dwell time was 20 milliseconds per point, the grid was 1024 x 800 points, with X and Y increments of 2 μm. Figure 2.2 shows an EPMA BSE image of the mineral cluster mapped.

For KM1024 D20-R01 Pyroxene 2 with Olivine 21 included, the accelerating voltage was 15 keV, the beam current was 25 nA, and the beam diameter was 1 microns. The dwell time was 20 milliseconds per point, the grid was 1024 x 800 points, with X and Y increments of 2.5 μm. Figure 2.3 shows an EPMA BSE image of the mineral cluster mapped.

For KM1024 D20-R01 Olivine 16 with Pyroxene 12 surrounding it, the accelerating voltage was 15 keV, the beam current was 25 nA, and the beam diameter was 1 microns. The dwell time was 20 milliseconds per point, the grid was 1024 x 1024 points, with X and Y increments of 1 μm. Figure 2.4 shows an EPMA BSE image of the mineral cluster mapped.

For KM1024 D20-R01 Pyroxene 13, the accelerating voltage was 15 keV, the beam current was 25 nA, and the beam diameter was 1 microns. The dwell time was 20 milliseconds per point, the grid was 1024 x 800 points, with X and Y increments of 1 μm. Figure 2.5 shows an EPMA BSE image of the mineral cluster mapped.

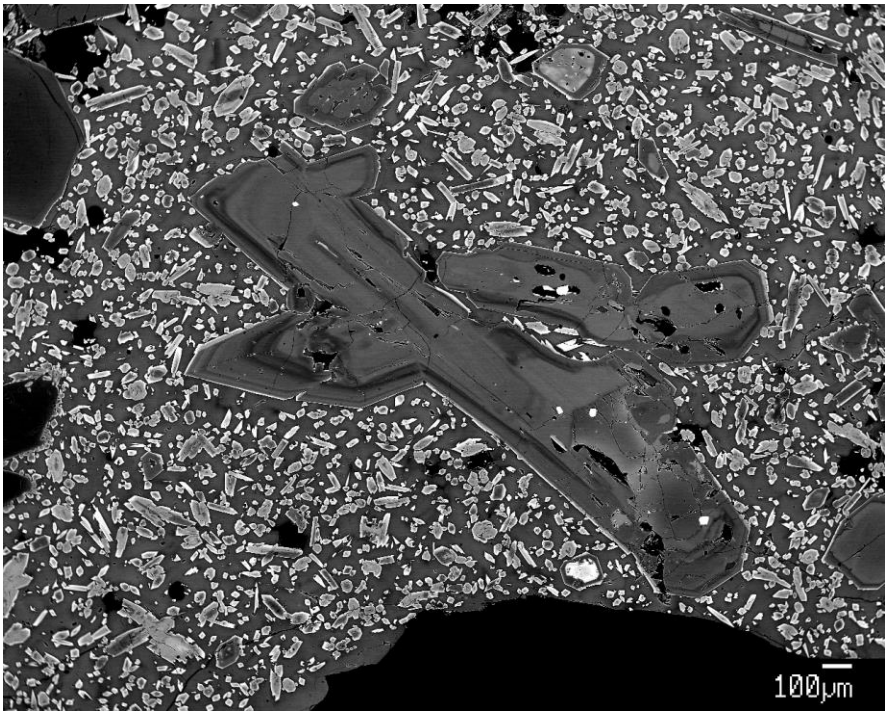


Figure 2.2. EPMA BSE image of KM1024 D20-R01 Pyroxene 1 with Olivine 15 included

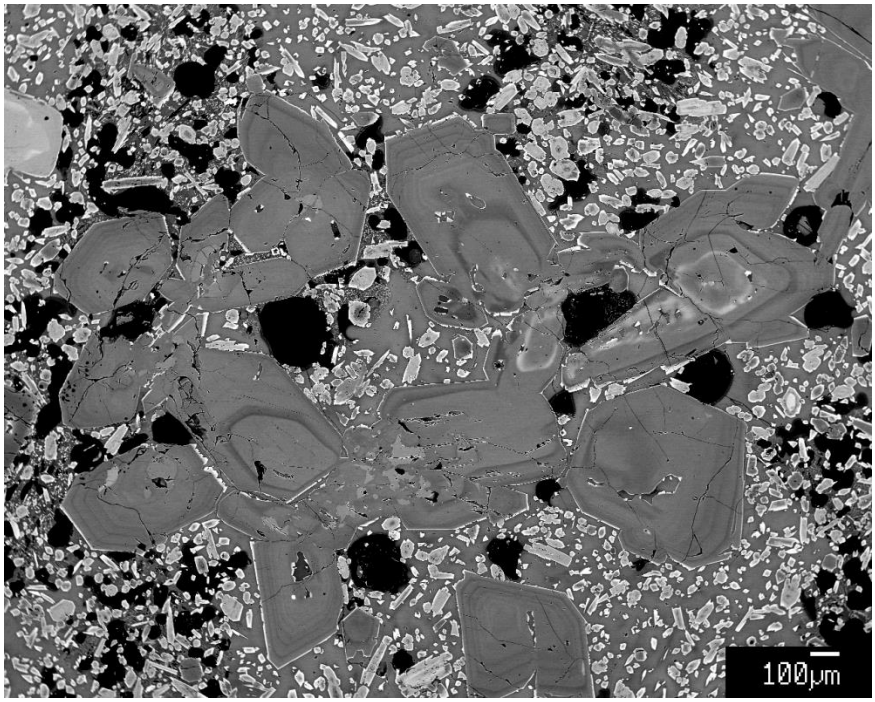


Figure 2.3. EPMA BSE image of KM1024 D20-R01 Pyroxene 2 with Olivine 21 included

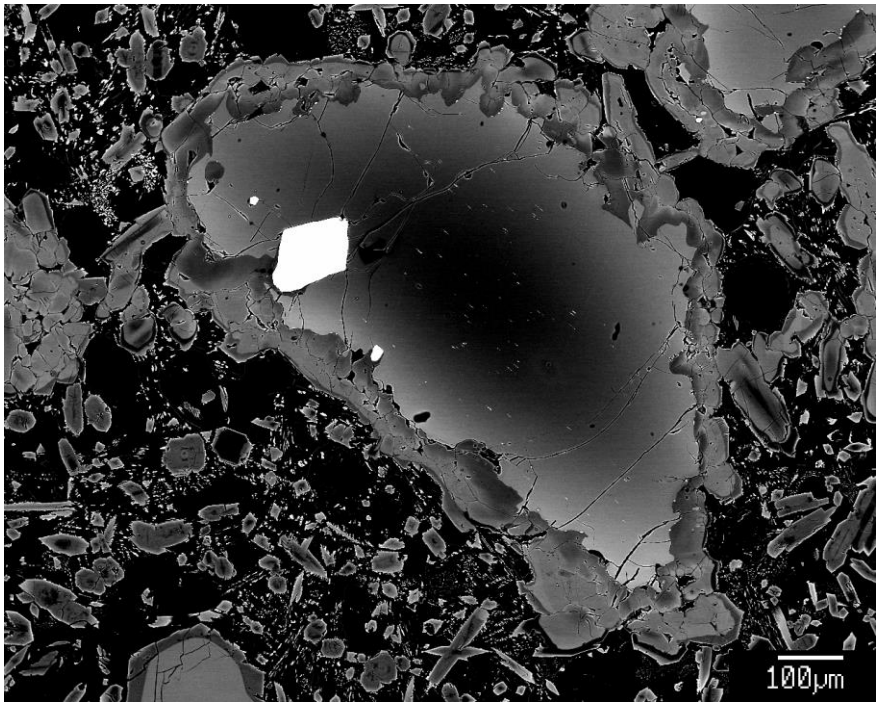


Figure 2.4. EPMA BSE image of KM1024 D20-R01 Olivine 16 with Pyroxene 12

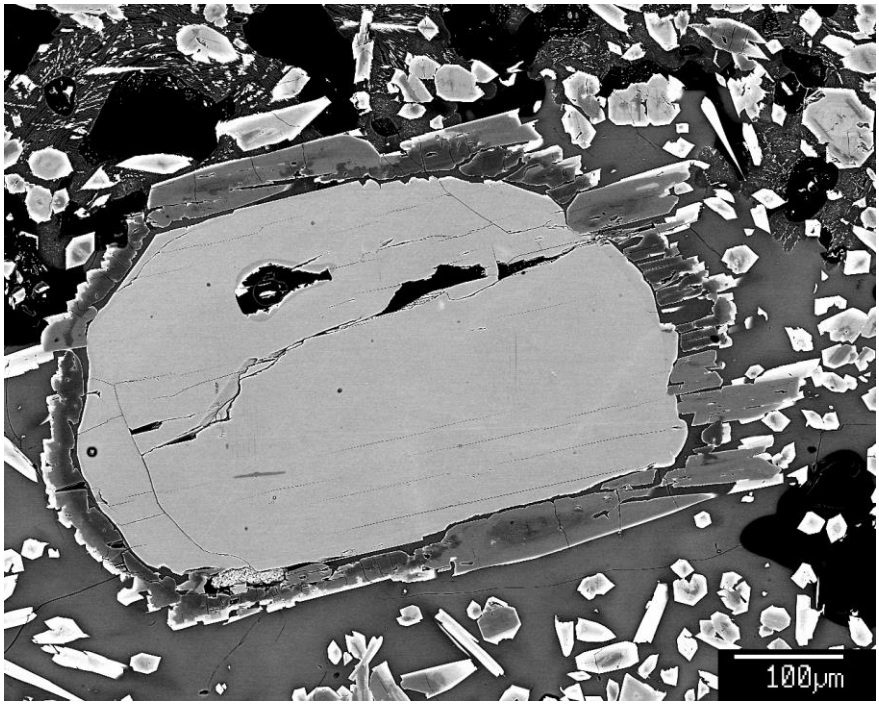


Figure 2.5. EPMA BSE image of KM1024 D20-R01 Pyroxene 13

**Olivine P Maps**

The maps were acquired by Eric Hellebrand using the University of Hawai'i JEOL JXA-8500F five-spectrometer electron microprobe for Al, P, Ca, and Fe. Al was measured on TAP, P was measured on two PETH crystals, Fe was measured on LIF, and Ca was measured on PETJ.

The accelerating voltage was 15 keV, the beam current was 200 nA, and the beam was a focused beam. The dwell time was 100 milliseconds per point, the grid was 1024 x 950 points, with X and Y increments of 0.5 μm.

**Electron Microprobe Glass Analysis**

Glass was chipped from rock samples and washed at sea. In the lab, approximately five to ten glass chips per sample were selected under a binocular microscope. Glassy, crystal free, un-altered chips were selected. The chips were washed in an ultrasonic bath. Chips were mounted in 1-inch round epoxy probe mounts, polished, and carbon coated.

Samples were analyzed using the University of Hawai'i JEOL JXA-8500F five-spectrometer electron microprobe over a series of runs. $SiO_2$, $TiO_2$, $Al_2O_3$, FeO, MnO, CaO, $Na_2O$, $K_2O$, $P_2O_5$, Cl, and $SO_3$ were measured in all runs. Count times and spectrometer assignments were the same for every run and are included in the Table 2.4.

Analytical conditions were the same for most samples. All samples were measured with an accelerating voltage of 15 keV and a beam current of 10 nA. Most samples were measured with a beam diameter of 10 microns. In a few cases, samples were too crystalline to be measured at 10 microns and were measured with a smaller beam diameter. Generally, three points were measured on each of three glass chips for each sample and the reported average for a sample is the average of these nine points. Appendix A reports analytical conditions for the samples. Standards were measured before and after every three samples. Three points on two different standards, VG-2 and STG-56, were measured. To avoid the problem of Na loss, Na was measured first. Armstrong/Love Scott ZAF or Phi-Rho-Z calculations were used for matrix

corrections (Armstrong 1988). A linear background correction was used for all elements except for Cl, for which an exponential correction was used.

Standards used for data reduction were kept as consistent as possible between runs. During each run, standards were assigned to produce the highest quality data, as measured by deviation of standards measured as unknowns from accepted values. At the end of data collection, the standards that were run as unknowns during each run were compared and standard assignments were changed if necessary to minimize offset between various runs. This is discussed in detail in Appendix A. Table 2.5 lists the standards used for glass analysis.

Drift corrections were applied to glass runs where necessary. A total of sixteen samples were drift corrected for $SiO_2$. All other elements were kept constant. Linear drift corrections were applied based on the measured concentration of the standards measured before and after a set of three samples. On average, samples that were drift corrected were affected by about half a weight percent. The effect of the drift corrections is minor. $SiO_2$ was affected by less than 2% in all samples where a drift correction was applied. Chapter Four lists the samples that were drift corrected (Table 4.4).

Table 2.4. Count times (in seconds) and crystal assignments for elements analyzed in glass chips.

| Element | Crystal | On Peak | Off-peak |
|---|---|---|---|
| **Si** | TAP | 50 | 50 |
| **Ti** | LiFH | 40 | 40 |
| **Al** | TAP | 60 | 60 |
| **Fe** | LiFH | 30 | 30 |
| **Mn** | LiFH | 40 | 40 |
| **Mg** | TAP | 80 | 80 |
| **Ca** | PETH | 30 | 30 |
| **Na** | TAP | 30 | 30 |
| **K** | PETJ | 40 | 40 |
| **P** | PETH | 30 | 30 |
| **Cl** | PETJ | 70 | 70 |
| **S** | PETH | 40 | 40 |

Table 2.5. Standard names, assigned standard numbers, and references for glass analysis.

| Assigned Number | Lab Standard Number | Standard Name | Official Standard Name | Source |
|---|---|---|---|---|
| 1 | 135 | Synthetic Glass, STG-56 | STG-56 | Unknown |
| 2 | 134 | Juan de Fuca Glass, VG-2 | USNM 111240/51 | Jarosewich *et al.* (1980) |
| 3 | 133 | Makaopuhi Lake Glass, A99 | USNM 113498/1 | Jarosewich *et al.* (1980) |
| 4 | 111 | Sphene glass | | Eggler, personal communication (unpublished) |
| 5 | 102 | Garnet, Verma | | Jones, personal communication (unpublished) |
| 6 | 115 | Amelia Albite | Amelia Albite (UCLA) | Jones, personal communication (unpublished) (after Deer *et al.*, 1966) |
| 7 | 119 | Orthoclase, OR-1 | 5-168 | Goldich *et al.* (1967) |
| 8 | 176 | Fluor-apatite | USNM 104021 | Jarosewich *et al.* (1980) |
| 9 | 143 | Troilite FeS (Staunton Meteorite) | | Unknown |
| 10 | 178 | Scapolite | USNM R6600-1 | Jarosewich *et al.* (1980) |

**Revised Standard Values for Synthetic Glass STG-56 Standard.**

Synthetic glass STG-56 (STG-56) is an in-house glass standard with an unknown source. Three points were measured on STG-56 between every three samples in each of the glass runs. STG-56 was analyzed a total of 188 times. Table 2.6 displays accepted and measured values for STG-56. Because one of the microprobe sessions (Session 3) produced consistently lower values for CaO, measurements from this microprobe session were not used in calculating the average measured value for CaO. Figure 2.6 depicts differences between accepted and measured values for the elements measured. See Appendix B for more information.

Table 2.6. Accepted and Measured values for STG-56. I recommend using the newly measured values for STG-56.

| | SiO2 | $TiO_2$ | $Al_2O_3$ | FeO | MnO | MgO | CaO | $Na_2O$ | $K_2O$ | $P_2O_5$ | Cl | $SO_3$ | Total |
|---|---|---|---|---|---|---|---|---|---|---|---|---|---|
| Accepted Values | 56.0 | 1.3 | 16.77 | 8.8 | 0.2 | 4.0 | 8.0 | 3.3 | 1.2 | 0.15 | | | |
| Measured Values | 56.04 | 1.33 | 17.06 | 8.76 | 0.22 | 3.88 | 8.14 | 3.39 | 1.20 | 0.15 | 0.01 | 0.00 | 100.14 |
| Standard Deviation | 0.33 | 0.04 | 0.14 | 0.09 | 0.02 | 0.03 | 0.07 | 0.05 | 0.02 | 0.03 | 0.00 | 0.01 | 0.46 |
| Standard Error | 0.02 | 0.00 | 0.01 | 0.01 | 0.00 | 0.00 | 0.01 | 0.00 | 0.00 | 0.00 | 0.00 | 0.00 | 0.03 |
| n | 188 | 188 | 188 | 188 | 188 | 188 | 140 | 188 | 188 | 188 | 188 | 188 | 188 |

STG-56 is an in house standard with an unknown source.

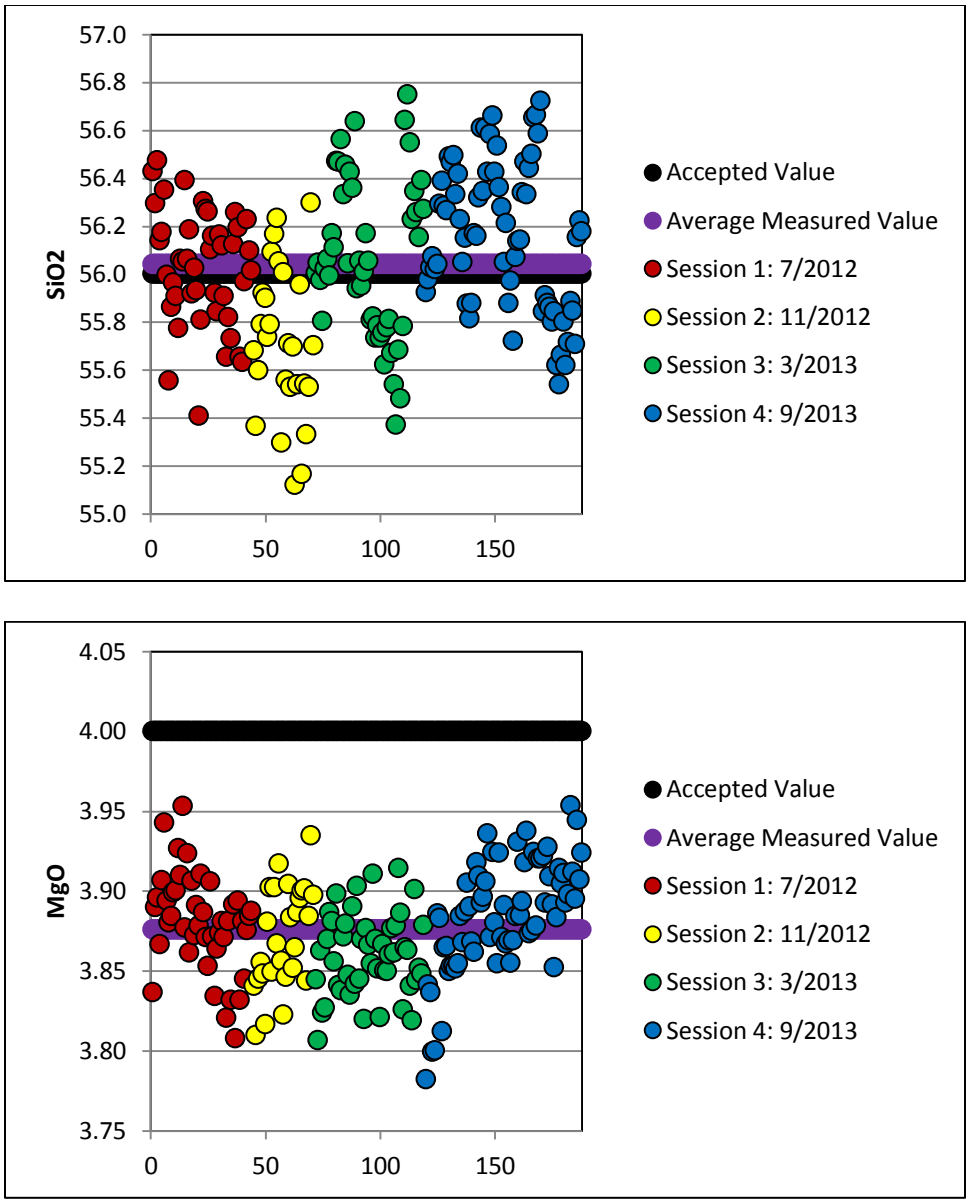


Figure 2.6. Measured values for STG-56 comparing the average measured value and the accepted value for $SiO_2$ and MgO. Each point is a single spot analysis. Some elements are offset, such as MgO, while others are not, such as $SiO_2$.

**Data quality and uncertainty.**

Data quality is measured by comparisons between accepted standard values and measured standard values for VG-2 when run as an unknown. Table 2.7 reports these values and uncertainties associated with glass measurements.

Table 2.7. Reported standard quality data using measurements of VG-2 as an unknown.

| | $SiO_2$ | $TiO_2$ | $Al_2O_3$ | FeO | MnO | MgO | CaO | $Na_2O$ | $K_2O$ | $P_2O_5$ | Cl | $SO_3$ |
|---|---|---|---|---|---|---|---|---|---|---|---|---|
| **Accepted Standard Value** | 50.81 | 1.85 | 14.06 | 11.84 | 0.22 | 6.71 | 11.12 | 2.62 | 0.19 | 0.2 | 0.03 | 0.14 |
| **Average Measured Value** | 50.76 | 1.88 | 14.11 | 11.87 | 0.21 | 6.73 | 11.12 | 2.67 | 0.19 | 0.20 | 0.03 | 0.14 |
| **Standard Deviation** | 0.27 | 0.05 | 0.12 | 0.11 | 0.02 | 0.05 | 0.11 | 0.04 | 0.01 | 0.03 | 0.01 | 0.01 |
| **Standard Deviation/ Square Root of 9** | 0.09 | 0.02 | 0.04 | 0.04 | 0.01 | 0.02 | 0.04 | 0.01 | 0.00 | 0.01 | 0.00 | 0.00 |
| **Standard Deviation/ Square Root of 212** | 0.02 | 0.00 | 0.01 | 0.01 | 0.00 | 0.00 | 0.01 | 0.00 | 0.00 | 0.00 | 0.00 | 0.00 |

Standard Error is calculated two ways: 1. dividing by the square root of 9, the typical number of measurements taken for each individual sample, and 2. dividing by 212, the number of total measurements of VG-2 as an unknown. Accepted standard values for VG-2 are from Jarosewich *et al*. (1980), except for Cl and S. Cl and S were measured by Jenner and O'Neill (2012).

## Microprobe Olivine Analysis

Olivine crystals were measured in thin sections prepared at UH and by Wagner Petrographic. Thin sections were carbon coated at UH. Samples were analyzed using the University of Hawai'i JEOL JXA-8500F five-spectrometer electron microprobe over a series of runs. Samples were measured with an accelerating voltage of 20 keV and a beam current of 200 nA and a beam diameter of 10 microns. $SiO_2$, FeO, NiO MnO, MgO, and CaO were measured in all runs. Count times and spectrometer assignments are included in Table 2.8. Standards used for olivine analysis are listed in Table 2.9. Drift corrections were not used. Armstrong/Love Scott ZAF or Phi-Rho-Z calculations were used for matrix corrections (Armstrong, 1988). A linear background correction was used for all elements.

### Data quality and uncertainty

Data quality is measured by comparisons between accepted standard values and measured standard values for San Carlos Olivine and Springwater Olivine run as unknowns. San Carlos Olivine was measured 124 times and Springwater Olivine was measured 132 times. The following Tables 2.10 and 2.11 report these values and uncertainties associated with olivine measurements. The following chapters will refer to measurements of San Carlos Olivine when discussing data quality.

Table 2.8. Count times and crystal assignments for all elements analyzed in olivine crystals.

| Element | Crystal | On Peak | Off-Peak |
|---|---|---|---|
| **Si** | TAP | 100 | 90 |
| **Fe** | LiF | 30 | 30 |
| **Ni** | LiFH | 100 | 90 |
| **Mn** | LiF | 60 | 60 |
| **Mg** | TAP | 100 | 90 |
| **Ca** | PETH | 100 | 90 |

Table 2.9. Standard names, assigned standard numbers, and references for olivine analysis.

| Assigned Number | Lab Standard Number | Standard Name | Official Standard Name | Source |
|---|---|---|---|---|
| 5 | 102 | Garnet, Verma | | Jones, personal communication (unpublished) |
| 11 | 106 | San Carlos Olivine | USNM 111312/444 | Jarosewich *et al*. 1980 |
| 12 | 103 | Springwater Olivine | USNM 2366 | Jarosewich *et al*. 1980 |
| 13 | 110 | Kakanui Augite | USNM 122142 | Jarosewich *et al*., 1980 and Klügel *et al*., 2005 |

Values for Kakanui Augite are from Jarosewich *et al*. (1980) except for values for $Al_2O_3$, $Cr_2O_3$, and FeO, which are from Klügel *et al*. (2005).

Table 2.10. Reported standard quality data using measurements of San Carlos Olivine as an unknown.

| | $SiO_2$ | FeO | NiO | MnO | MgO | CaO | Total |
|---|---|---|---|---|---|---|---|
| **Accepted value for San Carlos Olivine** | 40.81 | 9.55 | 0.37 | 0.14 | 49.42 | <0.05 | 100.29 |
| **Average measured value for San Carlos Olivine** | 40.40 | 9.50 | 0.370 | 0.136 | 49.32 | 0.074 | 99.79 |
| **Standard deviation** | 0.39 | 0.07 | 0.004 | 0.003 | 0.27 | 0.006 | 0.57 |
| **Standard error** | 0.01 | 0.01 | 0.000 | 0.000 | 0.02 | 0.001 | 0.05 |

Table 2.11. Reported standard quality data using measurements of Springwater Olivine as an unknown.

| | $SiO_2$ | FeO | NiO | MnO | MgO | CaO | Total |
|---|---|---|---|---|---|---|---|
| **Accepted value for Springwater Olivine** | 38.95 | 16.62 | | 0.30 | 43.58 | | 99.47 |
| **Average measured value for Springwater Olivine** | 39.04 | 16.59 | 0.001 | 0.307 | 43.56 | 0.000 | 99.49 |
| **Standard deviation** | 0.35 | 0.11 | 0.001 | 0.004 | 0.22 | 0.001 | 0.51 |
| **Standard error** | 0.03 | 0.01 | 0.01 | 0.000 | 0.02 | 0.000 | 0.04 |

## Microprobe Clinopyroxene and Orthopyroxene Analysis

Orthopyroxene and clinopyroxene crystals were measured in the same runs from thin sections prepared at UH and by Wagner Petrographic. Thin sections were carbon coated at UH. Samples were analyzed using the University of Hawai'i JEOL JXA-8500F five-spectrometer electron microprobe over a series of runs. Samples were measured with an accelerating voltage of 15 keV and a beam current of 15 nA and a beam diameter of 10 microns. $SiO_2$, $TiO_2$, $Al_2O_3$, $Cr_2O_3$, FeO, MnO, CaO, $Na_2O$, and $K_2O$ were measured in all runs. Count times and spectrometer assignments are included in Table 2.12. Table 2.13 lists the standards used for pyroxene analysis. Armstrong/Love Scott ZAF or Phi-Rho-Z calculations were used for matrix corrections (Armstrong, 1988). Manual drift corrections of microprobe data were not used. A linear background correction was used for all elements.

### Data quality and uncertainty

Data quality is measured by comparisons between accepted standard values and measured standard values for Kakanui Augite (measured 128 times) and San Carlos Olivine (measured 109 times) run as unknowns. Tables 2.14 and 2.15 report these values and uncertainties associated with olivine measurements. The following chapters will refer to measurements of Kakanui Augite when discussing data quality.

Table 2.12. Count times and crystal assignments for all elements analyzed in orthopyroxene and clinopyroxene crystals.

| Element | Crystal | On Peak | Off-Peak |
|---|---|---|---|
| **Si** | TAP | 30 | 30 |
| **Ti** | LiFH | 30 | 30 |
| **Al** | TAP | 30 | 30 |
| **Cr** | LiFH | 30 | 30 |
| **Fe** | LiF | 30 | 30 |
| **Mn** | LiF | 30 | 30 |
| **Mg** | TAP | 30 | 30 |
| **Ca** | PETH | 30 | 30 |
| **Na** | TAP | 30 | 30 |
| **K** | PETH | 30 | 30 |

Table 2.13 . Standard names, assigned standard numbers, and references for pyroxene analysis.

| Assigned Number | Lab Standard Number | Standard Name | Official Standard Name | Source |
|---|---|---|---|---|
| 4 | 111 | Sphene Glass | | Eggler, personal communication (unpublished) |
| 5 | 102 | Garnet, Verma | | Jones, personal communication (unpublished) |
| 6 | 115 | Amelia Albite | Amelia Albite (UCLA) | Jones, personal communication (unpublished) after Deer *et al*. (1966) |
| 7 | 119 | Orthoclase, OR-1 | 5-168 | Goldich *et al*. (1967) |
| 11 | 106 | San Carlos Olivine | USNM 111312/444 | Jarosewich *et al*. (1980) |
| 13 | 110 | Kakanui Augite | USNM 122142 | Jarosewich *et al*. (1980) and Klugel *et al*. (2005) |
| 14 | 107 | Hypersthene (Johnstown) | USNM 746 | Jarosewich *et al*. (1980) |
| 15 | 114 | Diopside-1 | USNM 117733 | Jarosewich *et al*. (1980) |
| 16 | 112 | Chromite | USNM 117075 | Jarosewich *et al*. (1980) and Barnes (1998) |

Values for Kakanui Augite are from Jarosewich *et al*. (1980) except for values for $Al_2O_3$, $Cr_2O_3$, and FeO, which are from Klügel *et al*. (2005). Values for chromite are from Jarosewich *et al*., (1980) except for $TiO_2$, which was not measured by Jarosewich *et al*., (1980). The standard $TiO_2$ value is from Barnes (1998).

Table 2.14. Reported standard quality data using measurements of Kakanui Augite as an unknown.

| | $SiO_2$ | $TiO_2$ | $Al_2O_3$ | $Cr_2O_3$ | FeO | MnO | MgO | CaO | $Na_2O$ | $K_2O$ |
|---|---|---|---|---|---|---|---|---|---|---|
| **Accepted Value** | 50.73 | 0.74 | 8.72 | 0.15 | 6.31 | 0.13 | 16.65 | 15.82 | 1.27 | 0.00 |
| **Average Measured Value** | 49.94 | 0.87 | 8.70 | 0.15 | 6.26 | 0.13 | 16.29 | 15.86 | 1.30 | 0.00 |
| **Standard Deviation** | 0.57 | 0.03 | 0.07 | 0.02 | 0.13 | 0.02 | 0.26 | 0.11 | 0.03 | 0.00 |
| **Standard Error** | 0.05 | 0.00 | 0.01 | 0.00 | 0.01 | 0.00 | 0.02 | 0.01 | 0.00 | 0.00 |

All accepted values are from Jarosewich *et al*. (1980) except for values for $Al_2O_3$, $Cr_2O_3$, and FeO, which are from Klügel *et al*. (2005).

Table 2.15. Reported standard quality data using measurements of San Carlos Olivine as an unknown.

| | $SiO_2$ | $TiO_2$ | $Al_2O_3$ | $Cr_2O_3$ | FeO | MnO | MgO | CaO | $Na_2O$ | $K_2O$ |
|---|---|---|---|---|---|---|---|---|---|---|
| **Accepted Value** | 40.81 | | | | 9.55 | 0.14 | 49.42 | <0.05 | | |
| **Average Measured Value** | 40.54 | 0.01 | 0.03 | 0.01 | 9.58 | 0.14 | 49.20 | 0.09 | 0.01 | 0.00 |
| **Standard Deviation** | 0.33 | 0.01 | 0.01 | 0.01 | 0.16 | 0.02 | 0.42 | 0.01 | 0.01 | 0.01 |
| **Standard Error** | 0.03 | 0.00 | 0.00 | 0.00 | 0.01 | 0.00 | 0.04 | 0.00 | 0.00 | 0.00 |

All accepted values are from Jarosewich *et al*. (1980).

## XRF Whole Rock Major and Trace Element Analysis

Samples were crushed by two jaw crushers to pieces less than 1 cm in diameter and washed. The rock chips were washed and handpicked to remove any altered pieces. Next samples were powdered in an aluminum mill except for two samples (RR1211 Q325-R03 and KM1024 D22-R02) that were processed in a tungsten carbide ball mill due to the small amount of sample available. Plugs from these powders were made at UH by Chuck Fraley. Major elements were measured on fused disks made by mixing powdered sample with lithium metaborate and igniting the mix at 900°C. Trace elements were analyzed on pressed pellets. 5.5g of powdered sample is pressed into a pellet sheathed with boric acid. XRF analysis was conducted at UH by Eric Hellebrand and John Sinton using a Siemens 303 AS XRF spectrometer. An Rh-target, end-window x-ray tube was used. Multiple natural rock standards were used for calibration. Standards, including BHVO-1, AGV-1, and BIR-1, were run as unknowns throughout the runs. Data for AGV-1 is provided in Table 2.16. Major elements are analyzed by the methods of Norrish and Chappell (1977). Background, line interference, and matrix absorption corrections were applied to peak intensities for trace elements. These corrections are similar to those of Chappell (1992). Accuracy and precision data for standards measured as unknowns by this method were previously reported by Sinton et al. (2005).

Some offsets were observed in standard data for certain elements on some of the runs. Ken Rubin corrected raw XRF data for these offsets. Major elements that required adjustments are Na and Si. For trace elements, corrections were made for Zr, Ni, Nb, and V where necessary.

### Data quality and uncertainty

Data quality for XRF whole rock major element data is measured by comparisons between accepted standard values and measured standard values for AGV-1, run as unknowns. AGV-1 was measured 31 times. Table 2.16 reports these values and uncertainties associated with XRF whole rock measurements. Data quality for XRF whole rock trace element data is measured by comparisons between accepted standard values and measured standard values for AGV-1, run as unknowns. AGV-1 was measured 6 times.

Generally, measured values match literature data well. Cr is the only element for which significant variation from the standard value is observed. The Cr concentration in standard AGV-1 is near the detection limit of the XRF (Eric Hellebrand, personal communication). These samples have much higher values of Cr and are considered more accurate than those for AGV-1. Measured Cr values for standards with higher concentrations of Cr match well with accepted values. For example the average measured value for Cr in BHVO-1 is 309 ppm, with a standard deviation of 5.73 and a standard error of 2.34. BHVO-1 was measured six times. Zellmer *et al*. (2008) measured Cr in BHVO-1 to be 308 ppm by XRF (also at the University of Hawaii). This is consistent with standard measurements by others. Similarly the average measured value of Cr in W2 is 106 ppm with a standard deviation of 0.70 and a standard error of 0.32. W2 was measured 5 times. Zellmer *et al*. (2008) measured the concentration of Cr in W2 at 104 ppm by XRF. This is consistent with standard measurements by others. Table 2.17 reports these values and uncertainties associated with XRF whole rock measurements.

Table 2.16. Reported standard quality data using measurements of AGV-1 as an unknown for XRF whole rock major element analysis.

| | $SiO_2$ | $TiO_2$ | $Al_2O_3$ | FeO | MnO | MgO | CaO | $Na_2O$ | $K_2O$ | $P_2O_5$ |
|---|---|---|---|---|---|---|---|---|---|---|
| **Accepted Value** | 60.25 | 1.1 | 17.4 | 6.34 | 0.10 | 1.52 | 4.84 | 4.31 | 2.96 | 0.52 |
| **Average Measured Value** | 60.65 | 1.08 | 17.44 | 6.24 | 0.10 | 1.65 | 5.05 | 4.33 | 3.00 | 0.54 |
| **Standard Deviation** | 0.29 | 0.01 | 0.15 | 0.04 | 0.00 | 0.15 | 0.03 | 0.44 | 0.02 | 0.04 |
| **Standard Error** | 0.05 | 0.00 | 0.03 | 0.01 | 0.00 | 0.03 | 0.00 | 0.08 | 0.00 | 0.01 |

All accepted values are from Guevara *et al*. (2005).

Table 2.17. Reported standard quality data using measurements of AGV-1 as an unknown for XRF whole rock incompatible trace element analysis (in ppm).

| | Nb | Zr | Y | Sr | Rb | Ba | Co | Cr | V | Zn | Ni | Sc |
|---|---|---|---|---|---|---|---|---|---|---|---|---|
| **Accepted Value** | 14.6 | 231 | 19 | 660 | 66 | 1200 | 17 | 9.4 | 119 | 87 | 20 | 12.3 |
| **Average Measured Value** | 14.6 | 236 | 19.5 | 660 | 68.2 | 1239 | 16 | 17.2 | 121 | 88.5 | 21.3 | 14.5 |
| **Standard Deviation** | 0.35 | 4.03 | 0.42 | 2.37 | 0.23 | 23.4 | 1.37 | 1.55 | 2.57 | 1.05 | 2.65 | 0.9 |
| **Standard Error** | 0.14 | 1.65 | 0.17 | 0.97 | 0.09 | 9.54 | 0.56 | 0.63 | 1.05 | 0.43 | 1.08 | 0.37 |

Standard values for Nb, Zr, Y, Sr, Ba, V, Zn, and Sc are based on a compilation of standard values used by the UH probe lab (Eric Hellebrand, personal communication). Values for Co, Cr, Ni and Rb are from Hanano *et al*. (2010).

# CHAPTER 3. MINERALOGY AND PETROLOGY

This chapter summarizes petrographic data from the Mata Volcano samples. This chapter includes observations of rock and mineral textures, point counts, thin section and mineral EPMA maps, EPMA BSE images, and textures and geochemistry of major mineral phases.

## Petrographic Analysis

### Methods

This section relies on visual analysis by petrographic microscope, visual analysis of EPMA BSE images and EPMA element distribution maps and point counting to describe Mata samples. Five thin sections were mapped with the microprobe at UH Manoa, as discussed in the prior chapter. Two thin sections were from West Mata sample J2-413-R13. An additional sample from West Mata, J2-418-R18 was mapped. Two northern Mata samples were mapped: KM1024 D20-R01 from Tolu and KM1024 D23-R01 from Fitu. All maps were made by Eric Hellebrand using the University of Hawaii at Manoa's microprobe.

Nineteen thin sections were point counted for the Mata volcanoes. The samples are heterogeneous. Significant variation is visible within an individual hand sample or thin section, as can be seen in the EPMA Mg maps (Figures 3.1-3.5). Therefore the section of the sample selected for point counting can affect the result (See Chapter Two for more details)

More detailed qualitative analysis of matrix by EPMA BSE images allowed further characterization of the samples. Images of major crystal phases were also acquired. This data will be mentioned here but discussed in further detail in the Olivine and Pyroxene sections of this chapter.

### General Findings

Resing et al. (2011) provide a petrographic description of newly erupted West Mata lavas. They reported vesicular (10 to 40%) samples with abundant crystals of olivine and

pyroxene (21 and 28% crystallinities in two point counted samples), but lacking plagioclase phenocrysts. Orthopyroxene is the most common phase followed by roughly equal percentages of clinopyroxene and olivine. Crystals can be euhedral, occur in intergrown glomerocrysts, and can be zoned. Matrix textures range from glassy to glassy microlitic, with euhedral groundmass crystals.

This project finds similar textures in a large number of samples from West Mata, including samples from previous eruption(s). Additionally, samples from the Northern Matas and East Mata are now included and are found to often be broadly similar to those at West Mata. The following section provides more detail and discusses similarities and differences in textures of Mata samples.

In general, the Mata volcanoes erupt vesicular, crystal rich lavas. Samples from West Mata and the Northern Matas contain 8-38% vesicles. However, one sample from East Mata only contains 2% vesicles. The total percentage of crystals present ranges from 5-28% for samples from West Mata and the Northern Matas. For East Mata, the percentage of phenocrysts is lower, only 2-3%, but the matrix is almost entirely crystalline, consisting of intergrown microlites (Tables 3.4 and 3.5, Figures 3.6-3.7). The lavas consist primarily of volcanic glass or a matrix of volcanic glass and microphenocrysts and secondarily of crystals. The main crystal phases are olivine, clinopyroxene, orthopyroxene, with less than a percent of Cr-spinel. East Mata samples are different from other volcano samples because of the almost total absence of olivine.

The following EPMA Mg maps (Figures 3.1-3.5) for Mata samples show examples of textures present in Mata volcano samples. The samples shown are vesicular. Vesicle sizes and shapes vary, but vesicles are generally rounded. The most common phase in the samples is a glassy matrix. Detailed EPMA BSE images of the matrix were obtained and will be discussed later in this section. These maps show the three main mineral phases present: olivine, clinopyroxene, and orthopyroxene. These minerals occur both as individuals and as complicated intergrowths or inclusions. Textures range from euhedral to anhedral inclusions. A range of

mineral textures can be present, even within an individual thin section. Cr-spinel is not visible at this magnification. For more detail on mineral textures and compositions see Olivine Section and Pyroxene Section of this chapter. Tables 3.1 and 3.2 and Figures 3.6-3.7 show the proportions of phases counted and crystal proportions at West Mata and at the Northern Matas. East Mata is not included in Figures 3.6-3.7 as very few counts were phenocrysts and thus the relative phenocryst proportions are not representative of the actual percentages of these phenocrysts in the rocks. The major phase in these samples was a cryptocrystalline groundmass consisting of clinopyroxene and orthopyroxene crystals that were too small to count using the petrographic microscope.

Textures shown in the EPMA maps are typical of most of the samples from West Mata and the Northern Matas. Some samples, particularly those from East Mata (KM1024 D14-R02 and KM1024 D14-R07) and Taha (KM1024 D16-R04) have a matrix that is more crystalline than glassy. KM1024 D14-R07 is also less vesicular than the other samples. The samples shown have three main mineral phases: olivine, clinopyroxene, and orthopyroxene. These three main mineral phases are the main mineral phases for most samples. The East Mata samples are an exception because they contain almost no olivine.

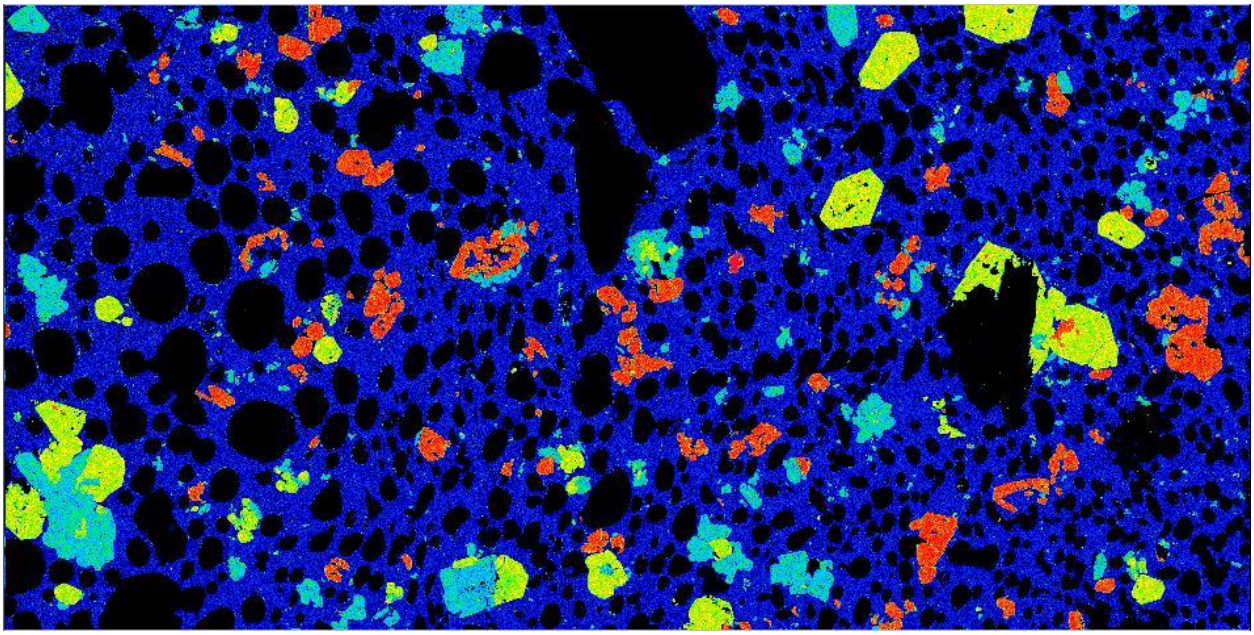

Figure 3.1. EPMA Mg Map for sample J2-418-R18 from West Mata. The three main mineral phases can be seen in this map, olivine (orange), clinopyroxene (light blue), and orthopyroxene (green). These minerals can occur individually or in intergrowths. The matrix is glassy (dark blue) and often includes microlites. Vesicles are present (vesicles are black).

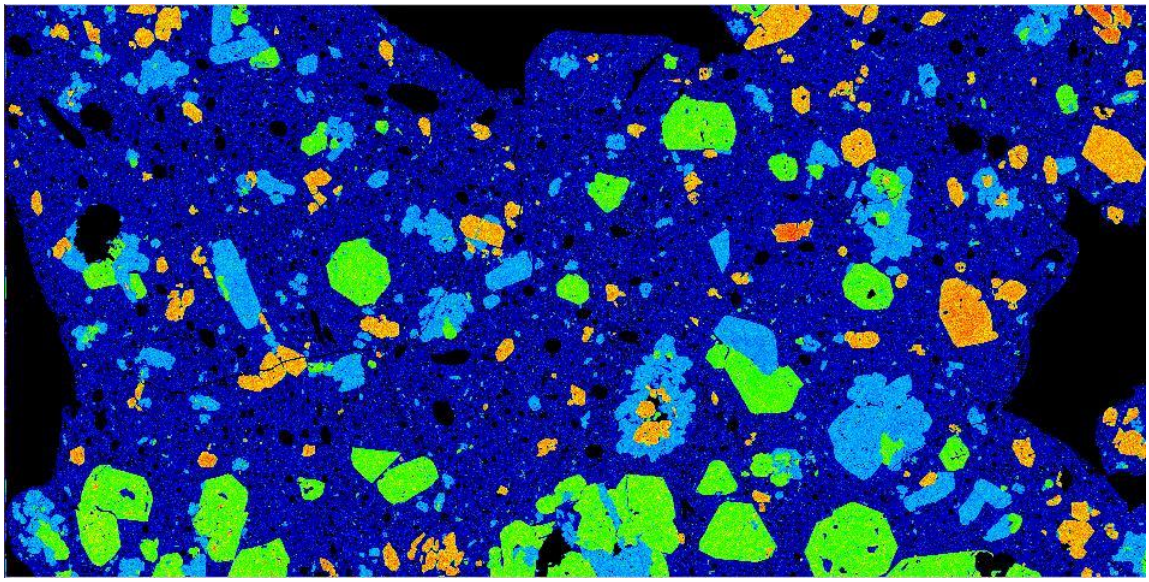

Figure 3.2. EPMA Mg Map for sample J2-413-R13a from West Mata. The three main mineral phases can be seen in this map, olivine (orange), clinopyroxene (light blue), and orthopyroxene (green). These minerals occur individually or in intergrowths. The matrix is glassy (dark blue) and includes microlites. Vesicles are present (vesicles are black).

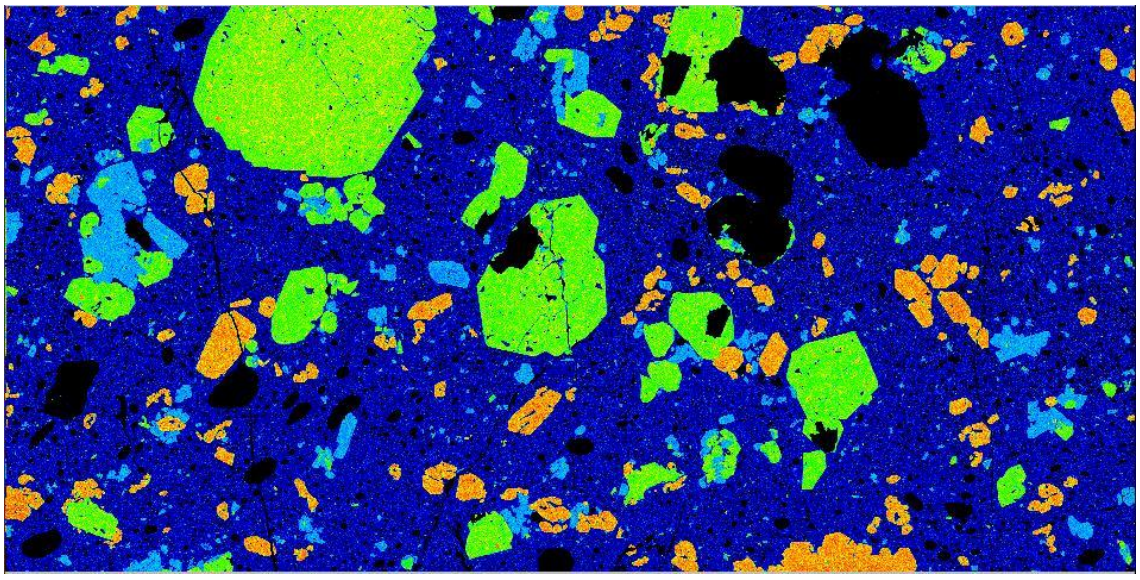

Figure 3.3. EPMA Mg Map for sample J2-413-R13b from West Mata. The three main mineral phases can be seen in this map: olivine (orange), clinopyroxene (light blue), and orthopyroxene (green). These minerals can occur individually or in intergrowths. The matrix is glassy (dark blue) and often includes microlites. Vesicles are present (vesicles are black).

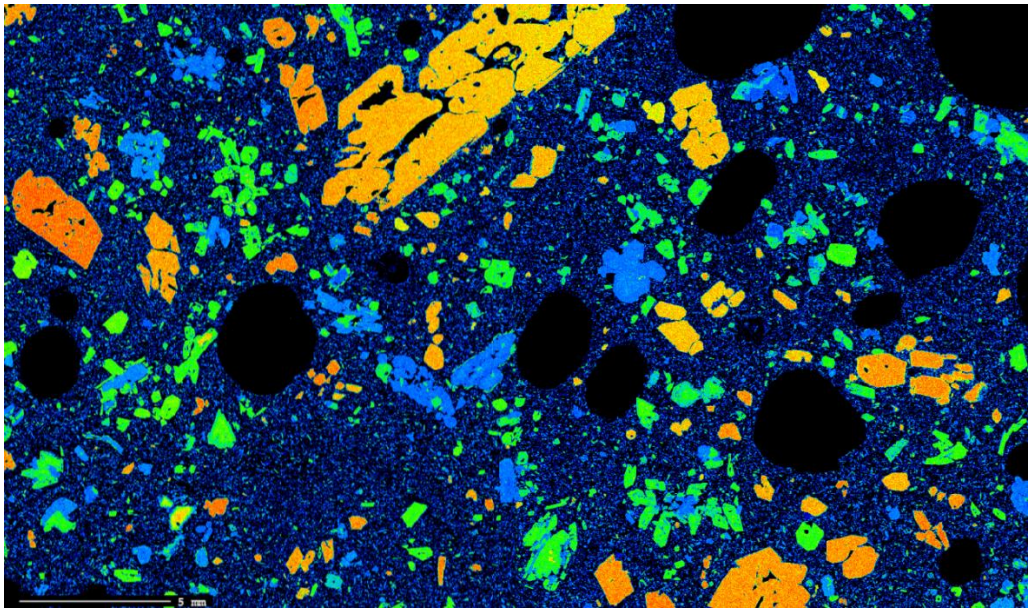

Figure 3.4. EPMA Mg Map for sample KM1024 D20-R01 from Mata Tolu. The three main mineral phases can be seen in this map: olivine (orange), clinopyroxene (light blue), and orthopyroxene (green). These minerals can occur individually or in intergrowths. The matrix is glassy (dark blue) and often includes microlites. Vesicles are present (vesicles are black).

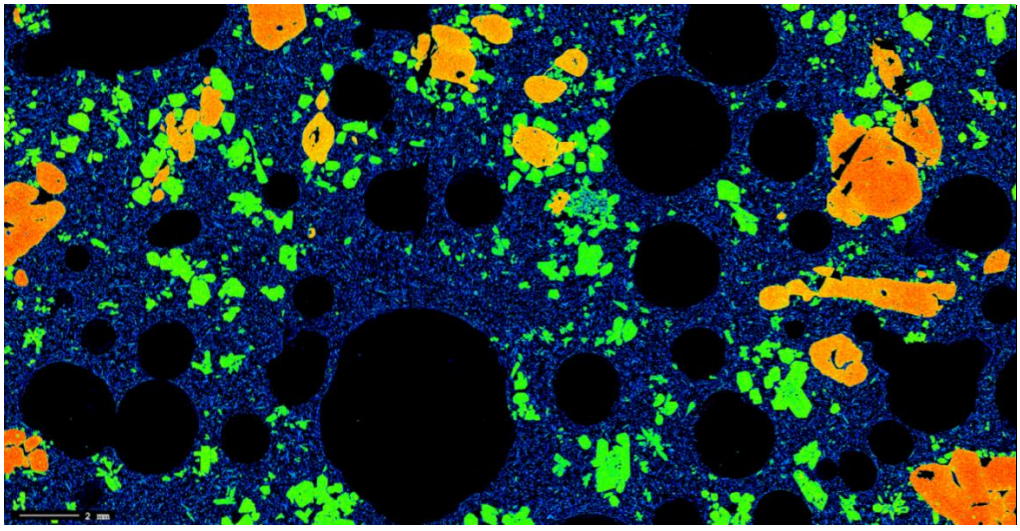

Figure 3.5. EPMA Mg Map for sample KM1024 D20-R01 from Mata Tolu. The three main mineral phases can be seen in this map:, olivine (orange), clinopyroxene (light blue), and orthopyroxene (green). These minerals can occur individually or in intergrowths. The matrix is glassy (dark blue) and often includes microlites. Vesicles are present (vesicles are black).

Table 3.1. Phase proportions determined by point counting samples.

| Location | Sample | CPX | OPX | Olivine | Vesicle | Matrix/ Glass |
|---|---|---|---|---|---|---|
| East Mata | KM1024 D14-R02 | >1 | 1 | >1 | 24 | 74 |
| East Mata | KM1024 D14-R07 | 1 | 2 | >1 | 2 | 95 |
| West Mata | J2-413-R04 | 6 | 6 | 8 | 29 | 52 |
| West Mata | J2-413-R13 | 12 | 5 | 4 | 11 | 68 |
| West Mata | J2-418-R01 | 10 | 7 | >1 | 13 | 70 |
| West Mata | J2-418-R11 | 4 | 6 | 4 | 22 | 64 |
| West Mata | J2-418-R18 | 4 | 4 | 4 | 38 | 51 |
| West Mata | J2-420-R02 | 8 | 11 | 8 | 15 | 58 |
| West Mata | J2-420-R17 | 4 | 8 | 6 | 36 | 47 |
| Taha | KM1024 D16-R04 | 1 | >1 | 14 | 8 | 76 |
| Ua | KM1024 D18-R01 | >1 | >1 | 5 | 15 | 80 |
| Ua | KM1024 D18-R02 | >1 | >1 | 17 | 12 | 71 |
| Tolu | KM1024 D20-R01 | 4 | 7 | 9 | 16 | 64 |
| Fa | KM1024 D21-R02 | >1 | >1 | 18 | 21 | 60 |
| Ono | KM1024 D22-R01 D | >1 | 1 | 15 | 24 | 60 |
| Ono | KM1024 D22-R01 L | >1 | >1 | 17 | 10 | 72 |
| Ono | KM1024 D22-R02 | 4 | 5 | 6 | 30 | 55 |
| Fitu | KM1024 D23-R01 | 4 | 6 | 7 | 32 | 52 |
| Fitu | KM1024 D23-R04 | 4 | 6 | 2 | 27 | 62 |

1000 points were counted on each sample at a magnification of 100x. Phases counted are clinopyroxene (CPX), orthopyroxene (OPX), olivine, vesicles, and matrix/glass. J2-418-R01, J2-418-R11, and J2-420-R02 are not from the new eruption of West Mata. The other J2 samples are from the new eruption of West Mata. The two samples from East Mata have very few phenocrysts and are mostly matrix and/or matrix and vesicles. Therefore, the crystal proportions are not very accurate for the East Mata samples. The percentage of olivine in the East Mata samples is not representative of the actual amount of olivine in these samples, as the matrix mostly consists of pyroxene phenocrysts. This is discussed further in the text.

Table 3.2. Proportions of crystal phases present determined by point counting samples.

| Location | Sample | CPX | OPX | Olivine |
|---|---|---|---|---|
| East Mata | KM1024 D14-R02 | 21 | 74 | 5 |
| East Mata | KM1024 D14-R07 | 35 | 58 | 8 |
| West Mata | J2-413-R04 | 29 | 29 | 42 |
| West Mata | J2-413-R13 | 57 | 26 | 18 |
| West Mata | J2-418-R01 | 57 | 41 | 2 |
| West Mata | J2-418-R11 | 28 | 44 | 29 |
| West Mata | J2-418-R18 | 32 | 32 | 36 |
| West Mata | J2-420-R02 | 30 | 40 | 31 |
| West Mata | J2-420-R17 | 23 | 45 | 32 |
| Taha | KM1024 D16-R04 | 6 | 3 | 91 |
| Ua | KM1024 D18-R01 | 2 | 4 | 94 |
| Ua | KM1024 D18-R02 | 1 | 2 | 98 |
| Tolu | KM1024 D20-R01 | 19 | 36 | 45 |
| Fa | KM1024 D21-R02 | 2 | 1 | 97 |
| Ono | KM1024 D22-R01 D | 2 | 7 | 90 |
| Ono | KM1024 D22-R01 L | 1 | 2 | 97 |
| Ono | KM1024 D22-R02 | 26 | 33 | 41 |
| Fitu | KM1024 D23-R01 | 22 | 36 | 41 |
| Fitu | KM1024 D23-R04 | 31 | 50 | 19 |

1000 points were counted on each sample at a magnification of 100x. Crystal phases counted are clinopyroxene (CPX), orthopyroxene (OPX), and olivine. J2-418-R01 and J2-420-R02 are not from the new eruption of West Mata. The two samples from East Mata have very few phenocrysts and are mostly matrix and/or matrix and vesicles. Therefore, the crystal proportions are not very accurate for the East Mata samples. The percentage of olivine in the East Mata samples is not representative of the actual amount of olivine in these samples, as the matrix mostly consists of pyroxene phenocrysts. This is discussed further in the text.

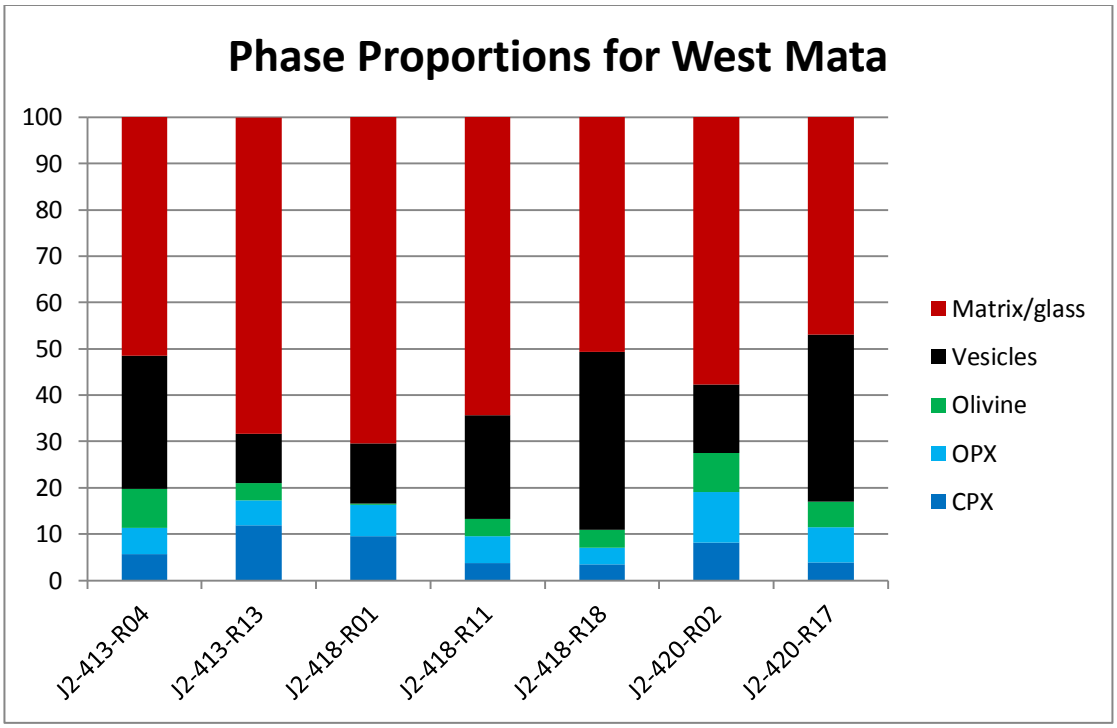


A.

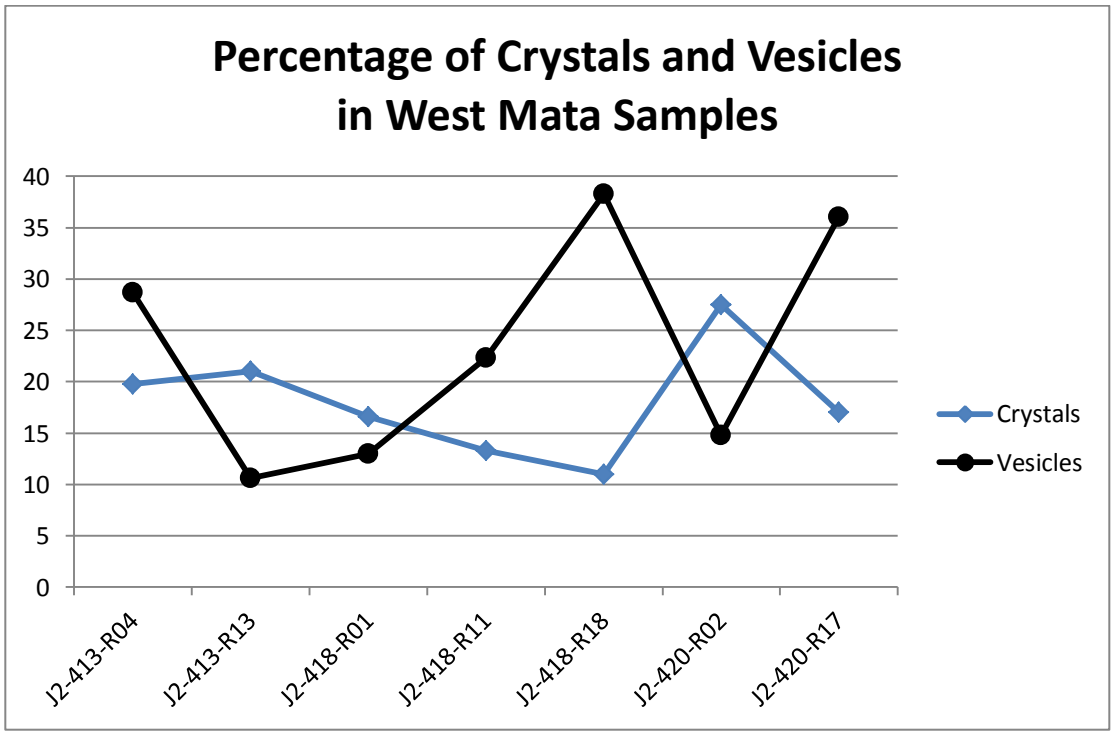


B.

Figure 3.6. See next page for figure caption

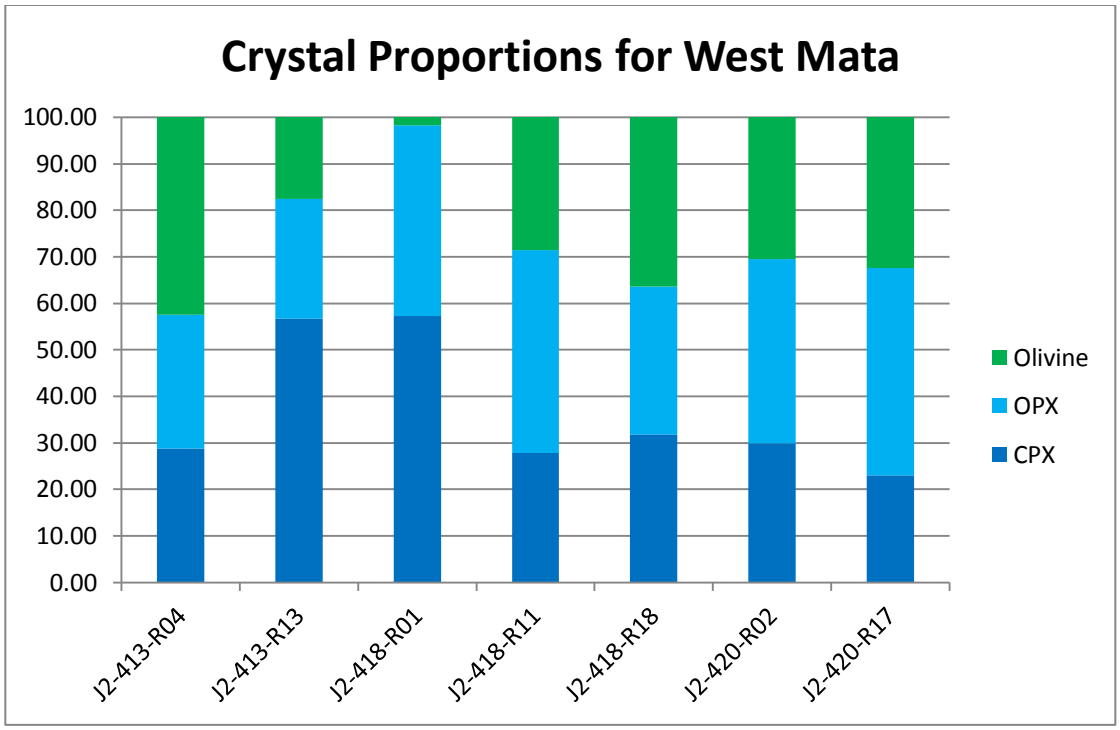


C.

Figure 3.6, continued. A. Histogram of phase proportions in West Mata, B. Graph showing the percentage of total crystals (olivine + clinopyroxene + orthopyroxene) and vesicles in West Mata, and C. histogram of mineral proportions in West Mata. J2-418-R01 and J2-420-R02 are not from the new eruption of West Mata.

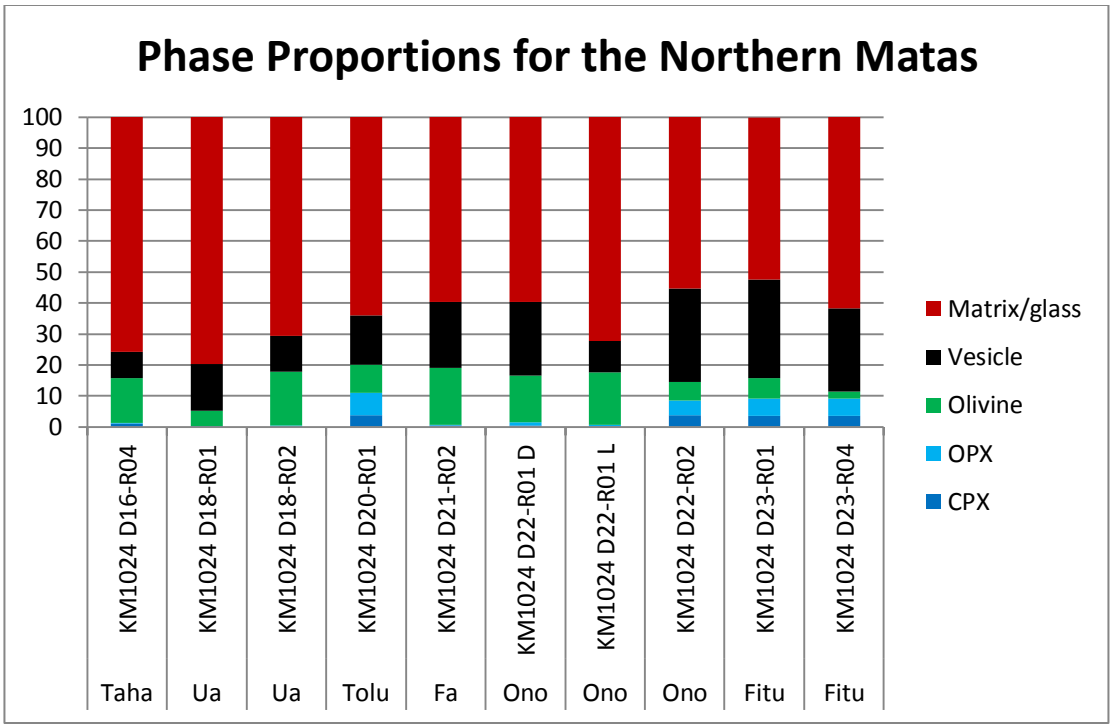


A.

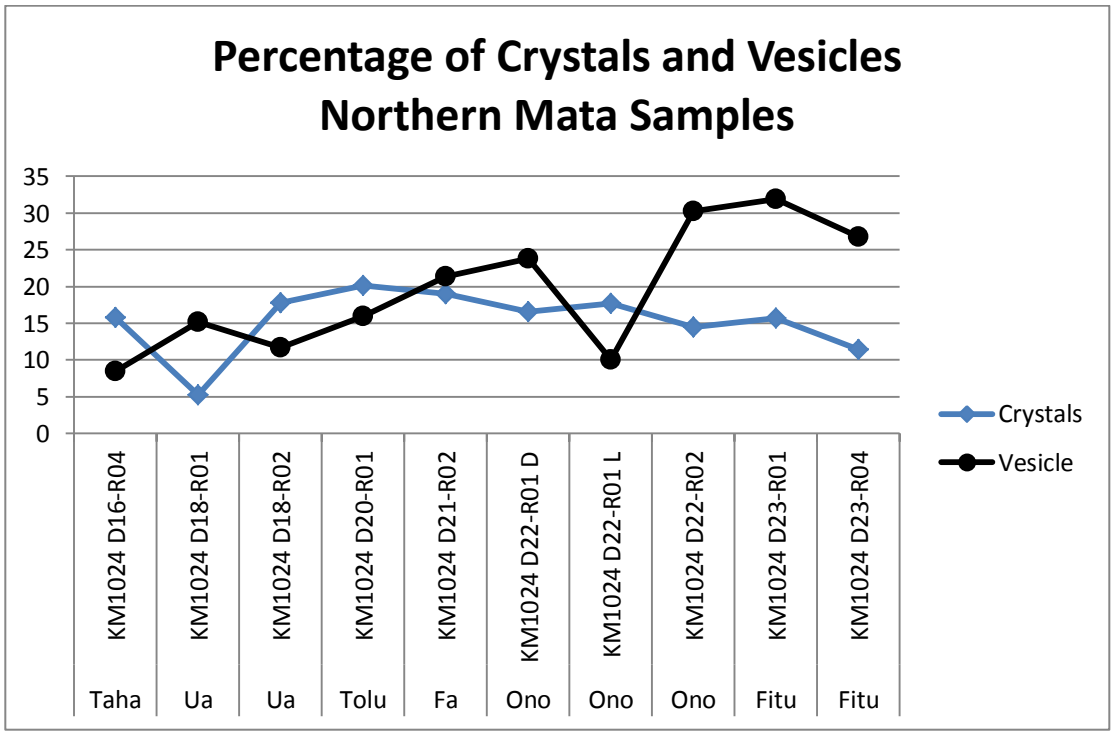


B.

Figure 3.7. See next page for figure caption.

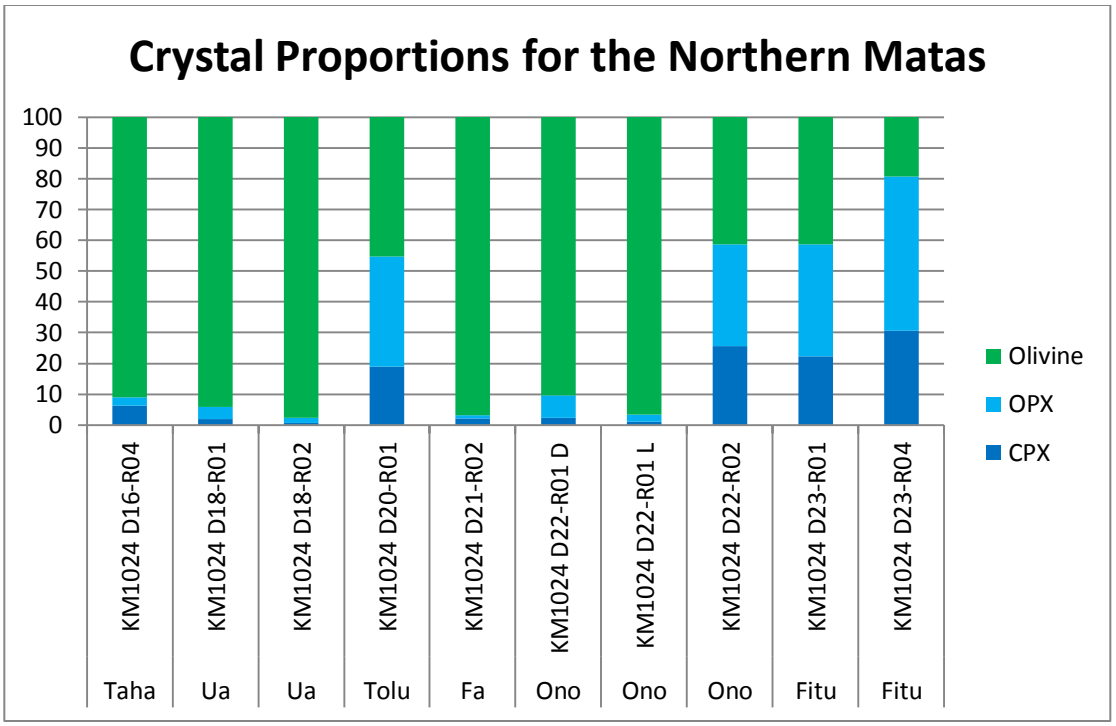

C.

Figure 3.7, continued. A. Histogram of phase proportions in the Northern Matas, B. Graph showing the percentage of total crystals (olivine + clinopyroxene + orthopyroxene) and vesicles in the Northern Matas, and C. histogram of mineral proportions in the Northern Matas. The volcano is listed below the sample name.

**Comparison with previous work**

Resing *et al*. (2011) report point counts for two samples from the new eruption of West Mata, J2-413-R13 and J2-418-R18. These point counts were conducted digitally using EPMA maps. In this thesis project, point counts were done on these and additional samples in this project by petrographic microscope. This section compares results from the two methods.

Both methods report similar crystallinities; the reported vesicle-free crystallinities by Resing *et al*. (2011) are slightly higher. For sample, J2-413-R13, Resing *et al*. (2011) report a crystallinity of 28%, while point counting with a petrographic microscope yields a value of 24%. For J2-418-R18, these values are 21 and 18% respectively. For comparison, when two different parts of J2-413-R13 were counted with 250 points each, the crystallinities from these two counts were 16% and 28%. This suggests that the difference between the methods is within the variation of the samples and thus within the uncertainty of the methods.

The two methods yield different mineral modes. For J2-418-R18, results from the two methods are very similar. Resing *et al*. (2011) report equal amounts of olivine and clinopyroxene, with slightly more orthopyroxene present. Point counts by petrographic microscope yield roughly equal amounts of all three minerals. For J2-413-R13, the results diverge more. Resing *et al*. (2011) report that orthopyroxene is the dominant phase followed by clinopyroxene and then olivine, while point counts by petrographic microscope find clinopyroxene as the dominant phase followed by orthopyroxene than olivine (Table 3.3).

The differences in the results between the two methods may be due to differences in defining if a crystal is part of the groundmass/matrix or is a phenocryst phase. For both of these samples, there is a continuum of crystal sizes from crystals that are visible in hand sample to true microphenocrysts only visible at high magnification on the microprobe. Borderline groundmass and groundmass crystals in these two samples are primarily orthopyroxene and clinopyroxene. These crystals were counted as part of the groundmass, while they appear to have been included in the point count as phenocryst phases in the Resing *et al*. (2011) analysis. This results in a higher crystallinity in the Resing *et al*. (2011) analysis and a higher percentage of clinopyroxene

and orthopyroxene relative to olivine as phenocryst phases. As there is variation throughout the sample, differences could have also been introduced by counting different parts of the samples by the two different methods.

For the purposes of this project, only the point counts by petrographic microscope will be used. Because these are all counted using the same methods and cut-offs for mineral phases vs. groundmass or matrix, comparisons can be made between data for the different samples.

East Mata samples consist mostly of a crystalline matrix with crystals too small to identify with confidence by microscope. Only a few phenocrysts are present. Microprobe work shows that the matrix consists of clinopyroxene and orthopyroxene. No significant amount of olivine was found. However, for the two point counts conducted, only 1-2 points out of 1000 total points were olivine. However as there are so few phenocryst counts, the amount of olivine in the crystal portions in this sample falsely implies that there is a significant amount of olivine in the samples. In the following section, samples are broken into groups and the East Mata samples are given their own group.

Table 3.3. Comparison of digital point counts by Resing *et al*. (2011) to point counts by petrographic microscope conducted as part of this thesis project.

| Method | Author/ Analyst | Sample | Crystallinities | Mineral Proportions | | |
|---|---|---|---|---|---|---|
| | | | | ol | cpx | opx |
| Digital | Resing et al. (2011) | J2-413-R13 | 28 | 1 | 2 | 3 |
| Petrographic Microscope | Glancy (this thesis) | J2-413-R13 | 24 | 2 | 7 | 3 |
| Digital | Resing et al. (2011) | J2-418-R18 | 21 | 3 | 3 | 5 |
| Petrographic Microscope | Glancy (this thesis) | J2-418-R18 | 18 | 1 | 1 | 1 |

Crystallinities (in percent) on a vesicle free basis and mineral proportions are reported for olivine (ol), clinopyroxene (cpx) and orthopyroxene (opx). Two samples from the new eruption at West Mata, J2-413-R13 and J2-418-R18, were point counted by both methods. Resing *et al*. (2011) only report point counts for these two samples. Additional samples are point counted by petrographic microscope for this thesis project. Resing *et al*. (2011) report higher crystallinities and different mineral proportions than found with traditional point counting using a petrographic microscope. This is suspected to be due to different cut-offs the two methods used for defining if a crystal was a phenocryst phase or part of the groundmass/matrix. See the text for more explanation of these differences.

**Petrographic groups**

Based on point counts by petrographic microscope as part of this project and textural analysis of EPMA BSE images, samples can be divided into four main groups. Group 1 consists of samples with approximately equal amounts of olivine, clinopyroxene, and orthopyroxene. Group 2 is characterized by samples with abundant orthopyroxene and clinopyroxene and little olivine. Group 3 has mostly olivine with lesser amounts of clinopyroxene and orthopyroxene. Group 4 samples are mostly cryptocrystalline.

*Group 1. Roughly equal amounts of olivine, clinopyroxene, and orthopyroxene*

The first group contains approximately equal amounts of the three main mineral phases (Tables 3.4 and 3.5 and Figures 3.6 and 3.7). Almost all of the West Mata samples (except for sample J2-418-R01), and about half of the northern Mata samples fall into this group: KM1024 D20-R01 from Tolu, KM1024 D22-R02 from Ono, KM1024 D23-R01 from Fitu, and KM1024 D23-R04 from Fitu. In detail, excluding vesicles and matrix, the amount of orthopyroxene ranges from 26 to 50%, the amount of clinopyroxene ranges from 19 to 57%, and the amount of olivine ranges from 18 to 45%.

Subgroup 1A consists of the West Mata samples J2-413-R04, J2-413-R13, and J2-420-R17 and the northern Mata samples in Group 1. The West Mata samples in this group all have a glassy matrix with some microlites. There are many complicated intergrowths between pyroxene crystals and pyroxene and olivine crystals and inclusions of olivine in pyroxene. Free standing olivines are often equant. J2-413-R13 records many rapid growth textures. In general, the Northern Mata samples in this group have a range of olivine textures, including olivine with rapid growth textures, normally zoned olivine, reversely zoned olivine, and unzoned olivine. All samples have a groundmass of equant and elongate pyroxenes in a glassy matrix. KM1024 D23-R01 and KM1024 D23-R04 also have some feather-like dendrites. All samples have pyroxene with complicated zoning patterns (pyroxene was not analyzed for KM1024 D23-R04, so pyroxene was not extensively imaged for this sample). KM1024 D20-R01 and KM1024 D23-R01 have a significantly high number of extremely complicated pyroxene intergrowths, often

with included or intergrown olivine. These intergrowths can occur in other samples, but are prominent in these two.

Subgroup 1B consists of J2-418-R11 and J2-420-R02. The groundmass of these samples is almost entirely crystalline. Individual olivine crystal textures vary, including rapidly grown examples. Intergrowths with pyroxene and inclusions in pyroxene are also present.

*Group 2: Orthopyroxene and Clinopyroxene abundant, Olivine rare*

The sample that is lowest in olivine, J2-418-R01, falls into its own group (Group 2). This sample consists of 57% clinopyroxene, 41% orthopyroxene, and minor amounts of olivine. Olivine ranges from inclusions in pyroxene to euhedral olivine. In contrast to olivine from most other thin sections, these olivine crystals are not zoned and clear rapid growth structures are not present. This sample is different from other Mata samples in that it has many compositionally homogeneous, unzoned, simple euhedral orthopyroxene and clinopyroxene crystals. Two measured unzoned orthopyroxenes have a rounded olivine inclusion in them, but others do not. Some more complicated pyroxene crystals are also present. A few have a rounded, possibly resorbed, inner zone that is compositionally different than the euhedral rim. Others are intergrown and/or have complicated sector or oscillatory zoning. This sample also differs from many of the others in that a few small plagioclase crystals are present (~generally 200 nm long and 50 nm wide, but one larger crystal/intergrowth is ~500 nm long and ~200 to 300 nm wide). One small orthopyroxene-plagioclase intergrowth is present (pyroxene 10) (Tables 3.4 and 3.5 and Figures 3.6 and 3.7).

*Group 3: Olivine-rich, orthopyroxene and clinopyroxene-poor*

The phenocrysts in a third group of samples are mostly olivine with a very small proportion of clinopyroxene and orthopyroxene (Tables 3.4 and 3.5 and Figures 3.6 and 3.7). This group includes KM1024 D16-R01 from Taha, KM1024 D18-R01 and KM1024 D18-R02 from Ua, KM1024 D21-R02 from Fa, and KM1024 D22-R01 Dark and KM1024 D22-R01 Light from Ono. KM1024 D22-R01 Light and Dark were two thin sections made from different parts

of one rock sample. These two portions appeared different at sea. The difference is textural. The KM1024 D22-R01 Dark thin section has more vesicles and less matrix (Tables 3.4 and 3.5 and Figure 3.7). Excluding vesicles and matrix, the amount of orthopyroxene present in samples from this group ranges from 1 to 7%, the amount of clinopyroxene ranges from 0.5 to 6%, and the amount of olivine ranges from 90 to 97%. These samples can be subdivided into two groups.

Subgroup 3A has a groundmass that consists of microlites and glass and contains KM1024 D18-R01, KM1024 D18-R02, KM1024 D21-R02, KM1024 D22-R01 Dark, and KM1024 D22-R01 Light. Groundmass crystals in KM1024 D18-R01 and KM1024 D18-R02 can be either equant or elongate and are often zoned. Groundmass crystals in KM1024 D21-R02 are primarily distinctive feather-like dendrites with some equant often euhedral pyroxene crystals also present. These feather-like dendrites are also the primary groundmass phenocryst in KM1024 D22-R01 D, with some equant pyroxenes present as well. KM1024 D22-R01 L has a very unique groundmass texture. Groundmass crystals are much smaller than in the other thin sections and are concentrated into areas. Some areas are entirely crystalline, but glassy areas are also present. Vesicles are often elongated. Olivine textures are complex. KM1024 D21-R02 has the simplest olivine; all olivine are normally zoned. Some crystals show rapid growth textures and other do not. For the other samples, generally, multiple textures, including rapidly growing olivine and equant euhedral olivine are present. Often normally zoned, reversely zoned, and unzoned olivine are present in the same thin section. Pyroxene crystals show complicated oscillatory or sector zoning patterns. (Note that pyroxene was not analyzed on sample KM1024 D18-R02, so pyroxene was not extensively imaged for this sample). Many of the pyroxene crystals in KM1024 D18-R01 and KM1024 D18-R02 have rounded, possibly resorbed centers.

KM1024 D16-R04 from Taha forms its own subgroup (3B). It has very little to no glass present in the groundmass, which consists primarily of elongate pyroxene crystals, some equant pyroxene crystals and very tiny crystals filling in the gaps between these other crystals. Most olivine crystals in this thin section show rapid growth textures. Reversely and normally zoned crystals as well as unzoned crystals are present.

*Group 4: Cryptocrystalline*

The two East Mata samples (KM1024 D14-R02 and KM1024 D14-R07) comprise a fourth group (Tables 3.4 and 3.5 and Figures 3.6 and 3.7). These samples consist almost entirely of a cryptocrystalline matrix. Only a few small phenocrysts comprise only 1.9 to 2.6% of the total sample. A close look at the matrix in EPMA microprobe images shows individual microphenocrysts surrounded by glass. For KM1024 D14-R02, most are needle-like dendritic pyroxenes with a few euhedral crystals. For KM1024 D14-R07, they are mostly equant or elongate crystals. Most phenocrysts are clinopyroxenes and orthopyroxenes. These crystals are zoned. Olivine was observed in only a few cases under the microprobe as an anhedral inclusion in a pyroxene crystal in KM1024 D14-R02.

*Geochemical composition of textural groups*

The groups listed above are based on textures, not location or chemistry. Samples from an individual volcano can fall into different groups. For example, samples from West Mata are found in Groups 1 and 2 and samples from Mata Ono are found in Groups 1 and 3. An individual group can contain samples from multiple volcanoes. For example, Group 1 has samples from West Mata, Tolu, Ono, and Fitu. Group 3 has samples from Matas Taha, Ua, Fa, and Ono. It is unknown if the dredge samples (the KM1024 samples) from an individual volcano are from the same eruption. However, for dive samples from West Mata, it is known that at least two eruptions are represented in Group 1: the most recent eruption (represented by J2-413-R04, J2-413-R14, J2-418-R18, and J2-420-R17) and from a previous eruption(s) (represented by J2-418-R11 and J2-420-R02). Therefore, samples from an individual textural group do not represent samples all evolved from the same parent melt.

A comparison of the composition of samples from the different groups was conducted. Comparison is difficult as some groups do not have many samples. Additionally, Groups 1 and 2 have a significant variation in composition for most elements that overlaps with each other and often the other groups.

Some differences between the groups are present in major element chemistry. For a full discussion of geochemical data, see Chapter Four. Group 2 is the lowest in MgO and CaO and the highest in $SiO_2$ in microprobe glass. It is also the second lowest in MgO in XRF whole rock data. Group 4 has an intermediate MgO value in microprobe glass data, but the lowest MgO in XRF whole rock. The lower MgO content in XRF whole rock data in these two groups may be attributed to the low percentages of olivine minerals in Groups 2 and 4. Group 4 is lower in $Al_2O_3$ and $SO_3$ in microprobe glass than Group 2. It is offset from the others in the $Al_2O_3$ vs. MgO trend because it has lower $Al_2O_3$ for its MgO content. However no offset is observed for XRF whole rock data. It is unclear what is causing this offset as plagioclase phenocrysts were not observed as a major mineral phase in these samples (see next section). Microprobe glass data is only available for KM1024 D14-R02.

The trace element compositions of these samples were also compared. For a full discussion of geochemical data see the Chapter Four. Generally Groups 2 and 4 were lowest in compatible trace elements measured by whole rock XRF analysis. Group 4 was the lowest in Cr and Ni. Group 2 was the second lowest in these elements. Groups 2 and 4 were lower in Co than the other groups. The lower Ni in Groups 2 and 4 may be due to the lower percentage of olivine in samples from these groups. There is significant overlap in all of the groups for incompatible trace elements and significant variations with the groups that have more samples.

**Plagioclase**

Samples from the Mata volcanoes are unusual compared to most oceanic lavas because they contain almost no plagioclase, although little to no plagioclase is an expected characteristic of boninite. To determine the presence or absence of plagioclase in glass samples, glass rinds were visually examined in EPMA BSE images. In some cases, EDS was used to confirm the presence of plagioclase in some of the glass samples. Based on this work, samples were placed in three categories: samples containing plagioclase (12 samples), samples not containing plagioclase (61 samples), and samples that may contain plagioclase (two samples). The latter two samples that may contain minute amounts of plagioclase had a few very small crystals that

potentially could be plagioclase, but further confirmation from EDS work would be required for verification. Samples containing plagioclase and the corresponding MgO content of these glasses as measured by EPMA at UH Manoa are listed in the following Table 3.7. For each category, samples are sorted from lowest MgO content to highest MgO content. Compositions of all glass rinds are discussed in Chapter 4.

Samples that do contain plagioclase range in MgO content from 0.49 to 4.98 wt%. Of these 12 samples, eight have a MgO content less than 4 wt% (67% of the samples), two have a MgO content between 4.0 and 4.5 wt% (17% of the samples), and two have a MgO content between 4.5 and 5.0 wt% (17% of the samples). Plagioclase was not found in any samples with a MgO content of 5.0 wt% or higher.

Samples that do not contain plagioclase range in MgO content from 4.29 to 8.58 wt%. Of the 61 samples that do not contain plagioclase, none have a MgO content less than 4 wt%, only two have a MgO content less than 4.5 wt% (only 3% of the samples) and only seven have a MgO content less than 5 wt% (only 11% of the samples).

There is a slight overlap from about 4.0 to 5.0 wt% MgO between the group of samples that contain plagioclase and the group of samples that do not contain plagioclase. The two samples that may contain plagioclase fall into this range, with 4.13 and 4.78 wt% MgO (Table 3.4).

The presence or absence of plagioclase does not correlate with specific volcanoes. For example, some analyzed samples from West Mata, East Mata, and Mata Ua contain plagioclase while other analyzed samples from the same volcanoes do not. These samples are from multiple volcanoes. On West Mata, samples are from at least two eruptions, the most recent eruption and an older eruption or older eruptions. Thus the samples would not be expected to be from the same parent magma. The relatively consistent presence of plagioclase in glasses containing less than 4.5 wt% MgO and the absence of plagioclase in glasses containing more than 4.5 wt% MgO suggests that, in general, plagioclase starts to form as a groundmass phase in these magmas as they evolve to MgO contents of less than 4.5 wt% despite likely differences in parent magma

compositions and potential differences in crystallization conditions. Chapter Six discusses crystallization of these samples and MELTS modeling of crystallization in more detail.

Table 3.4. Presence or absence of plagioclase in the groundmass of glass samples from the Mata volcanoes and corresponding MgO contents of the glasses of these samples.

| Location | Sample | Plagioclase? | MgO |
|---|---|---|---|
| East Mata | KM1129a D02-R01 | Yes | 0.49 |
| East Mata | KM1129a D02-R03 | Yes | 1.10 |
| East Mata | KM1129a D02-R04 | Yes | 1.13 |
| West Mata | KM1024 D15-R05 | Yes | 2.70 |
| West Mata | J2-418-R01 | Yes | 3.36 |
| West Mata | KM1024 D12-R01 | Yes | 3.63 |
| West Mata | J2-420-R01 | Yes | 3.65 |
| West Mata | KM1024 D12-R08 | Yes | 3.70 |
| West Mata | KM1024 D12-R06 | Yes | 4.01 |
| West Mata | J2-420-R02 | Yes | 4.15 |
| Ua | RR1211 Q325-R01 | Yes | 4.71 |
| West Mata | RR1211 Q327-R02 | Yes | 4.98 |
| West Mata | J2-418-C02 | Maybe | 4.13 |
| Taha | KM1024 D16-R01 | Maybe | 4.78 |
| West Mata | J2-418-R04 | No | 4.29 |
| West Mata | J2-418-R05 | No | 4.41 |
| Taha | KM1024 D16-R02 | No | 4.51 |
| East Mata | KM1024 D14-R05 | No | 4.86 |
| Tolu | KM1024 D20-R01 | No | 4.97 |
| East Mata | KM1129a D01-R03 | No | 4.98 |
| East Mata | KM1024 D14-R09 | No | 4.98 |
| East Mata | KM1129a D01-R04 | No | 5.03 |

The location lists the volcano at which each sample was found. Sample KM1024 D13-R01a is from a lava flow near West Mata. Samples are grouped into those that contain plagioclase in the groundmass of the glass (denoted as "Yes" in the table), those that do not contain plagioclase (denoted as "No" in the table), and those that may contain plagioclase but require additional analysis for verification (denoted as "Maybe" in the table). All of the samples within a group are sorted from lowest MgO content to highest MgO content. Note that plagioclase is generally present in samples with a MgO content of the glass lower than 4.5 wt% and absent in samples with a MgO content of the glass greater than 4.5 wt%. Only two samples with a MgO content of greater than 4.5 wt% contain plagioclase and only two samples with a MgO content less than 4.5 wt% do not contain plagioclase.

Table 3.4 (continued).

| Location | Sample | Plagioclase? | MgO |
|---|---|---|---|
| Tolu | KM1129a D09-R01 | No | 5.13 |
| Tolu | KM1024 D20-R02 | No | 5.22 |
| Tolu | KM1129a D09-R02 | No | 5.29 |
| Tolu | KM1129a D08-R01 | No | 5.34 |
| Tolu | KM1129a D08-R04 | No | 5.35 |
| Tolu | RR1211 Q331-R16 | No | 5.36 |
| Fa | KM1024 D21-R04 | No | 5.37 |
| Tolu | KM1129a D08-R07 | No | 5.38 |
| Fitu | RR1211-Q329 R02 | No | 5.39 |
| Fa | KM1024 D21-R01 | No | 5.50 |
| West Mata | J2-420-R10 | No | 5.50 |
| East Mata | KM1024 D14-R02 | No | 5.57 |
| Tolu | RR1211 Q331-R02 | No | 5.58 |
| Ua | KM1024 D18-R01 | No | 5.69 |
| Ua | KM1024 D18-R04 | No | 5.69 |
| Ua | KM1024 D18-R05 | No | 5.71 |
| Ua | KM1024 D17-R01 | No | 5.76 |
| Ua | KM1129a D10-R02 | No | 5.78 |
| West Mata | RR1211 Q332-R05 | No | 5.79 |
| West Mata | RR1211 Q327-BS06 | No | 5.81 |
| Fa | KM1024 D21-R02 | No | 5.82 |
| West Mata | RR1211 Q332-R02 | No | 5.84 |

Presence or absence of plagioclase in the groundmass of glass samples from the Mata volcanoes and corresponding MgO contents of the glasses of these samples. The location lists the volcano at which each sample was found. Sample KM1024 D13-R01a is from a lava flow near West Mata. Samples are grouped into those that contain plagioclase in the groundmass of the glass (denoted as "Yes" in the table), those that do not contain plagioclase (denoted as "No" in the table), and those that may contain plagioclase but require additional analysis for verification (denoted as "Maybe" in the table). All of the samples within a group are sorted from lowest MgO content to highest MgO content. Note that plagioclase is generally present in samples with a MgO content of the glass lower than 4.5 wt% and absent in samples with a MgO content of the glass greater than 4.5 wt%. Only two samples with a MgO content of greater than 4.5 wt% contain plagioclase and only two samples with a MgO content less than 4.5 wt% do not contain plagioclase.

Table 3.4 (continued).

| Location | Sample | Plagioclase? | MgO |
|---|---|---|---|
| Ua | RR1211 Q325-R04 | No | 5.85 |
| West Mata | RR1211 Q332-R01 | No | 5.85 |
| West Mata | RR1211 Q332-R04 | No | 6.02 |
| Lava Flow | KM1024 D13-R01a | No | 6.02 |
| West Mata | J2-413-R13 | No | 6.03 |
| West Mata | J2-420-R13 | No | 6.06 |
| West Mata | RR1211 Q332-R03 | No | 6.07 |
| West Mata | J2-420-R08 | No | 6.13 |
| Tolu | KM1129a D08-R08 | No | 6.22 |
| West Mata | J2-418-R18 | No | 6.24 |
| Ua | KM1129a D10-R01 | No | 6.28 |
| West Mata | J2-420-R16 | No | 6.31 |
| West Mata | KM1024 D15-R03 | No | 6.36 |
| West Mata | J2-420-R23 | No | 6.38 |
| West Mata | J2-413-R02 | No | 6.46 |
| West Mata | KM1024 D15-R01 | No | 6.51 |
| West Mata | J2-418-R11 | No | 6.51 |
| Tolu | KM1129a D07-R02 | No | 6.51 |
| Fitu | KM1024 D23-R01 | No | 6.54 |
| Tolu | RR1211 Q331-R01 | No | 6.55 |
| Ua | RR1211 Q328-R03 | No | 6.64 |
| Ua | RR1211 Q328-R11 | No | 6.74 |

Presence or absence of plagioclase in the groundmass of glass samples from the Mata volcanoes and corresponding MgO contents of the glasses of these samples. The location lists the volcano at which each sample was found. Sample KM1024 D13-R01a is from a lava flow near West Mata. Samples are grouped into those that contain plagioclase in the groundmass of the glass (denoted as "Yes" in the table), those that do not contain plagioclase (denoted as "No" in the table), and those that may contain plagioclase but require additional analysis for verification (denoted as "Maybe" in the table). All of the samples within a group are sorted from lowest MgO content to highest MgO content. Note that plagioclase is generally present in samples with a MgO content of the glass lower than 4.5 wt% and absent in samples with a MgO content of the glass greater than 4.5 wt%. Only two samples with a MgO content of greater than 4.5 wt% contain plagioclase and only two samples with a MgO content less than 4.5 wt% do not contain plagioclase.

Table 3.4 (continued).

| Location | Sample | Plagioclase? | MgO |
|---|---|---|---|
| Ua | KM1129a D10-R03 | No | 6.77 |
| Ua | RR1211 Q325-R03 | No | 6.77 |
| Fitu | KM1024 D23-R04 | No | 6.84 |
| Fitu | RR1211-Q329 R01 | No | 6.92 |
| Ono | KM1024 D22-R02 | No | 7.23 |
| Ono | KM1024 D22-R01 | No | 7.30 |
| Tolu | KM1129a D07-R01 | No | 7.35 |
| Ua | KM1129a D10-R06 | No | 7.77 |
| Ua | RR1211 Q328-R12 | No | 8.58 |

Presence or absence of plagioclase in the groundmass of glass samples from the Mata volcanoes and corresponding MgO contents of the glasses of these samples. The location lists the volcano at which each sample was found. Sample KM1024 D13-R01a is from a lava flow near West Mata. Samples are grouped into those that contain plagioclase in the groundmass of the glass (denoted as "Yes" in the table), those that do not contain plagioclase (denoted as "No" in the table), and those that may contain plagioclase but require additional analysis for verification (denoted as "Maybe" in the table). All of the samples within a group are sorted from lowest MgO content to highest MgO content. Note that plagioclase is generally present in samples with a MgO content of the glass lower than 4.5 wt% and absent in samples with a MgO content of the glass greater than 4.5 wt%. Only two samples with a MgO content of greater than 4.5 wt% contain plagioclase and only two samples with a MgO content less than 4.5 wt% do not contain plagioclase.

## Olivine Textures and Compositions

Seven elements (Si, Fe, Ni, Mn, Mg, and Ca) in olivine were analyzed in 17 thin sections from seven of the Mata Volcanoes by EPMA at UH Manoa, using the high-precision (high-current and long counting times) method described in Chapter Two. The samples analyzed are listed in Table 3.5. For each sample, points were measured in olivine cores and rims. BSE images of each olivine analyzed were captured by EPMA at UH Manoa and points analyzed were recorded manually. In some cases, midpoints were also measured.

Table 3.5. Samples in which olivine was analyzed for the Mata Volcanoes.

| Location | Number of Samples for which Olivine was Analyzed | Samples |
|---|---|---|
| West Mata | 7 | J2-413-R04 |
| | | J2-413-R13 |
| | | J2-418-R01 |
| | | J2-418-R11 |
| | | J2-418-R18 |
| | | J2-420-R02 |
| | | J2-420-R17 |
| Taha | 1 | KM1024 D16-R04 |
| Ua | 2 | KM1024 D18-R01 |
| | | KM1024 D18-R02 |
| Tolu | 1 | KM1024 D20-R01 |
| Fa | 1 | KM1024 D21-R02 |
| Ono | 3 | KM1024 D22-R01 D |
| | | KM1024 D22-R01 L |
| | | KM1024 D22-R02 |
| Fitu | 2 | KM1024 D23-R01 |
| | | KM1024 D23-R04 |

**Overall textural observations**

This section summarizes findings from observations of olivine phenocrysts with a petrographic microscope, imaging of olivine phenocrysts with EPMA BSE images, and four EPMA element maps.

Overall a range of olivine textures was observed. Crystals ranged in size from large several mm long crystals to groundmass or close to groundmass sized crystals. Many olivine crystals with rapid growth textures, such as dendritic olivine or olivine with many melt inclusions, were observed (Figure 3.8). Euhedral olivine crystals with no evidence of rapid growth were also present (Figure 3.8).

An olivine crystal showing textural evidence for rapid crystal growth was analyzed from sample RR1211 Q331-R16 glass chip 1 for P (on two spectrometers), Al, Ca, and Fe (EPMA maps by Eric Hellebrand). Oscillatory zoning in Fe is present, representing changes in the fosterite content of the crystal. However, these changes are not well correlated with the other elements. For many olivine crystals, core, middle, and rim points were measured. Oscillatory patterns were rare, with normal, reversed, or unzoned patterns as the most common (see Olivine composition section). Fosterite zoning can also be observed in BSC images. The results of element mapping of an olivine from RR1211 Q331-R16 is shown in Figure 3.9.

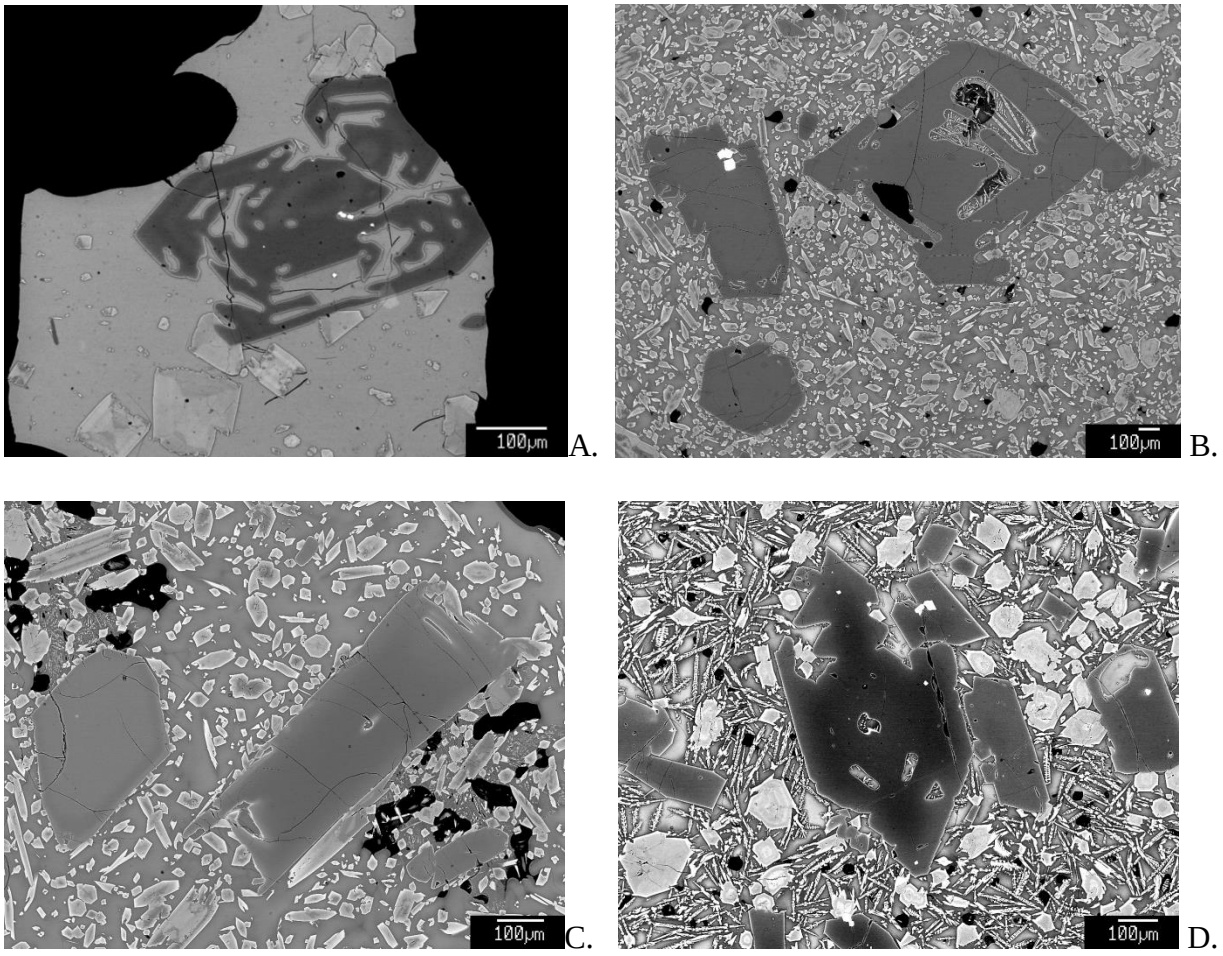


Figure 3.8. Examples of olivine crystals showing rapid growth textures. A. Skeletal olivine showing rapid growth textures. EPMA BSE image from a glass chip from sample KM1024 D16-R01 (Mata Taha). B. Olivine with multiple melt inclusions (center right and left) showing rapid growth textures. EPMA BSE image of olivine 1 (right) from a thin section from sample KM1024 D18-R02 (Mata Ua). C. Euhedral olivine crystal (left) and olivine showing rapid growth textures (right). EPMA BSE image of olivine 3 (right) and 4 (left) from a thin section from sample KM1024 D18-R01 (Mata Ua). D. The central olivine in the image shows evidence of rapid growth (Olivine 1 from sample KM1024 D21-R02).

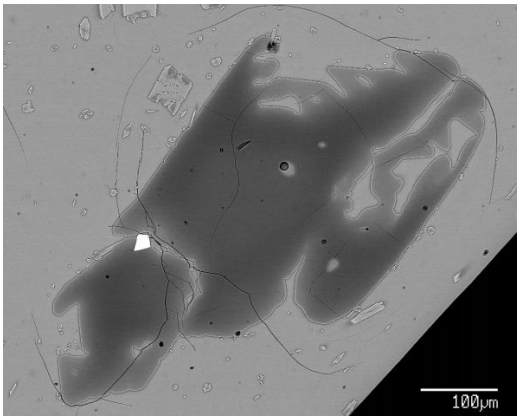

A.

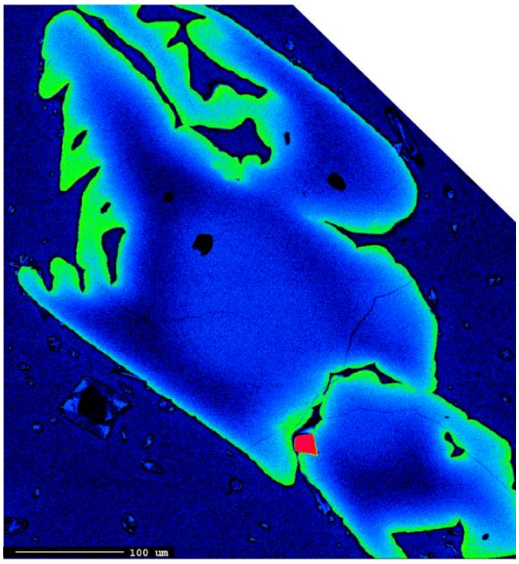

B.

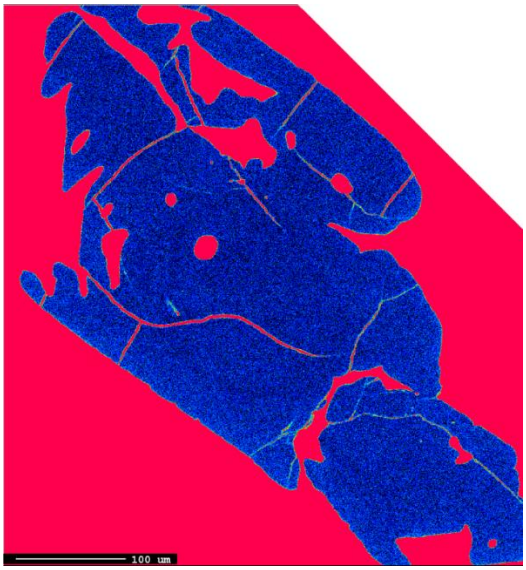

C.

Figure 3.9. See next page for full figure caption

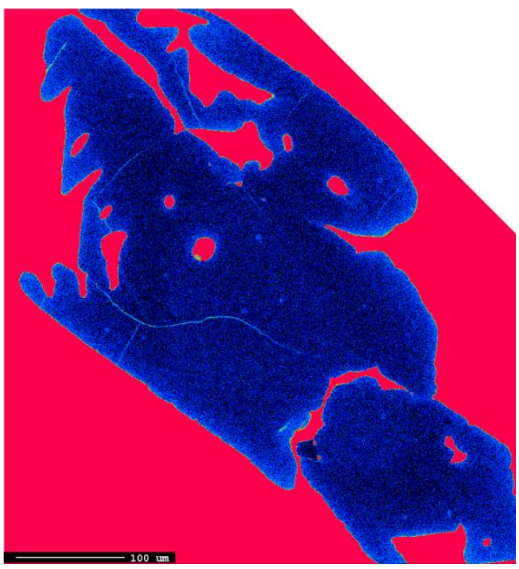

D.
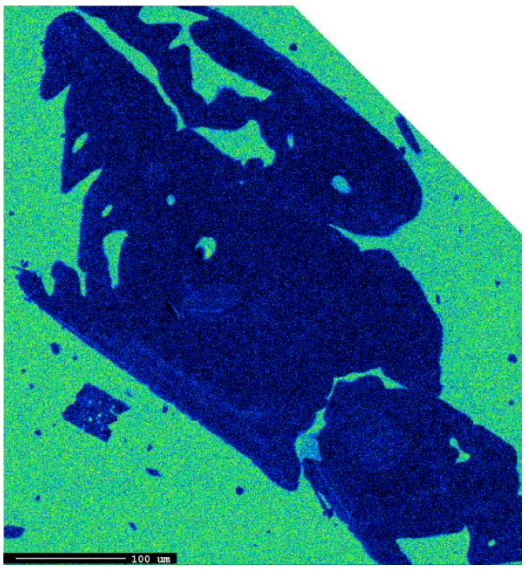

E.

Figure 3.9. BSE images and EPMA maps of a rapidly growing olivine crystal. EPMA BSE image. A hint of oscillatory zoning can be seen in this BSE image, but is clear in panel B. Note that this image is rotated 90 degrees relative to the EPMA maps. B. Fe map of rapidly growing olivine crystal. Note the different zones in the olivine crystal. The crystal has a Fe-rich core and an Fe-poor middle part (reverse zoning). From the middle to the rim is normally zoned. The most Fe-rich section of this olivine is the outer rim. C. Al map of rapidly growing olivine crystal. The olivine crystal is homogeneous in its Al content. D. Ca map of rapidly growing olivine crystal. The olivine crystal is relatively homogeneous in its Ca content except for the rims that have slightly higher concentrations of Ca. There is a faint Ca enrichment in the core, apparently continuous across both grains. E. Combined P map (using the counts of two spectrometers equipped with PETH crystals) of rapidly growing olivine crystal. Minor P zoning is present, but not enough detail is present to use this information to better understand the growth of this crystal. Olivine from glass chip one of sample RR1211 Q331-R16 (Tolu).

Some individual anhedral olivine crystals are present that are not intergrown with or included in pyroxene. Additionally, some anhedral olivine grains are present inside pyroxene crystals. These may be relicts of partially resorbed crystals (Figure 3.10). Olivine crystals from an individual volcano and even in an individual thin section can span the range of textures.

Two olivine inclusions in pyroxene were mapped, both found in a thin section from KM1024 D20-R01 (EPMA maps by Eric Hellebrand) (Figures 3.11 and 3.12). These inclusions may be the products of partial resorption of olivine. To see if there are any compositional variations or structures in these olivines or their host pyroxenes, Al, Ca, Cr, Fe, and Mg were measured (further discussion of pyroxene crystals can be found in the pyroxene section). The olivine crystals show zoning for Fe and Mg, representing changes in fosterite content. However, no zoning in Al, Ca, or Cr is apparent for the first olivine. The second olivine shows some variation in Ca, but no variation in Cr or Al. The surrounding host pyroxene crystals show strong complicated zoning patterns.

A very texturally unique olivine (olivine 16) was also mapped in a thin section from sample KM1024 D20-R01 (EPMA maps by Eric Hellebrand) (Figure 3.13). This olivine is anhedral and surrounded by pyroxene intergrowths. It has exsolutions despite its low moderate to low fosterite content (71 to 85) and its low NiO content (0.10 to 0.11). The olivine crystal shows significant fosterite zoning, as evidenced in Mg and Fe maps. The olivine is very homogeneous in Al, Ca and Cr except where the exsolutions are present and immediately around the inclusions, in the case of Cr. This olivine may be a xenocryst.

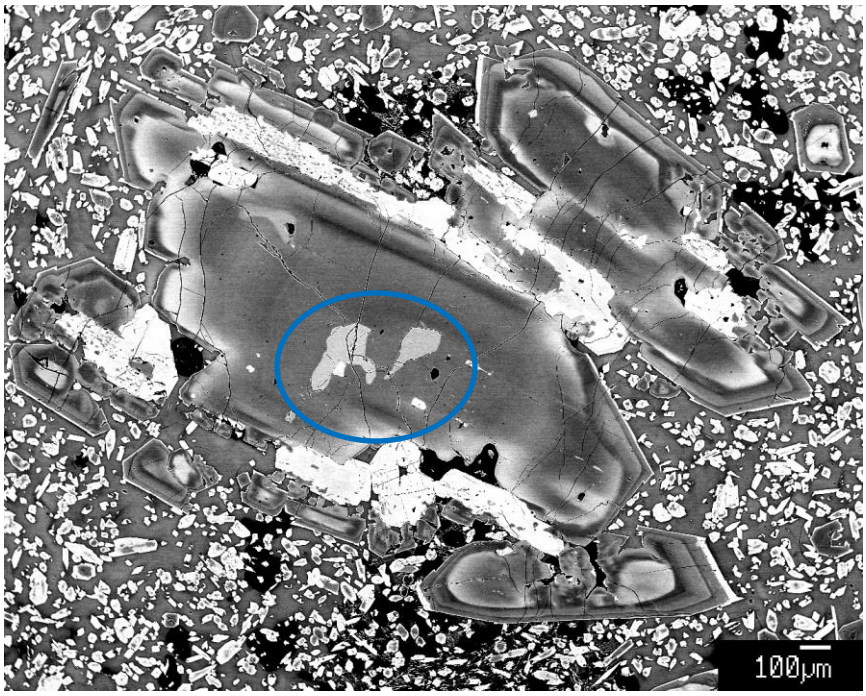

A.

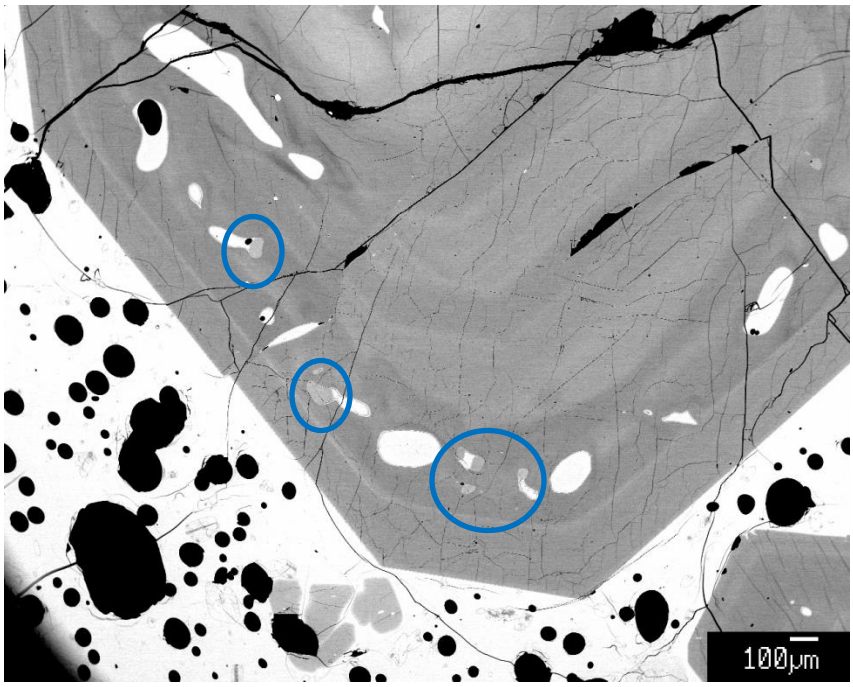

B.

Figure 3.10. Examples of anhedral olivine inclusions in pyroxene. A. EPMA BSE image of Olivines 6 and 7 from a thin section from sample KM1024 D20-R01 (Mata Tolu). B. EPMA BSE image of olivines 6-9 in orthopyroxene 4. Olivine in both images are circled in blue. Melt inclusions are bright. Olivines are only slightly brighter than host pyroxene.

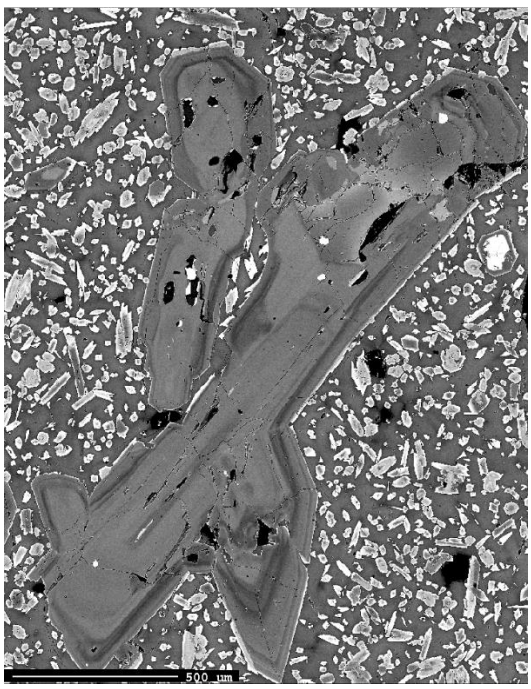

A.
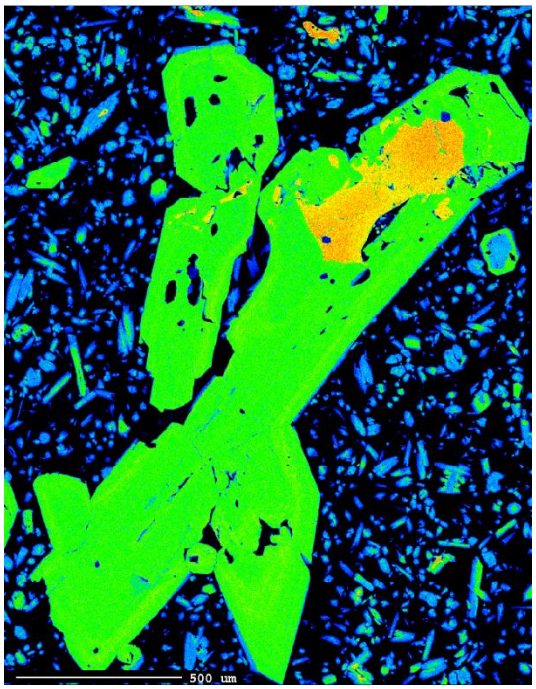

B.

Figure 3.11. EPMA BSE image (A) and EPMA element map (B) of olivine inclusion in pyroxene. A. BSE image. B. EPMA Mg map of an olivine from a thin section of sample KM1024 D20-R01 included in orthopyroxene (Tolu, Olivine 15, Pyroxene 1). Note the zoning pattern in the included olivine (orange to yellow).

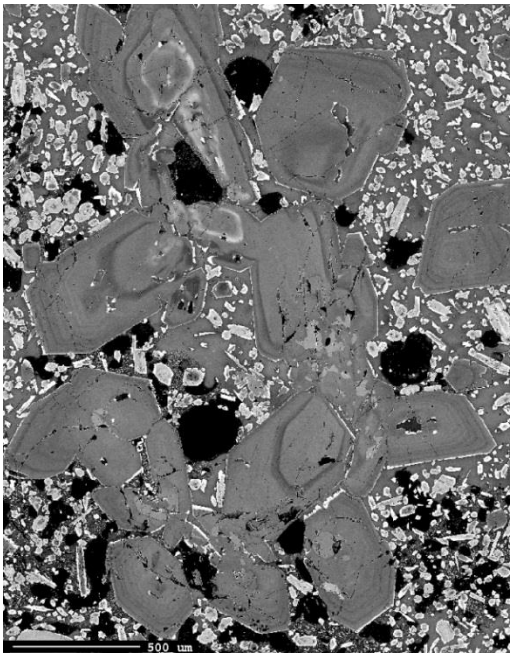

A.
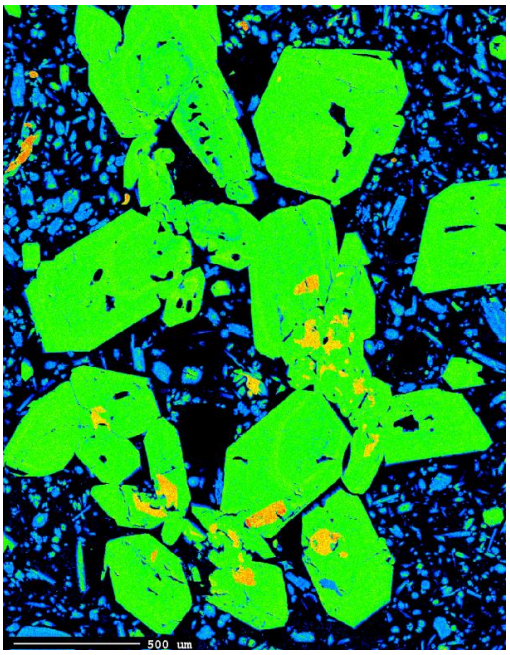

B
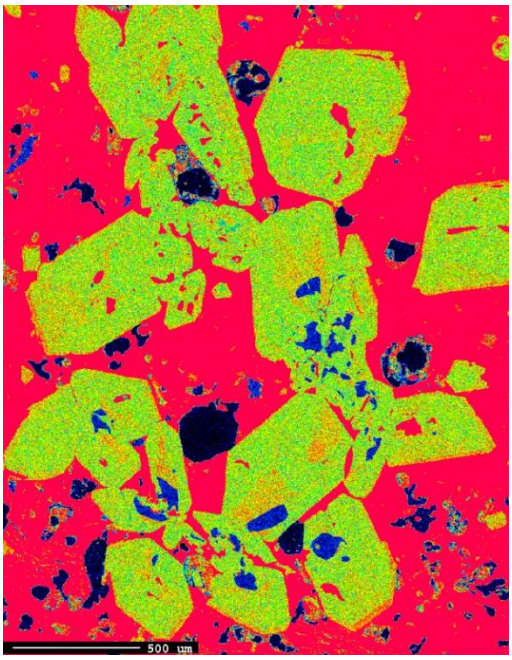

C.

Figure 3.12. EPMA BSE image and EMPA element maps of olivine inclusion in orthopyroxene. A. EPMA BSE image of an olivine included in orthopyroxene. B. EPMA Mg map. Note the zoning pattern in the included olivine (yellow, orange, red). C. EPMA Ca map. Note that the olivine inclusions (blue) do not show much variation in Ca. EPMA BSE image and maps from a thin section of sample KM1024 D20-R01 (Tolu, Olivine 21, Pyroxene 2).

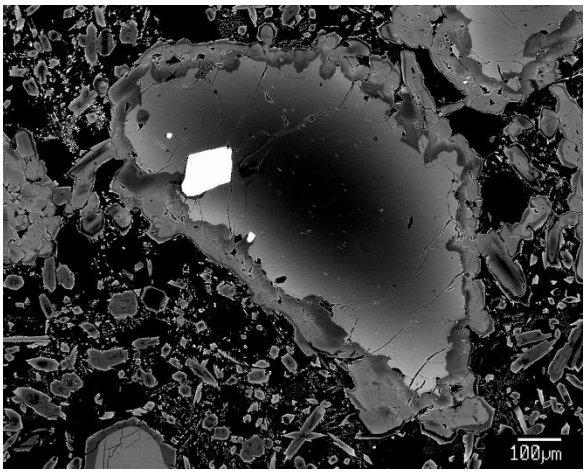

A.

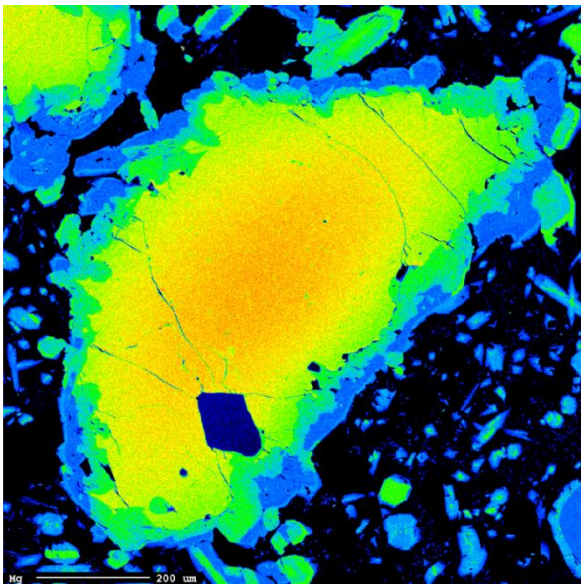

B.

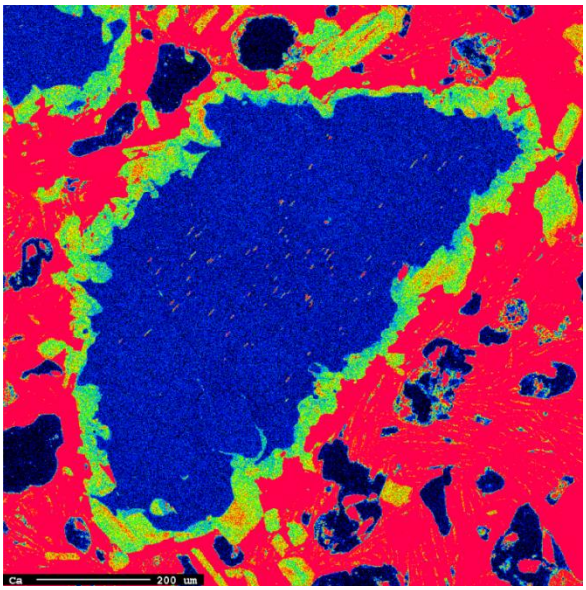

C.

Figure 3.13. Anhedral olivine xenocryst with exsolutions surrounded by pyroxene. A. EPMA BSE image. Note that this image is rotated relative to the other images. B. EPMA Mg map. Note the zoning pattern in the included olivine. C. EPMA Ca map. The olivine crystal is very homogeneous in Ca except for where the exsolutions are present. All panels show an olivine from a thin section of sample KM1024 D20-R01 (Mata Tolu).

**Olivine composition**

A range of compositions in olivine crystals was observed. Overall fosterite ranged from 71 to 93. NiO content ranged from 0.07 to 0.4 wt%. There is significant overlap in composition between the different volcanoes as shown in Figure 3.14.

However, a few trends can also be observed. All of the Matas show a linear sloped trend except for West Mata and Tolu. Mata Tolu has the widest range in fosterite contents. Many of the measured olivine from West Mata tend to have lower fosterite, and often lower NiO than many of the volcanoes from the Northern Matas. With the exception of the core of one large anhedral olivine, olivine from Mata Taha has lower NiO for similar fosterite content than the other Northern Matas (This olivine (2) is different than the others in the sample and may be a xenocryst). Olivine crystals from Mata Tolu do not extend to as high of fosterite content as olivine crystals from some of the other volcanoes. There is also a significant population of anhedral olivine inclusions in pyroxene at Mata Tolu. These are the low fosterite olivine and may be resorbed. Olivine in Matas Ua, Ono, and Fitu appear on the whole compositionally similar. Those from Mata Fa occupy a much higher trend that extends to higher fosterite and NiO content.

The data can be further examined by looking at the average composition of olivine cores and rims for each volcano, as presented in the Tables 3.6 and 3.7.

Average fosterite values of olivine cores range from 87.2 at West Mata to 91.6 at Fa. The most northern Mata volcanoes (Fa, Ono, and Fitu) seem to have slightly higher measured fosterite core values on average. Average NiO values of olivine cores range from 0.15 at Taha to 0.31 at Fa. West Mata, Taha, Tolu and Ono have similar values of 0.15 to 0.17 wt% NiO. Ua (0.22), Fitu (0.23), and Fa (0.31) have significantly higher NiO values.

Average fosterite values of olivine rims range from 85.6 at West Mata to 89.5 at Taha. NiO ranges from 0.17 at Taha to 0.22 at Fitu. Ua (.21) and Fitu (.22) have higher NiO in the rims than the other volcanoes, which range from 0.15 to 0.18 wt% NiO.

Cores of olivine crystals from Mata Fa have the highest fosterite (91.6) and NiO (0.31) values. Rims of olivine crystals from Mata Fa have higher fosterite (88.8) and NiO (0.18) values, but not the highest values. This is the only higher $TiO_2$ non-boninite melt represented, so the data suggest there may be slight compositional differences in crystal chemistry between the boninites and non-boninites. Analysis of olivine from additional higher $TiO_2$ non-boninite melts would be helpful in answering this question.

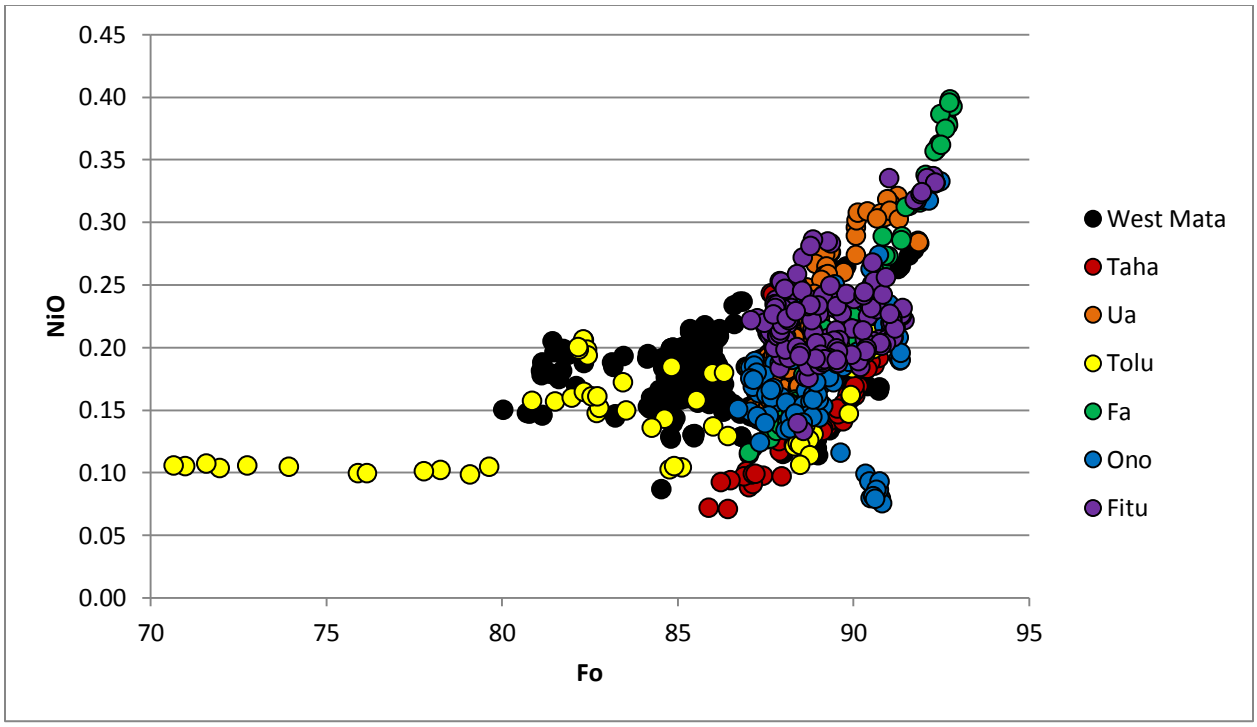


Figure 3.14. NiO content (wt%) vs. Fosterite content for all measured olivine grouped by volcano. There is significant overlap in composition between the different volcanoes. The low-Fo Tolu olivines at 0.1% NiO are all pyroxene-hosted inclusions.

Table 3.6. Composition of average olivine cores for the Mata Volcanoes.

| Volcano | | $SiO_2$ | FeO | NiO | MnO | MgO | CaO | Total | Fo |
|---|---|---|---|---|---|---|---|---|---|
| **West** | Average | 39.83 | 12.29 | 0.17 | 0.19 | 47.01 | 0.16 | 99.65 | 87 |
| | Standard Deviation | 0.69 | 1.70 | 0.04 | 0.02 | 1.49 | 0.03 | 0.36 | 1.88 |
| **Taha** | Average | 40.07 | 10.59 | 0.15 | 0.17 | 48.39 | 0.15 | 99.52 | 89 |
| | Standard Deviation | 0.32 | 1.41 | 0.04 | 0.02 | 1.20 | 0.01 | 0.36 | 1.54 |
| **Ua** | Average | 40.19 | 10.83 | 0.22 | 0.18 | 48.50 | 0.14 | 100.06 | 89 |
| | Standard Deviation | 0.25 | 1.30 | 0.06 | 0.02 | 1.12 | 0.01 | 0.30 | 1.41 |
| **Tolu** | Average | 39.61 | 11.36 | 0.16 | 0.18 | 47.65 | 0.13 | 99.10 | 88 |
| | Standard Deviation | 2.31 | 2.82 | 0.04 | 0.04 | 2.91 | 0.01 | 4.47 | 3.11 |
| **Fa** | Average | 40.56 | 8.20 | 0.31 | 0.13 | 50.02 | 0.15 | 99.37 | 92 |
| | Standard Deviation | 0.21 | 1.02 | 0.06 | 0.02 | 0.81 | 0.02 | 0.26 | 1.09 |
| **Ono** | Average | 40.48 | 10.03 | 0.17 | 0.17 | 49.12 | 0.14 | 100.10 | 90 |
| | Standard Deviation | 0.35 | 1.36 | 0.06 | 0.02 | 1.27 | 0.02 | 0.42 | 1.50 |
| **Fitu** | Average | 40.24 | 9.58 | 0.23 | 0.15 | 49.25 | 0.12 | 99.57 | 90 |
| | Standard Deviation | 0.51 | 1.20 | 0.04 | 0.02 | 1.03 | 0.02 | 0.46 | 1.30 |

The number of thin sections analyzed and points analyzed for the volcanoes are as follows: seven thin sections from seven different rock samples and a total of 130 points for West Mata, one thin section and a total of 44 points for Mata Taha, two thin sections from two different rock samples and a total of 39 points for Mata Ua, one thin section with a total of 45 points for Mata Tolu, one thin section with a total of 24 points for Mata Fa, three thin sections from two rock samples with a total of 47 points for Mata Ono, two thin sections from two different rock samples with a total of 54 points for Mata Fitu

Table 3.7. Composition of average olivine rims for the Mata Volcanoes.

| Volcano | | $SiO_2$ | FeO | NiO | MnO | MgO | CaO | Total | Fo |
|---|---|---|---|---|---|---|---|---|---|
| **West** | Average | 39.61 | 13.67 | 0.16 | 0.21 | 45.82 | 0.19 | 99.67 | 86 |
| | Standard Deviation | 0.60 | 1.28 | 0.02 | 0.01 | 1.31 | 0.03 | 0.59 | 1.47 |
| **Taha** | Average | 40.14 | 10.23 | 0.15 | 0.17 | 48.71 | 0.17 | 99.56 | 89 |
| | Standard Deviation | 0.22 | 0.96 | 0.03 | 0.02 | 0.85 | 0.01 | 0.32 | 1.05 |
| **Ua** | Average | 40.18 | 10.95 | 0.21 | 0.19 | 48.37 | 0.16 | 100.05 | 89 |
| | Standard Deviation | 0.23 | 0.71 | 0.04 | 0.01 | 0.64 | 0.02 | 0.32 | 0.77 |
| **Tolu** | Average | 39.67 | 13.15 | 0.16 | 0.21 | 46.45 | 0.13 | 99.78 | 86 |
| | Standard Deviation | 1.23 | 6.04 | 0.04 | 0.09 | 4.92 | 0.03 | 0.25 | 6.97 |
| **Fa** | Average | 40.10 | 10.77 | 0.18 | 0.18 | 47.79 | 0.19 | 99.21 | 89 |
| | Standard Deviation | 0.17 | 0.95 | 0.05 | 0.02 | 0.74 | 0.02 | 0.29 | 1.03 |
| **Ono** | Average | 40.31 | 11.20 | 0.16 | 0.19 | 48.08 | 0.17 | 100.11 | 88 |
| | Standard Deviation | 0.34 | 0.82 | 0.03 | 0.01 | 0.90 | 0.02 | 0.52 | 0.93 |
| **Fitu** | Average | 40.02 | 11.21 | 0.22 | 0.18 | 47.78 | 0.14 | 99.55 | 88 |
| | Standard Deviation | 0.57 | 0.63 | 0.02 | 0.01 | 0.59 | 0.02 | 0.59 | 0.70 |

The number of thin sections analyzed and points analyzed for the volcanoes are as follows: seven thin sections from seven different rock samples and a total of 108 points for West Mata, one thin section and a total of 42 points for Mata Taha, two thin sections from two different rock samples and a total of 38 points for Mata Ua, one thin section with a total of 35 points for Mata Tolu, one thin section with a total of 24 points for Mata Fa, three thin sections from two rock samples with a total of 32 points for Mata Ono, two thin sections from two different rock samples with a total of 58 points for Mata Fitu

**Texture and Composition**

Texture and composition of olivine crystals often do not correlate. For example, in a single thin section, not all of the olivine crystals with similar textures have similar compositions. For example, rapidly grown olivine in an individual thin section may be normally zoned, reversely zoned, and unzoned in fosterite. Zoning in fosterite does not necessarily correlate with zoning in NiO. Table 3.8 summarizes types of textures and fosterite zoning observed in Mata thin sections.

A wide range of textures and compositions are observed in most thin sections. All thin sections have olivine crystals with and without evidence of rapid growth. Note that this is to some degree qualitative as the angle at which the grain is cut during thin section preparation can affect if evidence of rapid growth can be observed regardless of its presence. Most thin sections have intergrowths of olivine and pyroxene minerals or inclusions of olivine in pyroxene minerals. A distinction between intergrowths and inclusions is not made in this table as an intergrowth can appear to be an inclusion depending on the angle at which the crystals are cut. Unzoned and normally zoned olivine are present in most thin sections. This analysis documents reversely zoned crystals only in Northern Mata thin sections. Additional data would be needed to state this conclusively, as apparent zoning and textures can be affected by the cutting angle and the number of olivine crystals measured. For example, a normally or reversely zoned olivine can appear to have no zoning if a cut only shows the outer rim. Regardless of the uncertainty created by the fact that the olivine crystals may be cut differently, these data demonstrate that the olivine from the Mata volcanoes have complicated and varying textures and compositions.

Table 3.8. Table listing textures and compositions of olivine crystals present in thin sections from the Mata volcanoes.

| Location | Sample | Textures | | | Zoning (Fosterite) | | |
|---|---|---|---|---|---|---|---|
| | | A | B | C | U | N | R |
| West | J2-413-R04 | X | X | X | X | X | |
| West | J2-413-R13 | X | X | X | X | X | |
| West | J2-418-R01 | X | X | X | X | | |
| West | J2-418-R11 | X | X | X | X | X | |
| West | J2-418-R18 | X | X | X | X | X | |
| West | J2-420-R02 | X | X | X | X | X | |
| West | J2-420-R17 | X | X | X | X | X | |
| Taha | KM1024 D16-R04 | X | X | | X | X | X |
| Ua | KM1024 D18-R01 | X | X | | X | X | X |
| Ua | KM1024 D18-R02 | X | X | | X | X | X |
| Tolu | KM1024 D20-R01 | X | X | X | X | X | X |
| Fa | KM1024 D21-R02 | X | X | | | X | |
| Ono | KM1024 D22-R01D | X | X | | X | X | X |
| Ono | KM1024 D22-R01L | X | X | | | X | X |
| Ono | KM1024 D22-R02 | X | X | X | X | X | |
| Fitu | KM1024 D23-R01 | X | X | X | X | X | |
| Fitu | KM1024 D23-R04 | X | X | X | X | X | |

Textural groups are: A.) No evidence of rapid growth, B.) Rapidly grown, and C.) Olivine-pyroxene intergrowths or olivine inclusions in pyroxene. Types of fosterite zoning are: U=unzoned, N=normally zoned, R=reversely zoned. If an olivine or multiple olivine crystals are present in the thin section with a type of texture or zoning, an X is put in that category. If a type of texture or zoning is not present, it is left blank.

## Pyroxene Results

### Introduction and Methods

Ten elements (Si, Ti, Al, Cr, Fe, Mn, Mg, Ca, Na, and K) in pyroxene crystals were analyzed in 15 thin sections from eight of the Mata Volcanoes by EPMA at UH Manoa. Clinopyroxene and orthopyroxene crystals were measured together in the same runs. The samples analyzed are listed in the following table 3.9.

Table 3.9. Samples in which pyroxene were analyzed for the Mata Volcanoes.

| Location | Number of Samples for which Pyroxene was Analyzed | Samples |
|---|---|---|
| East Mata | 2 | KM1024 D14-R02 |
| | | KM1024 D14-R07 |
| West Mata | 7 | J2-413-R04 |
| | | J2-413-R13 |
| | | J2-418-R01 |
| | | J2-418-R11 |
| | | J2-418-R18 |
| | | J2-420-R02 |
| | | J2-420-R17 |
| Taha | 1 | KM1024 D16-R04 |
| Ua | 1 | KM1024 D18-R01 |
| Tolu | 1 | KM1024 D20-R01 |
| Fa | 1 | KM1024 D21-R02 |
| Ono | 1 | KM1024 D22-R02 |
| Fitu | 1 | KM1024 D23-R01 |

For each sample, points were taken both in pyroxene cores and rims. In some cases, midpoints were also taken or transects were taken. BSE images of each pyroxene analyzed were captured by EPMA at UH Manoa and points analyzed were recorded manually

**Pyroxene Textures**

Overall a range of pyroxene textures was observed in BSE images and microprobe element maps. Crystals ranged in size from large several mm long crystals to groundmass or close to groundmass sized crystals. Pyroxene crystals are generally euhedral to subhedral. However, the majority have complicated zoning or oscillatory zoning patterns readily apparent in EPMA BSE images. This can be observed in pyroxene crystals from to small scale pyroxene crystals to large phenocrysts. Unzoned or lightly zoned crystals are rare. J2-418-R01, from an older eruption of West Mata, is the only thin section for which pyroxene crystals were measured in which homogeneous, unzoned pyroxenes were common. Interestingly, many of these unzoned pyroxene crystals contained rounded olivine inclusions. Individual pyroxene crystals as well as intergrowths are present. Intergrowths or clusters of clinopyroxene and orthopyroxene, of a pyroxene and olivine, and of two pyroxenes and olivine are not uncommon. In many situations, the olivine may be reacting to form pyroxene. Pyroxene crystals from an individual volcano and even in an individual thin section can span the range of textures.

Several EPMA element maps of texturally distinct pyroxene crystals were made using the microprobe at UH Manoa. EPMA element maps allow us to see the structure of these crystals beyond quantitative spot analysis. This section will summarize types of pyroxene textures observed in EPMA BSE images and element maps

Figure 3.15 shows examples of pyroxene with little or no apparent zoning. The first element map is of intergrown crystals that appear relatively unzoned (Figures 3.16), at least in a BSE image, KM1024 D20-R01 pyroxene 13. The inner clinopyroxene does not show much zoning/variation in Ca, Fe or Mg while the outer orthopyroxene does. Both show variation/zoning in Al. Some variation is apparent in Cr in the orthopyroxene and probably the clinopyroxene as well. Some of these variations are not visible in the BSE image and cannot be understood by just a few spot analysis, so it is possible that the pyroxene crystals in this study are more complicated than can be inferred from a handful of spot analyses.

Figure 3.17 shows examples of pyroxenes with complicated zoning and intergrown pyroxenes. For some examples of olivine-pyroxene intergrowths where the olivine crystals appear to be resorbed, see Figures 3.10-3.12. Two pyroxenes with olivine inclusions were also analyzed, both found in a thin section from KM1024 D20-R01. These may be the products of partial resorption of olivine. Figure 3.18-3.19 show maps of these pyroxene crystals.

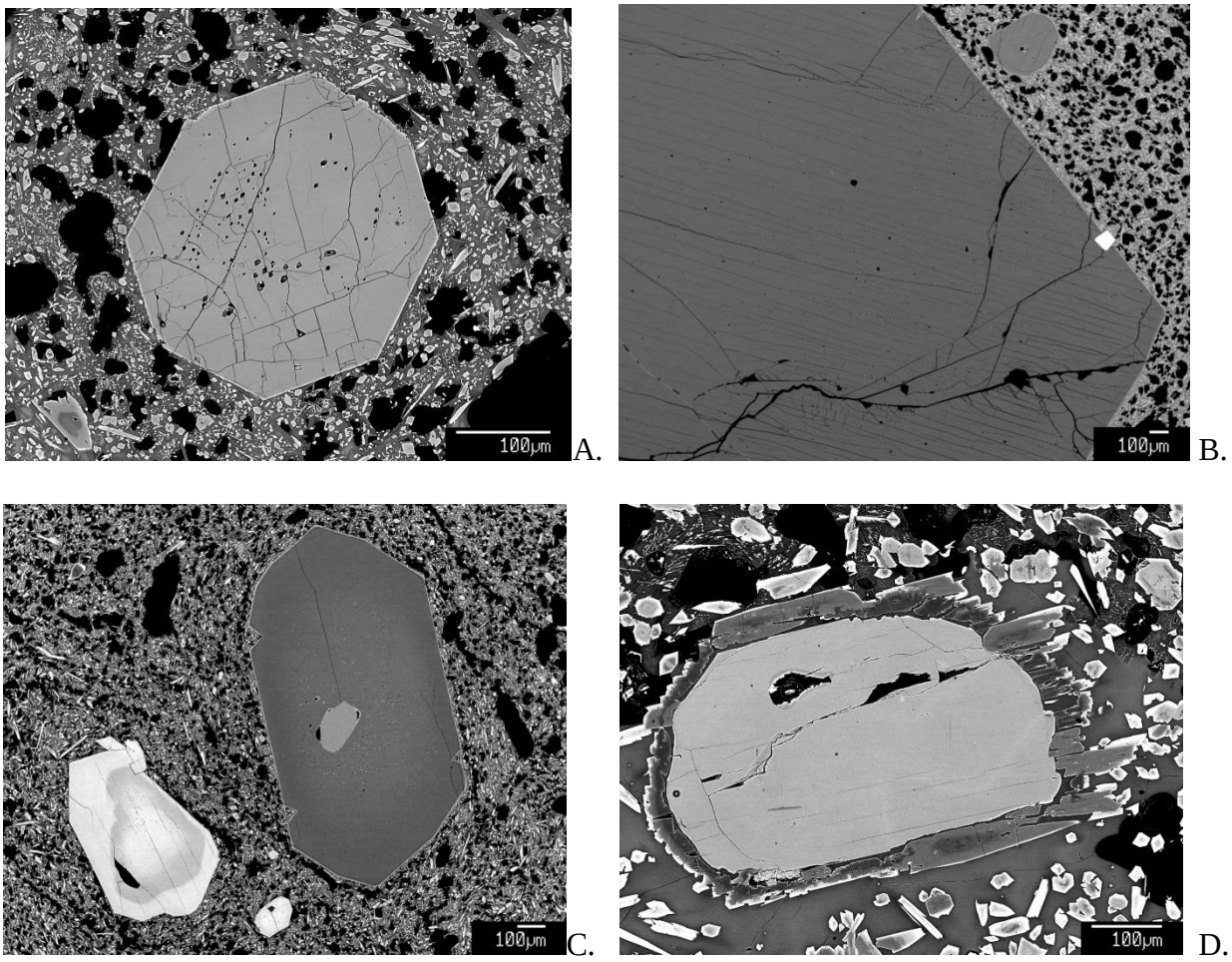


Figure 3.15. Pyroxenes that do not show obvious zoning. A. Euhedral clinopyroxene with no apparent zoning from J2-418-R01 (pyroxene 4). Spot analysis of this pyroxene did not show evidence of zoning. The dark inclusions are melt inclusions. B. Euhedral orthopyroxene with no apparent zoning from J2-418-R01 (pyroxene 8). Spot analysis of this pyroxene did not show evidence of zoning. C. Euhedral orthopyroxene (right) with a rounded olivine inclusion and weak reverse zoning from J2-418-R01 (pyroxene 2, olivine 2). Spot analysis of this pyroxene did not show evidence of zoning. The strongly zoned light-grey crystal on the left is a clinopyroxene that was not measured. D. BSE image of a topoaxial overgrowth of orthopyroxene (medium-dark grey) on a subrounded clinopyroxene core (center, light grey) (sample KM1024 D20-R01, pyroxene 13, Mata Tolu). EPMA element maps were made of this overgrown pyroxene and will be discussed in the next section (Figure 3.16). Despite the apparent lack of zoning in the clinopyroxene in this image, EPMA element maps reveal zoning patterns.

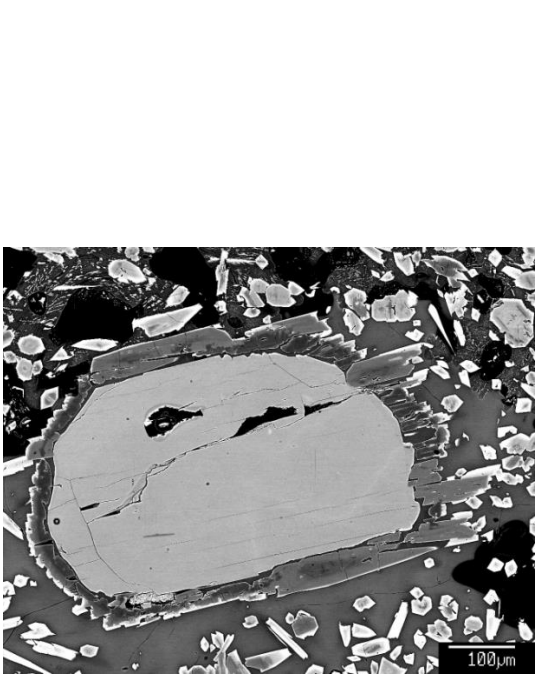


A

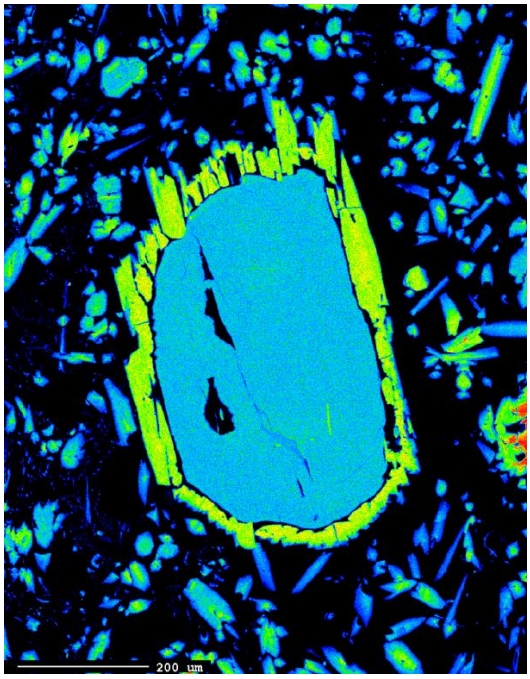


B.

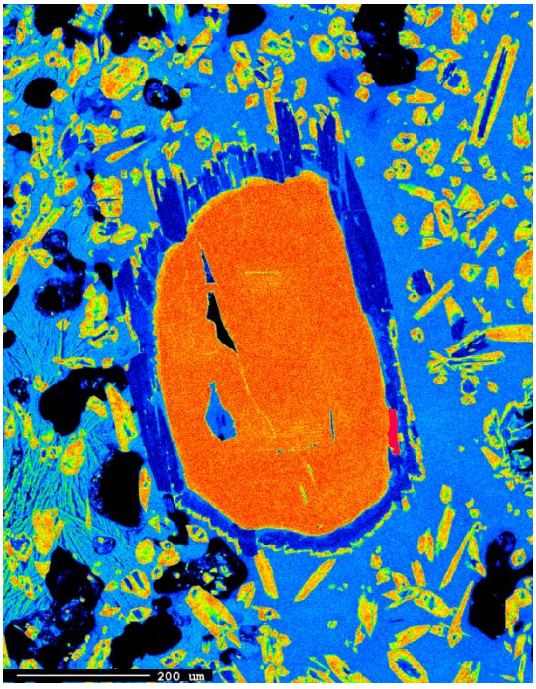


C.

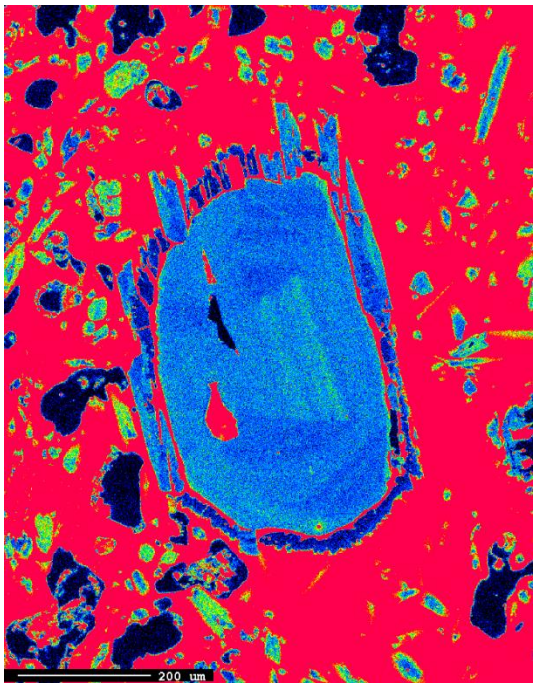


D.

Figure 3.16. See next page for full image caption.

Figure 3.16. BSE image and EPMA element maps of a topoaxial overgrowth of orthopyroxene (medium-dark grey) on a subrounded clinopyroxene core (center, light grey) (sample KM1024 D20-R01, pyroxene 13, Mata Tolu). A. BSE image in which the clinopyroxene does not appear to have any zoning, but as shown in panel D, zoning in Al is present. B. EPMA element map in which the clinopyroxene does not appear to have significant Mg zoning, while variations are apparent throughout the orthopyroxene. Note that the view is rotated relative to the BSE image. C. The clinopyroxene does not appear to have significant Ca zoning/variation, except for a few areas that appear slightly more enriched. Variations are apparent throughout the orthopyroxene. D. The clinopyroxene and orthopyroxene both show zoning/variation in Al.

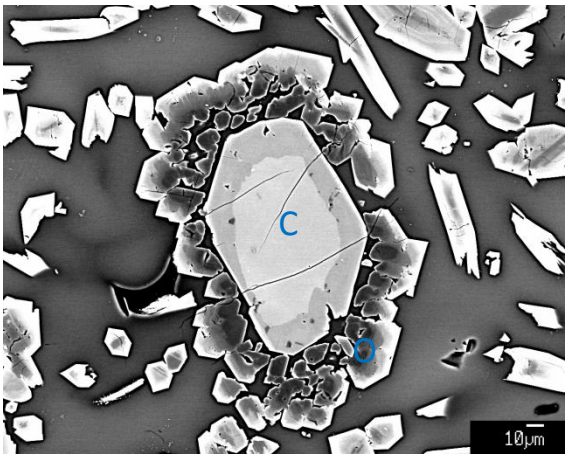

A.

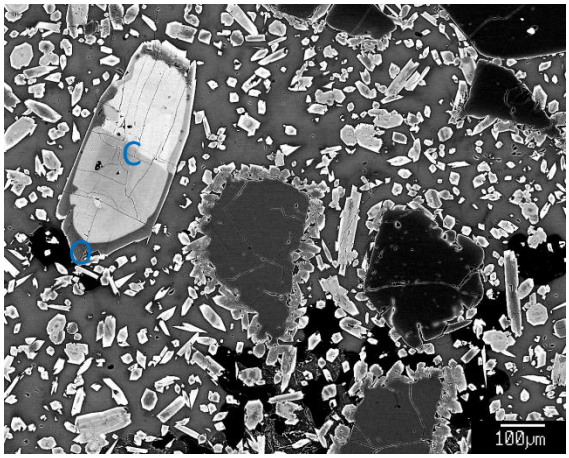

B.

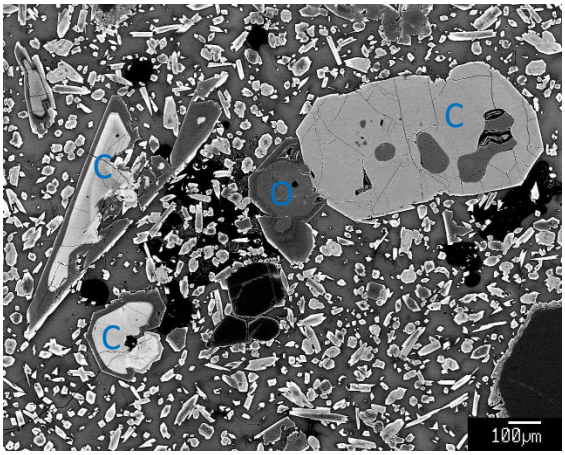

C.

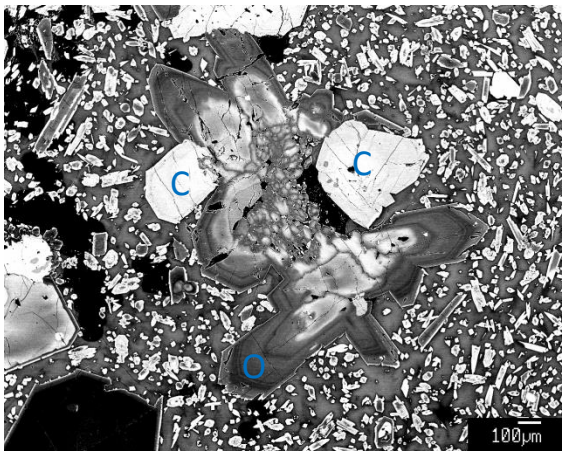

D.

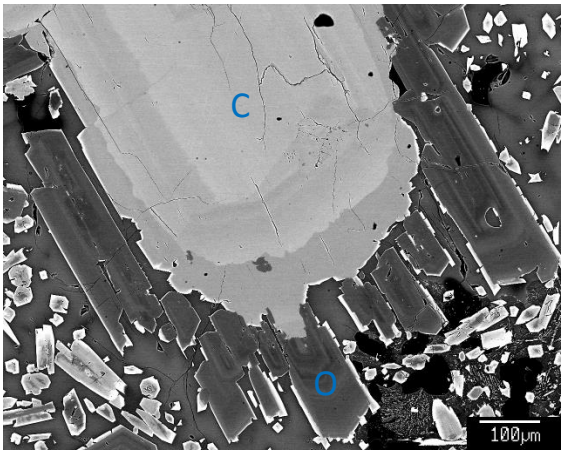

E.

Figure 3.17. See next page for full figure caption

Figure 3.17. BSE images of complex pyroxene intergrowths. Crystals in the images are labeled "C" for clinopyroxene and "O" for orthopyroxene. A. BSE image of complexly zoned two-pyroxene pair. The core consists of an irregular to subrounded low-Mg# clinopyroxene, overgrown by a more Mg-rich rim forming a euhedral crystal, topoaxially overgrown by skeletal orthopyroxene that grows to Fe-rich compositions outward (dark-medium grey). The outermost bright euhedral crystal faces are clinopyroxene (KM1024 D20-R01, Mata Tolu). B. The crystal in the upper left-hand corner has a rounded clinopyroxene center. The two tones of light grey may represent sector zoning in this crystal. It has been overgrown by a orthopyroxene rim that appears compositionally uniform. The thin light rim on the outside is clinopyroxene. These pyroxenes were not analyzed (KM1024 D20-R01 from Mata Tolu). C. Three pyroxene intergrowths can be seen here. The two on the left have rounded clinopyroxene cores. The composition of these cores varies. They are overgrown by a zone of orthopyroxene (dark grey) then a thin rim of clinopyroxene (white). The pyroxene on the left consists of a light grey clinopyroxene with anhedral orthopyroxene inclusions in it (dark grey). In 3D this could also be an intergrowth. An orthopyroxene is intergrown with the left rim of this clinopyroxene. While the clinopyroxene looks compositionally homogeneous, the orthopyroxene has oscillatory zoning. Both are surrounded by a very thin rim of clinopyroxene. These pyroxenes were not analyzed. (KM1024 D20-R01 from Mata Tolu). D. This clinopyroxene-orthopyroxene intergrowth has a series of rounded crystals in the center. They appear to have clinopyroxene in the center and orthopyroxene on the outside. Moving to the outer edges of the intergrowth, there is a large oscillatory zoned orthopyroxene rim or zone. Two larger clinopyroxenes are intergrown with the outside of this zone. Both also show oscillatory zoning. This clinopyroxene-orthopyroxene intergrowth was not analyzed (KM1024 D20-R01). E. The inner portion of this intergrowth is a oscillatory zoned and sector zoned clinopyroxene crystal. Orthopyroxene has grown around the rim. The orthopyroxene also shows oscillatory zoning. A very thin outer rim of clinopyroxene is present. ( KM1024 D20-R01 Pyroxene 4)

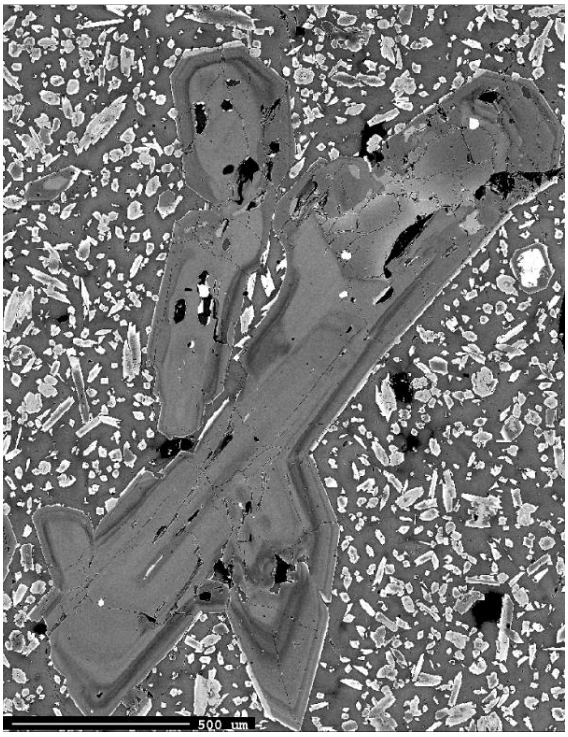


A.

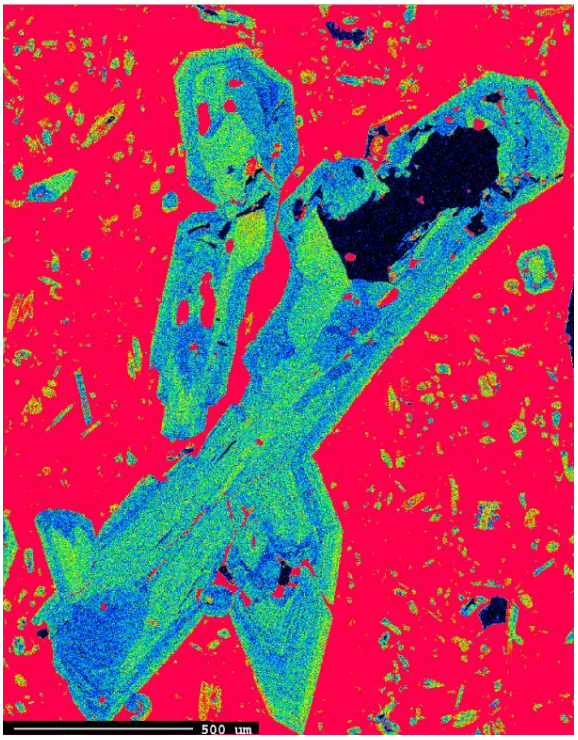


B.

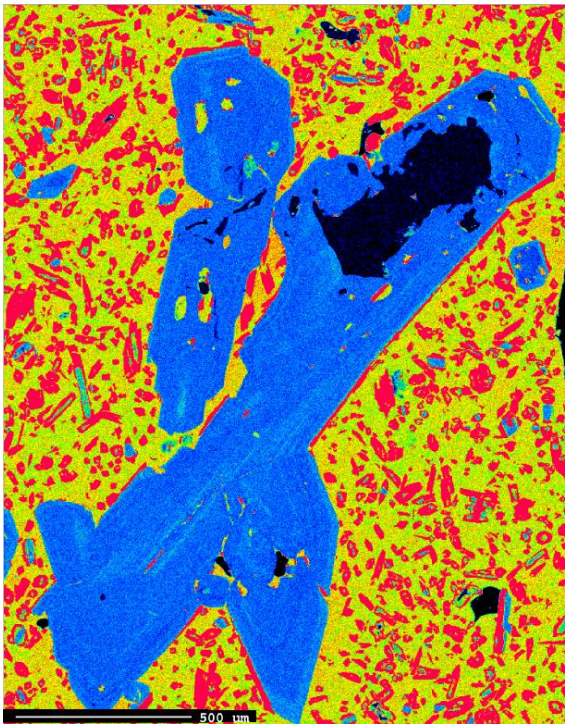


C.

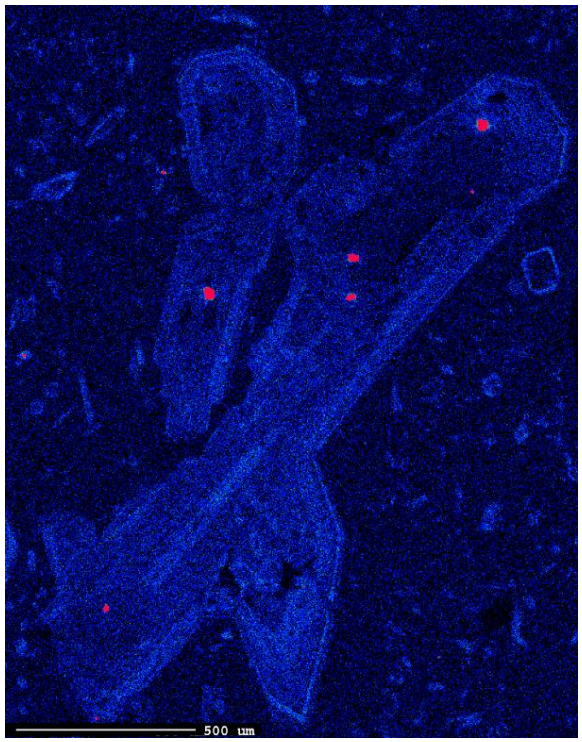


D.

Figure 3.18. See next page for full figure caption.

E.
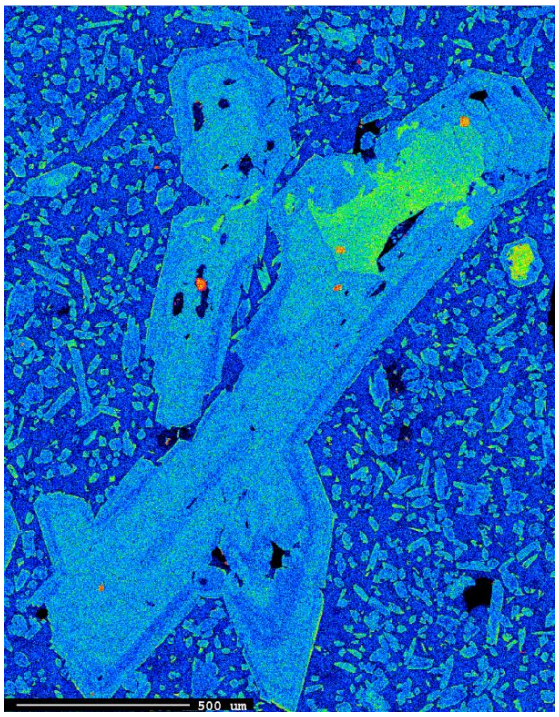

F.

Figure 3.18, continued. Pyroxene with large olivine and tiny spinel inclusions from a thin section of sample KM1024 D20-R01 (Mata Tolu). A. BSE image. B. EPMA Al map of a pyroxene. Note the Low vs. High Al sector zoning patter. Fine oscillatory zoning is also present. C. EPMA Ca map. Note the little bit of zoning in the oscillatory pyroxene (blue). The dark blue is the olivine. D. EPMA Cr map. Note the oscillatory zoning and sector zoning pattern in the pyroxene. E. EPMA Mg map. Note the oscillatory zoning pattern in the pyroxene (orange to red). F. Pyroxene with olivine inclusion. EPMA Fe map. Note the oscillatory zoning pattern in the pyroxene (blue).

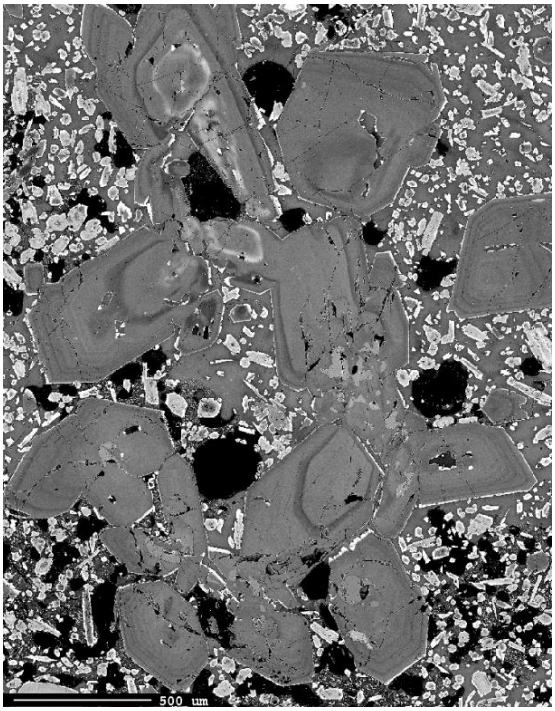


A.

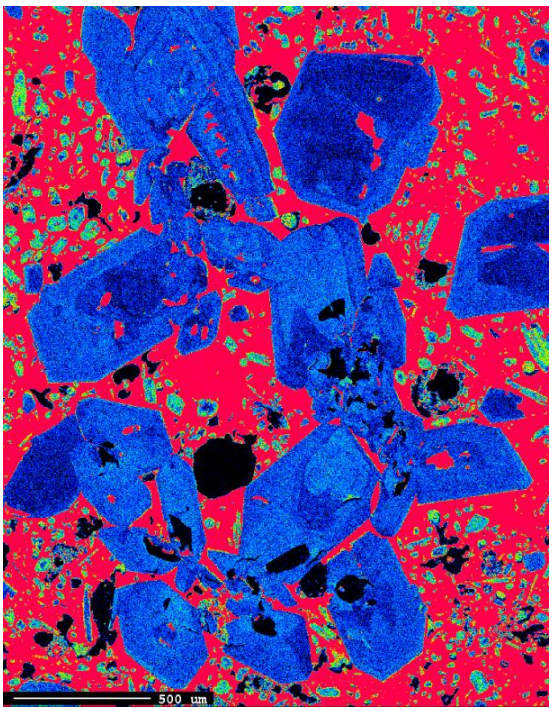


B.

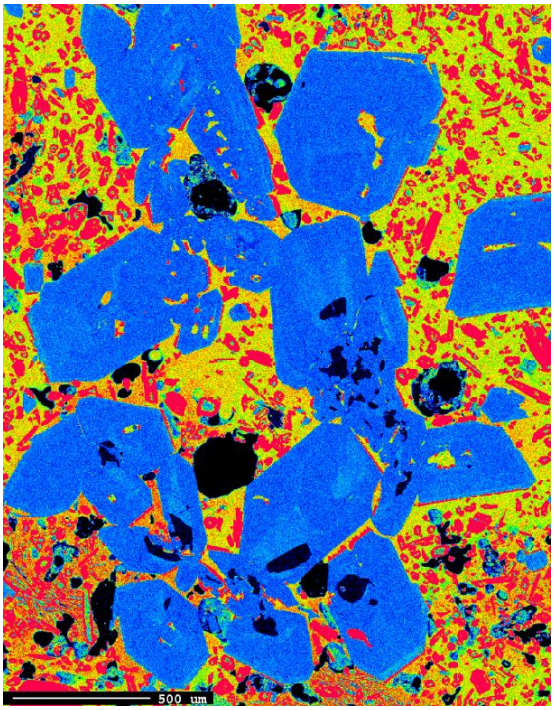


C.

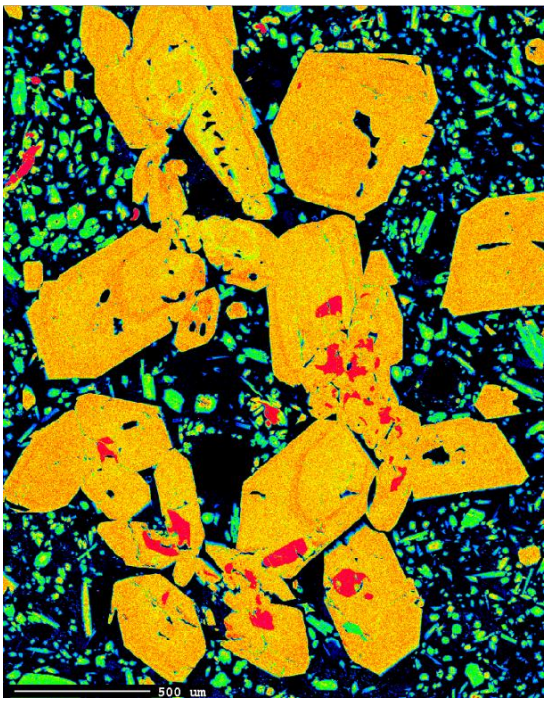


D.

Figure 3.19. See next page for full figure caption

Figure 3.19. Pyroxene with olivine inclusion pyroxene from a thin section of sample KM1024 D20-R01 (Mata Tolu). A. BSE image. B. EPMA Al map. Note the zoning pattern in the pyroxene (blue). The dark blue is the olivine. C. EPMA Ca map. Note the little bit of zoning in the pyroxene (blue). The dark blue is the olivine. D. EPMA Mg. Note the zoning pattern in the pyroxene (yellow to orange to red).

**Pyroxene Compositions**

Both clinopyroxene and orthopyroxene were observed and measured in Mata samples. For all Mata samples, $TiO_2$ content in clinopyroxene ranges from 0.04 to 0.57 wt%. $Al_2O_3$ content ranges from 0.52 to 5.50 wt%. $Cr_2O_3$ content ranges from 0.00 to 1.09 wt%. FeO ranges from 3.98 to 10.43 wt%. MgO ranges from 14.56 to 20.92 wt%. CaO ranges from 15.09 to 21.62 wt%. $Na_2O$ ranges from 0.07 to 0.24 wt%. Percentages of end-members vary from 30% to 43% wollastonite, from 41 to 58% enstatite, and from 6 to 19% ferrosilite.

For all Mata samples, $TiO_2$ content in orthopyroxene ranges from 0.00 to 0.28 wt%. $Al_2O_3$ content ranges from 0.3 to 3.43 wt%. $Cr_2O_3$ content ranges from 0.00 to 0.73 wt%. FeO ranges from 6.75 to 21.42 wt%. MgO ranges from 22.19 to 33.98 wt%. CaO ranges from 1.00 to 3.85 wt%. $Na_2O$ ranges from 0.00 to 0.12 wt%. Percentages of end-members vary from 2% to 7% wollastonite, from 64 to 88% enstatite, and from 10 to 34% ferrosilite. Figure 3.20 shows the range of pyroxene compositions measured. Most clinopyroxene plot near the diopside end-member. Most orthopyroxene plot by the enstatite end-member. Generally samples from the different volcanoes and samples from the older eruption(s) and the new eruption at West Mata overlap in compositions. Tables 3.10 -3.13 summarize clinopyroxene and orthopyroxene average rim compositions.

Table 3.10. Average clinopyroxene rim composition

| Volcano | | $SiO_2$ | $TiO_2$ | $Al_2O_3$ | $Cr_2O_3$ | FeO | MnO | MgO | CaO | $Na_2O$ | $K_2O$ | Total |
|---|---|---|---|---|---|---|---|---|---|---|---|---|
| **East** | Avg. | 53.94 | 0.12 | 1.37 | 0.41 | 6.48 | 0.22 | 19.68 | 17.64 | 0.12 | 0.01 | 100.00 |
| | Stdev. | 0.36 | 0.04 | 0.25 | 0.10 | 0.74 | 0.02 | 0.76 | 1.31 | 0.02 | 0.01 | 0.20 |
| **West** | Avg. | 53.00 | 0.13 | 1.56 | 0.45 | 6.07 | 0.17 | 18.58 | 19.16 | 0.13 | 0.00 | 99.27 |
| | Stdev. | 1.00 | 0.04 | 0.54 | 0.27 | 1.33 | 0.04 | 1.14 | 0.96 | 0.02 | 0.00 | 0.82 |
| **Taha** | Avg. | 51.99 | 0.22 | 2.27 | 0.34 | 7.08 | 0.20 | 18.26 | 18.52 | 0.16 | 0.01 | 99.05 |
| | Stdev. | 0.35 | 0.02 | 0.25 | 0.18 | 0.78 | 0.04 | 0.50 | 1.15 | 0.02 | 0.01 | 0.63 |
| **Tolu** | Avg. | 53.10 | 0.20 | 1.93 | 0.30 | 6.52 | 0.20 | 18.09 | 19.50 | 0.14 | 0.00 | 99.97 |
| | Stdev. | 0.40 | 0.07 | 0.36 | 0.18 | 0.64 | 0.02 | 0.70 | 0.36 | 0.02 | 0.01 | 0.15 |
| **Fa** | Avg. | 53.01 | 0.37 | 1.96 | 0.72 | 5.48 | 0.14 | 18.32 | 19.32 | 0.20 | 0.01 | 99.53 |
| | Stdev. | 0.25 | 0.07 | 0.37 | 0.26 | 0.75 | 0.03 | 0.59 | 1.02 | 0.01 | 0.01 | 0.39 |
| **Fitu** | Avg. | 50.26 | 0.36 | 5.01 | 0.06 | 9.44 | 0.21 | 15.97 | 17.77 | 0.20 | 0.01 | 99.29 |
| | Stdev. | 0.42 | 0.02 | 0.54 | 0.02 | 0.52 | 0.04 | 0.68 | 1.01 | 0.02 | 0.01 | 0.52 |

The number of thin sections analyzed and points analyzed for the volcanoes are as follows: One thin section for a total of six points from East Mata, six thin sections from six different rock samples and a total of 44 points for West Mata, one thin section and a total of seven points for Mata Taha, one thin section and a total of five points for Mata Tolu, one thin section with a total of seven points for Mata Fa, one thin section with a total of four points for Mata Fitu

Table 3.11. Average clinopyroxene end member percentages in rim measurements

| Volcano | | Wo | En | Fs |
|---|---|---|---|---|
| **East** | Avg. | 35.2 | 54.7 | 10.1 |
| | Stdev. | 2.7 | 1.8 | 1.1 |
| **West** | Avg. | 38.5 | 51.9 | 9.5 |
| | Stdev. | 1.9 | 2.8 | 2.2 |
| **Taha** | Avg. | 37.4 | 51.4 | 11.2 |
| | Stdev. | 2.2 | 1.3 | 1.3 |
| **Tolu** | Avg. | 39.2 | 50.6 | 10.2 |
| | Stdev. | 0.8 | 1.8 | 1.0 |
| **Fa** | Avg. | 39.4 | 51.9 | 8.7 |
| | Stdev. | 2.2 | 1.6 | 1.2 |
| **Fitu** | Avg. | 46.0 | 40.9 | 13.1 |
| | Stdev. | 16.5 | 9.4 | 7.5 |

The number of thin sections analyzed and points analyzed for the volcanoes are as follows: One thin section for a total of six points from East Mata, six thin sections from six different rock samples and a total of 44 points for West Mata, one thin section and a total of seven points for Mata Taha, one thin section and a total of five points for Mata Tolu, one thin section with a total of seven points for Mata Fa, one thin section with a total of four points for Mata Fitu

Table 3.12. Average orthopyroxene rim composition

| Volcano | | $SiO_2$ | $TiO_2$ | $Al_2O_3$ | $Cr_2O_3$ | FeO | MnO | MgO | CaO | $Na_2O$ | $K_2O$ | Total |
|---|---|---|---|---|---|---|---|---|---|---|---|---|
| **East** | Avg. | 56.38 | 0.06 | 0.79 | 0.36 | 9.18 | 0.25 | 30.75 | 2.49 | 0.05 | 0.01 | 100.32 |
| | Stdev. | 0.32 | 0.02 | 0.18 | 0.13 | 0.36 | 0.02 | 0.48 | 0.41 | 0.02 | 0.01 | 0.45 |
| **West** | Avg. | 55.37 | 0.06 | 0.86 | 0.27 | 10.25 | 0.23 | 30.54 | 2.07 | 0.02 | 0.00 | 99.69 |
| | Stdev. | 0.75 | 0.02 | 0.25 | 0.12 | 1.73 | 0.04 | 1.46 | 0.18 | 0.01 | 0.00 | 0.77 |
| **Ua** | Avg. | 56.42 | 0.08 | 1.25 | 0.49 | 8.77 | 0.23 | 30.79 | 2.42 | 0.03 | 0.01 | 100.49 |
| | Stdev. | 0.37 | 0.01 | 0.29 | 0.24 | 0.83 | 0.05 | 0.86 | 0.24 | 0.01 | 0.01 | 0.17 |
| **Tolu** | Avg. | 55.81 | 0.09 | 1.10 | 0.35 | 11.32 | 0.26 | 30.11 | 2.16 | 0.03 | 0.00 | 101.23 |
| | Stdev. | 1.00 | 0.03 | 0.27 | 0.08 | 3.32 | 0.07 | 2.65 | 0.29 | 0.02 | 0.00 | 0.33 |
| **Ono** | Avg. | 56.94 | 0.05 | 0.83 | 0.41 | 8.08 | 0.22 | 32.02 | 2.02 | 0.03 | 0.01 | 100.59 |
| | Stdev. | 0.40 | 0.02 | 0.21 | 0.11 | 0.18 | 0.02 | 0.43 | 0.23 | 0.01 | 0.01 | 0.25 |
| **Fitu** | Avg. | 56.82 | 0.05 | 0.82 | 0.38 | 8.09 | 0.22 | 32.58 | 1.78 | 0.04 | 0.01 | 100.78 |
| | Stdev. | 0.47 | 0.03 | 0.22 | 0.08 | 0.54 | 0.02 | 0.73 | 0.22 | 0.02 | 0.01 | 0.57 |

The number of thin sections analyzed and points analyzed for the volcanoes are as follows: One thin section for a total of six points from East Mata, seven thin sections from seven different rock samples and a total of 45 points for West Mata, one thin section and a total of four points for Mata Ua, one thin section and a total of ten points for Mata Tolu, one thin section with a total of ten points for Mata Ono, one thin section with a total of 14 points for Mata Fitu

Table 3.13. Average orthopyroxene end member percentages in rim measurements

| Volcano | | Wo | En | Fs |
|---|---|---|---|---|
| **East** | Avg. | 2.5 | 0.0 | 0.0 |
| | Stdev. | 0.4 | 0.0 | 0.0 |
| **West** | Avg. | 3.7 | 69.5 | 26.8 |
| | Stdev. | 0.3 | 2.9 | 2.8 |
| **Ua** | Avg. | 4.7 | 82.2 | 13.1 |
| | Stdev. | 0.5 | 1.8 | 1.3 |
| **Tolu** | Avg. | 4.1 | 79.1 | 16.8 |
| | Stdev. | 0.6 | 5.6 | 5.3 |
| **Ono** | Avg. | 3.8 | 84.3 | 11.9 |
| | Stdev. | 0.5 | 0.7 | 0.3 |
| **Fitu** | Avg. | 3.3 | 84.8 | 11.8 |
| | Stdev. | 0.4 | 1.3 | 0.9 |

The number of thin sections analyzed and points analyzed for the volcanoes are as follows: One thin section for a total of six points from East Mata, seven thin sections from seven different rock samples and a total of 45 points for West Mata, one thin section and a total of four points for Mata Ua, one thin section and a total of ten points for Mata Tolu, one thin section with a total of ten points for Mata Ono, one thin section with a total of 14 points for Mata Fitu

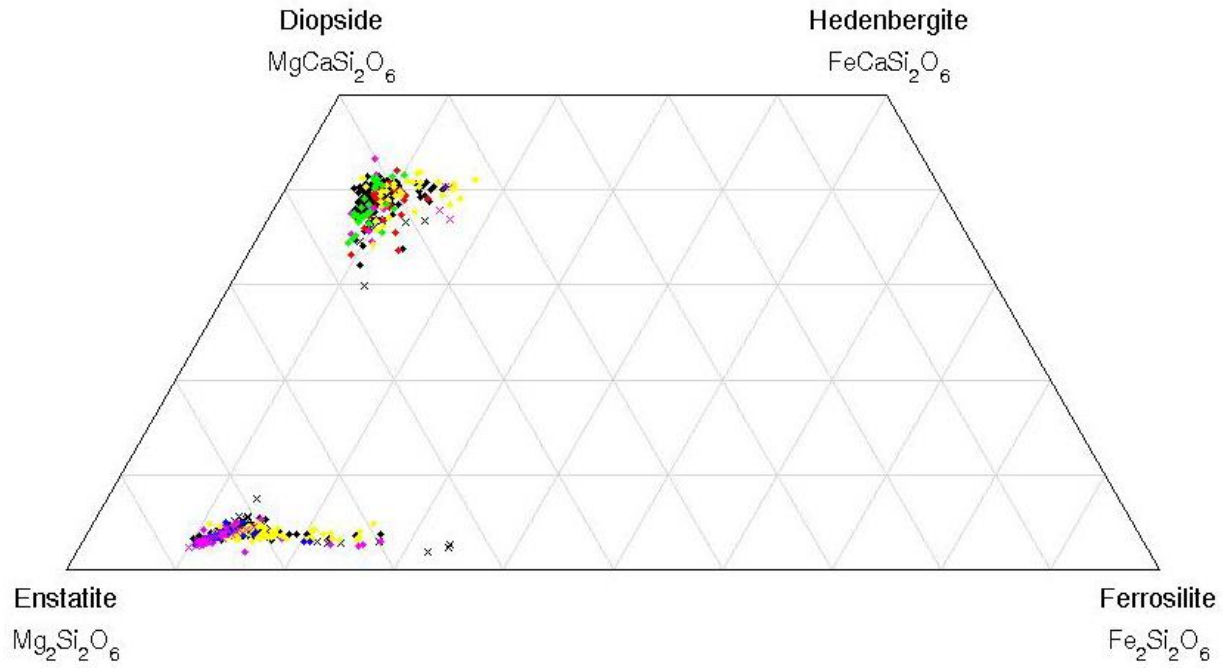


Figure 3.20. Pyroxene compositions for all Mata Volcanoes. Xs are from East Mata. Black diamonds are from West Mata. Red diamonds are from Mata Taha. Pink diamonds are from Mata Ua. Yellow diamonds are from Mata Taha. Green diamonds are from Mata Fa. Blue diamonds are from Mata Ono. Purple Diamonds are from Mata Fitu. Diagram made using a Matlab script written by Emily First.

A detailed look at clinopyroxene compositions reveals significant complexity within a sample and usually within an individual pyroxene crystal. For most thin sections, an overall look at the data shows what appears to be differentiation trends. For example, the $Al_2O_3$ vs FeO plot for clinopyroxene crystals from West Mata sample J2-418-R01 shows apparent evolution of the crystal compositions to higher $Al_2O_3$ and FeO content. For many thin sections, these trends are clearer or only clear for some elements (Figure 3.20).

However, a closer examination of the compositional data and cross comparison of the textural data and images with the compositional data indicate that these pyroxene are not all normally zoned and evolving through simple fractionation. Complicated oscillatory zoning and sector zoning is present. The more evolved points are not necessarily at the rims.

In a few cases, there are several distinct compositional groups that can be observed within a single thin section. In one case, for West Mata sample J2-418-R18, the two compositional groups are a remnant core and new overgrowth. However for the other samples that have clinopyroxene compositional subgroups (Mata Tolu sample KM1024 D20-R01 and Mata Fa sample KM1024 D21-R02), the relationship is not clear. For the Mata Tolu sample, clinopyroxene crystals mostly fall into the groups with some compositional overlap. Interestingly, for the Mata Fa sample, clinopyroxene crystals do not neatly fall into one group or another. Instead different points within an individual clinopyroxene crystal will fall in different groups. This suggests that portions of different crystals grew under the same conditions. This could suggest changes in the melt composition due to magma mixing or recharge. The crystallization history of samples from the Mata Volcanoes will be discussed in more detail in Chapter 5.

Similar observations can be made for the orthopyroxenes analyzed. Similar to the clinopyroxene data, for most thin sections, an overall look at the data shows what appears to be differentiation trends. For many thin sections, these trends are clearer or only clear for some elements (Figure 3.21). Again a closer examination and comparison of the compositional data

with images shows that they did not evolve through simple fractionation alone. Oscillatory zoning and sector zoning is present.

Generally there is overlap, but in a few cases there are compositional groups. For West Mata sample 418-R18, a resorbed core is distinct from the other crystals and overgrowth. Groups are also observed at East Mata (KM1024 D14-R07) and Mata Ua (KM1024 D18-R01). These two groups are made of individual points within separate pyroxene crystals. This suggests that portions of different crystals grew under the same conditions. Similar to the clinopyroxene data, this could suggest changes in the melt composition due to magma mixing or recharge. The crystallization history of samples from the Mata Volcanoes will be discussed in more detail in Chapter Five.

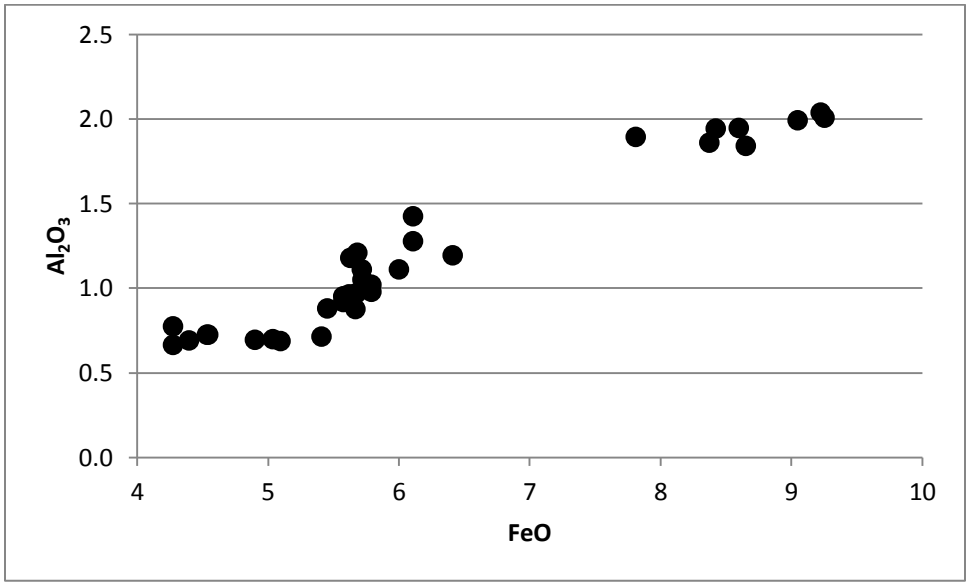


Figure 3.21. $Al_2O_3$ vs FeO plot for clinopyroxene crystals from West Mata sample J2-418-R01. Each point represents an individual measurement. Multiple measurements can be taken on different parts of the same pyroxene crystal. Five clinopyroxene crystals are represented in this graph.

# CHAPTER 4. RESULTS—GEOCHEMISTRY OF WHOLE ROCK AND GLASS

This chapter presents results of analysis of whole rock and glass samples from the Mata Volcanoes. Whole rock data includes major element and trace element analysis. Whole rock data is compared to boninite analysis in literature. Major element data is presented for glass analysis.

## Major Elements in XRF Whole Rock Analysis

Most samples from the Mata volcanoes are high in MgO and low in $TiO_2$, with less than 1 wt% $TiO_2$ (Table 4.1 and Figure 4.1). Samples can be classified into three groups: 1. Boninites, 2. Samples similar to boninites but with higher concentrations of $TiO_2$, and 3. Magmatically evolved samples. Boninites are defined as rocks with greater than 8 wt% MgO and less than 0.5 wt% $TiO_2$ in the whole rock (le Bas, 2000). Samples in Group 2 have greater than 0.5 but less than 1.0 wt% $TiO_2$. Samples in Group 3 have less than 8.0 wt% MgO. Boninite is found at all volcanoes except for Mata Fa, where only Type 2 higher $TiO_2$ rocks are found. Most of the evolved samples are from East Mata.

The magnesium number (Mg#) of an igneous rock is often used to indicate how primitive the rock is, with higher numbers corresponding to more primitive compositions. The Mg# is calculated using the cation percentages of Mg and $Fe^{2+}$ in the melt using Equation 4.1.

$$Mg\# = Mg/(Mg + Fe^{2+})$$

Equation 4.1

Under igneous conditions, iron can be present as both $Fe^{2+}$ and $Fe^{3+}$. Calculation of the Mg# of the melt requires knowledge of the composition of MgO and $FeO^{total}$ in the melt and knowledge of the amount of $Fe^{2+}$ and $Fe^{3+}$ in the melt. In this thesis, the composition of MgO and $FeO^{total}$ is directly measured, but the percentage of $Fe^{2+}$ and $Fe^{3+}$ in the melt is not directly measured. Therefore, the Mg# is not presented in this chapter. This will be discussed in Chapters 5, 6, and 7.

Table 4.1. XRF whole rock major element data for samples from the Mata Volcanoes (in wt%).

| Type | Mata | Sample | $SiO_2$ | $TiO_2$ | $Al_2O_3$ | FeO | MnO | MgO | CaO | $Na_2O$ | $K_2O$ | $P_2O_5$ | Total |
|---|---|---|---|---|---|---|---|---|---|---|---|---|---|
| 1 | East | KM1024-D14-R02 | 58.31 | 0.41 | 11.26 | 8.95 | 0.17 | 8.53 | 9.66 | 1.04 | 0.89 | 0.15 | 99.38 |
| 1 | East | KM1024-D14-R07 | 58.03 | 0.42 | 10.75 | 8.97 | 0.17 | 9.40 | 10.14 | 1.59 | 0.83 | 0.18 | 100.49 |
| 1 | West | J2-413-R13 | 54.35 | 0.44 | 10.09 | 9.06 | 0.17 | 14.26 | 9.21 | 1.27 | 0.54 | 0.13 | 99.51 |
| 1 | West | J2-418-R18 | 54.56 | 0.45 | 10.63 | 9.14 | 0.17 | 13.20 | 9.61 | 1.36 | 0.53 | 0.15 | 99.81 |
| 1 | West | J2-413-R02 | 53.80 | 0.40 | 9.61 | 9.08 | 0.17 | 15.43 | 8.93 | 1.16 | 0.48 | 0.13 | 99.19 |
| 1 | West | J2-420-R17 | 54.62 | 0.37 | 9.89 | 9.01 | 0.16 | 14.30 | 9.50 | 1.00 | 0.45 | 0.11 | 99.40 |
| 1 | West | J2-414-R12 | 55.17 | 0.45 | 11.74 | 9.24 | 0.15 | 11.31 | 10.28 | 1.69 | 0.53 | 0.12 | 100.66 |
| 1 | West | J2-417-R09 | 53.81 | 0.41 | 9.82 | 9.30 | 0.16 | 15.37 | 9.40 | 1.29 | 0.45 | 0.11 | 100.12 |
| 1 | West | RR1211 Q332-R03 | 54.93 | 0.44 | 10.44 | 8.99 | 0.16 | 13.40 | 9.56 | 1.37 | 0.52 | 0.13 | 99.95 |
| 1 | West | RR1211 Q332-R05 | 55.03 | 0.48 | 11.30 | 8.93 | 0.16 | 11.97 | 9.99 | 1.71 | 0.59 | 0.20 | 100.36 |
| 1 | West | J2-418-R05 | 57.26 | 0.39 | 9.80 | 9.15 | 0.17 | 11.98 | 9.59 | 1.09 | 0.67 | 0.09 | 100.19 |
| 1 | West | J2-420-R05 | 54.89 | 0.42 | 11.35 | 9.13 | 0.16 | 11.67 | 10.03 | 1.26 | 0.50 | 0.14 | 99.56 |
| 1 | West | J2-418-R01 | 56.65 | 0.36 | 10.46 | 8.94 | 0.17 | 9.81 | 9.65 | 1.38 | 0.63 | 0.12 | 98.15 |
| 1 | West | J2-418-R11 | 55.06 | 0.44 | 11.80 | 8.98 | 0.16 | 10.66 | 10.25 | 1.28 | 0.51 | 0.13 | 99.26 |
| 1 | West | J2-414-R27 | 55.42 | 0.38 | 10.16 | 9.13 | 0.16 | 14.08 | 9.42 | 1.30 | 0.44 | 0.10 | 100.59 |
| 1 | West | J2-417-R02 | 55.46 | 0.40 | 10.68 | 9.21 | 0.16 | 12.96 | 9.80 | 1.48 | 0.46 | 0.11 | 100.71 |
| 1 | West | J2-420-R01 | 57.57 | 0.36 | 10.19 | 9.03 | 0.16 | 11.62 | 9.61 | 1.68 | 0.61 | 0.10 | 100.91 |
| 1 | West | J2-420-R02 | 57.34 | 0.37 | 10.54 | 9.06 | 0.16 | 10.87 | 9.69 | 1.72 | 0.63 | 0.11 | 100.50 |
| 1 | West | J2-420-R16 | 54.92 | 0.41 | 9.64 | 9.18 | 0.16 | 15.24 | 9.10 | 1.22 | 0.46 | 0.11 | 100.44 |
| 1 | West | KM1024 D12-R01 | 57.55 | 0.34 | 10.40 | 8.87 | 0.17 | 10.88 | 9.61 | 0.87 | 0.60 | 0.10 | 99.39 |
| 1 | West | KM1024 D15-R01 | 55.21 | 0.38 | 10.17 | 9.12 | 0.16 | 13.71 | 9.40 | 0.82 | 0.45 | 0.09 | 99.52 |
| 1 | West | KM1024 D15-R04 | 54.78 | 0.40 | 10.96 | 9.00 | 0.16 | 11.72 | 10.00 | 1.10 | 0.48 | 0.11 | 98.72 |
| 1 | Taha | KM1024 D16-R01 | 55.31 | 0.41 | 10.76 | 8.93 | 0.17 | 12.29 | 9.81 | 1.13 | 0.57 | 0.15 | 99.53 |
| 1 | Taha | KM1024 D16-R03 | 55.18 | 0.43 | 10.96 | 8.94 | 0.17 | 12.29 | 9.89 | 1.52 | 0.60 | 0.17 | 100.15 |
| 1 | Taha | KM1024 D16-R04 | 55.04 | 0.41 | 10.89 | 8.96 | 0.17 | 12.42 | 9.82 | 1.50 | 0.60 | 0.16 | 99.99 |
| 1 | Taha | KM1024 D16-R06 | 55.13 | 0.42 | 10.77 | 8.94 | 0.17 | 12.62 | 9.85 | 1.62 | 0.61 | 0.19 | 100.32 |
| 1 | Ua | KM1024 D18-R01 | 56.20 | 0.38 | 11.33 | 8.42 | 0.16 | 11.63 | 9.36 | 1.12 | 0.64 | 0.13 | 99.37 |
| 1 | Ua | KM1129a D10-R01 | 54.56 | 0.31 | 8.28 | 9.19 | 0.16 | 17.73 | 7.23 | 0.81 | 0.68 | 0.03 | 99.00 |

Samples can be divided into three groups: 1) boninites, 2) samples similar to boninites with higher concentrations of $TiO_2$, and 3) evolved samples.

Table 4.1 (continued). XRF whole rock major element data for samples from the Mata Volcanoes (in wt%).

| Type | Mata | Sample | $SiO_2$ | $TiO_2$ | $Al_2O_3$ | FeO | MnO | MgO | CaO | $Na_2O$ | $K_2O$ | $P_2O_5$ | Total |
|---|---|---|---|---|---|---|---|---|---|---|---|---|---|
| 1 | Ua | KM1129a D10-R5 | 52.53 | 0.36 | 9.65 | 8.55 | 0.16 | 17.70 | 9.44 | 1.16 | 0.55 | 0.16 | 100.27 |
| 1 | Ua | KM1129a D10-R06 | 54.69 | 0.32 | 8.28 | 9.13 | 0.16 | 17.92 | 7.17 | 0.90 | 0.68 | 0.03 | 99.27 |
| 1 | Ua | RR1211 Q325-R01 | 56.44 | 0.40 | 11.89 | 8.21 | 0.16 | 10.02 | 9.76 | 1.41 | 0.64 | 0.13 | 99.07 |
| 1 | Tolu | KM1024 D20-R01 | 55.35 | 0.40 | 9.96 | 9.03 | 0.17 | 14.37 | 8.23 | 0.97 | 0.59 | 0.13 | 99.22 |
| 1 | Tolu | KM1129a D07-R01 | 54.06 | 0.38 | 10.18 | 8.59 | 0.17 | 15.78 | 8.82 | 1.76 | 0.42 | 0.23 | 100.40 |
| 1 | Tolu | KM1129a D07-R02 | 54.31 | 0.39 | 10.03 | 8.63 | 0.15 | 16.23 | 8.72 | 1.41 | 0.43 | 0.08 | 100.40 |
| 1 | Tolu | KM1129a D08-R01 | 53.41 | 0.37 | 9.89 | 8.74 | 0.15 | 15.95 | 8.58 | 1.27 | 0.41 | 0.09 | 98.86 |
| 1 | Tolu | KM1129a D08-R07 | 55.30 | 0.41 | 10.19 | 9.13 | 0.16 | 13.80 | 8.48 | 1.16 | 0.62 | 0.06 | 99.31 |
| 1 | Tolu | RR1211 Q331-R16 | 55.53 | 0.44 | 10.94 | 8.59 | 0.16 | 13.42 | 9.28 | 1.69 | 0.63 | 0.20 | 100.88 |
| 1 | Ono | KM1024 D22-R1 | 53.13 | 0.44 | 8.91 | 9.04 | 0.17 | 18.04 | 7.90 | 0.85 | 0.63 | 0.13 | 99.26 |
| 1 | Ono | KM1024 D22-R2 | 56.01 | 0.31 | 10.21 | 8.83 | 0.16 | 14.28 | 8.61 | 1.15 | 0.51 | 0.11 | 100.18 |
| 1 | Fitu | KM1024 D23-R1 | 56.54 | 0.32 | 10.23 | 8.63 | 0.16 | 13.75 | 8.26 | 0.87 | 0.47 | 0.10 | 99.33 |
| 1 | Fitu | KM1024 D23-R4 | 56.27 | 0.33 | 10.58 | 8.66 | 0.16 | 13.03 | 8.49 | 1.29 | 0.48 | 0.10 | 99.40 |
| 2 | Ua | KM1129a D10-R02 | 55.06 | 0.66 | 10.02 | 8.72 | 0.16 | 14.28 | 9.24 | 1.12 | 0.88 | 0.06 | 100.20 |
| 2 | Ua | RR1211 Q325-R02 | 53.67 | 0.79 | 11.54 | 9.07 | 0.17 | 10.90 | 11.05 | 1.63 | 0.99 | 0.19 | 100.01 |
| 2 | Ua | RR1211 Q325-R03 | 53.33 | 0.79 | 11.46 | 9.04 | 0.17 | 11.88 | 10.69 | 1.97 | 1.10 | 0.26 | 100.69 |
| 2 | Tolu | KM1129a D09-R01 | 50.55 | 0.69 | 7.93 | 9.47 | 0.16 | 20.04 | 8.07 | 1.26 | 0.83 | 0.19 | 99.20 |
| 2 | Fa | KM1024 D21-R01 | 52.38 | 0.90 | 9.98 | 9.45 | 0.16 | 15.61 | 9.21 | 1.44 | 0.75 | 0.16 | 100.05 |
| 2 | Fa | KM1024-D21-R04 | 51.78 | 0.89 | 9.97 | 9.47 | 0.17 | 15.42 | 9.29 | 1.73 | 0.75 | 0.30 | 99.77 |
| 2 | Fa | KM1024-D21-R02 | 52.07 | 0.89 | 9.90 | 9.51 | 0.17 | 15.22 | 9.22 | 1.27 | 0.73 | 0.24 | 99.24 |
| 2 | Fitu | RR1211 Q329-R01 | 56.38 | 0.56 | 12.44 | 8.32 | 0.16 | 9.05 | 11.22 | 1.48 | 0.55 | 0.12 | 100.29 |
| 3 | East | KM1129a D02-R01 | 61.28 | 0.41 | 12.19 | 7.61 | 0.14 | 6.08 | 8.10 | 2.11 | 1.27 | 0.09 | 99.30 |
| 3 | East | KM1129a D02-R04 | 61.68 | 0.39 | 11.66 | 7.92 | 0.14 | 6.66 | 8.58 | 2.10 | 1.23 | 0.10 | 100.47 |

Samples can be divided into three groups: 1) boninites, 2) samples similar to boninites with higher concentrations of $TiO_2$, and 3) evolved samples.

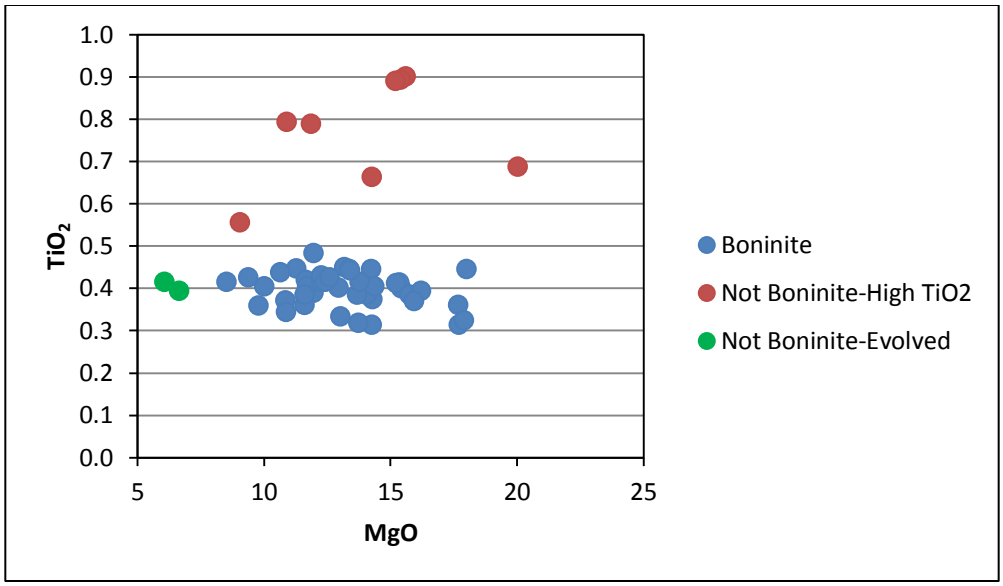


Figure 4.1. XRF whole rock data showing types of lava found at the Mata Volcanoes. Three main groups are present: 1. boninites with greater than 8.0 wt% MgO and less than 0.5 wt% $TiO_2$ (le Bas, 2000), 2. samples that are similar to boninites, but with higher $TiO_2$, $TiO_2$ contents between 0.5 and 1.0 wt%, and 3. evolved samples, with less than 8.0 wt% MgO.

**Trace Elements in XRF Whole Rock Analysis**

Trace element analysis was performed on whole rock samples by XRF for Nb, Zr, Y, Sr, Rb, Ba, Sc, U, Th, Pb, Co, Cr, V, Zn, Ni, Mn and Cu (Tables 4.2 and 4.3). Samples generally had such low concentrations of U, Th, and Pb and were at or below the detection limit of the XRF and will not be discussed in this study. Co data is not reported for nine samples due to Co contamination during preparation of these samples. Nb is not reported for RR1211 Q325-R03 for the same reason. See Appendix C for more information.

Generally samples from the Mata volcanoes are enriched in fluid mobile elements such as Rb and Ba. These fluid mobile elements enrichments are indicative of influx of elements along with water from the dehydrating slab (e.g. Stern, 2002; Elliot, 2003). Samples are depleted in Y, which like the HREE, are not fluid mobile and are indicative of the mantle source. Because these elements are not mobilized by fluids from the subducted slab, they come primarily from the mantle source region and their concentrations are indicative of the concentrations in the source and mantle melting processes (eg. Stern, 2002; Hawkesworth *et al.*, 1991).

Group 2 non-boninite samples with higher $TiO_2$ contents than Group 1boninites are generally more enriched in fluid-mobile elements, such as Ba, Rb, and Sr, than boninites (Figure 4.2). Interestingly, Group 2 samples are also generally more enriched in non-fluid mobile elements (Figure 4.2). Non-fluid mobile elements are generally thought to be indicative of mantle source enrichment or depletion, such as Y, Zr, and Nb. Samples have similar ranges in V, but Group 3 evolved samples are slightly offset from the other groups (Figure 4.3).

Compatible trace elements generally correlate with MgO for all samples from the Mata volcanoes, as shown for Ni vs. MgO below. Exceptions are sometimes compatible elements Zn and Mn vs MgO where no trend is observed. These elements are roughly constant for the range of MgO values of the Mata Volcanoes. This means that the concentration of these elements is not being strongly affected by crystallization. All of the three groups generally overlap for the compatible trace elements (Figures 4.4 and 4.5).

Ratios of fluid mobile to non-fluid mobile elements vary. For example, Ba/Nb ratios range from 9.2 to 37 for all of the samples from the Mata volcanoes (Figure 4.6 and 4.7). Interestingly, the three groups generally overlap in ratios of fluid mobile to non-fluid mobile elements. There is often a significant range in the data for the boninite and the higher $TiO_2$ groups. The evolved group does not show as wide of a range, but is only represented by two samples. Ratios of non-fluid mobile elements that are typically indicative of source can be compared to study variations in mantle source. These ratios vary for the Mata volcanoes and the three groups generally overlap.

Table 4.2. XRF whole rock trace element data for Nb, Zr, Y, Sr, Rb, and Ba (in ppm).

| Type | Mata | Sample | Nb | Zr | Y | Sr | Rb | Ba |
|---|---|---|---|---|---|---|---|---|
| 1 | East | KM1024-D14-R02 | 8.80 | 40.9 | 7.43 | 273 | 18.4 | 184 |
| 1 | East | KM1024-D14-R07 | 14.40 | 52.5 | 8.48 | 335 | 24.9 | 273 |
| 1 | West | J2-413-R13 | 6.57 | 34.5 | 7.89 | 216 | 9.3 | 127 |
| 1 | West | J2-418-R18 | 6.45 | 34.9 | 7.82 | 225 | 10.3 | 126 |
| 1 | West | J2-413-R02 | 6.14 | 33.3 | 7.41 | 206 | 9.3 | 123 |
| 1 | West | J2-420-R17 | 5.92 | 30.1 | 7.28 | 186 | 8.6 | 105 |
| 1 | West | J2-414-R12 | 6.80 | 35.0 | 8.65 | 216 | 10.3 | 123 |
| 1 | West | J2-417-R09 | 5.67 | 32.1 | 7.10 | 194 | 8.2 | 107 |
| 1 | West | RR1211 Q332-R03 | 6.95 | 35.7 | 7.75 | 220 | 9.5 | 133 |
| 1 | West | RR1211 Q332-R05 | 7.19 | 37.9 | 8.41 | 237 | 10.7 | 143 |
| 1 | West | J2-418-R05 | 6.63 | 31.3 | 6.88 | 210 | 13.4 | 137 |
| 1 | West | J2-420-R05 | 6.54 | 33.5 | 7.92 | 211 | 11.0 | 118 |
| 1 | West | J2-418-R01 | 5.84 | 29.6 | 7.44 | 218 | 13.6 | 137 |
| 1 | West | J2-418-R11 | 7.03 | 36.4 | 8.54 | 224 | 10.2 | 125 |
| 1 | West | J2-414-R27 | 5.91 | 30.9 | 7.06 | 184 | 8.6 | 94 |
| 1 | West | J2-417-R02 | 6.42 | 32.3 | 7.70 | 195 | 8.9 | 103 |
| 1 | West | J2-420-R01 | 5.69 | 29.8 | 6.74 | 204 | 12.4 | 123 |
| 1 | West | J2-420-R02 | 6.09 | 31.3 | 6.93 | 212 | 12.6 | 124 |
| 1 | West | J2-420-R16 | 5.89 | 31.8 | 7.28 | 197 | 9.0 | 116 |
| 1 | West | KM1024 D12-R01 | 5.41 | 28.9 | 6.47 | 206 | 12.0 | 119 |
| 1 | West | KM1024 D15-R01 | 6.05 | 29.8 | 7.21 | 184 | 9.0 | 110 |
| 1 | West | KM1024 D15-R04 | 6.68 | 33.5 | 8.11 | 208 | 9.2 | 126 |
| 1 | Taha | KM1024 D16-R01 | 12.09 | 45.7 | 8.53 | 238 | 11.8 | 144 |
| 1 | Taha | KM1024 D16-R03 | 12.24 | 45.3 | 8.74 | 241 | 12.3 | 139 |
| 1 | Taha | KM1024 D16-R04 | 12.11 | 45.7 | 8.56 | 241 | 12.3 | 143 |
| 1 | Taha | KM1024 D16-R06 | 12.28 | 46.6 | 8.68 | 241 | 11.9 | 145 |

Nb data is not reported for sample RR1211 Q325-R03 because Nb was contaminated for this sample during sample preparation. See Appendix C for more information.

Table 4.2. XRF whole rock trace element data for Nb, Zr, Y, Sr, Rb, and Ba (in ppm).

| Type | Mata | Sample | Nb | Zr | Y | Sr | Rb | Ba |
|---|---|---|---|---|---|---|---|---|
| 1 | Ua | KM1024 D18-R01 | 7.33 | 33.2 | 7.72 | 217 | 12.8 | 138 |
| 1 | Ua | KM1129a D10-R01 | 3.92 | 20.4 | 5.36 | 162 | 12.8 | 123 |
| 1 | Ua | KM1129a D10-R5 | 5.68 | 25.1 | 6.74 | 161 | 12.0 | 106 |
| 1 | Ua | KM1129a D10-R06 | 3.85 | 20.0 | 5.20 | 161 | 13.2 | 118 |
| 1 | Ua | RR1211 Q325-R01 | 7.48 | 34.5 | 8.32 | 227 | 13.8 | 148 |
| 1 | Tolu | KM1024 D20-R01 | 8.68 | 34.8 | 7.13 | 201 | 11.5 | 145 |
| 1 | Tolu | KM1129a D07-R01 | 13.45 | 35.6 | 7.73 | 298 | 8.3 | 222 |
| 1 | Tolu | KM1129a D07-R02 | 12.74 | 34.0 | 7.74 | 272 | 8.9 | 201 |
| 1 | Tolu | KM1129a D08-R01 | 13.61 | 33.3 | 8.08 | 289 | 8.4 | 224 |
| 1 | Tolu | KM1129a D08-R07 | 8.41 | 33.2 | 7.40 | 199 | 12.3 | 141 |
| 1 | Tolu | RR1211 Q331-R16 | 8.11 | 36.2 | 7.46 | 204 | 12.9 | 130 |
| 1 | Ono | KM1024 D22-R1 | 7.25 | 34.1 | 7.52 | 174 | 15.0 | 124 |
| 1 | Ono | KM1024 D22-R2 | 5.29 | 23.1 | 6.45 | 145 | 10.8 | 104 |
| 1 | Fitu | KM1024 D23-R1 | 6.35 | 32.3 | 7.04 | 158 | 8.4 | 108 |
| 1 | Fitu | KM1024 D23-R4 | 5.97 | 32.3 | 7.20 | 162 | 9.4 | 101 |
| 2 | Ua | KM1129a D10-R02 | 5.87 | 27.9 | 8.80 | 215 | 21.0 | 216 |
| 2 | Ua | RR1211 Q325-R02 | 9.90 | 45.0 | 10.79 | 295 | 20.2 | 283 |
| 2 | Ua | RR1211 Q325-R03 |  | 44.3 | 10.57 | 287 | 20.0 | 274 |
| 2 | Tolu | KM1129a D09-R01 | 18.24 | 64.2 | 8.77 | 330 | 20.4 | 245 |
| 2 | Fa | KM1024 D21-R01 | 17.20 | 68.1 | 11.20 | 288 | 17.5 | 187 |
| 2 | Fa | KM1024-D21-R04 | 17.36 | 71.0 | 11.18 | 296 | 17.9 | 179 |
| 2 | Fa | KM1024-D21-R02 | 16.98 | 70.9 | 11.15 | 296 | 17.3 | 196 |
| 2 | Fitu | RR1211 Q329-R01 | 8.47 | 38.6 | 10.08 | 220 | 11.5 | 146 |
| 3 | East | KM1129a D02-R01 | 13.09 | 50.4 | 7.83 | 328 | 24.0 | 262 |
| 3 | East | KM1129a D02-R04 | 9.14 | 41.7 | 7.21 | 264 | 17.1 | 171 |

Nb data is not reported for sample RR1211 Q325-R03 because Nb was contaminated for this sample during sample preparation. See Appendix C for more information.

Table 4.3. XRF whole rock trace element data for selected transition metals (in ppm) compatible elements.

| Type | Mata | Sample | Co | Cr | V | Zn | Ni | Sc |
|---|---|---|---|---|---|---|---|---|
| 1 | East | KM1024-D14-R02 | 37.8 | 408 | 271 | 76.4 | 53.0 | 47.8 |
| 1 | East | KM1024-D14-R07 | 25.9 | 260 | 231 | 67.9 | 28.0 | 36.1 |
| 1 | West | J2-413-R13 | 49.9 | 984 | 242 | 70.2 | 216.0 | 45.4 |
| 1 | West | J2-418-R18 | 52.2 | 928 | 252 | 70.4 | 209.0 | 45.7 |
| 1 | West | J2-413-R02 | 55.6 | 1009 | 227 | 68.6 | 234.0 | 44.1 |
| 1 | West | J2-420-R17 | 54.2 | 1021 | 233 | 68.0 | 221.0 | 44.4 |
| 1 | West | J2-414-R12 | 48.2 | 729 | 246 | 70.8 | 167.0 | 42.6 |
| 1 | West | J2-417-R09 | 57.5 | 1114 | 223 | 68.3 | 251.0 | 42.9 |
| 1 | West | RR1211 Q332-R03 | 55.4 | 928 | 238 | 73.7 | 209.0 | 43.0 |
| 1 | West | RR1211 Q332-R05 | 50.4 | 779 | 252 | 74.1 | 174.0 | 46.0 |
| 1 | West | J2-418-R05 | 46.0 | 741 | 256 | 71.1 | 120.0 | 49.1 |
| 1 | West | J2-420-R05 | 47.8 | 783 | 264 | 71.0 | 181.0 | 46.7 |
| 1 | West | J2-418-R01 | 39.5 | 413 | 260 | 71.6 | 71.0 | 50.7 |
| 1 | West | J2-418-R11 | 44.0 | 604 | 262 | 67.9 | 145.0 | 42.8 |
| 1 | West | J2-414-R27 | 56.0 | 1032 | 229 | 70.0 | 232.0 | 44.2 |
| 1 | West | J2-417-R02 | 51.3 | 887 | 243 | 69.1 | 206.0 | 47.1 |
| 1 | West | J2-420-R01 | 44.8 | 695 | 250 | 69.8 | 113.0 | 47.0 |
| 1 | West | J2-420-R02 | 44.3 | 634 | 252 | 72.1 | 110.0 | 46.4 |
| 1 | West | J2-420-R16 | 57.7 | 1146 | 222 | 66.8 | 256.0 | 43.3 |
| 1 | West | KM1024 D12-R01 | 43.2 | 583 | 255 | 70.7 | 100.0 | 48.5 |
| 1 | West | KM1024 D15-R01 | 55.7 | 1006 | 235 | 71.1 | 212.0 | 46.6 |
| 1 | West | KM1024 D15-R04 |  | 775 | 252 | 76.3 | 166.0 | 46.0 |
| 1 | Taha | KM1024 D16-R01 |  | 818 | 236 | 70.7 | 124.0 | 44.2 |
| 1 | Taha | KM1024 D16-R03 | 48.7 | 812 | 236 | 74.1 | 124.0 | 43.8 |
| 1 | Taha | KM1024 D16-R04 | 50.8 | 786 | 226 | 73.2 | 131.0 | 39.3 |
| 1 | Taha | KM1024 D16-R06 | 51.1 | 786 | 234 | 73.7 | 130.0 | 39.5 |

Co data is not reported for several samples because Co was contaminated for this sample during sample preparation. See Appendix C for more information.

Table 4.3. XRF whole rock trace element data for selected transition metals (in ppm)

| Type | Mata | Sample | Co | Cr | V | Zn | Ni | Sc |
|---|---|---|---|---|---|---|---|---|
| 1 | Ua | KM1024 D18-R01 | | 722 | 248 | 68.9 | 186 | 42.8 |
| 1 | Ua | KM1129a D10-R01 | 62.8 | 1508 | 201 | 69.5 | 419 | 37.6 |
| 1 | Ua | KM1129a D10-R5 | 62.6 | 1530 | 207 | 68.8 | 430 | 36.0 |
| 1 | Ua | KM1129a D10-R06 | 64.3 | 1598 | 205 | 70.5 | 453 | 37.4 |
| 1 | Ua | RR1211 Q325-R01 | 41.4 | 582 | 258 | 72.1 | 133 | 42.3 |
| 1 | Tolu | KM1024 D20-R01 | | 990 | 238 | 71.8 | 226 | 42.4 |
| 1 | Tolu | KM1129a D07-R01 | 57.0 | 1250 | 214 | 74.1 | 292 | 37.2 |
| 1 | Tolu | KM1129a D07-R02 | 57.4 | 1379 | 214 | 70.2 | 315 | 39.4 |
| 1 | Tolu | KM1129a D08-R01 | 57.9 | 1331 | 209 | 70.3 | 303 | 37.4 |
| 1 | Tolu | KM1129a D08-R07 | 54.8 | 931 | 238 | 73.4 | 197 | 42.7 |
| 1 | Tolu | RR1211 Q331-R16 | 48.0 | 828 | 238 | 72.5 | 196 | 39.3 |
| 1 | Ono | KM1024 D22-R1 | | 1494 | 208 | 71.7 | 363 | 38.4 |
| 1 | Ono | KM1024 D22-R2 | | 1015 | 220 | 74.1 | 213 | 37.8 |
| 1 | Fitu | KM1024 D23-R1 | | 1026 | 224 | 66.8 | 220 | 39.2 |
| 1 | Fitu | KM1024 D23-R4 | 51.2 | 932 | 220 | 69.3 | 209 | 35.6 |
| 2 | Ua | KM1129a D10-R02 | 52.7 | 1094 | 251 | 68.5 | 233 | 41.3 |
| 2 | Ua | RR1211 Q325-R02 | 44.3 | 603 | 273 | 76.0 | 113 | 41.9 |
| 2 | Ua | RR1211 Q325-R03 | | 605 | 264 | 75.3 | 144 | 40.8 |
| 2 | Tolu | KM1129a D09-R01 | 73.5 | 1501 | 193 | 74.1 | 413 | 33.2 |
| 2 | Fa | KM1024 D21-R01 | 62.1 | 1179 | 245 | 78.3 | 305 | 40.1 |
| 2 | Fa | KM1024-D21-R04 | 61.2 | 1191 | 237 | 80.1 | 304 | 37.9 |
| 2 | Fa | KM1024-D21-R02 | | 1192 | 235 | 76.5 | 295 | 39.8 |
| 2 | Fitu | RR1211 Q329-R01 | 39.2 | 504 | 266 | 72.4 | 86 | 44.0 |
| 3 | East | KM1129a D02-R01 | 28.7 | 287 | 237 | 69.2 | 25 | 39.0 |
| 3 | East | KM1129a D02-R04 | 39.6 | 462 | 254 | 75.2 | 51 | 42.1 |

Co data is not reported for several samples because Co was contaminated for this sample during sample preparation. See Appendix C for more information.

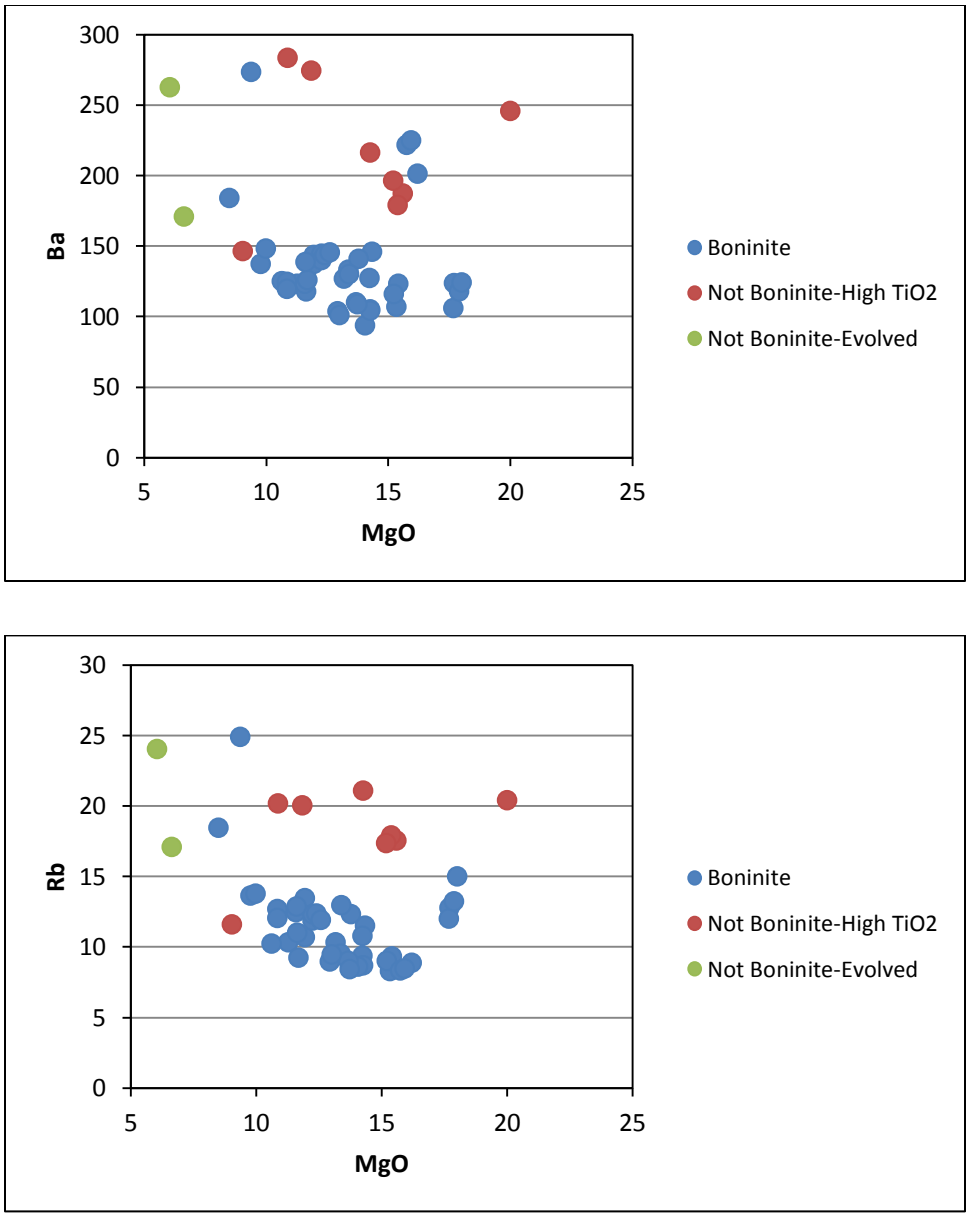


Figure 4.2. Concentration of fluid mobile elements vs MgO content in the three sample groups. Group 2 samples, which are not boninite samples due to their higher $TiO_2$ contents, tend to have higher concentrations of fluid mobile elements than Group 1 boninite samples.

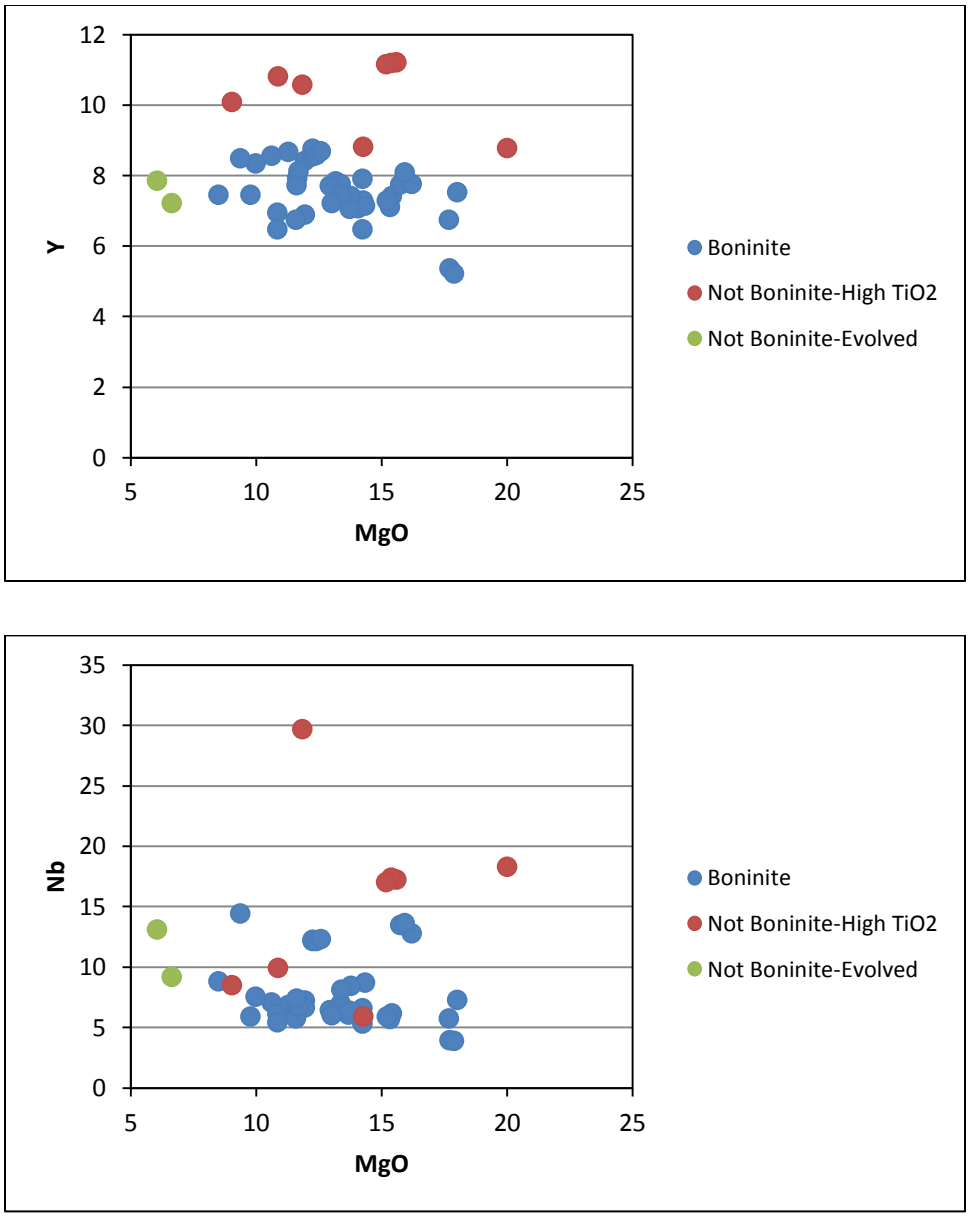


Figure 4.3. Concentration of non-fluid mobile elements vs MgO content in the three sample groups. Group 2 samples, which are not boninite samples due to their higher $TiO_2$ contents, tend to have higher concentrations of non-fluid mobile elements than Group 1 boninite samples.

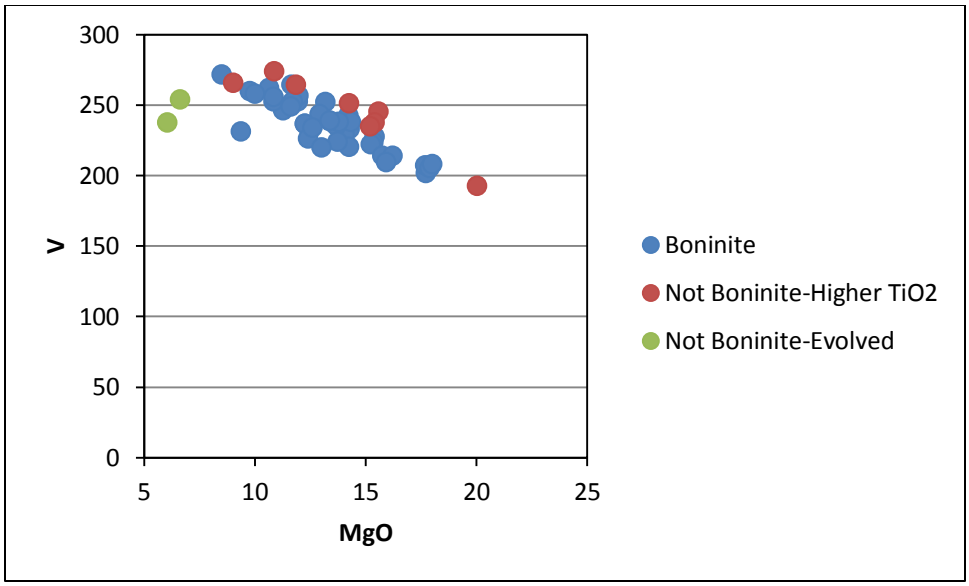


Figure 4.4. V vs. MgO in whole rock for all Mata samples. Group 1 boninite samples and Group 2 higher $TiO_2$ samples have similar ranges of V vs MgO content.

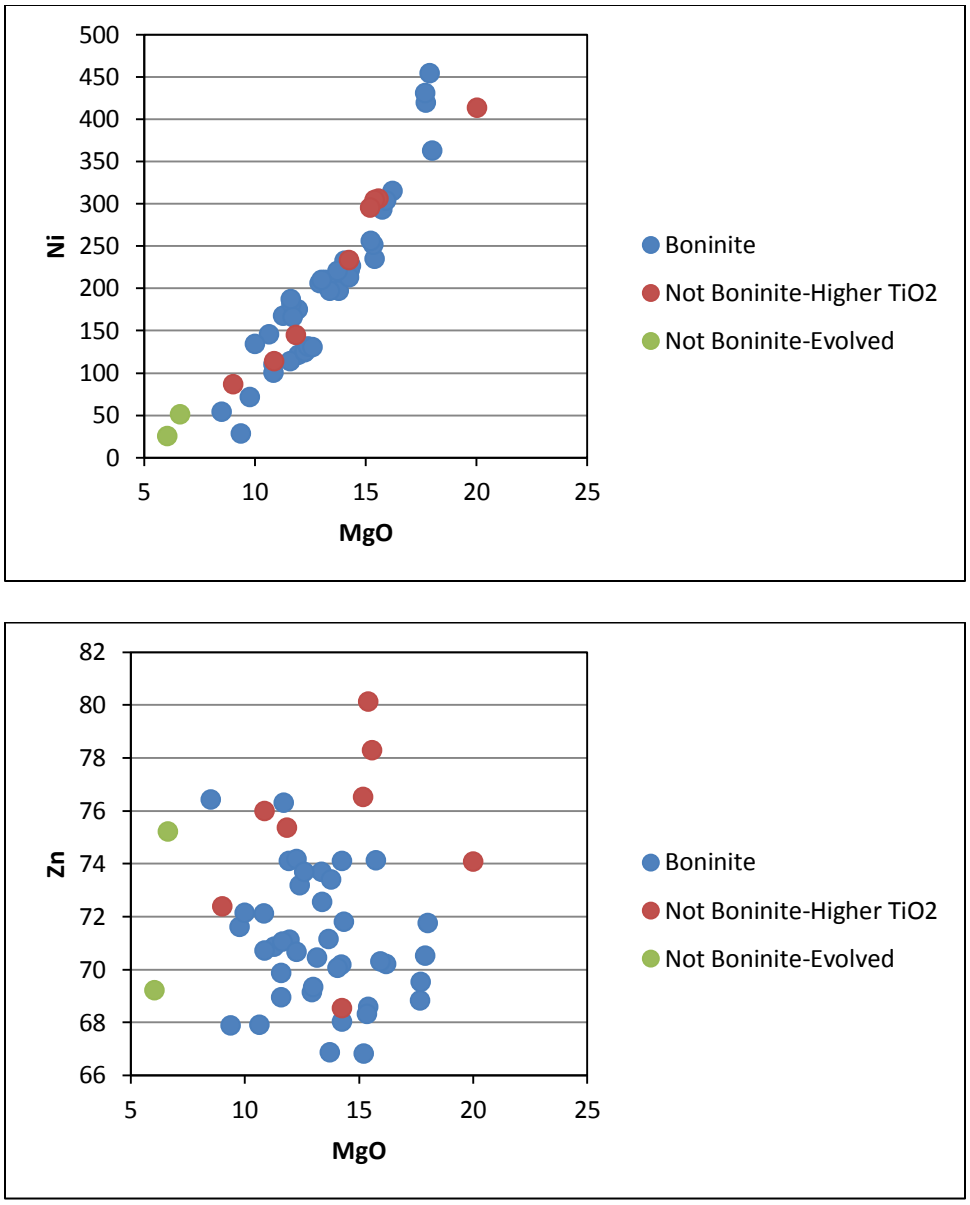


Figure 4.5. Two examples of compatible elements (Ni vs Zn) vs MgO for the Mata Volcanoes. Most elements, such as Ni (shown here) vs MgO show trends while others, such as Zn (shown here) and Mn (not shown) do not appear to vary systematically with changes in MgO.

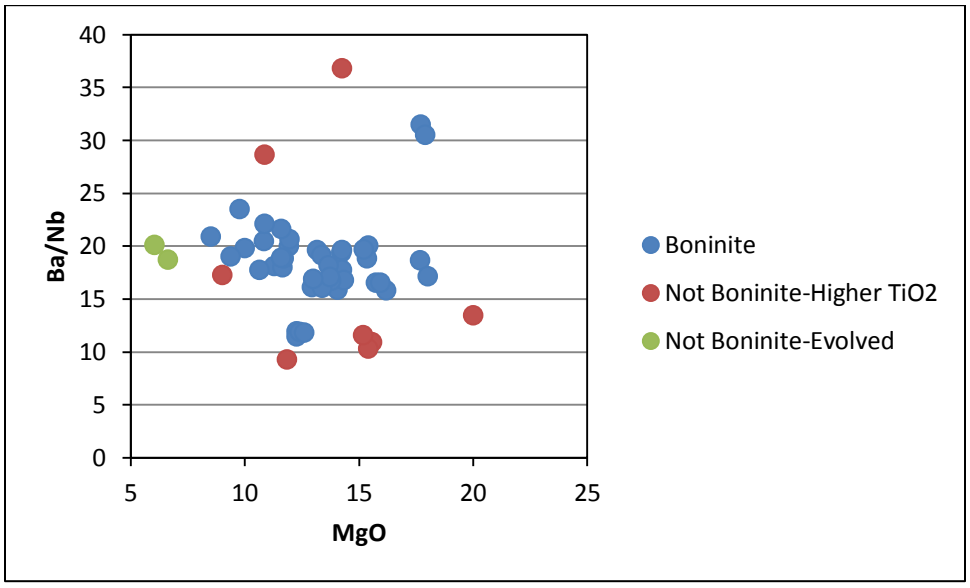


Figure 4.6. Ratio of fluid mobile Ba to non-fluid mobile Nb vs MgO for the Mata Volcanoes. For the boninite and the higher $TiO_2$ groups, there is a significant range in Ba/Nb ratios. There is significant overlap between the three groups.

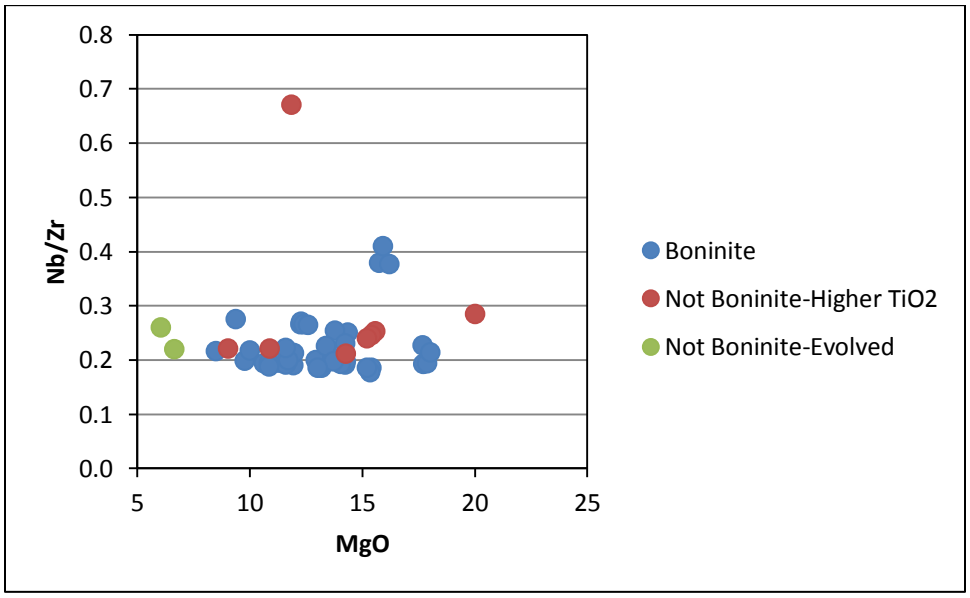


Figure 4.7. Ratio of non-fluid mobile Nb to non-fluid mobile Zr vs MgO for the Mata Volcanoes. For the boninite and the higher $TiO_2$ groups, there is a significant range in Nb/Zr ratios. There is significant overlap between the three groups.

## Comparison

Boninites have previously been found and studied in suprasubduction zone settings. They have been studied in both modern suprasubduction zone settings, such as in the Marianas arc region and in the Tofua Arc/Lau Basin region, and in ophiolites among other places (For more details, see Chapter 1). This section presents a cursory comparison of the boninites found at the Mata Volcanoes to Mid Ocean Ridge Basalts (MORB), boninites found in the Tofua Arc/Lau Basin region, and to some boninites outside the Lau Basin including New Caledonia, the Bonin Islands, Cape Vogel, New Zealand, and Cyprus. One difficulty in comparing these young boninite samples to other work is the possibility that older boninites have been altered by post-depositional weathering processes. Thus, I must be cautious about making comparisons. This section uses a strict definition of boninite. Samples must have less than 0.5 wt% $TiO_2$ and greater than 8.0 wt% MgO in the whole rock (Le Bas, 2000). Samples similar in composition to boninites but not strictly fitting the definition of boninite are not included.

Whole rock XRF data from the Mata Volcanoes is compared to other igneous samples. Sources for literature data and types of rocks for comparison are as follows: MORB data is based on microprobe glass work by Jenner and O'Neil (2012). As MORB basalts are usually aphyric or mostly aphyric, this glass composition can be compared with the whole rock compositions from other sources. Whole rock boninite data from the Lau Basin are from (Acland, 1996; Danyushevsky *et al.*, 1995; Falloon *et al.*, 1989, 2007, 2008; Falloon and Crawford, 1991). Other boninite data includes samples from Japan (Cameron *et al.*, 1983), New Caledonia (Cameron, 1989; Cameron *et al.*, 1983; Umino, 1986) and other locations such as Cape Vogel, New Zealand, and Cyprus (Cameron *et al.*, 1983; Rogers *et al.*, 1989).

When compared to MORB, previously published boninites are much lower in $TiO_2$ and Y, which is thought to reflect the depletion in the mantle sources of the boninites (Figure 4.8). The Mata boninites are no exception. MORB samples also have higher concentrations of Zr than the Mata boninites and most published boninite data. Boninite samples from the Lau Basin, both from previously published studies and the Mata Volcanoes, tend to have higher concentrations of fluid mobile elements, such as Ba and Sr, than most MORB samples. In contrast, some boninites

from other areas, including New Caledonia, Bonin Islands, Cape Vogel, New Zealand, and Cyprus, tend to have lower concentrations of these elements (Figures 4.8).

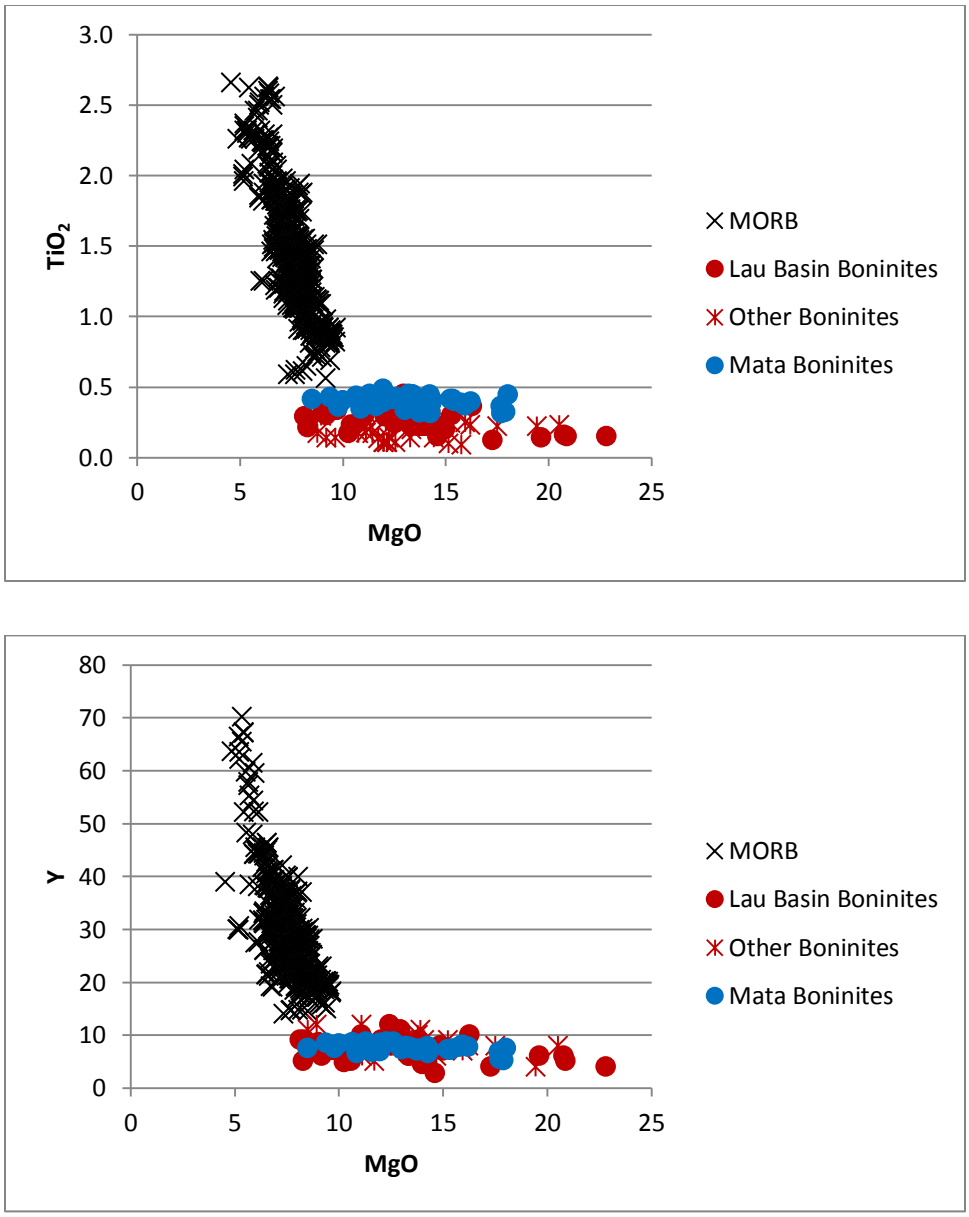


Figure 4.8. Comparison of whole rock major element data for Mata boninites to literature data for $TiO_2$ (wt%), and Y, Ba, and Sr (ppm). MORB samples tend to have higher concentrations of $TiO_2$ and Y. Boninites from the Lau Basin, including those from this study, tend to have higher concentrations of Ba and Sr than the majority of the MORB samples and some boninite samples from outside the Lau Basin. See text for references.

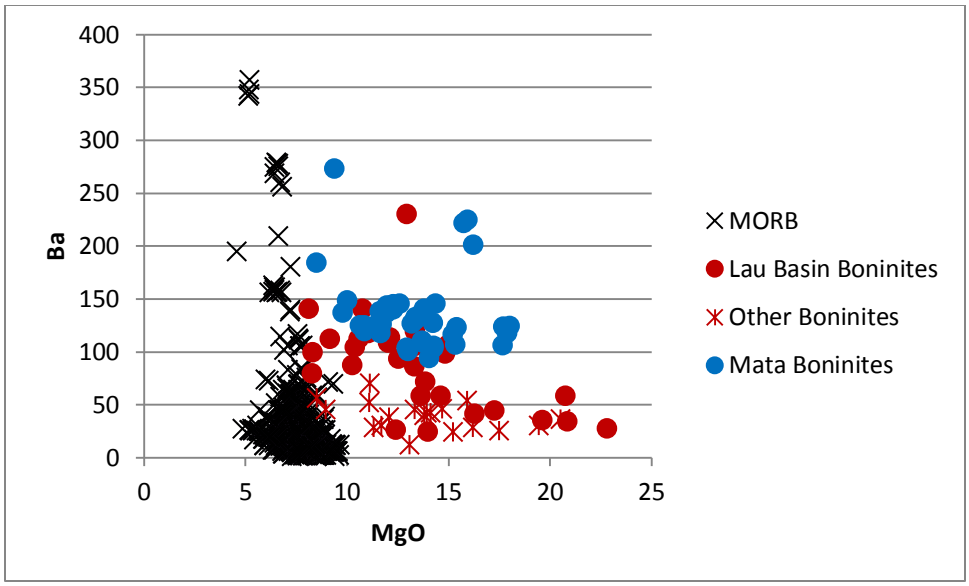


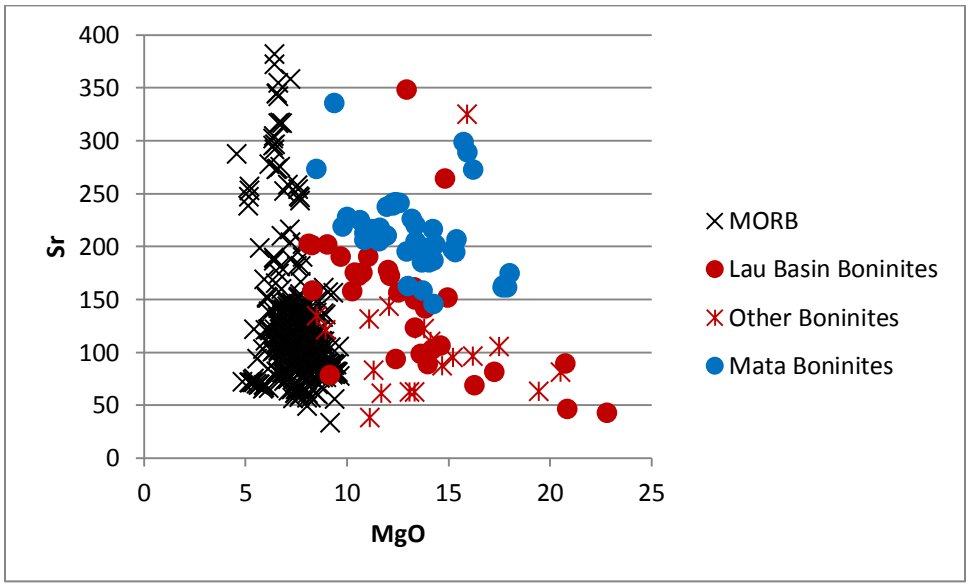


Figure 4.8, continued. Comparison of whole rock major element data for Mata boninites to literature data for $TiO_2$ (wt%), and Y, Ba, and Sr (ppm). MORB samples tend to have higher concentrations of $TiO_2$ and Y. Boninites from the Lau Basin, including those from this study, tend to have higher concentrations of Ba and Sr than the majority of the MORB samples and some boninite samples. See text for references.

All of the Mata boninites, as well as most boninites from the Lau Basin, are high Ca boninites. When comparing whole rock major elements, boninite lavas erupted at the Mata volcanoes are geochemically similar to those erupted elsewhere in the Lau Basin. The main difference is the higher concentrations of $TiO_2$ and $P_2O_5$ in whole rock analyses of the Mata boninites than the other Lau Basin boninites (Figures 4.9).

Whole rock trace element data provides clues to the composition of the parent magma(s) in the northern Lau Basin. Elements such as Y, Zr, Nb, and Ti are often thought to be indicative of the original mantle source in a subduction zone. These elements are not fluid mobile and thus are not thought to be mobilized by fluids dehydrating off the subducting slab or sediments. However, concentrations of these elements can also be affected by the degree of melting. Enriching components, such as addition of a plume source, can also affect the concentration of these elements (See Chapter One for more details). Most boninites from the northern Lau Basin have similar concentrations of Y to those of the Mata boninites. However, Mata boninites generally have higher concentrations of other non-fluid mobile elements, such as Zr and Nb, than other Lau Basin boninites. This geochemical data could suggest either a distinctive difference in mantle source between the Mata boninites and other northern Lau boninites or additional enriching components for the Mata boninites' parent mantle source/parent magma.

The Mata boninites are also generally more enriched in fluid mobile elements, such as Ba, and Sr, than the other Lau Basin boninites. These elements are mobilized by fluids dehydrating off the subducted slab and/or sediments and are often studied in subduction zones to study the nature of the subduction component (See Chapter One for more details). The increased levels of fluid mobile elements could suggest that the source of the Matas' lavas are receiving or at some point received more subduction related component(s) than the other boninites (Figure 4.10). However, the concentration of these elements can also be affected by other processes including additional enrichments or degree of mantle melting or crystallization. By studying different elements and isotopes, the contribution of these different processes can be unraveled. Further work would be required to determine this with more certainty, but some of the possibilities can be examined with the data currently available. For example, if different degrees of crystallization was the cause, the samples would be expected to have different percentages of MgO, which decreases with increasing degrees of crystallization. Because there is significant

overlap between the MgO contents of the samples throughout the Lau Basin, this is not a likely explanation. If the cause was varying degrees of mantle melting, one set of samples should be more enriched in both fluid mobile trace elements, such as Ba, and non-fluid mobile trace elements, such as Zr, Nb, and Y. The Mata samples are more enriched in most elements, including Ba, Zr, and Nb, but have similar concentrations of Y to other boninite samples from the Lau Basin. This makes varying degrees of mantle melting an unlikely explanation for the difference in fluid mobile elements. To determine the amount of contribution of various subduction related components, such as dehydrated fluids and sediment melt, and potential contribution of additional enriching components, additional analysis and isotope work would be helpful.

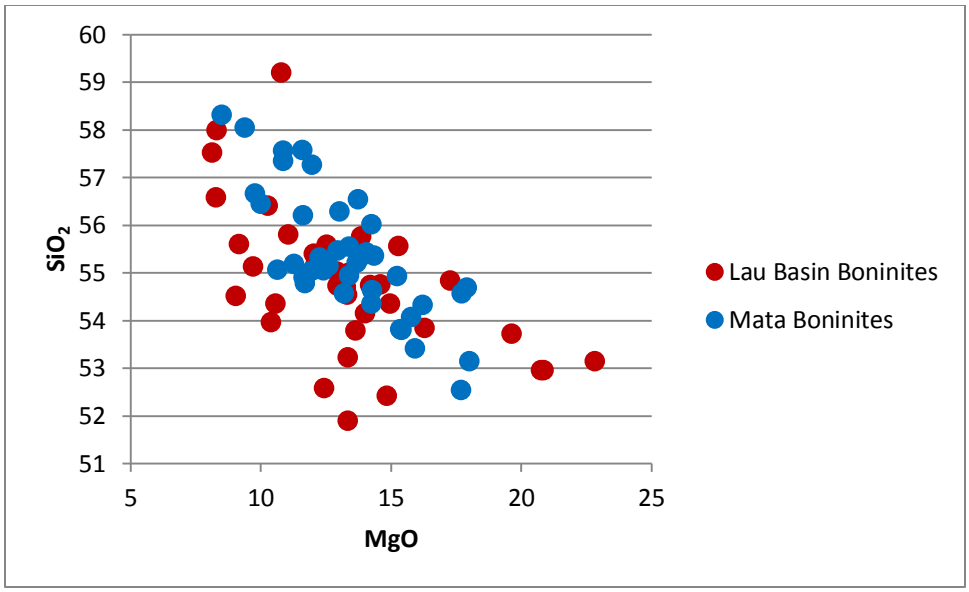


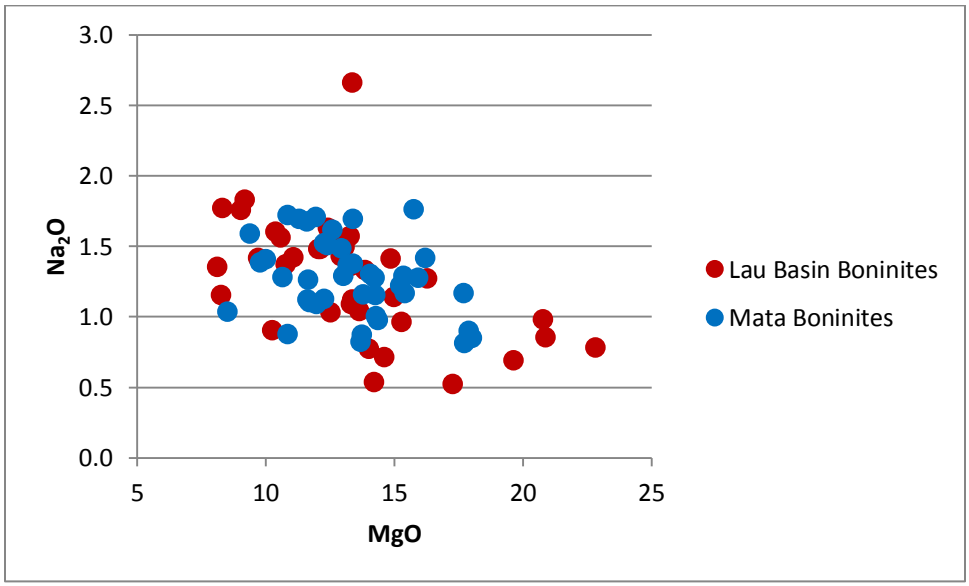


Figure 4.9. Comparison of whole rock major element data for Mata boninites to northern Lau Basin boninites from published studies. The two groups are very similar for all major elements at a given MgO content, as shown here by similarities in $SiO_2$ and $Na_2O$, with the exceptions of $TiO_2$ and $P_2O_5$. See text for references.

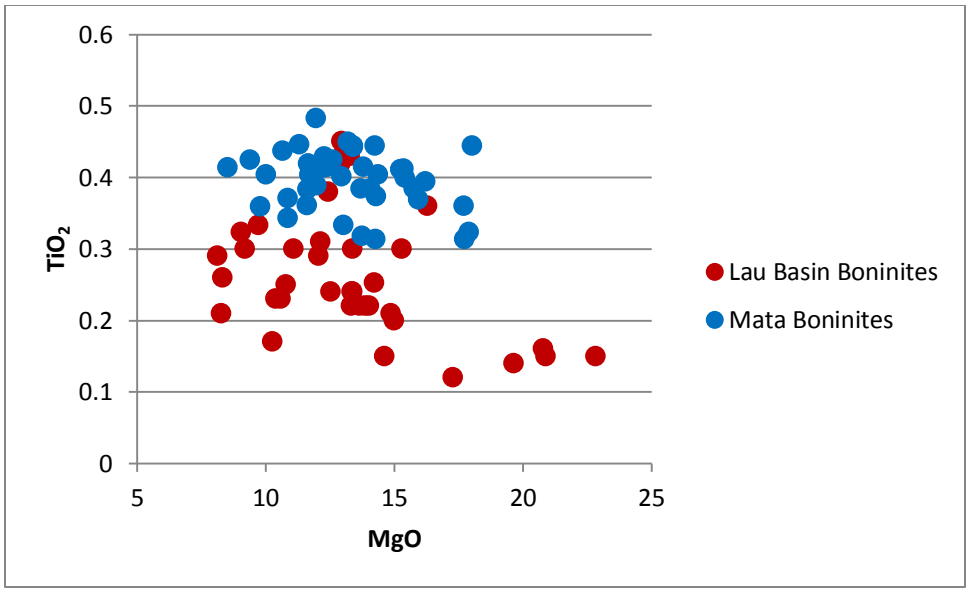


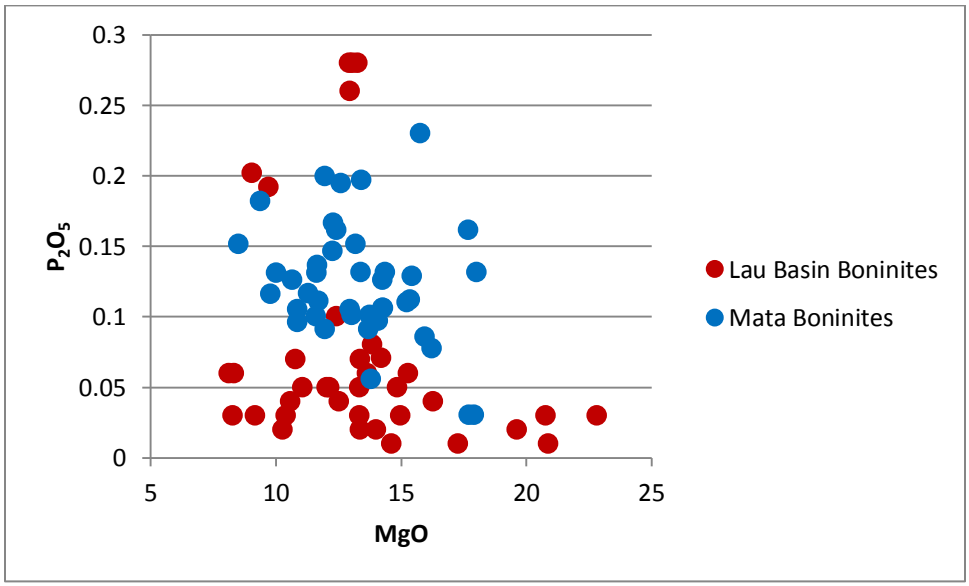


Figure 4.9, continued. Comparison of whole rock major element data for Mata boninites to northern Lau Basin boninites from published studies. The two groups are very similar for all major elements at a given MgO content, as shown here by similarities in $SiO_2$ and $Na_2O$, with the exceptions of $TiO_2$ and $P_2O_5$. See text for references.

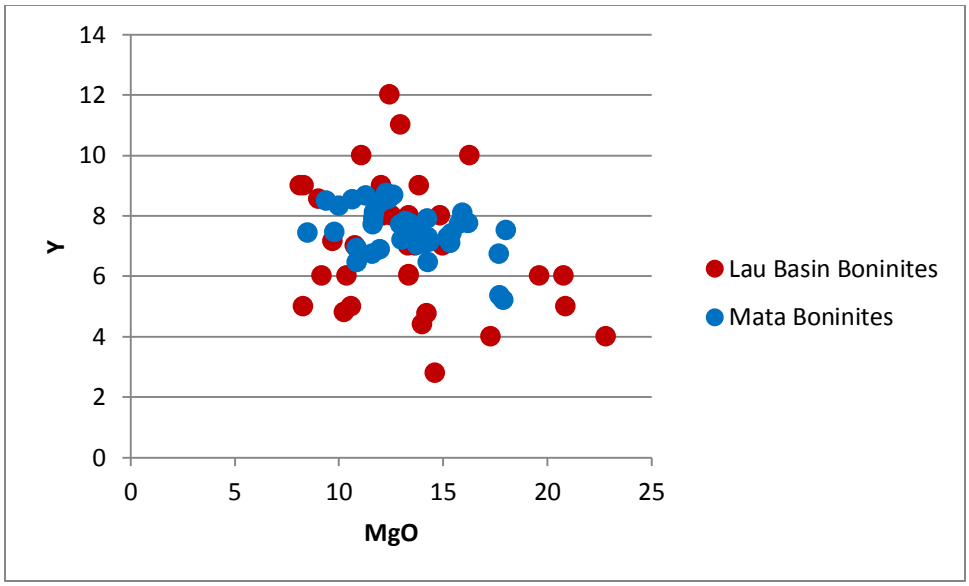


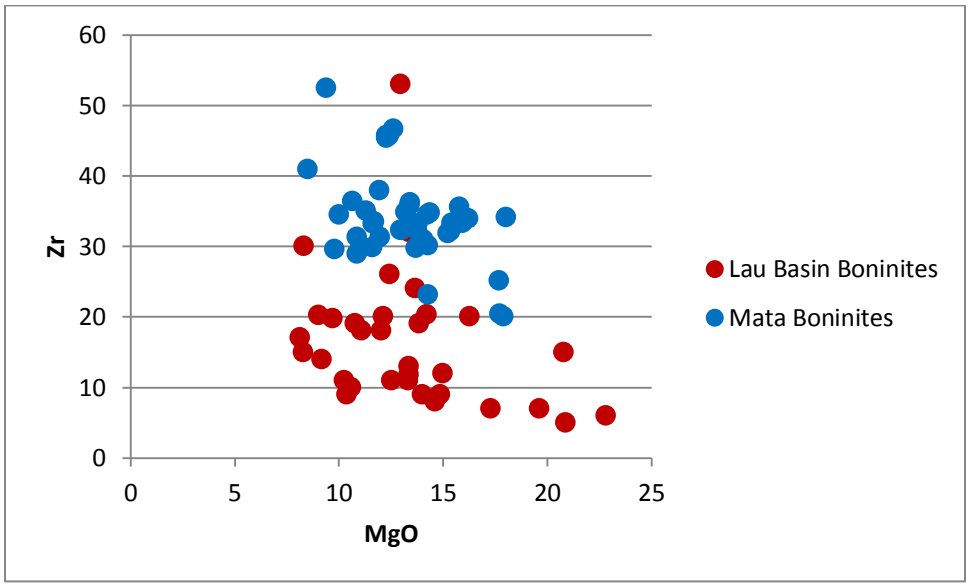


Figure 4.10. Comparison of whole rock trace element data for Mata boninites to literature data for the Lau Basin for Y, Zr, and Ba vs MgO. The two groups have very similar concentrations of Y, but Mata boninites are generally more enriched in both fluid mobile trace elements, such as Ba, and non-fluid mobile trace elements such as Zr. See text for references.

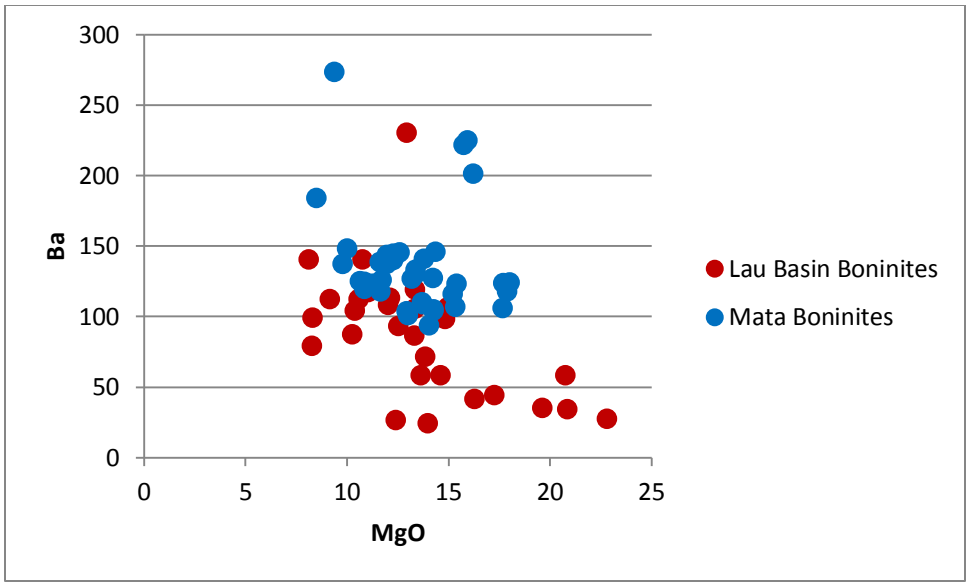


Figure 4.10, continued. Comparison of whole rock trace element data for Mata boninites to literature data for the Lau Basin for Y, Zr, and Ba vs MgO. The two groups have very similar concentrations of Y, but Mata boninites are generally more enriched in both fluid mobile trace elements, such as Ba, and non-fluid mobile trace elements such as Zr. See text for references.

Examinations of some fluid mobile to non-fluid mobile trace element ratios, such as Ba/Nb or Ba/Zr, do not depict a strong trend (Figure 4.11). Instead, plots show an overlapping pattern for most elements. Fluid mobile to non-fluid mobile ratios are typically studied in subduction zones to understand the nature of enrichment from the subducting slab or sediments. These ratios compare a fluid mobile element, such as Ba, that is mobile in fluids dehydrating from the subduction zone to a non-fluid mobile element, such as Nb, that is not fluid mobile and is thus thought to be representative of the mantle source region (See Chapter 1 for more details). The Mata boninites form a tighter array than boninites from previous studies in the Lau Basin which extend to lower and higher values than the Mata boninites.

However, when fluid mobile elements, such as Ba are compared to non-fluid mobile Y, a difference can be noted between the Mata boninites and other boninites from the Lau Basin. Mata boninites generally trend to higher values of Ba/Y. As both sets of boninites have similar concentrations of Y (Figures 4.10 and 4.11) and different concentrations of fluid mobile elements such as Ba (Figures 4.10 and 4.11), this difference in ratios can be attributed to the difference in Ba concentrations., possibly implying a greater enrichment in subduction related fluids in the Mata boninites when compared to the other Lau Basin boninites.

In general, Mata boninites also have higher concentrations of Nb and Zr, but similar concentrations of Y to previously published boninites in the northern Lau Basin. This causes the Mata boninites to have higher Nb/Y and Zr/Y ratios (Figures 4.10 and 4.11). Nb, Zr, and Y are not fluid mobile and thus would not be expected to come from fluids dehydrating off the subducting slab. The higher concentrations of Nb and Zr in the Mata boninites and similar concentrations of Y in the Mata boninites relative to other boninites from the Lau Basin may suggest variations in the mantle source between the different boninite suites or variations in additional enriching component(s).

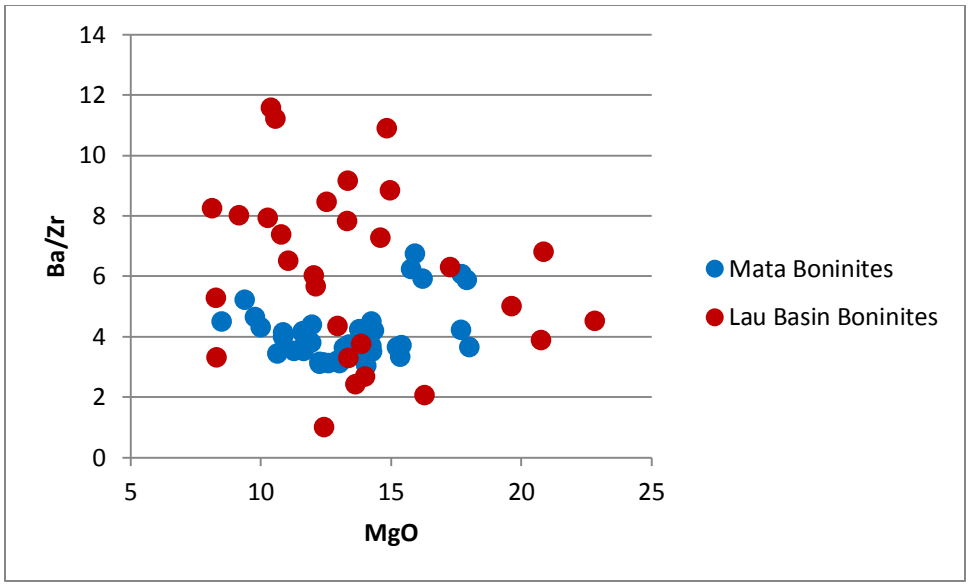


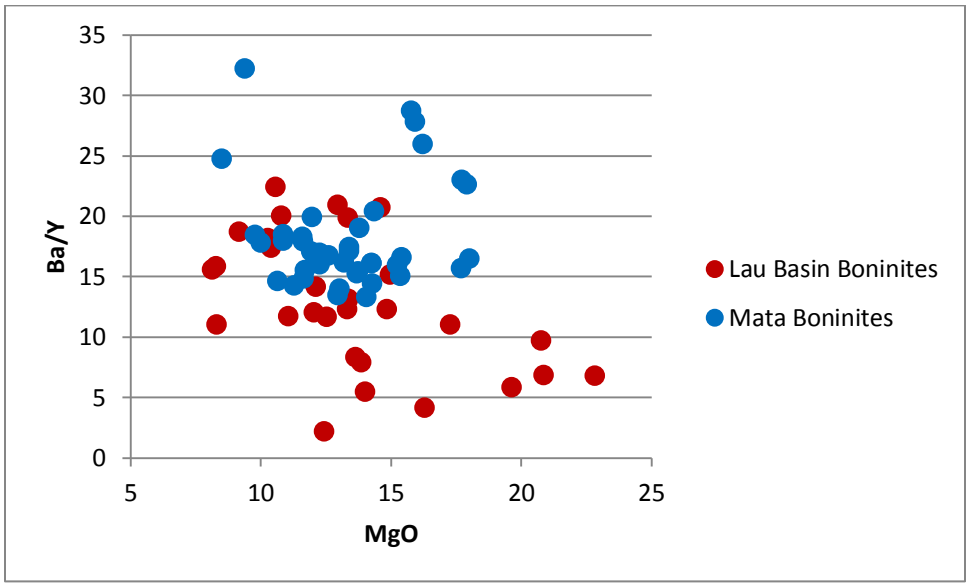


Figure 4.11. Comparison of whole rock trace element ratios (Ba/Zr, Ba/Y, and Zr/Y vs MgO) for Mata boninites to literature data for Lau Basin boninites. Ratios of fluid mobile to non-fluid mobile trace elements, such as Ba/Zr, do not show a strong trend. However ratios of fluid mobile and non-fluid mobile trace elements to Y, such as Ba/Y and Zr/Y tend to be higher for Mata boninites. See text for references.

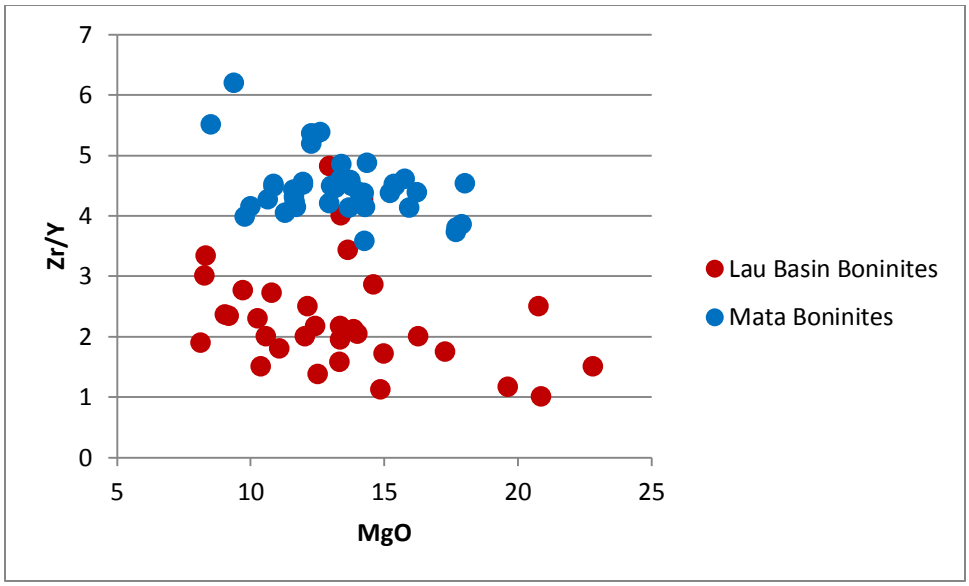


Figure 4.11, comparison. Comparison of whole rock trace element ratios (Ba/Zr, Ba/Y, and Zr/Y vs MgO) for Mata boninites to literature data for Lau Basin boninites. Ratios of fluid mobile to non-fluid mobile trace elements, such as Ba/Zr, do not show a strong trend. However ratios of fluid mobile and non-fluid mobile trace elements to Y, such as Ba/Y and Zr/Y tend to be higher for Mata boninites. See text for references.

## Major Elements in Glass

This section overviews major element data collected in glass samples by microprobe. This section summarizes and discusses the data, but a more thorough discussion of magma evolution will be discussed in Chapter 6. Information about the mineral phases that formed in these lavas is provided in Chapter 3 and again in Chapter 6.

The Mata volcanoes have a wide range of glass compositions from relatively primitive samples to evolved glasses. $SiO_2$ ranges from 53.9 to 70.7 wt%. MgO ranges from 0.49 to 8.58 wt%. $TiO_2$ ranges from 0.33 to 1.20 wt%. Glass compositions, determined by microprobe analysis, are more evolved than whole rock compositions (Table 4.4).

Table 4.4 Microprobe glass analysis for Mata samples (in wt%).

| Lab | Location | Sample | $SiO_2$ | $TiO_2$ | $Al_2O_3$ | FeO | MnO | MgO | CaO | $Na_2O$ | K2O | $P_2O_5$ | Cl | S | F |
|---|---|---|---|---|---|---|---|---|---|---|---|---|---|---|---|
| UH | East | KM1024 D14-R02 | 57.41 | 0.416 | 12.36 | 8.76 | 0.167 | 5.57 | 9.76 | 1.80 | 0.98 | 0.19 | 0.21 | 0.00 | |
| UH | East | KM1024 D14-R05 | 57.66 | 0.437 | 13.01 | 8.87 | 0.146 | 4.94 | 9.55 | 1.84 | 1.01 | 0.18 | 0.22 | 0.00 | |
| UH | East | KM1024 D14-R09 | 56.42 | 0.414 | 13.47 | 9.24 | 0.145 | 5.27 | 9.38 | 2.05 | 1.08 | 0.24 | 0.21 | 0.00 | |
| UH | East | KM1129a D01-R03 | 58.04 | 0.392 | 14.58 | 8.19 | 0.145 | 4.98 | 9.90 | 1.94 | 0.78 | 0.12 | 0.17 | 0.00 | |
| UH | East | KM1129a D01-R04 | 58.06 | 0.386 | 14.53 | 8.18 | 0.140 | 5.03 | 9.89 | 1.94 | 0.77 | 0.12 | 0.17 | 0.00 | |
| UH | East | KM1129a D02-R01 | 70.69 | 0.637 | 11.97 | 6.37 | 0.093 | 0.49 | 3.65 | 2.28 | 2.44 | 0.32 | 0.41 | 0.00 | |
| UH | East | KM1129a D02-R03 | 68.56 | 0.529 | 12.53 | 6.92 | 0.106 | 1.10 | 4.67 | 2.33 | 2.09 | 0.31 | 0.35 | 0.00 | |
| UH | East | KM1129a D02-R04 | 68.69 | 0.531 | 12.53 | 6.89 | 0.104 | 1.13 | 4.68 | 2.34 | 2.08 | 0.30 | 0.36 | 0.00 | |
| UT | West | J2-413-R01 | 55.64 | 0.567 | 13.93 | 8.69 | 0.150 | 6.49 | 10.36 | 1.93 | 0.66 | 0.23 | | | |
| UH | West | J2-413-R02 | 56.39 | 0.558 | 14.13 | 8.64 | 0.147 | 6.24 | 10.33 | 1.91 | 0.72 | 0.17 | 0.16 | 0.00 | |
| UT | West | J2-413-R03 | 55.75 | 0.567 | 13.91 | 8.60 | 0.170 | 6.39 | 10.42 | 1.90 | 0.69 | 0.19 | 0.14 | 0.00 | 0.03 |
| UT | West | J2-413-R04 | 56.09 | 0.577 | 14.24 | 8.69 | 0.140 | 6.08 | 10.22 | 1.99 | 0.71 | 0.19 | 0.14 | 0.00 | 0.03 |
| UT | West | J2-413-sed05B | 56.16 | 0.567 | 13.75 | 8.63 | 0.170 | 6.58 | 10.40 | 1.89 | 0.67 | 0.19 | 0.14 | 0.00 | 0.04 |
| UH | West | J2-413-R13 | 55.60 | 0.572 | 14.10 | 8.58 | 0.150 | 5.83 | 10.16 | 1.92 | 0.73 | 0.18 | 0.16 | 0.01 | |
| UT | West | J2-414-01 | 55.55 | 0.547 | 13.55 | 8.48 | 0.156 | 6.66 | 10.39 | 1.88 | 0.67 | 0.22 | 0.15 | 0.01 | 0.03 |
| UT | West | J2-413-R14 | 55.61 | 0.567 | 13.95 | 8.61 | 0.150 | 6.32 | 10.30 | 1.93 | 0.71 | 0.19 | 0.14 | 0.00 | 0.03 |
| UT | West | J2-414-12 | 55.87 | 0.567 | 13.88 | 8.76 | 0.180 | 6.58 | 10.41 | 1.87 | 0.68 | 0.21 | 0.14 | 0.00 | 0.04 |
| UT | West | J2-414-22 | 55.72 | 0.537 | 13.99 | 8.71 | 0.160 | 6.30 | 10.41 | 2.04 | 0.72 | 0.22 | 0.15 | 0.00 | 0.04 |
| UT | West | J2-414-R27 | 55.56 | 0.512 | 14.12 | 8.78 | 0.148 | 6.37 | 10.64 | 1.83 | 0.60 | 0.17 | 0.13 | 0.00 | 0.03 |
| UT | West | J2-417-R01 | 55.31 | 0.490 | 13.52 | 8.77 | 0.169 | 6.87 | 10.86 | 1.74 | 0.59 | 0.13 | 0.12 | 0.01 | 0.03 |
| UT | West | J2-417-R02 | 55.84 | 0.496 | 13.82 | 8.97 | 0.180 | 6.58 | 10.84 | 1.82 | 0.62 | 0.13 | 0.12 | 0.00 | 0.04 |
| UT | West | J2-417-R09 | 55.79 | 0.537 | 13.75 | 8.80 | 0.170 | 6.71 | 10.59 | 1.90 | 0.65 | 0.17 | 0.13 | 0.00 | 0.04 |
| UT | West | J2-417-R28Host | 56.12 | 0.586 | 14.82 | 8.79 | 0.154 | 5.51 | 9.86 | 2.05 | 0.76 | 0.17 | 0.14 | 0.01 | 0.03 |
| UH | West | J2-418-R01 | 58.69 | 0.484 | 14.51 | 8.88 | 0.144 | 3.24 | 8.31 | 1.98 | 0.94 | 0.15 | 0.19 | 0.00 | |
| UH | West | J2-418-C02 | 57.40 | 0.504 | 14.66 | 8.90 | 0.153 | 3.99 | 8.54 | 2.14 | 0.99 | 0.17 | 0.24 | 0.00 | |
| UH | West | J2-418-R04 | 57.54 | 0.539 | 14.41 | 8.85 | 0.132 | 4.15 | 8.82 | 2.11 | 1.00 | 0.19 | 0.24 | 0.00 | |
| UH | West | J2-418-R05 | 57.70 | 0.505 | 14.28 | 8.97 | 0.132 | 4.26 | 8.87 | 2.04 | 0.96 | 0.17 | 0.23 | 0.00 | |
| UT | West | J2-418-R06 | 55.87 | 0.512 | 14.35 | 8.82 | 0.170 | 6.12 | 10.54 | 1.90 | 0.63 | 0.18 | 0.14 | 0.00 | 0.03 |

Table 4.4. continued Microprobe glass analysis for Mata samples (in wt%).

| Lab | Location | Sample | $SiO_2$ | $TiO_2$ | $Al_2O_3$ | FeO | MnO | MgO | CaO | $Na_2O$ | $K_2O$ | $P_2O_5$ | Cl | S | F |
|---|---|---|---|---|---|---|---|---|---|---|---|---|---|---|---|
| UH | West | J2-418-R11 | 56.41 | 0.494 | 14.04 | 8.73 | 0.144 | 6.29 | 10.53 | 1.84 | 0.65 | 0.14 | 0.15 | 0.00 | |
| UH | West | J2-418-R18 | 55.77 | 0.574 | 13.99 | 8.54 | 0.146 | 6.02 | 10.29 | 1.88 | 0.72 | 0.17 | 0.16 | 0.00 | |
| UT | West | J2-418-R20 | 55.35 | 0.557 | 13.89 | 8.70 | 0.150 | 6.41 | 10.48 | 2.04 | 0.71 | 0.17 | 0.17 | 0.00 | 0.03 |
| UH | West | J2-420-R01 | 57.26 | 0.462 | 14.64 | 8.83 | 0.140 | 3.52 | 8.59 | 2.13 | 0.95 | 0.18 | 0.30 | 0.00 | |
| UH | West | J2-420-R02 | 57.06 | 0.460 | 14.37 | 8.85 | 0.149 | 4.00 | 8.87 | 2.06 | 0.91 | 0.15 | 0.25 | 0.01 | |
| UT | West | J2-420-R04 | 55.46 | 0.501 | 14.17 | 8.74 | 0.170 | 6.36 | 10.18 | 1.85 | 0.63 | 0.17 | 0.14 | 0.01 | 0.04 |
| UT | West | J2-420-R05 | 56.26 | 0.537 | 15.10 | 8.82 | 0.140 | 5.28 | 10.15 | 2.06 | 0.68 | 0.17 | 0.15 | 0.01 | 0.02 |
| UT | West | J2-420-R07 | 55.57 | 0.518 | 14.28 | 8.85 | 0.192 | 6.31 | 10.47 | 1.88 | 0.63 | 0.16 | 0.14 | 0.01 | 0.03 |
| UH | West | J2-420-R08 | 55.04 | 0.518 | 14.14 | 8.66 | 0.151 | 5.92 | 10.31 | 1.81 | 0.66 | 0.16 | 0.15 | 0.00 | |
| UT | West | J2-420-R09 | 54.97 | 0.510 | 14.30 | 8.87 | 0.150 | 6.13 | 10.40 | 1.89 | 0.63 | 0.16 | 0.14 | 0.01 | 0.04 |
| UH | West | J2-420-R10 | 55.45 | 0.525 | 14.90 | 8.85 | 0.142 | 5.31 | 10.07 | 1.92 | 0.67 | 0.15 | 0.16 | 0.00 | |
| UH | West | J2-420-R13 | 55.48 | 0.500 | 14.43 | 8.77 | 0.140 | 5.85 | 10.28 | 1.84 | 0.66 | 0.14 | 0.15 | 0.00 | |
| UH | West | J2-420-R16 | 56.71 | 0.507 | 14.28 | 8.77 | 0.144 | 6.09 | 10.51 | 1.83 | 0.65 | 0.14 | 0.15 | 0.01 | |
| UH | West | J2-420-R23 | 55.65 | 0.557 | 14.05 | 8.67 | 0.141 | 6.17 | 10.31 | 1.88 | 0.71 | 0.16 | 0.16 | 0.00 | |
| UT | West | J2-420-R17 | 55.70 | 0.526 | 14.43 | 8.96 | 0.140 | 6.04 | 10.51 | 1.94 | 0.66 | 0.09 | 0.13 | 0.00 | 0.04 |
| UT | West | J2-420-R12 | 55.70 | 0.516 | 14.79 | 8.96 | 0.170 | 5.69 | 10.29 | 1.96 | 0.65 | 0.21 | 0.14 | 0.00 | 0.03 |
| UH | West | KM1024 D12-R01 | 58.36 | 0.421 | 14.34 | 8.96 | 0.145 | 3.63 | 8.63 | 2.05 | 0.91 | 0.15 | 0.26 | 0.00 | |
| UH | West | KM1024 D12-R06 | 58.12 | 0.416 | 14.33 | 8.80 | 0.144 | 4.01 | 9.08 | 2.03 | 0.83 | 0.12 | 0.23 | 0.00 | |
| UH | West | KM1024 D12-R08 | 58.34 | 0.426 | 14.46 | 8.89 | 0.136 | 3.69 | 8.65 | 2.05 | 0.89 | 0.14 | 0.25 | 0.00 | |
| UH | West | KM1024 D15-R01 | 55.29 | 0.445 | 13.55 | 8.73 | 0.138 | 6.51 | 10.71 | 1.74 | 0.63 | 0.12 | 0.12 | 0.01 | |
| UH | West | KM1024 D15-R03 | 55.70 | 0.462 | 13.75 | 8.73 | 0.147 | 6.36 | 10.79 | 1.72 | 0.62 | 0.14 | 0.12 | 0.01 | |
| UH | West | KM1024 D15-R05 | 60.14 | 0.772 | 13.93 | 9.41 | 0.146 | 2.70 | 6.91 | 2.41 | 1.52 | 0.28 | 0.27 | 0.00 | |
| UH | West | RR1211 Q327-R02 | 56.09 | 0.546 | 14.98 | 8.83 | 0.151 | 4.99 | 10.17 | 1.99 | 0.71 | 0.16 | 0.15 | 0.01 | |
| UH | West | RR1211 Q327-BS06 | 55.79 | 0.525 | 14.44 | 8.71 | 0.135 | 5.81 | 10.63 | 1.84 | 0.66 | 0.14 | 0.14 | 0.00 | |
| UH | West | RR1211 Q332-R01 | 55.62 | 0.583 | 14.62 | 8.66 | 0.146 | 5.85 | 10.29 | 1.98 | 0.76 | 0.18 | 0.16 | 0.00 | |
| UH | West | RR1211 Q332-R02 | 55.39 | 0.573 | 14.61 | 8.69 | 0.151 | 5.85 | 10.29 | 1.97 | 0.76 | 0.18 | 0.16 | 0.00 | |
| UH | West | RR1211 Q332-R03 | 55.72 | 0.577 | 14.17 | 8.48 | 0.145 | 6.07 | 10.53 | 1.91 | 0.72 | 0.17 | 0.15 | 0.00 | |
| UH | West | RR1211 Q332-R04 | 55.41 | 0.573 | 14.33 | 8.58 | 0.145 | 6.02 | 10.36 | 1.92 | 0.73 | 0.18 | 0.15 | 0.00 | |

Table 4.4. continued Microprobe glass analysis for Mata samples (in wt%).

| Lab | Location | Sample | SiO2 | TiO2 | Al2O3 | FeO | MnO | MgO | CaO | Na2O | K2O | P2O5 | Cl | S | F |
|---|---|---|---|---|---|---|---|---|---|---|---|---|---|---|---|
| UH | West | RR1211 Q332-R05 | 55.52 | 0.577 | 14.53 | 8.58 | 0.154 | 5.79 | 10.32 | 1.95 | 0.75 | 0.16 | 0.16 | 0.00 | |
| UH | LF | KM1024 D13-R01 | 56.03 | 1.045 | 13.56 | 8.94 | 0.157 | 5.82 | 9.53 | 2.32 | 1.33 | 0.33 | 0.26 | 0.01 | |
| UH | Taha | KM1024 D16-R01 | 56.99 | 0.476 | 14.74 | 8.54 | 0.157 | 4.78 | 9.51 | 2.01 | 0.78 | 0.17 | 0.15 | 0.00 | |
| UH | Taha | KM1024 D16-R02 | 57.21 | 0.491 | 14.86 | 8.59 | 0.150 | 4.51 | 9.30 | 2.04 | 0.79 | 0.17 | 0.15 | 0.00 | |
| UH | Ua | KM1024 D17-R01 | 57.54 | 0.411 | 12.66 | 8.75 | 0.155 | 5.76 | 9.80 | 1.75 | 0.96 | 0.17 | 0.20 | 0.00 | |
| UH | Ua | KM1129a D10-R01 | 57.18 | 0.702 | 13.39 | 8.22 | 0.146 | 6.28 | 9.85 | 1.67 | 1.08 | 0.15 | 0.15 | 0.00 | |
| UH | Ua | KM1129a D10-R02 | 56.61 | 0.859 | 13.87 | 7.74 | 0.140 | 5.58 | 9.60 | 1.73 | 1.20 | 0.16 | 0.15 | 0.01 | |
| UH | Ua | KM1129a D10-R03 | 55.87 | 0.553 | 13.86 | 8.23 | 0.142 | 6.77 | 10.87 | 1.80 | 0.75 | 0.18 | 0.15 | 0.00 | |
| UH | Ua | KM1129a D10-R06 | 57.66 | 0.369 | 11.55 | 8.97 | 0.160 | 7.77 | 9.73 | 1.47 | 0.87 | 0.12 | 0.15 | 0.00 | |
| UH | Ua | KM1024 D18-R01 | 57.67 | 0.415 | 14.17 | 8.04 | 0.151 | 5.68 | 10.25 | 1.75 | 0.77 | 0.15 | 0.14 | 0.00 | |
| UH | Ua | KM1024 D18-R04 | 57.42 | 0.413 | 14.09 | 8.00 | 0.141 | 5.68 | 10.28 | 1.76 | 0.77 | 0.14 | 0.14 | 0.00 | |
| UH | Ua | KM1024 D18-R05 | 57.40 | 0.422 | 14.08 | 7.98 | 0.140 | 5.72 | 10.26 | 1.75 | 0.76 | 0.14 | 0.14 | 0.00 | |
| UH | Ua | RR1211 Q325-R01 | 57.90 | 0.473 | 14.69 | 8.04 | 0.126 | 4.72 | 9.21 | 1.77 | 0.77 | 0.16 | 0.17 | 0.00 | |
| UH | Ua | RR1211 Q325-R03 | 54.00 | 0.851 | 13.06 | 8.68 | 0.156 | 6.77 | 11.08 | 1.86 | 1.17 | 0.22 | 0.18 | 0.00 | |
| UH | Ua | RR1211 Q325-R04 | 56.97 | 0.413 | 13.61 | 8.58 | 0.145 | 5.85 | 9.92 | 1.51 | 0.66 | 0.13 | 0.15 | 0.00 | |
| UH | Ua | RR1211 Q328-R03 | 55.54 | 0.587 | 13.94 | 7.80 | 0.143 | 6.64 | 10.75 | 1.76 | 0.83 | 0.13 | 0.12 | 0.00 | |
| UH | Ua | RR1211 Q328-R11 | 55.80 | 0.679 | 13.06 | 8.13 | 0.149 | 6.74 | 10.57 | 1.87 | 1.02 | 0.19 | 0.18 | 0.00 | |
| UH | Ua | RR1211 Q328-R12 | 55.31 | 0.496 | 12.37 | 7.89 | 0.151 | 8.58 | 11.43 | 1.52 | 0.62 | 0.16 | 0.13 | 0.00 | |
| UH | Tolu | KM1024 D20-R01 | 57.71 | 0.509 | 14.52 | 8.19 | 0.145 | 4.97 | 9.59 | 1.89 | 0.86 | 0.18 | 0.17 | 0.01 | |
| UH | Tolu | KM1024 D20-R02 | 57.83 | 0.479 | 14.23 | 8.22 | 0.135 | 5.22 | 9.74 | 1.84 | 0.85 | 0.17 | 0.17 | 0.00 | |
| UH | Tolu | KM1129a D07-R01 | 56.72 | 0.407 | 13.01 | 7.79 | 0.143 | 7.34 | 10.70 | 1.85 | 0.50 | 0.21 | 0.11 | 0.00 | |
| UH | Tolu | KM1129a D07-R02 | 56.91 | 0.436 | 13.70 | 7.90 | 0.138 | 6.52 | 10.43 | 1.96 | 0.55 | 0.20 | 0.12 | 0.00 | |
| UH | Tolu | KM1129a D08-R01 | 57.50 | 0.498 | 14.36 | 8.50 | 0.145 | 5.34 | 9.94 | 1.86 | 0.85 | 0.18 | 0.17 | 0.00 | |
| UH | Tolu | KM1129a D08-R04 | 57.70 | 0.505 | 14.34 | 8.45 | 0.131 | 5.35 | 9.92 | 1.82 | 0.85 | 0.17 | 0.17 | 0.00 | |
| UH | Tolu | KM1129a D08-R07 | 57.49 | 0.499 | 14.25 | 8.46 | 0.144 | 5.39 | 9.93 | 1.82 | 0.85 | 0.18 | 0.17 | 0.00 | |
| UH | Tolu | KM1129a D08-R08 | 56.00 | 0.515 | 14.49 | 8.22 | 0.140 | 6.21 | 10.68 | 1.90 | 0.70 | 0.24 | 0.13 | 0.00 | |
| UH | Tolu | KM1129a D09-R01 | 55.21 | 1.112 | 14.02 | 8.99 | 0.147 | 5.13 | 9.08 | 2.59 | 1.43 | 0.44 | 0.22 | 0.01 | |
| UH | Tolu | KM1129a D09-R02 | 55.05 | 1.110 | 13.82 | 8.89 | 0.150 | 5.29 | 8.94 | 2.63 | 1.46 | 0.44 | 0.22 | 0.01 | |
| UH | Tolu | RR1211 Q331-R01 | 57.15 | 0.462 | 12.62 | 8.34 | 0.149 | 6.55 | 10.66 | 1.51 | 0.81 | 0.17 | 0.16 | 0.00 | |

Table 4.4. continued Microprobe glass analysis for Mata samples (in wt%).

| Lab | Location | Sample | SiO2 | TiO2 | Al2O3 | FeO | MnO | MgO | CaO | Na2O | K2O | P2O5 | Cl | S | F |
|---|---|---|---|---|---|---|---|---|---|---|---|---|---|---|---|
| UH | Tolu | RR1211 Q331-R02 | 56.91 | 0.517 | 14.51 | 7.87 | 0.142 | 5.58 | 10.19 | 1.82 | 0.82 | 0.16 | 0.17 | 0.00 | |
| UH | Tolu | RR1211 Q331-R16 | 56.80 | 0.540 | 14.76 | 7.86 | 0.153 | 5.36 | 10.15 | 1.84 | 0.84 | 0.16 | 0.18 | 0.01 | |
| UH | Fa | KM1024 D21-R01 | 53.85 | 1.161 | 13.96 | 9.14 | 0.153 | 5.50 | 9.81 | 2.24 | 1.04 | 0.31 | 0.21 | 0.00 | |
| UH | Fa | KM1024 D21-R02 | 53.98 | 1.144 | 13.76 | 9.09 | 0.161 | 5.82 | 9.98 | 2.20 | 1.01 | 0.31 | 0.21 | 0.00 | |
| UH | Fa | KM1024 D21-R04 | 54.40 | 1.197 | 14.24 | 9.13 | 0.157 | 5.41 | 9.75 | 2.24 | 1.05 | 0.30 | 0.21 | 0.00 | |
| UH | Ono | KM1024 D22-R01 | 57.06 | 0.557 | 12.36 | 8.15 | 0.153 | 7.30 | 10.65 | 1.56 | 0.84 | 0.16 | 0.14 | 0.00 | |
| UH | Ono | KM1024 D22-R02 | 56.70 | 0.332 | 12.86 | 8.39 | 0.157 | 7.23 | 10.68 | 1.36 | 0.65 | 0.11 | 0.13 | 0.00 | |
| UH | Fitu | KM1024 D23-R01 | 56.67 | 0.357 | 13.52 | 8.36 | 0.145 | 6.54 | 10.36 | 1.73 | 0.57 | 0.11 | 0.18 | 0.00 | |
| UH | Fitu | KM1024 D23-R04 | 56.43 | 0.357 | 13.40 | 8.34 | 0.136 | 6.84 | 10.29 | 1.70 | 0.58 | 0.13 | 0.17 | 0.00 | |
| UH | Fitu | RR1211-Q329-R01 | 55.51 | 0.576 | 13.23 | 8.22 | 0.154 | 6.92 | 11.03 | 1.61 | 0.58 | 0.12 | 0.13 | 0.00 | |
| UH | Fitu | RR1211-Q329-R02 | 55.87 | 0.697 | 14.99 | 8.03 | 0.139 | 5.39 | 10.26 | 1.84 | 0.68 | 0.15 | 0.15 | 0.00 | |
| UH | Niua | KM1129a D04-R04 | 77.77 | 0.249 | 12.06 | 2.15 | 0.055 | 0.31 | 2.07 | 3.25 | 1.76 | 0.03 | 0.21 | 0.00 | |

Most samples were measured at the University of Hawaii at Manoa (UH) by Sarah Glancy and Eric Hellebrand. Some West Mata samples were analyzed by Peter Michael at the University of Tulsa (UT). F was only measured at UT and is thus only reported for samples from UT. Drift corrections were applied to 16 samples measured at UH for $SiO_2$: KM1024 D14-R02, KM1024 D16-R01, KM1024 D16-R02, KM1024 D17-R01, KM1129a D10-R02, KM1129a D10-R03, KM1129a D10-R06, KM1024 D20-R01, KM1024 D20-R02, KM1129a D07-R01, KM1129a D07-R02, KM1129a D08-R04, KM1024 D21-R01, KM1024 D21-R02, KM1024 D21-R04, and KM1024 D23-R04. The location LF denotes for a lava flow near West Mata.

Most samples were measured at UH Manoa, but some samples were measured at the University of Tulsa by Peter Michael. A few samples were measured at both universities to ensure consistency in the dataset. The data is very consistent between the two universities. For most major elements, data deviates by less than 5% (For $SiO_2$ the range is 0.5 to 2.7%, for $TiO_2$, the range is 1.0 to 3.9%, for $Al_2O_3$, the range is 0.1 to 4.1%, and for CaO the range is 0.5 to 2.8%). For MgO, $Na_2O$, and $K_2O$ the data is within 10% (for MgO the range is 3.7 to 8.2%, for $Na_2O$ the range is 0.4 to 9.2%, and for $K_2O$, the range is 0.2 to 7.3%). MnO extends to just outside 10% (2.0 to 11.9 %). $P_2O_5$, Cl, and S can vary; however, these elements are in low concentrations in the samples. The difference in the overall totals is small (only 0.2 to 1.3 %). Therefore data measured at both universities are used in this project.

The Mata volcanoes can be divided into four compositional groups based on major element glass chemistry as shown in Table 4.5: 1. boninite samples with low $TiO_2$ ($TiO_2 < 0.70$ wt %), 2. samples with intermediate $TiO_2$ (0.70 wt% $\leq TiO_2 < 1.0$ wt%), 3. samples with high $TiO_2$ ($TiO_2 \geq 1.0$ wt%), 4.) evolved samples (MgO < 3 wt%).

The first group, the low $TiO_2$ group (Group 1) fits 85% of the sample set. These samples appear to fall along a series of several simple liquid lines of descent. MELTS modeling of these liquid lines of descent will be discussed in Chapter 6.

The medium $TiO_2$ group, Group 2, contains four samples with greater than 0.70 wt% $TiO_2$, but less than 1.0 wt% $TiO_2$. At similar MgO, these samples plot with the low $TiO_2$ group samples. They may be a subset of Group 1 or a result of mixing between Groups 1 and 3. This group contains three of the 14 samples from Mata Ua and one of four samples from Mata Fitu. Note that sample KM1129a D10-R02 is not a boninite based on whole rock XRF analysis due to its higher $TiO_2$ content.

Group 3 consists of the six high $TiO_2$ samples, samples with more than 1.0 wt% of $TiO_2$. This group contains all of the Mata Fa samples, two of the 13 Mata Tolu samples, and a sample from the lava flow near West Mata. These samples are distinct from Group 1 and Group 2. In addition to being much higher in $TiO_2$ for a given MgO compared to samples from the other groups, they are also slightly higher in $Na_2O$, $K_2O$, and $P_2O_5$ for a given MgO value (Figure 4.12). For other elements, there is not a significant difference between the groups.

Group 4 contains the evolved samples with less than 3 wt% MgO. There are three very evolved samples from East Mata and one sample from West Mata. These samples appear to fall on the same array as Group 1, but are just at the much lower MgO range.

Table 4.5 Mata compositional groups based on microprobe glass analysis

| **$TiO_2$ Group** | **Location** | **Sample** |
|---|---|---|
| Low | East Mata | KM1024 D14-R02 |
| Low | East Mata | KM1024 D14-R05 |
| Low | East Mata | KM1024 D14-R09 |
| Low | East Mata | KM1129a D01-R03 |
| Low | East Mata | KM1129a D01-R04 |
| Low | West Mata | J2-413-R01 |
| Low | West Mata | J2-413-R02 |
| Low | West Mata | J2-413-R03 |
| Low | West Mata | J2-413-R04 |
| Low | West Mata | J2-413-sed05B |
| Low | West Mata | J2-413-R13 |
| Low | West Mata | J2-413-R14 |
| Low | West Mata | J2-414-Rock01 |
| Low | West Mata | J2-414-R12 |
| Low | West Mata | J2-414-R22 |
| Low | West Mata | J2-414-R27 |
| Low | West Mata | J2-417-R01 |
| Low | West Mata | J2-417-R02 |
| Low | West Mata | J2-417-R09 |
| Low | West Mata | J2-417-R28Host |
| Low | West Mata | J2-418-R01 |
| Low | West Mata | J2-418-C02 |
| Low | West Mata | J2-418-R04 |
| Low | West Mata | J2-418-R05 |
| Low | West Mata | J2-418-R06 |
| Low | West Mata | J2-418-R11 |
| Low | West Mata | J2-418-R18 |
| Low | West Mata | J2-418-R20 |
| Low | West Mata | J2-420-R01 |
| Low | West Mata | J2-420-R02 |
| Low | West Mata | J2-420-R04 |
| Low | West Mata | J2-420-R05 |
| Low | West Mata | J2-420-R07 |
| Low | West Mata | J2-420-R08 |

Table 4.5 Continued, Mata compositional groups based on microprobe glass analysis

| **$TiO_2$ Group** | **Location** | **Sample** |
|---|---|---|
| Low | West Mata | J2-420-R09 |
| Low | West Mata | J2-420-R10 |
| Low | West Mata | J2-420-R12 |
| Low | West Mata | J2-420-R13 |
| Low | West Mata | J2-420-R16 |
| Low | West Mata | J2-420-R17 |
| Low | West Mata | J2-420-R23 |
| Low | West Mata | KM1024 D12-R01 |
| Low | West Mata | KM1024 D12-R06 |
| Low | West Mata | KM1024 D12-R08 |
| Low | West Mata | KM1024 D15-R01 |
| Low | West Mata | KM1024 D15-R03 |
| Low | West Mata | RR1211 Q327-R02 |
| Low | West Mata | RR1211 Q327-BS06 |
| Low | West Mata | RR1211 Q332-R01 |
| Low | West Mata | RR1211 Q332-R02 |
| Low | West Mata | RR1211 Q332-R03 |
| Low | West Mata | RR1211 Q332-R04 |
| Low | West Mata | RR1211 Q332-R05 |
| Low | Taha | KM1024 D16-R01 |
| Low | Taha | KM1024 D16-R02 |
| Low | Ua | KM1024 D17-R01 |
| Low | Ua | KM1129a D010-R03 |
| Low | Ua | KM1129a D010-R06 |
| Low | Ua | KM1024 D18-R01 |
| Low | Ua | KM1024 D18-R04 |
| Low | Ua | KM1024 D18-R05 |
| Low | Ua | RR1211 Q325-R01 |
| Low | Ua | RR1211 Q325-R04 |
| Low | Ua | RR1211 Q328-R03 |
| Low | Ua | RR1211 Q328-R11 |
| Low | Ua | RR1211 Q328-R12 |
| Low | Tolu | RR1211 Q331-R01 |
| Low | Tolu | RR1211 Q331-R02 |
| Low | Tolu | RR1211 Q331-R16 |

Table 4.5 Continued, Mata compositional groups based on microprobe glass analysis

| **$TiO_2$ Group** | **Location** | **Sample** |
|---|---|---|
| Low | Tolu | KM1024 D20-R01 |
| Low | Tolu | KM1024 D20-R02 |
| Low | Tolu | KM1129a D07-R01 |
| Low | Tolu | KM1129a D07-R02 |
| Low | Tolu | KM1129a D08-R01 |
| Low | Tolu | KM1129a D08-R04 |
| Low | Tolu | KM1129a D08-R07 |
| Low | Tolu | KM1129a D08-R08 |
| Low | Ono | KM1024 D22-R01 |
| Low | Ono | KM1024 D22-R02 |
| Low | Fitu | KM1024 D23-R01 |
| Low | Fitu | KM1024 D23-R04 |
| Low | Fitu | RR1211 Q329-R01 |
| Medium | Ua | KM1129a D010-R01 |
| Medium | Ua | KM1129a D10-R02 |
| Medium | Ua | RR1211 Q325-R03 |
| Medium | Fitu | RR1211 Q329-R02 |
| High | Lava flow near W. Mata | KM1024 D13-R01 |
| High | Tolu | KM1129a D09-R01 |
| High | Tolu | KM1129a D09-R02 |
| High | Fa | KM1024 D21-R01 |
| High | Fa | KM1024 D21-R02 |
| High | Fa | KM1024 D21-R04 |
| Evolved | East Mata | KM1129a D02-R01 |
| Evolved | East Mata | KM1129a D02-R03 |
| Evolved | East Mata | KM1129a D02-R04 |
| Evolved | West Mata | KM1024 D15-R05 |

The four groups are: 1. samples with low $TiO_2$ ($TiO_2 < 0.70$ wt %) 2. samples with intermediate $TiO_2$ ($0.70$ wt% $\leq TiO_2 < 1.0$ wt%) 3. samples with high $TiO_2$ ($TiO_2 \geq 1.0$ wt%) and 4. evolved samples (MgO < 3 wt%).

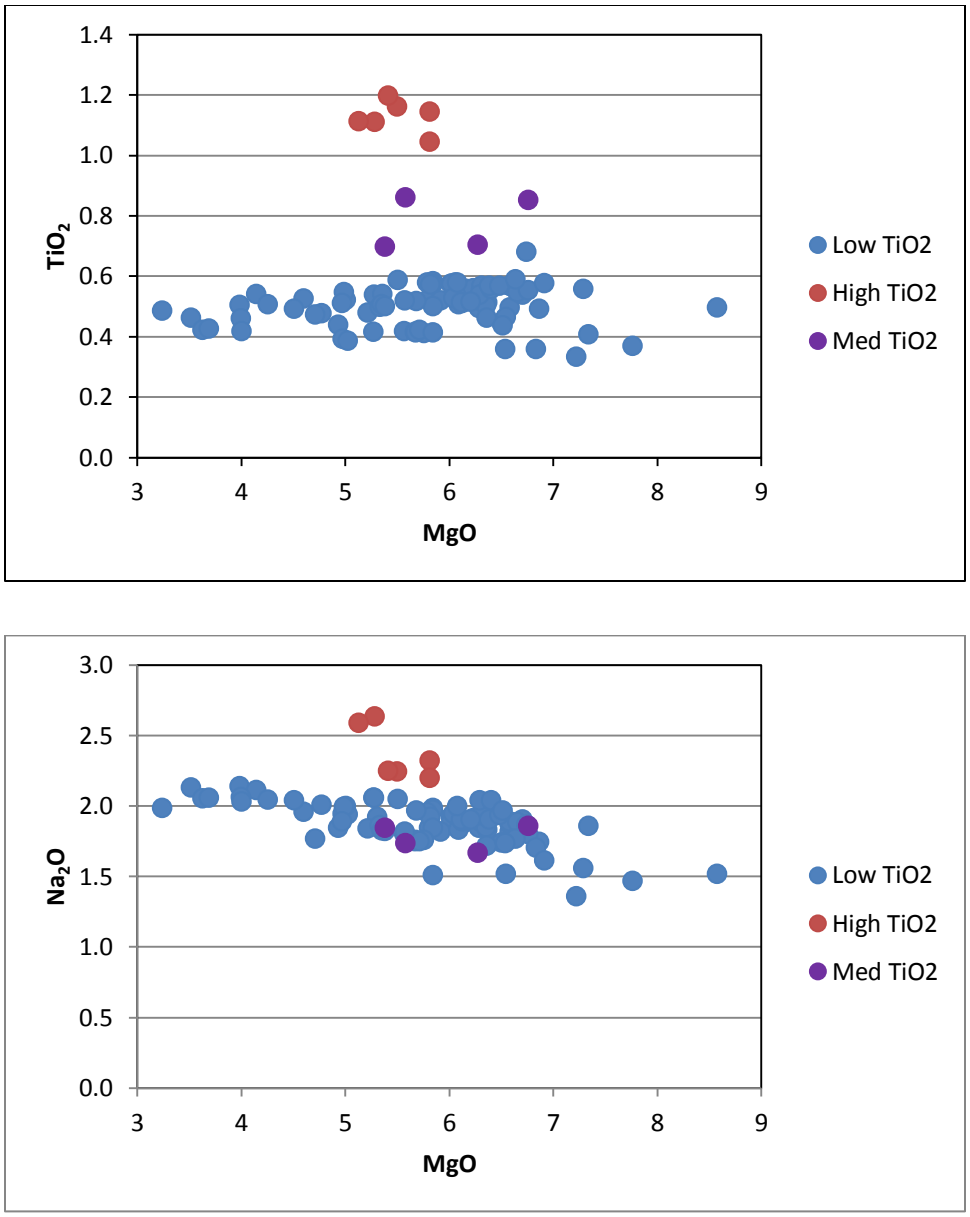


Figure 4.12. Graphs comparing high, medium, and low $TiO_2$ samples for selected oxides ($Na_2O$ vs $P_2O_5$) vs. MgO. The high $TiO_2$ group is distinct from the other groups due to its elevated concentrations of $TiO_2$, $Na_2O$, $K_2O$, and $P_2O_5$. The medium TiO2 group has an intermediate concentration of $TiO_2$ between Groups 1 and 3 but plots with Group 1 for $Na_2O$, $K_2O$, and $P_2O_5$. All three groups were very similar for other oxides measured but not shown here.

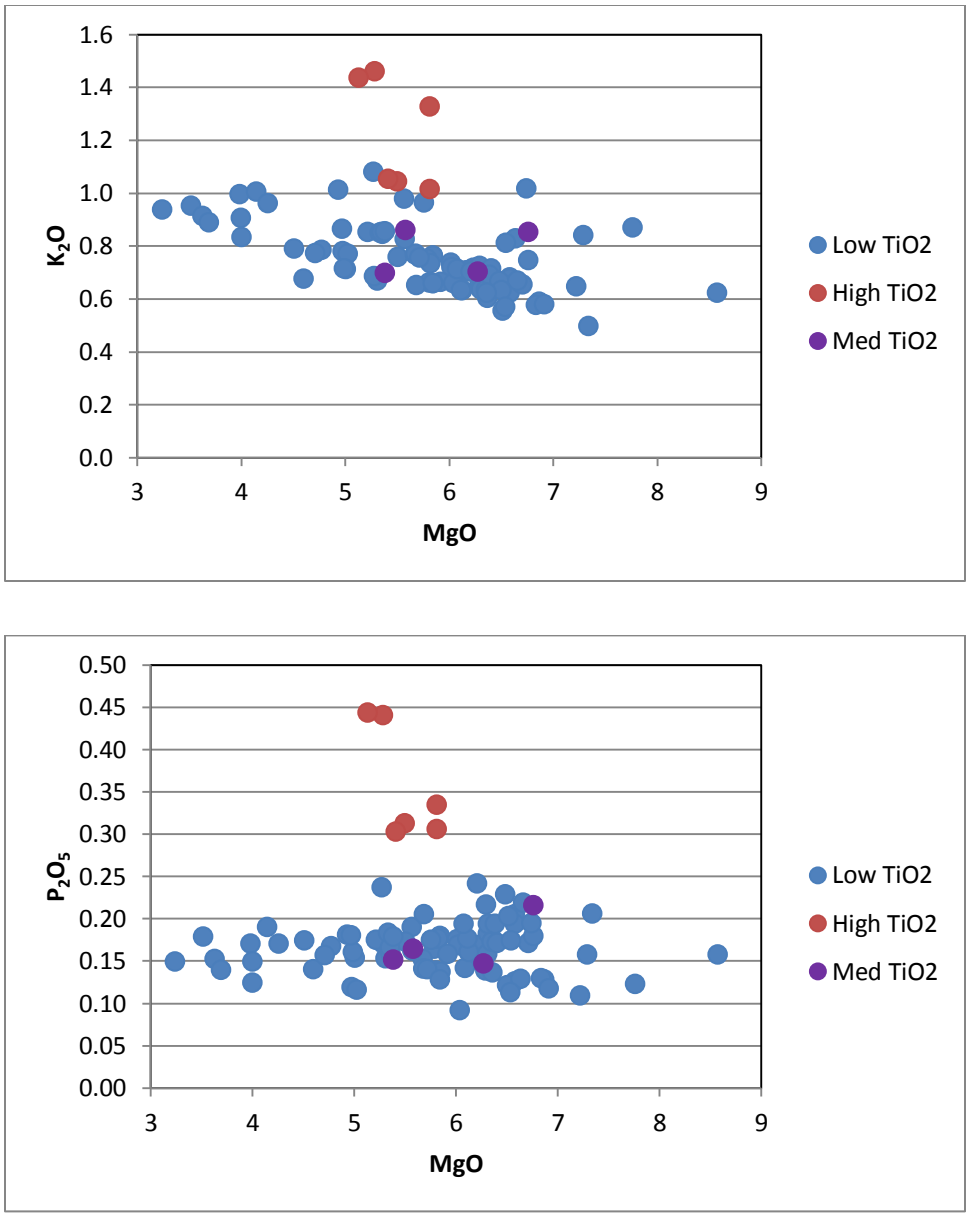


Figure 4.12, continued. Graphs comparing high, medium, and low $TiO_2$ samples for selected oxides vs. MgO. The high $TiO_2$ group is distinct from the other groups due to its elevated concentrations of $TiO_2$, $Na_2O$, $K_2O$, and $P_2O_5$. The medium TiO2 group has an intermediate concentration of $TiO_2$ between Groups 1 and 3 but plots with Group 1 for $Na_2O$, $K_2O$, and $P_2O_5$. All three groups were very similar for other oxides measured but not shown here.

Each volcano has a range of compositions. Due to the different number of samples from the volcanoes and the uneven sample distribution within the volcanoes, it is difficult to tell if some volcanoes have more variation in lava composition than others. For example, Mata Ua and Mata Tolu have the broadest range in composition as they have low to medium and low to high $TiO_2$ samples, respectively. But Mata Ua and Mata Tolu also have significantly more analyzed samples than the other northern Matas.

The following graphs (Figure 4.13) plot the composition of various oxides for the Mata volcanoes versus MgO, as measured by microprobe. There is no overall regional trend for compositional variations between the Matas. For example, samples do not become more enriched or depleted to the north or south. East Mata is generally more evolved than lavas from the other Mata volcanoes. Generally, samples have low concentrations of volatiles.

Individual volcanoes can have a range of glass compositions. For some elements, such as CaO vs. MgO (Figure 4.13), there is an overall trend representing the evolution of the magma as crystals form. With increasing degrees of crystallization, CaO and MgO both decrease. For some elements, such as CaO vs MgO the sample suite appears to follow a liquid line of descent. This would imply that the samples fractionated from the same or similar parent melts. However, examination of other components, such as $TiO_2$ and $K_2O$ shows that this is not the case. There is a range in $TiO_2$ and $K_2O$ concentrations at constant MgO (Figure 4.13). For example, samples from Mata Tolu can vary by over half a weight percent in $TiO_2$ at a constant MgO value. This variation would not be caused by crystallization, as increasing crystallization would cause a decrease in MgO. This variation could be explained by the presence of multiple parent melts with a range in composition. Evolution of the magmas and modeling of crystallization will be discussed further in Chapter 6.

Samples ranges from the different volcanoes generally show overlap for most elements. The major differences in glass compositions observed is not between volcanoes, but between the high, medium, and low $TiO_2$ glasses which can occur at multiple volcanoes. High $TiO_2$ glasses occur at Matas Tolu and Fa. Medium $TiO_2$ glasses occur at Matas Ua and Fitu. Low $TiO_2$ glasses occur at all of the Mata volcanoes except at Mata Fa. Another distinction is the existence of evolved samples, which are probably related to the boninites. These (with the exception of

one sample from West Mata) occur exclusively at East Mata. Note that some volcanoes, such as West Mata (with a total of 49 measured glass samples) are better sampled than others, such as Mata Fa (with a total of only 3 measured glass samples).

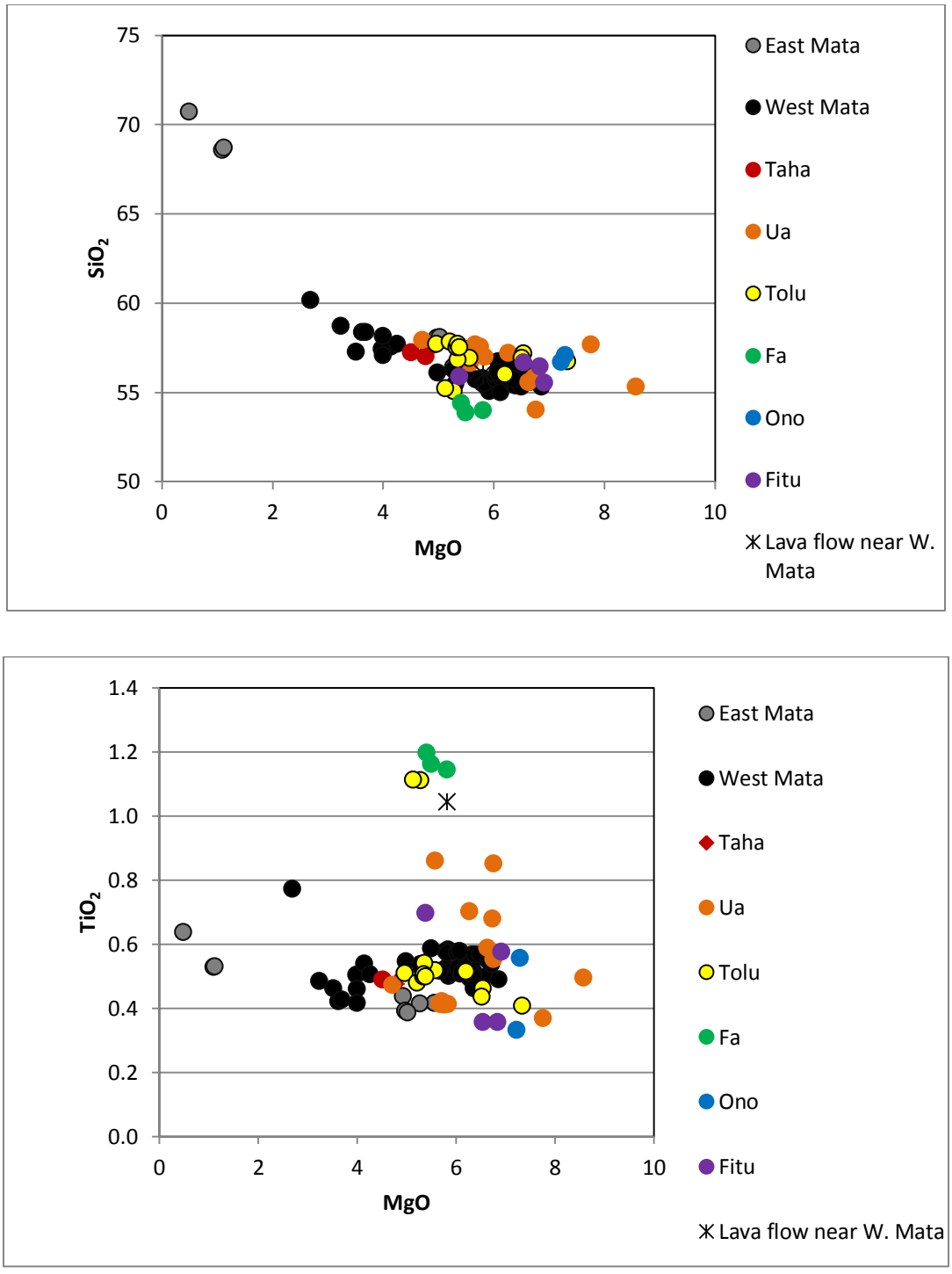


Figure 4.13. Plots of Oxides vs. MgO for all of the Mata volcanoes. Samples were measured by EPMA at UH Manoa by Eric Hellebrand and Sarah Glancy and at the University of Tulsa by Peter Michael. Cl and S were also measured at both universities and F was measured at UT. Volatiles were found to be in low concentrations and are reported in tables but not shown here.

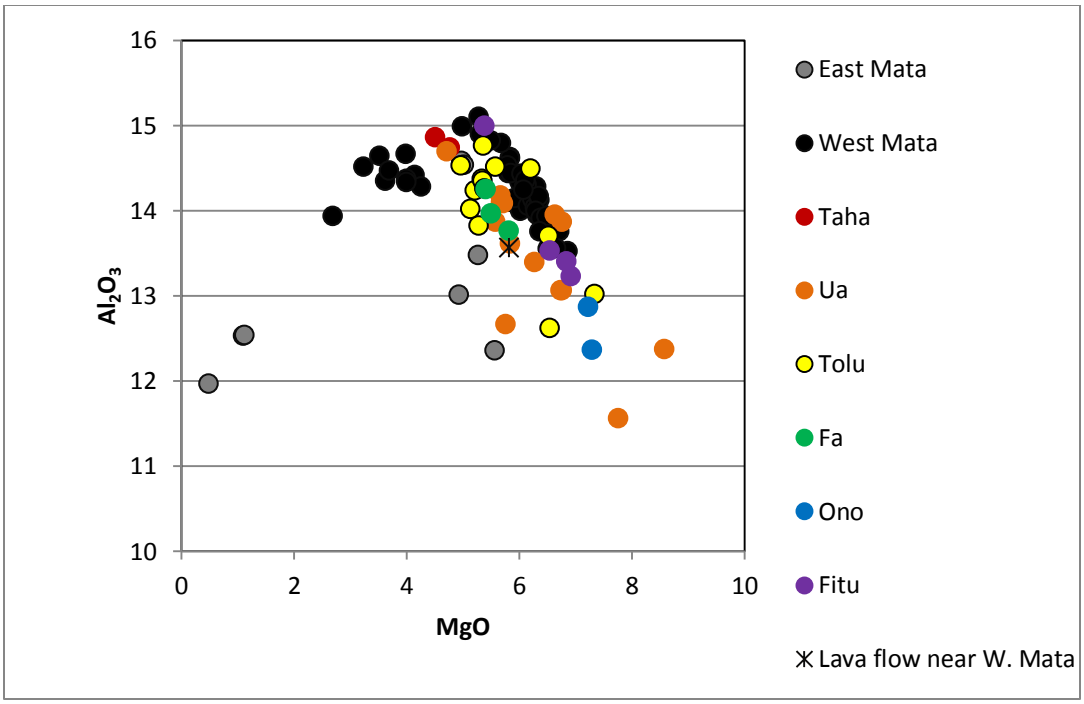


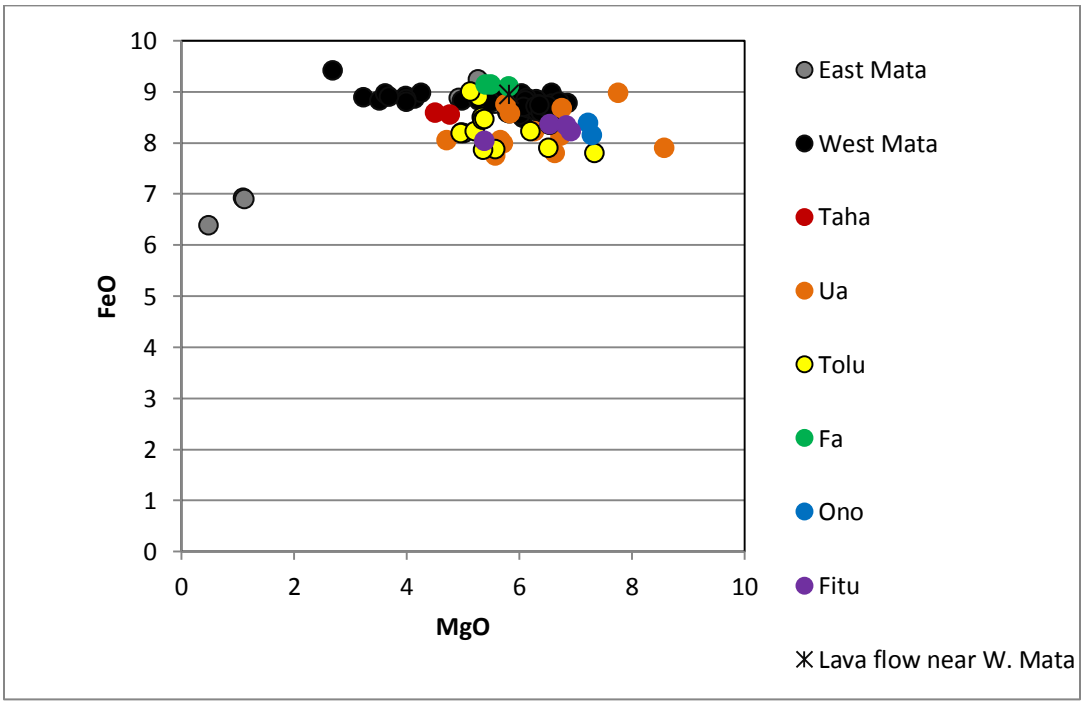


Figure 4.13, continued. Plots of Oxides vs. MgO for all of the Mata volcanoes. Samples were measured by EPMA at UH Manoa by Eric Hellebrand and Sarah Glancy and at the University of Tulsa by Peter Michael. Cl and S were also measured at both universities and F was measured at UT. Volatiles were found to be in low concentrations and are reported in tables but not shown here.

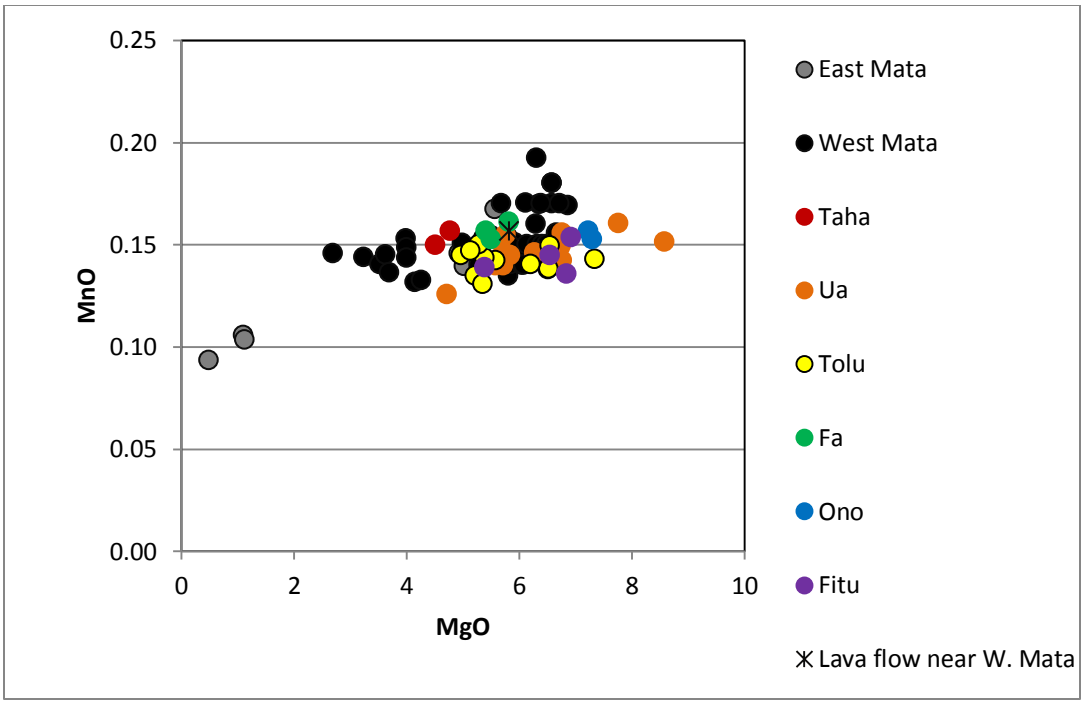


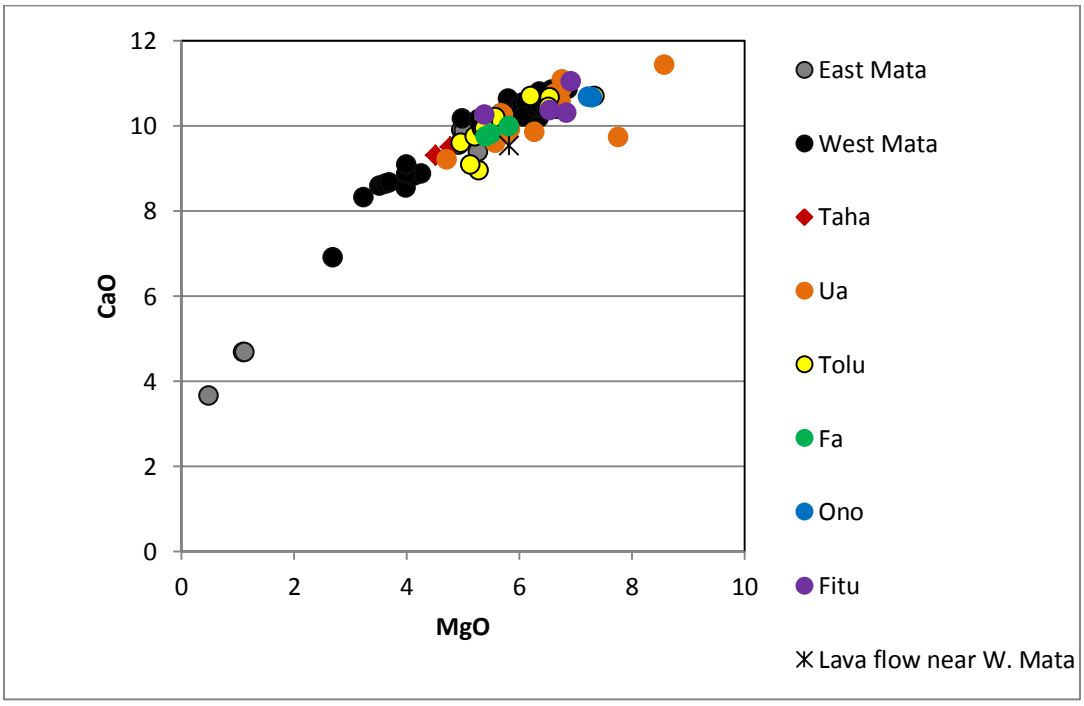


Figure 4.13, continued. Plots of Oxides vs. MgO for all of the Mata volcanoes. Samples were measured by EPMA at UH Manoa by Eric Hellebrand and Sarah Glancy and at the University of Tulsa by Peter Michael. Cl and S were also measured at both universities and F was measured at UT. Volatiles were found to be in low concentrations and are reported in tables but not shown here.

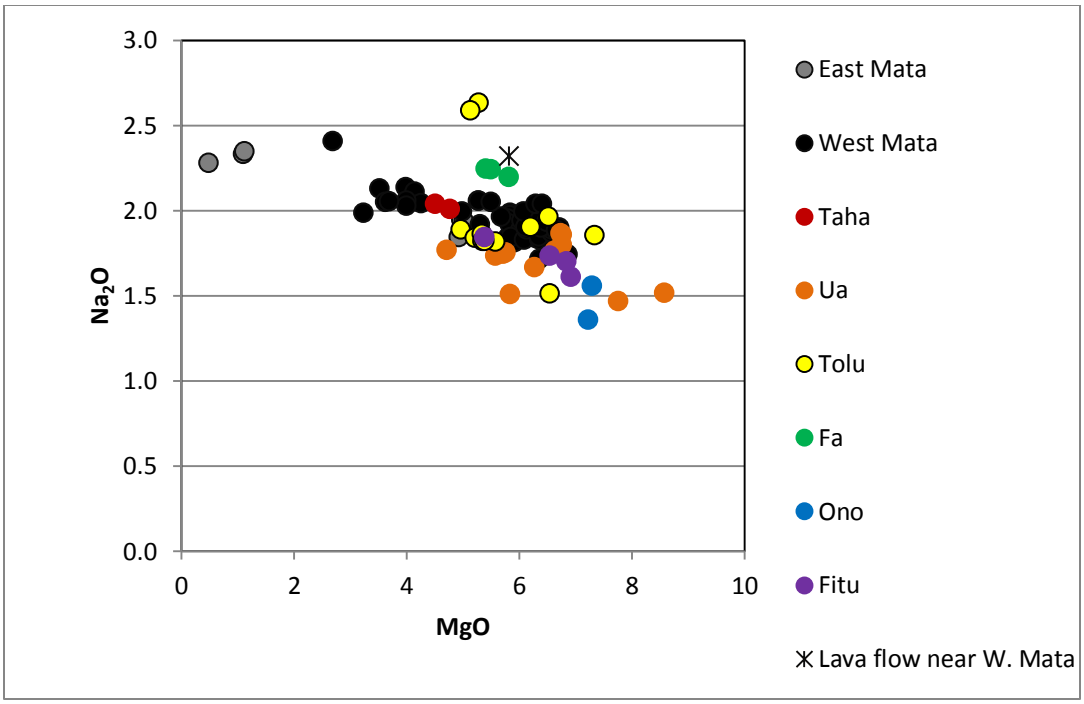


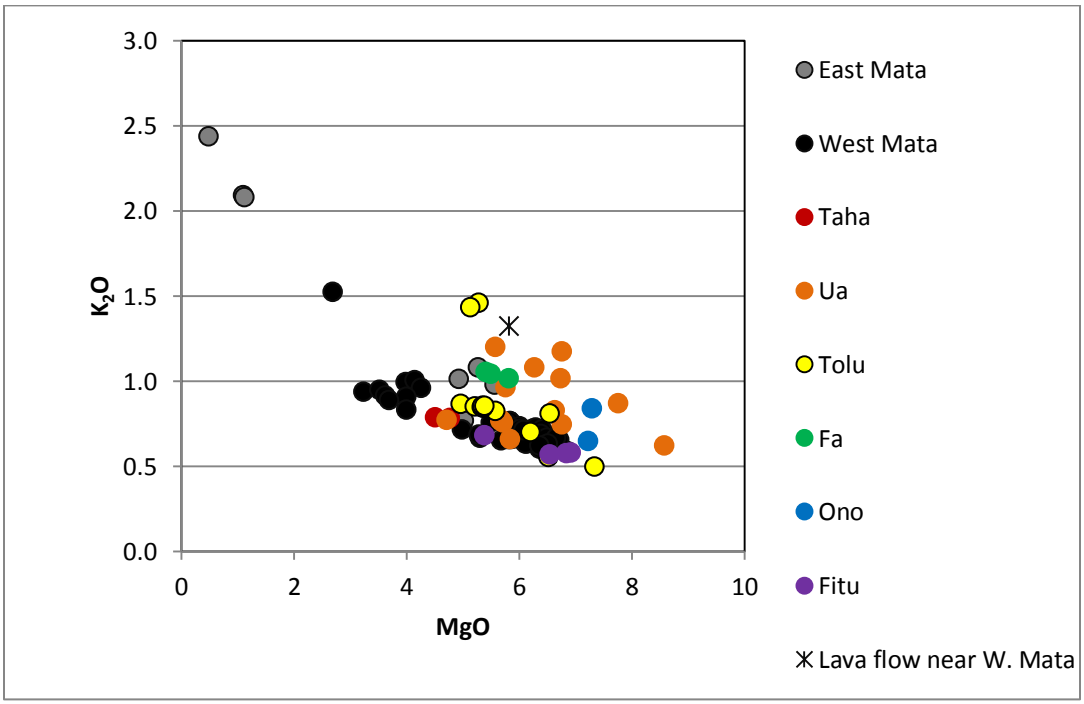


Figure 4.13, continued. Plots of Oxides vs. MgO for all of the Mata volcanoes. Samples were measured by EPMA at UH Manoa by Eric Hellebrand and Sarah Glancy and at the University of Tulsa by Peter Michael. Cl and S were also measured at both universities and F was measured at UT. Volatiles were found to be in low concentrations and are reported in tables but not shown here.

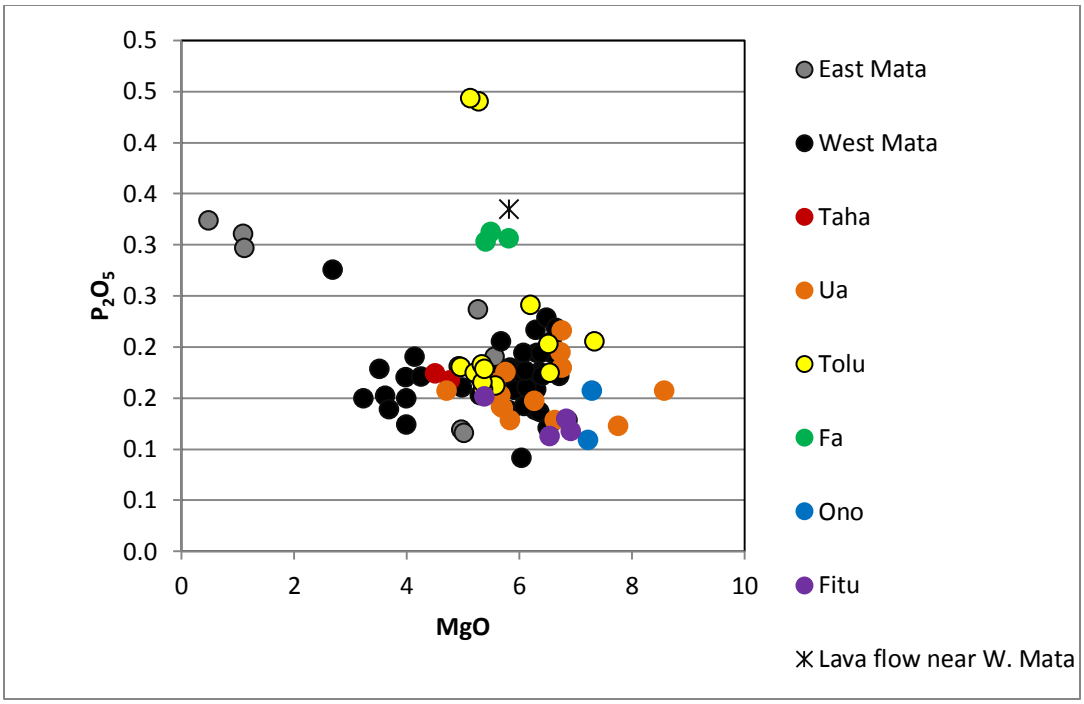


Figure 4.13, continued. Plots of Oxides vs. MgO for all of the Mata volcanoes. Samples were measured by EPMA at UH Manoa by Eric Hellebrand and Sarah Glancy and at the University of Tulsa by Peter Michael. Cl and S were also measured at both universities and F was measured at UT. Volatiles were found to be in low concentrations and are reported in tables but not shown here.

**Lower $SiO_2$, higher MgO samples at West Mata**

A higher SiO2, lower MgO group of samples from West Mata can be observed in both XRF whole rock and microprobe glass data. These samples are not from the new eruption at West Mata. Interestingly, not all older samples fall into this group. While differences between this group and other samples from West Mata can be observed in both XRF whole rock data and microprobe data, the differences are more pronounced in microprobe data. This discussion will be motivated by microprobe data. These samples are: J2-418-R01, J2-418-C02, J2-418-R04, J2-418-R05, J2-420-R01, J2-420-R02, and samples from KM1024 dredge 12.

At first glance, these samples may appear to just be more evolved than other samples, with higher $SiO_2$ and lower MgO. For example, they appear to follow a similar CaO vs. MgO evolution trend to other samples (Figure 4.14). However, they are offset from the other samples from West Mata in $Al_2O_3$ vs. MgO (4.14). This group of samples will be discussed further in Chapters 5-7.

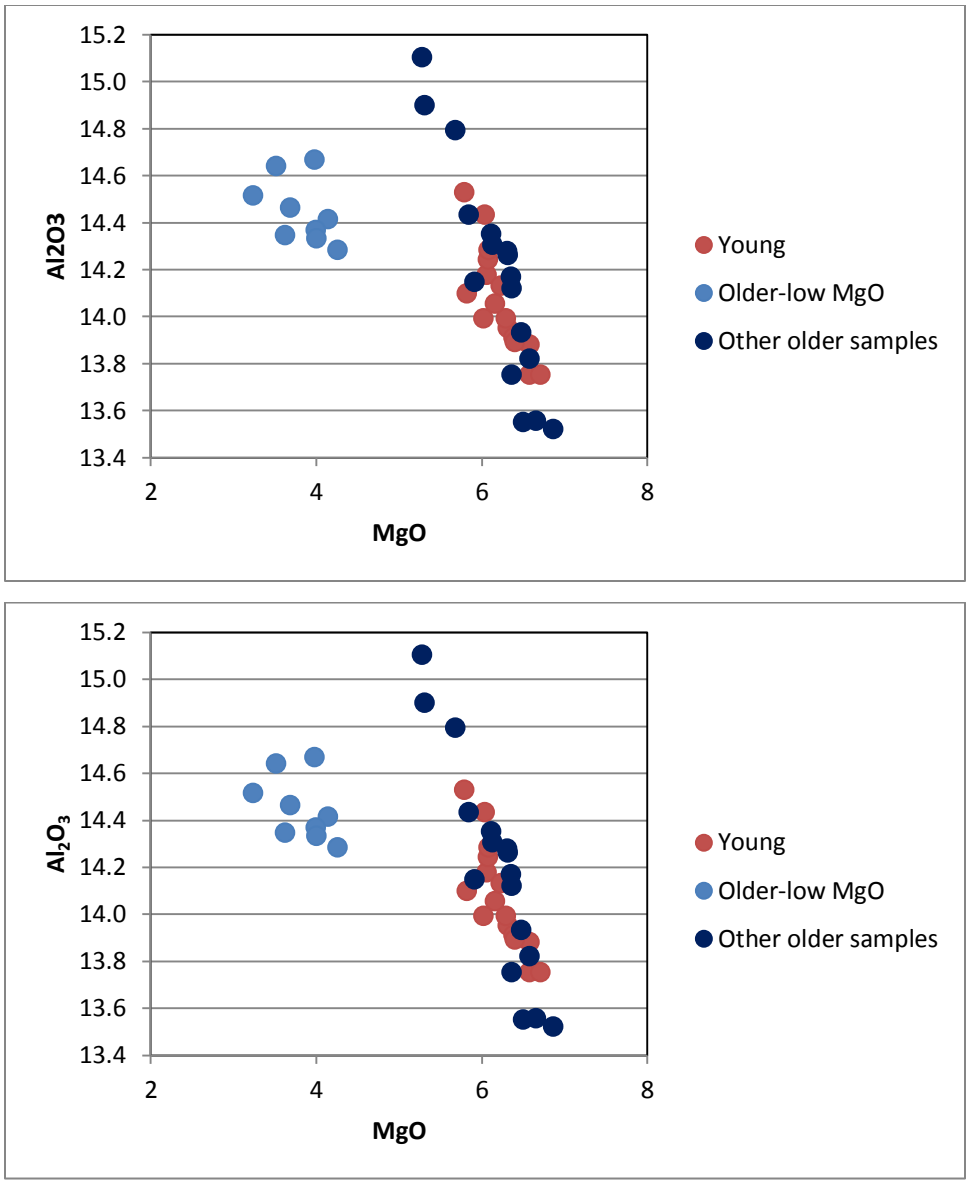


Figure 4.14. Plots of CaO and $Al_2O_3$ vs. MgO for West Mata samples. Many older samples are plot with samples from the new eruption. However a group of older samples with higher $SiO_2$ and lower MgO contents, labeled older-lower MgO, differ compositionally from other samples found at West Mata.

# CHAPTER 5: THERMOMETRY

The temperature of boninite formation is currently debated and previous work has been conducted to estimate temperatures for formation of boninite melts. This chapter will first overview previous work, discuss how temperatures of crystallization were determined as part of this study, and discuss calculated temperatures of crystallization for magmas from the Mata Volcanoes.

Falloon and Danyushevsky's (2000) studied the temperature at which the mantle melts to form boninitic melts. They used a boninitic whole rock composition and experimentally determined that a melt of this composition would form at temperatures as high as 1480º C. Cooper *et al*. (2010) studied differentiated lavas from Volcano A on the Tongan Arc. They believe these magmas started out as boninites. They argue that high mantle temperatures of > 1300 ºC not required at the time of melting to produce the parent melts that differentiated to form these lavas.

Several studies have concentrated on the temperature over which boninite melts crystallize. Van der Laan *et al*. (1989) experimentally studied phase relations as boninites start to crystallize, using boninite samples the Troodos ophiolite, Chichi-jima in the Bonin Islands, and Cape Vogel. The liquidus was found to be at temperatures up to 1268 ºC. Umino and Kushiro's melting experiments on boninites (1989) suggest that crystallization begins at temperatures from 1130 to 1315º C. In a PhD thesis, Acland (1996) used two pyroxene thermometers to calculate temperatures of formation of pyroxene crystals in four boninitic samples. This yielded a range from 1100-1230 ºC. This temperature range is probably generally lower than the maximum experimental temperatures found by Van der Laan *et al*. (1989) and Umino and Kushiro (1989) because it only represents a few samples. These are probably not the first formed crystals and thus may have slightly lower temperatures. Danyushevsky and Sobolev (1996) use olivine liquid thermometry of olivine and homogenized melt inclusions to determine temperatures of crystallization of boninites from the Lau Basin. They report that crystallization occurred below 1300 ºC, but do not report a range or calculated temperatures for individual samples (Danyushevsky and Sobolev, 1996).

The sample set from the Mata Volcanoes studied here provides an opportunity to study the temperature regime of boninite melts using thermometry and fresh, young samples. This work investigates if high temperatures were present during the evolution of the melts from the Mata Volcanoes. It compares calculated temperatures for boninites and non-boninites (both evolved samples and high $TiO_2$ samples) to see if the boninite samples differ from the others in their temperatures of formation. It examines if there are any regional temperature gradients between the Mata Volcanoes. Liquid, olivine-liquid, orthopyroxene-liquid, clinopyroxene-liquid, clinopyroxene-only, and two pyroxene thermometers are used to study the temperature regime of the Mata Volcanoes.

## Determining the $Fe^{2+}$ and $Fe^{3+}$ Content of the Melt

To apply a thermometer, phases must be in equilibrium with each other. For example, when using an olivine-liquid thermometer, olivine and the liquid must be in equilibrium with each other. Olivine rims should be in equilibrium with the melt because they would have formed from the melt just before eruption. There is no visual evidence from analysis with a petrographic microscope or with the microprobe that olivine rims in the sample set are not in equilibrium with the melt (Chapter Three).

However, olivine rims do not appear to be in equilibrium using Fe-Mg exchange tests, assuming all iron to be present as FeO. As shown in Figure 5.1, olivine rims and the liquid plot off the equilibrium line when the liquid Mg# is calculated, assuming that all iron is present in the melt as $Fe^{2+}$ (Equation 4.1). To show the effect of the concentration of $Fe^{2+}$ in the melt on the melt Mg#, I have plotted the olivine Mg# compared to the melt Mg# calculated by varying the amount of $Fe^{2+}$ in the melt for one sample, J2-418-R01 (Figure 5.2). This sample was chosen because it has the highest calculated percentage of $Fe^{3+}$ in the melt (Table 5.1).

Because some iron is present as $Fe_2O_3$, the relative percentages of $Fe^{2+}$ and $Fe^{3+}$ in the melt must be determined so that the thermometers can be accurately applied. To do so, I assumed that the average olivine rim composition for each sample was in equilibrium with its melt. I used the Fe-Mg exchange coefficient between olivine and melt of 0.30 (Roeder and Emslie, 1970) to calculate the percentage of $Fe^{2+}$ and corresponding $Fe^{3+}$ in the melt. This information can be used to calculate the Mg# of the melt. Keller *et al.*(2008) also used this

method to determine the percentage of $Fe^{2+}$ and $Fe^{3+}$ in lavas from the Fonualei Spreading Center and the Mangatolu Triple Junction in the Lau Basin. Table 5.1 and Figure 5.3 present the results of these calculations. The amount of $Fe^{2+}$ in the melt varies significantly, from 38.2 to 73.7%.

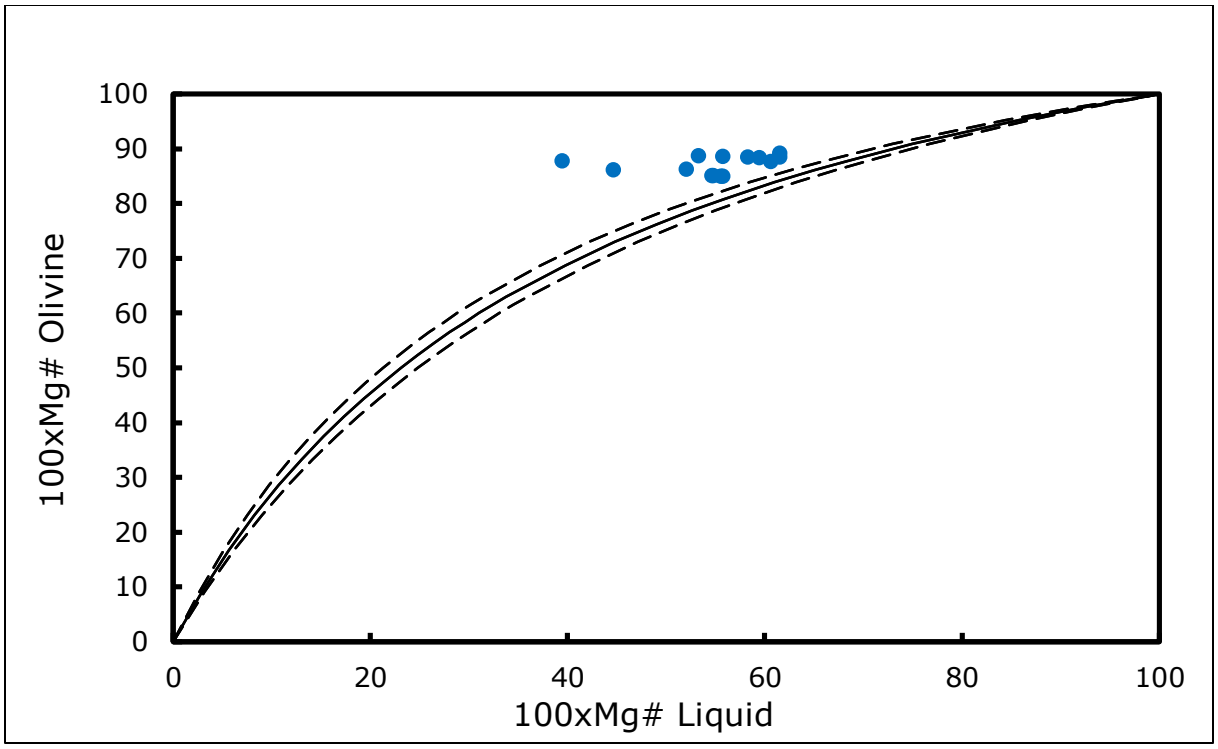


Figure 5.1. Olivine-liquid equilibrium when the Mg# of the liquid is calculated assuming that all iron is present as FeO (Equation 4.1). Olivine compositions plotted here are averages for olivine rims for 14 individual samples. The olivine rims should be in equilibrium with the melt, but plot off the equilibrium line (solid line), suggesting that some iron, but not all iron, is present as $Fe_2O_3$ in the melt. The equilibrium line is from Roeder and Emslie (1970). The dashed lines represent error bounds of ± 0.03.

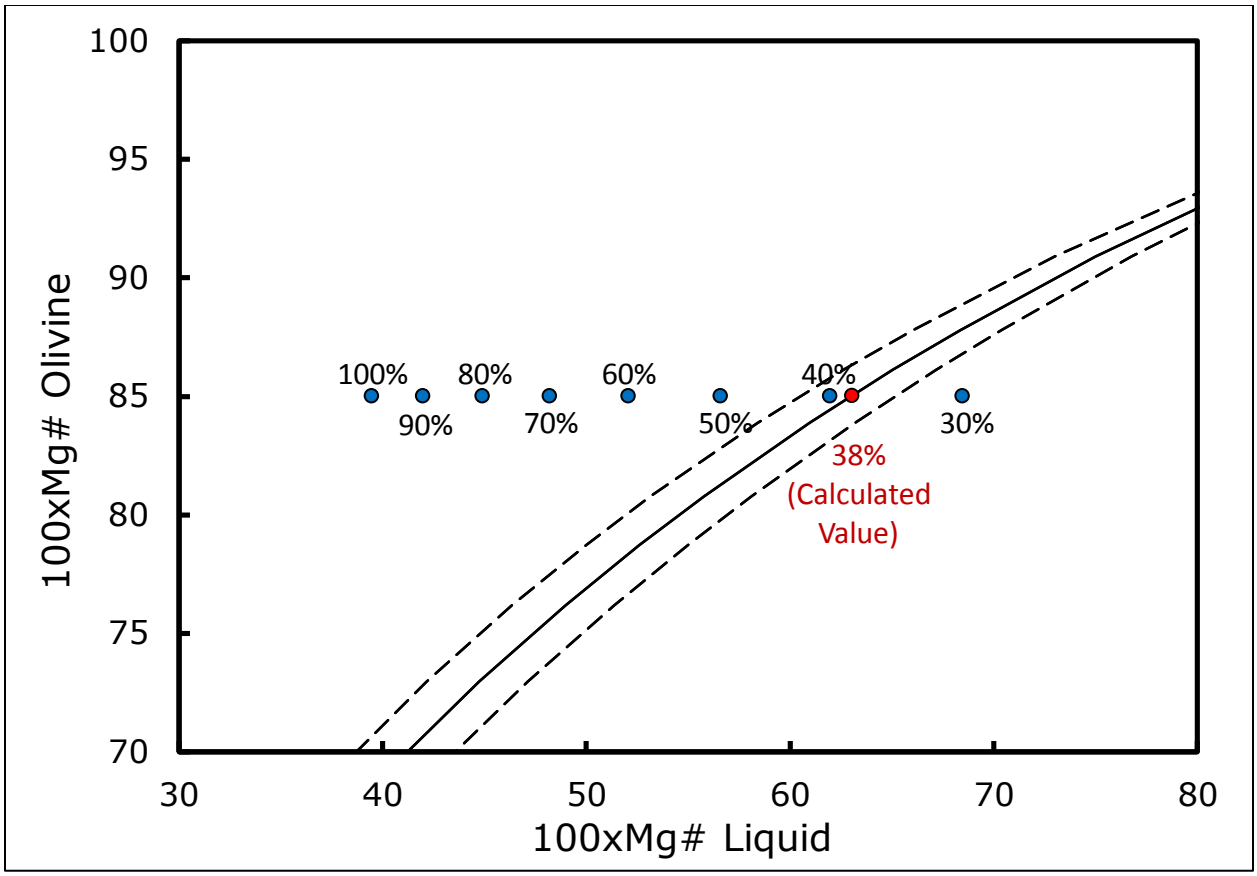


Figure 5.2. Olivine fosterite content vs the Mg# of the liquid calculated for various amounts of $Fe^{2+}$ present in the melt for sample J2-418-R01 (Equation 4.1). This sample was chosen because it had the lowest calculated $Fe^{2+}$ in the melt. The calculated value based on equilibrium between the olivine rims and the melt is shown in red, located on the equilibrium line (solid line). The equilibrium line is from Roeder and Emslie (1970). The dashed lines represent error bounds of ± 0.03. The atomic percentage of $Fe^{2+}$ relative to total Fe present in the melt is systematically varied from 100% to 30%, shown in blue. As the concentration of $Fe^{3+}$ in the melt increases, the concentration of $Fe^{2+}$ in the melt decreases, which increases the Mg# of the liquid.

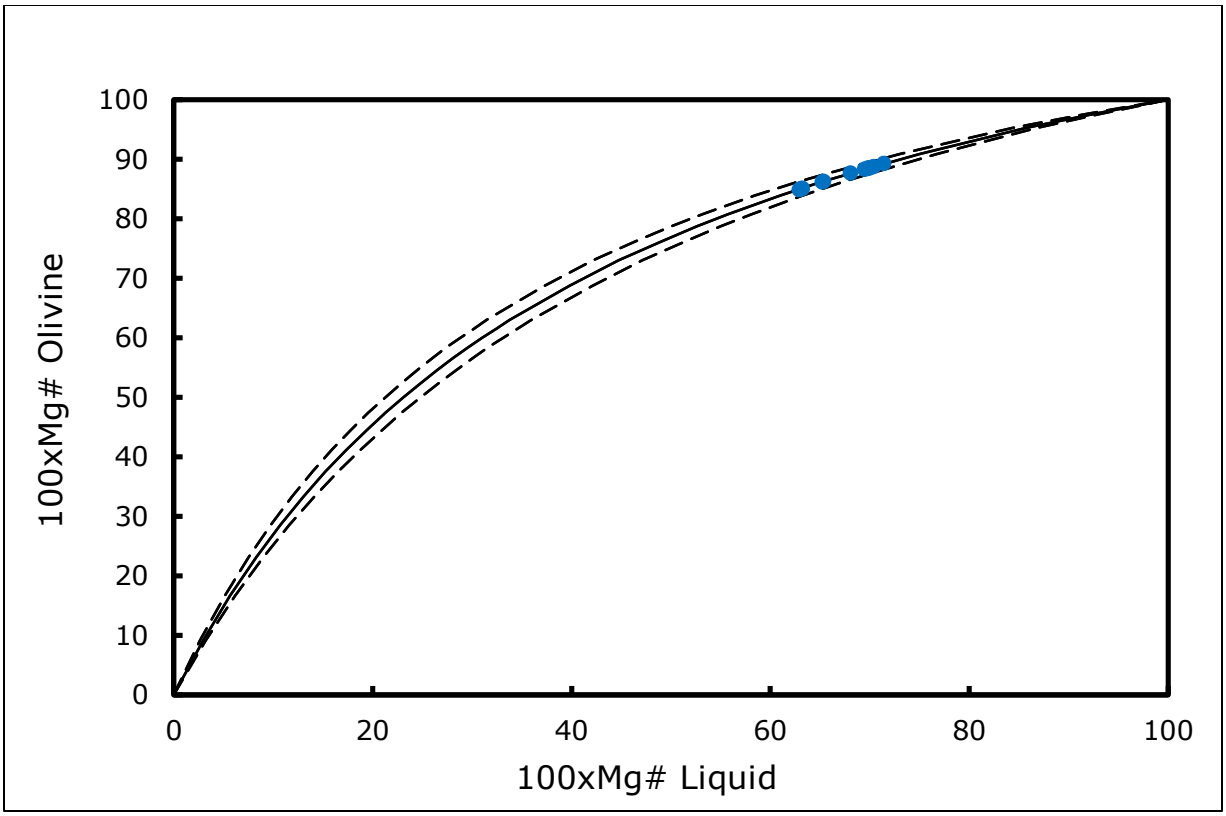


Figure 5.3. Olivine-liquid equilibrium when the Mg# of the liquid is calculated using calculated concentrations of $Fe^{2+}$ in the melt (Equation 4.1). Concentrations of $Fe^{2+}$ in the melt are calculated based on equilibrium between olivine rims and the melt. Olivine compositions plotted here are averages for olivine rims for 14 individual samples. Now the olivine rims plot on the equilibrium line (solid line), as compared to Figure 5.1. The equilibrium line is from Roeder and Emslie (1970). The dashed lines represent error bounds of ± 0.03.

Table 5.1. $Fe^{2+}$ and $Fe^{3+}$ content of the melt, Mg# of the melt, and oxygen fugacity of the melt.

| Location | Sample | $Fe^{2+}$ (%) | $Fe^{3+}$ (%) | Mg# | $fO_2$ |
|---|---|---|---|---|---|
| West Mata | J2-413-R04 | 73.6 | 26.4 | 0.63 | + 1.8 |
| West Mata | J2-413-R13 | 70.5 | 29.5 | 0.63 | + 2.1 |
| West Mata | J2-418-R01 | 38.2 | 61.8 | 0.63 | + 4.8 |
| West Mata | J2-418-R18 | 73.7 | 26.3 | 0.63 | + 1.8 |
| West Mata | J2-420-R02 | 43.0 | 57.0 | 0.65 | + 4.4 |
| West Mata | J2-420-R17 | 69.9 | 30.1 | 0.63 | + 2.1 |
| Ua | KM1024 D18-R01 | 53.9 | 46.1 | 0.70 | + 3.6 |
| Tolu | KM1024 D20-R01 | 57.3 | 42.7 | 0.65 | + 3.3 |
| Fa | KM1024 D21-R02 | 48.0 | 52.0 | 0.70 | + 3.9 |
| Ono | KM1024 D22-R01 (Ol-D) | 68.9 | 31.1 | 0.70 | + 2.2 |
| Ono | KM1024 D22-R01 (Ol-L) | 64.0 | 36.0 | 0.71 | + 2.7 |
| Ono | KM1024 D22-R02 | 72.1 | 27.9 | 0.68 | + 2.0 |
| Fitu | KM1024 D23-R01 | 60.5 | 39.5 | 0.70 | + 2.0 |
| Fitu | KM1024 D23-R04 | 64.2 | 35.8 | 0.70 | + 2.7 |

The $Fe^{2+}$ and $Fe^{3+}$ content of the melt and Mg# of the melt are calculated based on equilibrium between the average olivine rim composition and the melt (Roeder and Emslie, 1970). The oxygen fugacity ($fO_2$) of the melt is calculated using the equation of Kilinc *et al.* (1983) and presented relative to the QFM buffer (Frost, 1991)

## Oxygen Fugacity of the Mata Magmas

The concentration of a melt, including the percentages of $Fe^{2+}$ and $Fe^{3+}$, can be used to calculate the oxygen fugacity expected for the melt. There are many studies relating melt composition and the concentration of $Fe^{2+}$ and $Fe^{3+}$ in the melt to oxygen fugacity. Nikolaev *et al.* (1996) reviews several equations from different studies that can be used to relate the measured composition of volcanic glass to its expected oxygen fugacity. Keller *et al.* (2008) calculated the $Fe^{2+}$ and $Fe^{3+}$ concentrations in the melt using olivine-liquid equilibrium and used the work of Kilinc *et al.* (1983) to calculate the expected oxygen fugacity of volcanic glass from the Lau basin. Using a similar approach, this project also uses the work of Kilinc *et al.* (1983) to calculate the expected oxygen fugacity of volcanic glass from the Mata Volcanoes using measured concentrations by EPMA microprobe glass analysis and calculated $Fe^{2+}$ and $Fe^{3+}$ concentrations based on olivine rim-liquid equilibrium, as discussed in the previous section.

Table 5.1 and Figure 5.4 present the results of these calculations relative to the QFM buffer (Frost, 1991). Overall the calculated oxygen fugacity values of these lavas range from QFM + 1.8 to QFM + 4.8. Keller *et al.* (2008) found oxygen fugacity values of QFM + 0.5 for the Fonualei Spreading Center and QFM - 0.5 for the Mangatolu Triple Junction in the Lau Basin. My work results in more oxidizing values than those found by Keller *et al.* (2008) for other samples from the Lau Basin using the same methods.

The two largest values calculated in this study for the Mata Volcanoes are QFM + 4.4 and 4.8, from samples from the high $SiO_2$, low MgO group from an older eruption or eruptions at West Mata. The range for the other West Mata samples is QFM + 1.8 to 2.1. Thus, the measured samples from the older eruption(s) at West Mata are more oxidizing than the samples from the new eruption. Analysis of additional samples could further investigate this relationship. The range for the Northern Matas is QFM + 2.0 to 3.9.

The measured Northern Mata samples are more oxidizing than the sample from the new eruption at West Mata, but less oxidizing than the two older West Mata samples that were analyzed. Interestingly, Mata Fa, the only non-boninite sample represented by this analysis, has the most oxidizing calculated oxygen fugacity, QFM + 3.9, of the Northern Mata samples. Analysis of additional samples would help further investigate these trends.

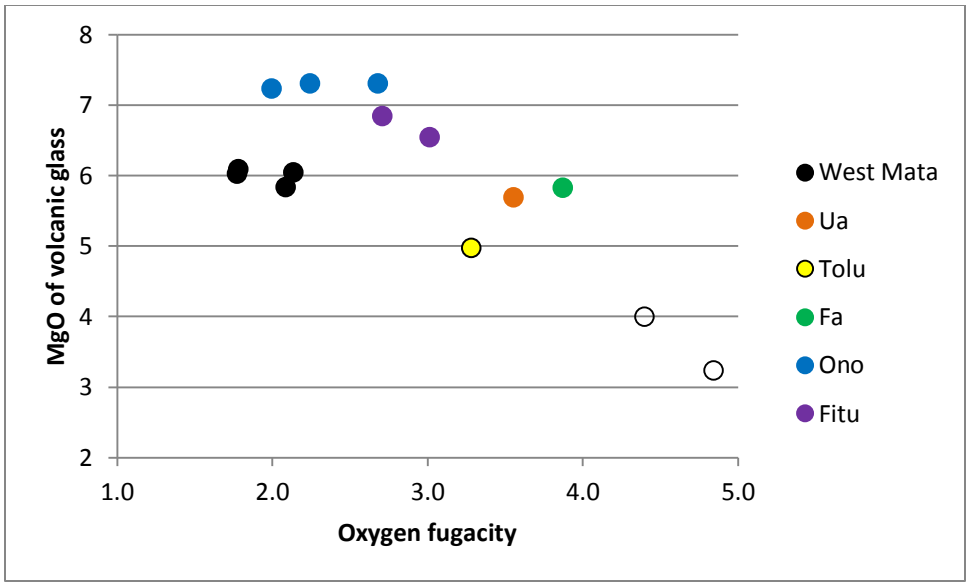


Figure 5.4 Measured MgO of volcanic glass vs. calculated oxygen fugacity of the glass relative to the QFM buffer. Closed black circles represent samples from the new eruption of West Mata. Open black circles represent higher $SiO_2$, lower MgO older samples from West Mata.

Danyushevsky and Sobolev (1995) measured homogenized melt inclusions in olivine and orthopyroxene to determine primitive melt compositions of boninites from the Lau Basin. They used melt-spinel pairs to determine the $Fe^{2+}/Fe^{3+}$ ratio in the melt. They then calculated the oxygen fugacity of the melt. They found a range of NNO +0 to NNO +1 for these boninites. For comparison, the oxygen fugacity values calculated in this study correspond to a range of NNO +1.07 to +4.13. Excluding the two higher $SiO_2$, older West Mata samples, the range is NNO +1.07 to +3.17.

There are several possible explanations for the discrepancy between higher values for the Mata Volcanoes when compared to previous work on boninites in the Lau Basin. One possibility is that the difference between the calculated values in the two studies represents a true difference in oxygen fugacity under which the samples formed. However, the cause of this difference is unclear.

There are other possible reasons why these calculated values could be different. One possible explanation is that this study's calculation of $Fe^{2+}/Fe^{3+}$ ratios in the melt based on olivine rim-liquid exchange did not yield accurate values for the melt. I used a distribution coefficient from Roeder and Emslie (1970) for these calculations. Perhaps this distribution coefficient was not representative of the system and overestimated the $Fe^{3+}$ concentration in the

melt, yielding different oxygen fugacity values. Furthermore, Nikolaev *et al.* (1996) caution that using these equations for calculating the oxygen fugacity for glass compositions other than basalt could yield inaccurate results. The use of different equations to calculate oxygen fugacity is one possible cause of a discrepancy.

## Methods and Equations

This section discusses the equations and assumptions used to apply liquid, mineral-liquid, and mineral thermometers in this project. All equations, uncertainties, and equation notations are from Putirka (2008). All negative components are set to zero during calculations. For all thermometers involving liquid components where the Mg# of the melt or the ratio of $Fe^{2+}$ and $Fe^{3+}$ in the melt were factors, calculated values based on olivine-liquid equilibria were used (Table 5.1). Only the first liquid thermometer (Equation 5.1), the clinopyroxene-only thermometer (Equation 5.7), and the two pyroxene thermometers (Equation 5.9 and 5.10) do not require Mg# or the ratio of $Fe^{2+}/Fe^{3+}$. The remaining thermometers that require information about the Mg# of the melt or the ratio of $Fe^{2+}$ and $Fe^{3+}$ in the melt can only be applied to samples where olivine and liquid were measured and thus where data was available to make these calculations. Some thermometers require knowledge of the water content of the melt (Equations 5.2-5.6) and the pressure of formation of the crystals (Equations 5.3-5.7, 5.9-5.10). Water contents and pressure are chosen for the thermometers based on best approximation MELTS runs (Chapter Seven). The best approximation conditions found for pressure and/or water dependent models in this chapter were pressures of 500 and 1000 bars and water contents of 1.7, 2, and 3 wt%. Similar temperatures were found using these two different pressures. Reported temperatures in this chapter were calculated using a pressure of 500 bars and a water content of 2 wt%.

### Liquid thermometers

The simplest type of liquid thermometer is based solely on the MgO content in weight percent of the liquid and has an uncertainty of 71 $^0$C:

$$T(^0C) = 26.3MgO + 994.4\ ^0C$$

Equation 5.1

The two additional liquid thermometers add additional components, which are also entered in weight percent except for Mg#. The first is pressure independent and has an uncertainty of 51 $^0$C:

$$T\ (^0C) = 754 + 190.6(Mg\#) + 25.52\left(MgO^{liq}\right) + 9.585\left(FeO^{liq}\right) + 14.85\left((Na_2O + K_2O)^{liq}\right) - 9.176(H_2O^{liq})$$

Equation 5.2

The final liquid thermometer used in this study is pressure dependent and has an uncertainty of 60 $^0$C:

$$T\ (^0C) = 815.3 + 265.5(Mg\#) + 15.37\left(MgO^{liq}\right) + 8.61\left(FeO^{liq}\right) + 6.646\left((Na_2O + K_2O)^{liq}\right) + 39.16\left(P(GPa)\right) - 12.83(H_2O^{liq})$$

Equation 5.3

**Olivine-Liquid thermometer**

Putirka et al. (2007)'s olivine-liquid thermometer is used in this study as it is best for hydrous systems. The melts in this study have a significant amount of water present (Chapter 6). The uncertainty is at least 27 °C. For a detailed explanation of all of the components in this and following equations and how to calculate them, see Putirka et al. (2007).

$$T(^0C) = (15294.6 + 1318.8P(GPa) + 2.4834\left(P(GPa)\right)^2)/(8.048 + 2.8352LnD_{Mg}^{\frac{ol}{liq}} + 2.097\ln(1.5C_{NM}^{L}) + 2.575\ln\left(3C_{SiO_2}^{liq}\right) - 1.41NF + 0.222H_2O^{liq} + 0.5P(GPa))$$

Equation 5.4

**Orthopyroxene-Liquid thermometer**

Putirka (2008) provides an orthopyroxene-liquid thermometer which calculates temperature to ±26 $^0$C for calibration data and to ±41 $^0$C for test data. For this and the following equations, notation $X_a^b$ represents the mole fraction of a component in phase b.

$$10^4/T(^0C) = 4.07 - 0.329P(GPa) + 0.12H_2O^{liq} + 0.567ln(X^{opx}_{Fm_2Si_2O_6}/(X^{liq}_{SiO_2})^2(X^{liq}_{FeO} + X^{liq}_{MnO} + X^{liq}_{MgO})^2) - 3.06X^{liq}_{MgO} - 6.17X^{liq}_{KO_{0.5}} + 1.89Mg\#^{liq} + 2.57X^{opx}_{Fe}$$

Equation 5.5

**Clinopyroxene-Liquid thermometer**

Putirka (2008) provides a clinopyroxene-liquid thermometer which has an uncertainty of 32-50 $^0$C:

$$10^4/T(^0C) = 7.53 - 0.14\ln\left(\frac{X^{cpx}_{Jd}X^{liq}_{CaO}X^{liq}_{Fm}}{X^{cpx}_{DiHd}X^{liq}_{Na}X^{liq}_{Al}}\right) + 0.007H_2O^{liq} - 14.9(X^{liq}_{CaO}X^{liq}_{SiO_2}) - 0.08\ln(X^{liq}_{TiO_2}) - 3.62(X^{liq}_{NaO_{1.5}} + X^{liq}_{KO_{0.5}}) - 1.1Mg\#^{liq} - 0.18\ln(X^{cpx}_{EnFs}) - 0.027P(kbar)$$

Equation 5.6

**Clinopyroxene only thermometer**

Putirka (2008) provides a clinopyroxene only thermometer but does not state the uncertainty of this thermometer. The advantage to the clinopyroxene only thermometer is that it does not require knowledge of the corresponding melt content and thus avoids the problems of estimating the $Fe^{2+}$ and $Fe^{3+}$ content of the melt and estimating more primitive melt contents in equilibrium with pyroxene cores. Thus, temperatures can be estimated from clinopyroxene cores that are not in equilibrium with the glass as measured by microprobe in this study.

$$T(K) = \frac{93100 + 544P(kbar)}{61.1 + 36.6X^{cpx}_{Ti} + 10.9X^{cpx}_{Fe} - 0.95(X^{cpx}_{Cr} + X^{cpx}_{Na} + X^{cpx}_{K}) + 0.395(\ln(a^{cpx}_{En}))^2}$$

Equation 5.7

**Two pyroxene thermometer**

Putirka provides two clinopyroxene-orthopyroxene thermometers with unspecified uncertainties. The advantage of clinopyroxene - orthopyroxene thermometry is that it does not require knowledge of the composition of the melt that would be in equilibrium with pyroxene cores. To use these thermometers, it was first determined if the pyroxene crystals were in equilibrium with each other using Equation 5.7, which is based on the Fe and Mg exchange between orthopyroxene and clinopyroxene (Putirka, 2008).

$$K_{\mathrm{D}}(Fe-Mg)^{cpx-opx}=\frac{\frac{X_{Fe}^{cpx}}{X_{Mg}^{cpx}}}{\frac{X_{Fe}^{cpx}}{X_{Mg}^{cpx}}}=1.09\pm0.14$$

Equation 5.8

By definition, if the calculated $K_D$ is within 1.09 $\pm$ 0.14, the two pyroxenes are in equilibrium with each other and the thermometers and barometers can be applied.

If the pyroxenes were in equilibrium with each other, the following two equations were used to determine their temperature of formation. The first model, shown below as Equation 5.9, uses Putirka's (2008) calibration based on pyroxene crystals with a variety of Mg#'s:

$$\frac{10^4}{T(^\circ C)}=11.2-1.96\ln\left(\frac{X_{EnFs}^{cpx}}{X_{EnFs}^{opx}}\right)-3.3\left(X_{Ca}^{cpx}\right)-25.8\left(X_{CrCaTs}^{cpx}\right)+33.2\left(X_{Mn}^{opx}\right)-23.6\left(X_{Na}^{opx}\right)$$
$$-2.08\left(X_{En}^{opx}\right)-8.33\left(X_{Di}^{opx}\right)-0.05P(kbar)$$

Equation 5.9

Putirka (2008) provides an additional equation to calculate temperature based on a regression using data only from experiments where $Mg\#^{cpx} > 0.75$ (Equation 5.10).

$$\frac{10^4}{T(°C)} = 13.4 - 3.4\ln\left(\frac{X_{EnFs}^{cpx}}{X_{EnFs}^{opx}}\right) + 5.59\ln\left(X_{Mg}^{cpx}\right) - 8.8(Mg\#^{cpx}) + 23.85\left(X_{Mn}^{opx}\right) + 6.48\left(X_{FmAl_2SiO_6}^{opx}\right) - 2.38\left(X_{Di}^{cpx}\right) - 0.044P(kbar)$$

Equation 5.10

Pyroxenes in this study's samples tend to have very complicated zoning patterns (Chapter 3). As pyroxene crystals varied significantly, pyroxene intergrowths were only used for these calculations. Pyroxene intergrowths were observed and measured in East Mata, West Mata, Mata Ua, Mata Tolu, and Mata Fitu. Many pyroxene intergrowths were not in equilibrium with each other, using the test for equilibrium from Putirka (2008) (Equation 5.8). Pyroxene intergrowths in equilibrium were found at East Mata, West Mata, Mata Ua, and Mata Tolu. For those that were in equilibrium, equilibrium was often very localized. For example, often only the points closest to the grain boundary were in equilibrium with each other. The following images show examples of pyroxene intergrowths used for these calculations (Figure 5.5).

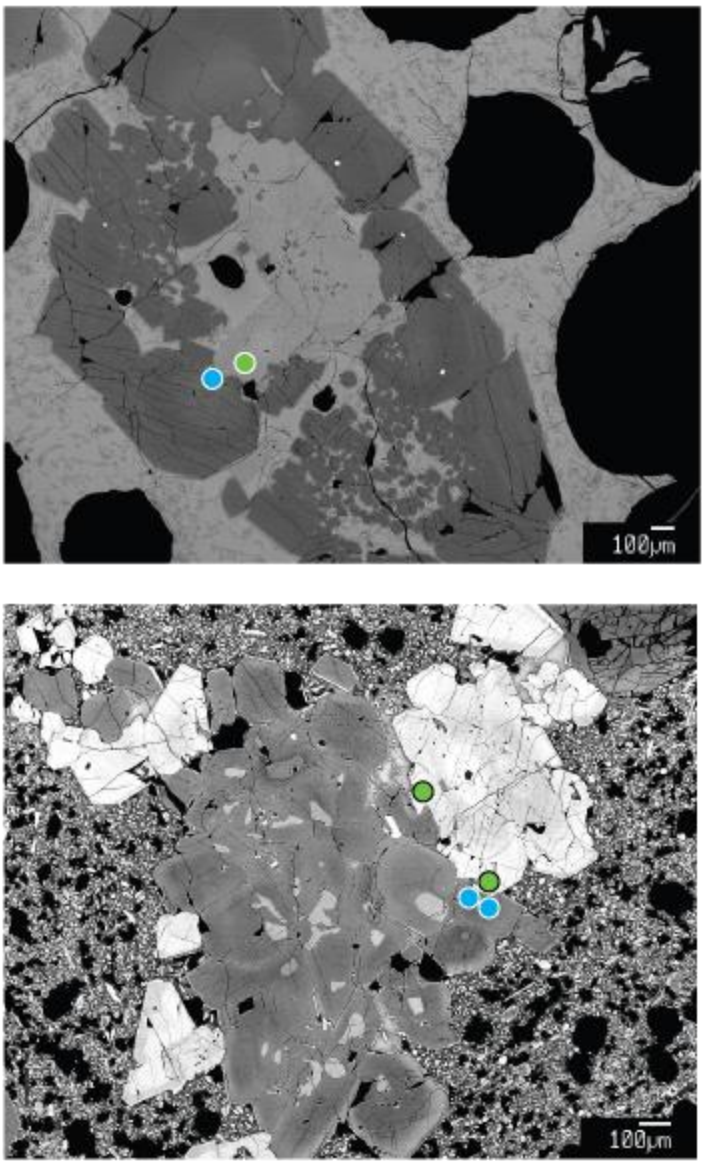


Figure 5.5. Examples of pyroxene intergrowths from West Mata used for two pyroxene thermometry. The top image shows an example of a relatively simple pyroxene intergrowth, J2-420-R17 pyroxene 5. The lighter grey clinopyroxene is partially surrounded by a darker grey orthopyroxene. Calculations were made using the green point for the clinopyroxene composition and the blue point for the orthopyroxene composition. The lower image shows a more complicated intergrowth, J2-420-R02 pyroxene 5. The white to light grey clinopyroxene crystals are intergrown with medium to dark grey orthopyroxene crystals with anhedral light to medium grey olivine inclusions in the orthopyroxene. Calculations were made using an average of the two green points for the clinopyroxene composition and an average of the two blue points as an orthopyroxene composition. Points were measured with a ten micron beam diameter. Dots are enlarged for clarity.

## Data Quality and Uncertainty

### Effect of variation in mineral rim content

To utilize mineral-liquid thermometers in this study, it is assumed that the average mineral rim composition is in equilibrium with the melt. Depending on where the measurement is taken, for example closer or farther from the rim, compositional variation can be introduced into such an average. To study this variation and determine its effect on calculated temperatures, all rim points were entered into the thermometer for each sample. The corresponding temperatures were averaged and the standard deviation was calculated. For the three mineral-liquid thermometers, the resulting deviations range from less than 1 to 32° C. Thus, in most cases, the uncertainty in the thermometers is greater than the deviation resulting from compositional differences.

### Effect of varying the amount of $Fe^{2+}$ in the melt and the Mg# of the melt

All liquid and mineral-liquid thermometers that require calculation of the Mg# of the melt are impacted by the amount of $Fe^{2+}$ in the melt because $Fe^{2+}$ is a variable in calculating the Mg# of the melt. As measuring the amount of $Fe^{2+}$ in the melt is beyond the scope of this thesis, I calculated the predicted amount of $Fe^{2+}$ in the melt based on the assumed equilibrium between the melt and the average olivine rims in a sample. To show the effect of this calculation on the melt Mg#, the olivine Mg# is plotted compared to the melt Mg# calculated by varying the amount of $Fe^{2+}$ in the melt for one sample, J2-418-R01 (Figure 5.2)

To determine how much of an effect this calculation could potentially have on calculated temperatures, the $Fe^{2+}$ content of the melt was systematically varied from 0 to 100% for three samples, generating a variation in the Mg# of the melt. Equations 5.2 and 5.3 were applied to three samples. J2-418-R18, J2-413-R13, and J2-418-R01 were selected to span a range of calculated $Fe^{2+}$ contents. J2-418-R18 had the highest calculated $Fe^{2+}$ content of the melt, 73.7%. J2-413-R13 had an intermediate value of 70.5%. J2-418-R01 had the lowest value of 38.2%. Varying $Fe^{2+}$ contents of the melt from 0 to 100% resulted in a maximum variation of 116 °C for Equation 5.2 and a maximum variation of 161 °C for Equation 5.3 (Table 5.2). These numbers represent the maximum possible error due to an incorrect assumption about the $Fe^{2+}$ content of

the melts. Using olivine-liquid equilibrium to calculate the expected $Fe^{2+}$ content of the melt yields a range of 38.2 to 73.6% of $Fe^{2+}$ based on measured Mata samples. Thus, it is unlikely that 0 or 100% of the iron in the Mata melts is present as $Fe^{2+}$. Although the uncertainty of the calculations of $Fe^{2+}$ in the melt is unknown, it is unlikely that this greatly impacts the resulting temperatures because the resulting mineral-liquid temperatures correspond well with values from other thermometers that do not require knowledge of the $Fe^{2+}$ content of the melt or the Mg# of the melt, such as the simple liquid thermometer (Equation 5.1) and the clinopyroxene only thermometer when applied to clinopyroxene rims (Equation 5.7) as discussed in the results section of this chapter below. A comparison of the various thermometers is presented in the following section.

Table 5.2. The effect of changing the percentage of FeO input into the glass thermometers for three samples (in °C)

| % FeO | J2-413-R13 | | J2-418-R01 | | J2-418-R18 | |
|---|---|---|---|---|---|---|
| | **Equation 5.2** | **Equation 5.3** | **Equation 5.2** | **Equation 5.3** | **Equation 5.2** | **Equation 5.3** |
| **100** | 1110 | 1120 | 1022 | 1044 | 1116 | 1125 |
| **90** | 1115 | 1127 | 1027 | 1051 | 1121 | 1132 |
| **80** | 1121 | 1134 | 1033 | 1058 | 1126 | 1139 |
| **70** | 1127 | 1143 | 1039 | 1067 | 1132 | 1148 |
| **60** | 1133 | 1152 | 1046 | 1077 | 1139 | 1157 |
| **50** | 1141 | 1162 | 1055 | 1089 | 1146 | 1167 |
| **40** | 1149 | 1174 | 1065 | 1104 | 1155 | 1178 |
| **30** | 1159 | 1187 | 1077 | 1121 | 1164 | 1191 |
| **20** | 1170 | 1202 | 1093 | 1142 | 1174 | 1206 |
| **10** | 1182 | 1220 | 1112 | 1169 | 1187 | 1223 |
| **0** | 1197 | 1240 | 1138 | 1205 | 1201 | 1243 |
| **Calculated** | 1126 | 1142 | 1067 | 1107 | 1130 | 1144 |

**Comparison of thermometers**

All of the glass thermometers using microprobe data and the liquid-mineral thermometers yield similar results. All of these thermometers are expected to yield similar results, as all of them are calculating the temperature of the system at or just before eruption as the last crystals are forming. The following plots compare all of the thermometers, except for the two pyroxene thermometers (Figures 5.6 and 5.7). The temperatures calculated from the clinopyroxene-only thermometer reported here are based on an average of clinopyroxene rims, and thus record the temperature as the last clinopyroxene crystals are forming. The two pyroxene thermometers are not included in these plots because most calculations are based on pyroxene core or mid points rather than on rim points.

Figure 5.6 presents the uncertainty of the thermometers compared in Figure 5.5 for sample J2-418-R01. J2-418-R01 was selected for this graph because it appears to have greater variation between the different thermometers. J2-418-R01 also has the lowest calculated $Fe^{2+}$ content of the samples and thus represents a more extreme composition. When uncertainty is taken into account, the thermometers yield similar temperatures.

It is difficult to directly compare the two pyroxene thermometers, as calculations for different samples are taken from different parts of the crystals and no uncertainty was provided for these thermometers. Thus the values may not represent the temperature right before the eruption as the final phenocrysts were forming. Thus, the two pyroxene thermometer will be discussed separately in the following section.

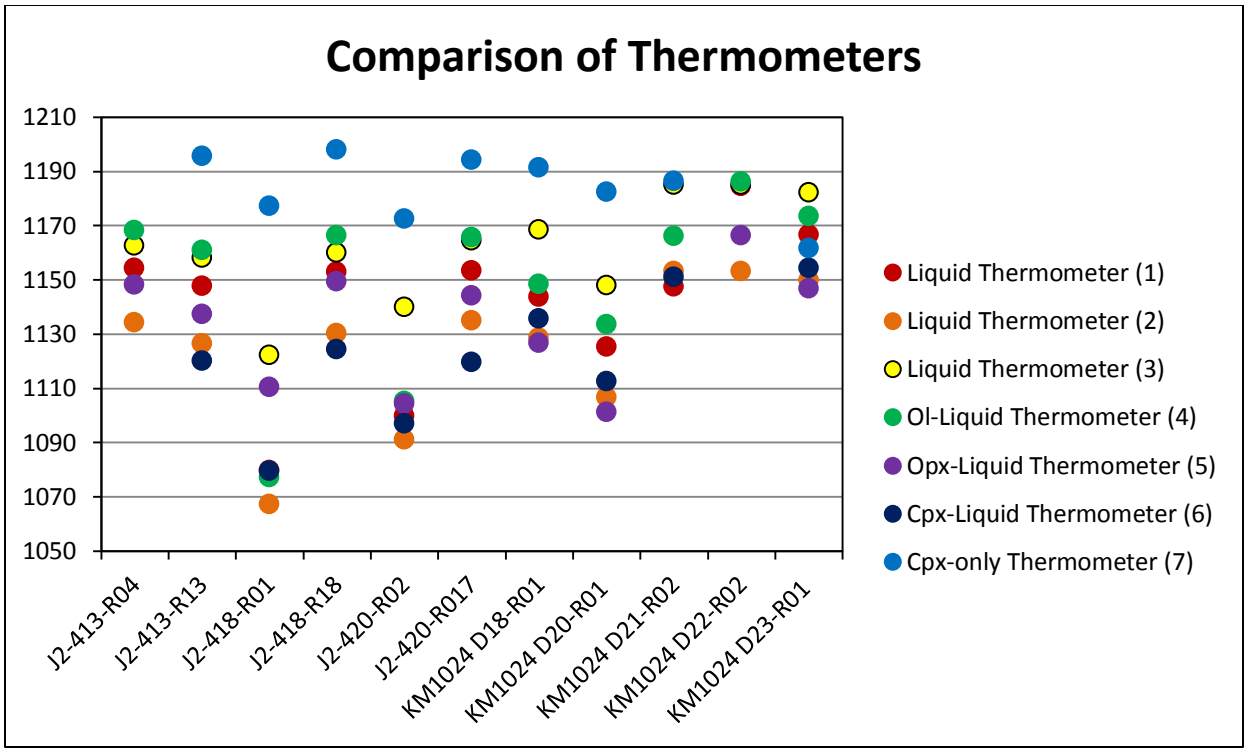


Figure 5.6. Comparison of seven different thermometers for eleven Mata samples. These thermometers include liquid and mineral-liquid thermometers plus a clinopyroxene only thermometer. For the mineral-liquid thermometers and the clinopyroxene-only thermometer, the average mineral rim content was used for calculations. Thus all of these thermometers are yielding a temperature at or just before eruption as the last minerals are forming. For thermometers where pressure and the water content of the melt are factors, calculations are made at a pressure of 500 bars and with a liquid water content of 2.0 wt%. In a few cases, some of the samples did not have the necessary data to apply a thermometer and thus these thermometer data points were excluded from this graph.

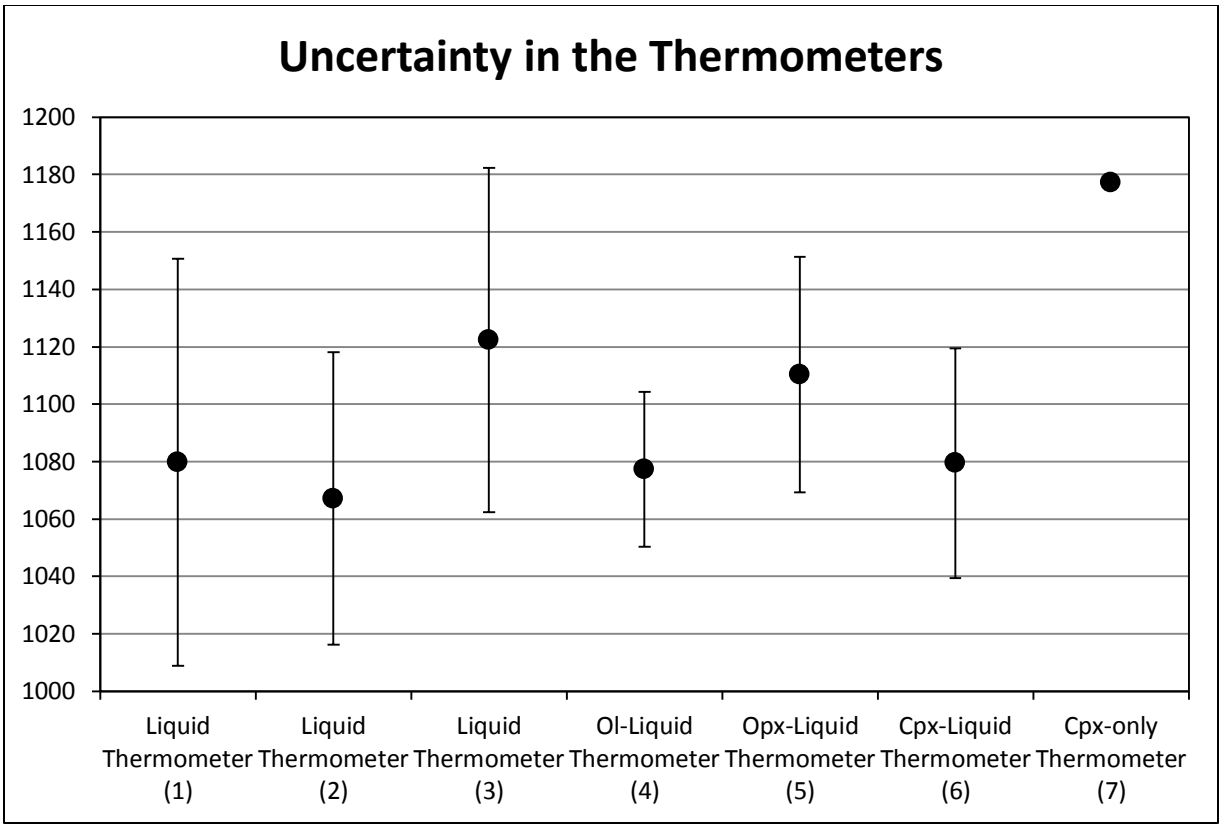


Figure 5.7. Comparison of calculated temperatures and uncertainties for West Mata sample J2-418-R01 using seven thermometers, pressure of 500 bars, and liquid water content of 2 wt%. For the olivine liquid thermometer (Equation 5.4), only a minimum uncertainty was provided. A range of uncertainties (32-50 ºC) was provided for the clinopyroxene-liquid thermometer (Equation 5.5), so an intermediate value of 40 ºC was used in this graph. No uncertainty was reported for the clinopyroxene-only thermometer.

## Results

### Liquid Thermometers (Equations 5.1-5.3)

Equations 5.1, 5.2, and 5.3 were applied to all microprobe glass data. Equation 5.1 was also applied to XRF whole rock data. Tables 5.3 and 5.4 summarize the data.

Equation 5.1, the simple liquid thermometer, is applied to both microprobe glass data and XRF whole rock data (Table 5.3, Figure 5.7). Calculated temperature ranges vary by the type of analysis. Some reasons for these variations are noted in the following paragraphs.

The microprobe glass data represents a true known melt composition. The volcanic glass was molten at the time of eruption and quenched on the seafloor. Therefore the temperatures calculated using microprobe glass data represent the temperature at or near the time of eruption.

XRF whole rock data could also represent what was once a liquid composition, but only in a completely closed system. If no additional crystals or magma is added during crystallization and all crystals remain in the melt, the whole rock composition would represent the original parent melt. If the whole rock represents the true liquid composition, then the thermometer would provide the temperature at which the system was molten. However, it is possible that crystals were removed or that crystal accumulation occurred. In this scenario, the bulk composition will not be representative of a true liquid composition and thus the calculated temperature is not representative of the system. Therefore, thermometry work on the XRF whole rock compositions must be used with caution.

Equation 5.1 liquid thermometer is based on the MgO content of the melt, with higher MgO contents yielding higher temperatures. Olivine accumulation or removal from the melt could greatly affect these calculations by increasing the MgO content of the system and thus raising the temperature or by removing MgO that was part of the original melt and thereby lowering the calculated temperature. Therefore, these calculations must be treated with caution, but can be used to see what temperatures these compositions would have had if they were true liquids.

As would be expected, the calculations using microprobe glass compositions yield lower values than those of the whole rock, which is a mixture of glass and crystals. As previously discussed, olivine causes a system to have higher MgO concentrations when the olivine is included in the calculations. If the whole rock compositions are truly a liquid composition, calculated temperatures from a few (5-10) samples, primarily from Mata Ua, Mata Tolu, and Mata Ono reach temperatures as high as those predicted by Falloon and Danyushevsky (2000)'s experiments (Table 5.4).

Looking in more detail at the comparison between the temperatures calculated based on microprobe glass data and XRF whole rock data, some interesting trends can be observed. For example, for Mata Ua, the temperatures calculated for glass and whole rock samples are positively correlated with each other. In contrast for Mata Fitu, there is a flat trend, with large differences (almost 200 °C) between temperatures calculated from whole rock data and little spread in temperatures calculated from glass data. Samples from West Mata form two distinct groups, a group with a higher glass temperature, which has a flat trend, and a group with a lower glass temperature, which has a flat or negative trend. These trends must be considered with caution as much is within the uncertainty of the thermometers.

Looking in detail at the microprobe glass data, overall, the Mata glass samples have a temperature range of just over two hundred degrees (1007 to 1220º C using Equation 5.1). This would represent the temperature at or soon before eruption (Figure 5.9). Calculations of temperature based on microprobe glass and whole rock XRF data (Figures 5.9 and 5.10) suggest the following findings:

- Individual volcanoes can have a significant range of temperatures.
- The more evolved East Mata samples have lower temperatures.
- There are no major temperature differences between the other volcanoes within the uncertainty of the thermometers.
- There is no obvious correlation between temperature and geographic location of the Mata Volcanoes within the uncertainty of the thermometers. However, the lowest temperatures recorded at each volcano increase to the north.

Additionally, as shown in Figure 5.11, there is no difference in temperature between the boninitic lavas and the non-boninitic lavas that are higher in $TiO_2$. While this observation holds for all of the three thermometers and using both XRF data and microprobe glass data to calculate temperature using Equation 5.1, only one thermometer is shown as an example.

Some samples from the older eruption or eruptions at West Mata consistently have a slightly lower temperature than samples from the new eruption (~50 ºC cooler). These are the higher $SiO_2$, lower MgO samples. However, this is within the uncertainties of the liquid thermometers reported in Figure 5.7.

Table 5.3. A Comparison of temperature ranges calculated for the Mata Volcanoes using a liquid thermometer (Equation 5.1) and measured microprobe glass and XRF whole rock data (in $^{o}$C)

| Volcano | Temperature Range in $^{0}$C from Liquid Thermometer (Equation 5.1) using Microprobe Glass | Temperature Range in $^{0}$C from Liquid Thermometer (Equation 5.1) using XRF whole Rock |
|---|---|---|
| **East Mata** | 1107-1139 | 1252-1400 |
| **West Mata** | 1065-1171 | 1154-1242 |
| **Taha** | 1113-1120 | 1318-1326 |
| **Ua** | 1118-1220 | 1258-1466 |
| **Tolu** | 1125-1188 | 1347-1521 |
| **Fa** | 1137-1147 | 1395-1405 |
| **Ono** | 1184-1186 | 1233-1356 |
| **Fitu** | 1136-1176 | 1233-1356 |

See Appendix D for additional data.

Table 5.4. Calculated temperature for Mata samples based on two liquid thermometers (Equations 5.2 And 5.3) using microprobe glass data (in $^{o}$C)

| Location | Sample | T $^{o}$C from Liquid only Thermometer (Equation 5.2) | T $^{o}$C from Liquid only Thermometer (Equation 5.3) |
|---|---|---|---|
| West Mata | J2-413-R13 | 1126 | 1158 |
| West Mata | J2-418-R18 | 1130 | 1160 |
| West Mata | J2-420-R17 | 1135 | 1164 |
| West Mata | J2-413-R04 | 1134 | 1162 |
| West Mata | J2-418-R01 | 1067 | 1122 |
| West Mata | J2-420-R02 | 1091 | 1140 |
| Ua | KM1024 D18-R01 | 1128 | 1168 |
| Tolu | KM1024 D20-R01 | 1107 | 1148 |
| Fa | KM1024 D21-R02 | 1153 | 1185 |
| Ono | KM1024 D22-R02 | 1160 | 1187 |
| Fitu | KM1024 D23-R01 | 1150 | 1182 |

Equations 5.2 and 5.3 are dependent on the water content of the melt. Equation 5.3 is also dependent on pressure.

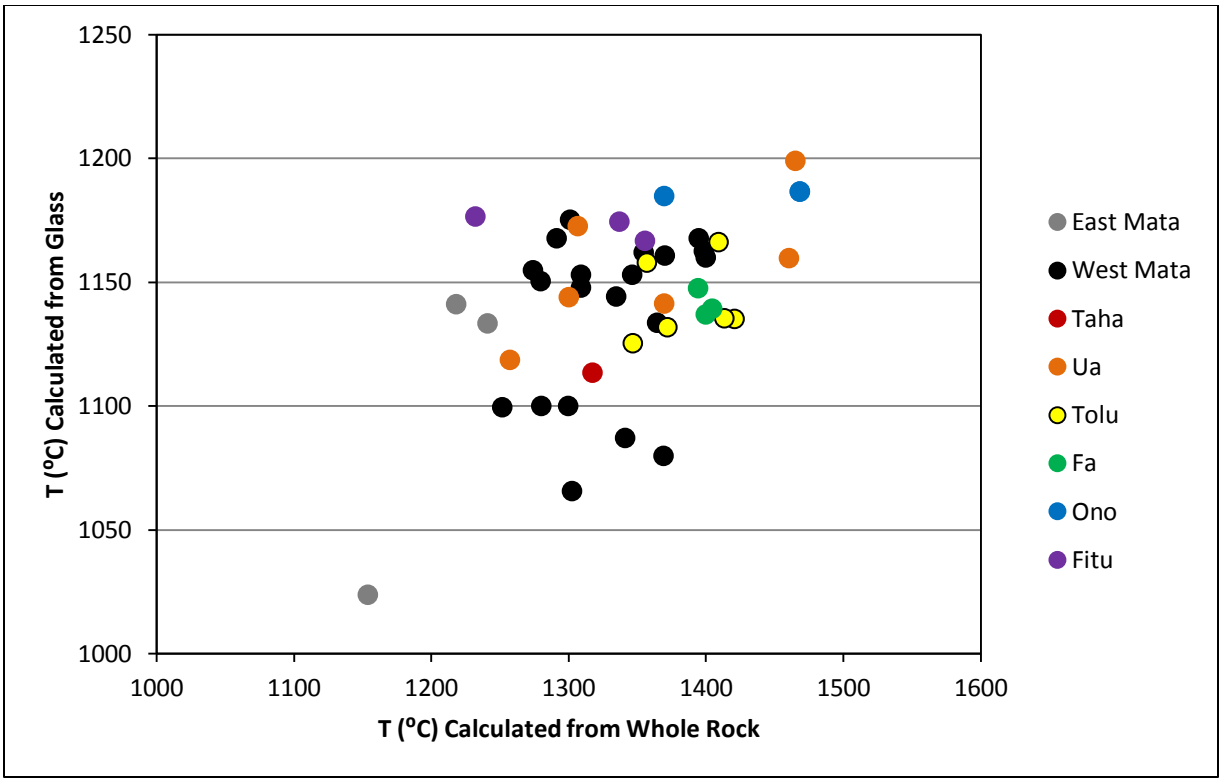


Figure 5.8. Comparison of temperatures calculated from microprobe glass and XRF whole rock analysis for the same samples (Equation 5.1). Calculated temperatures are lower for microprobe samples.

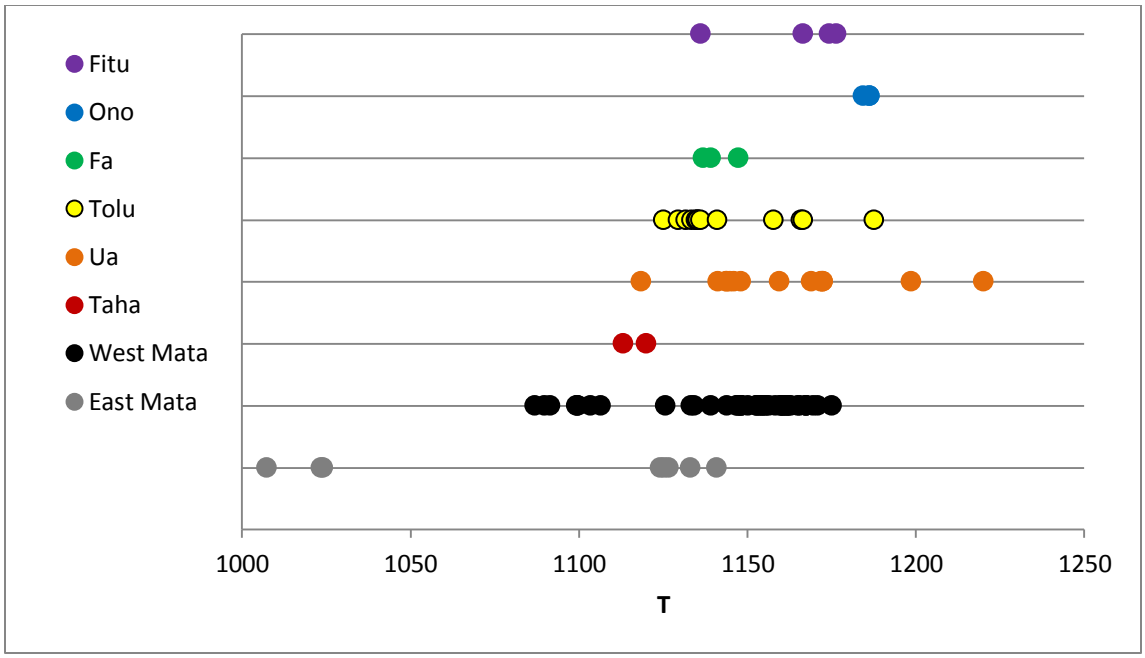


Figure 5.9. Temperature of samples calculated from microprobe glass data (Equation 5.1). Samples are plotted with others from the same volcano on the same line.

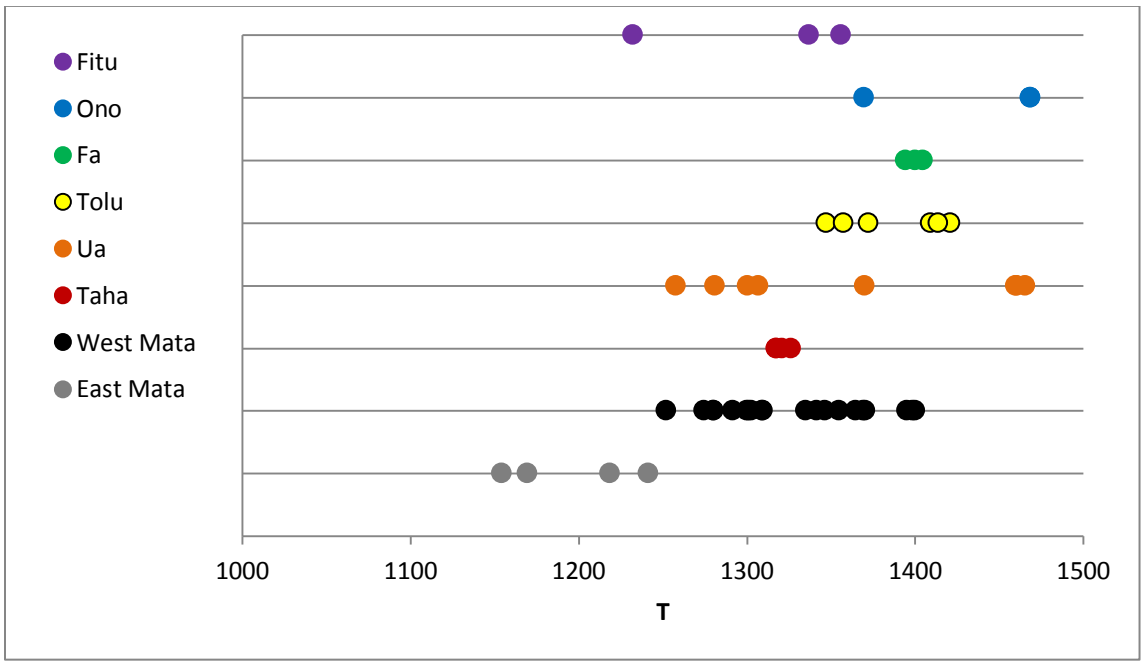


Figure 5.10. Temperature of samples calculated from XRF whole rock data (Equation 5.1). Samples are plotted with others from the same volcano on the same line.

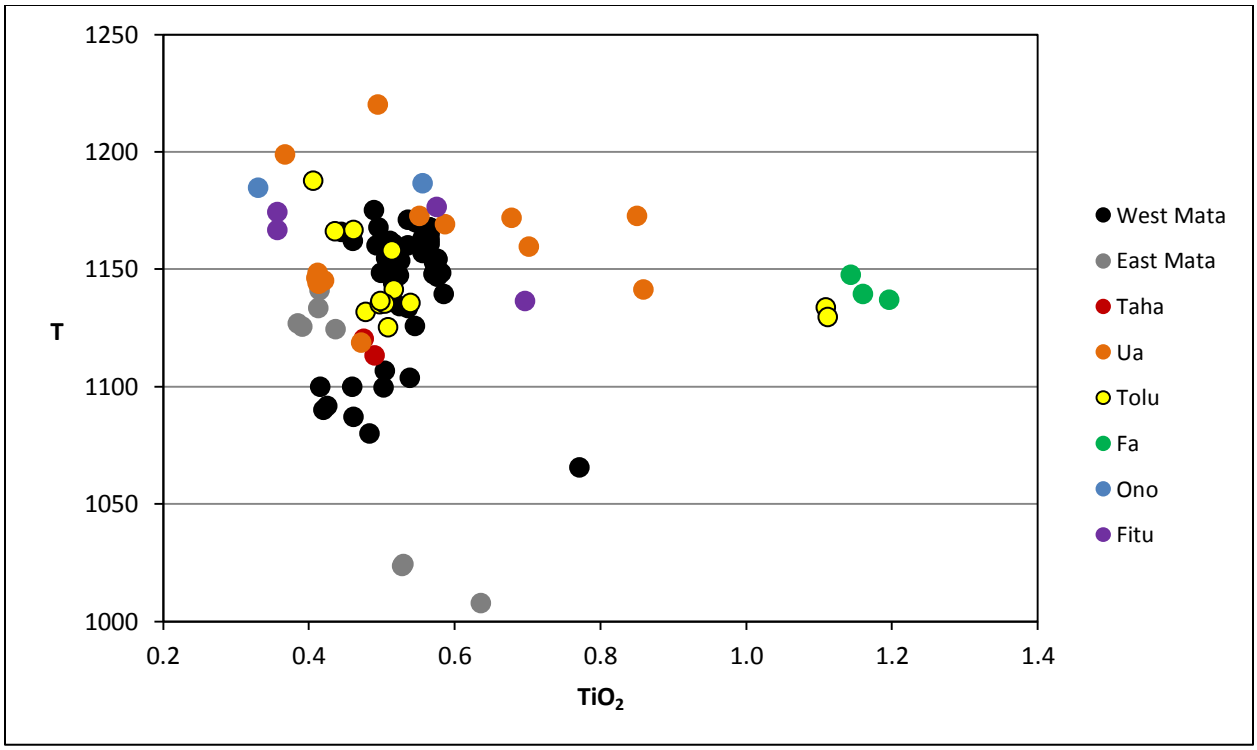


Figure 5.11. Temperature calculated from microprobe glass data for Mata samples compared to $TiO_2$ content of the glass (Equation 5.1). Sample $TiO_2$ content does not seem to correlate with temperature.

**Olivine-Liquid Thermometer (Equation 5.4)**

The olivine-liquid thermometer yields similar temperatures to the liquid thermometers (Table 5.4). The data suggest the following findings:

- There is no overall temperature gradient associated with the location of the Mata Volcanoes, within error of the thermometers. However, there is a slight temperature increase to the north.
- The high titanium sample from Mata Fa does not have a significantly higher or lower temperature than the samples from the other Mata Volcanoes.
- The measured samples from the older eruption or eruptions at West Mata (samples J2-418-R01 and J2-420-R02) were lower in temperature by 50-100 ºC. These samples are from the higher $SiO_2$, lower MgO group.

Table 5.5 reports calculated temperatures for the Mata Volcanoes using the olivine-liquid thermometer (Equation 5.4), orthopyroxene-liquid thermometer (Equation 5.5), clinopyroxene-liquid thermometer (Equation 5.6), and the clinopyroxene only thermometer (Equation 5.7).

Table 5.5. Calculated temperatures in for four different thermometers (in °C)

| Volcano | Sample | Ol-Liquid | Opx-Liquid | Cpx-liquid | Cpx only |
|---|---|---|---|---|---|
| West Mata | J2-413-R04 | 1168 | 1148 | | |
| West Mata | J2-413-R13 | 1161 | 1137 | 1120 | 1196 |
| West Mata | J2-418-R01 | 1077 | 1110 | 1079 | 1177 |
| West Mata | J2-418-R18 | 1166 | 1149 | 1124 | 1198 |
| West Mata | J2-420-R02 | 1105 | 1104 | 1097 | 1173 |
| West Mata | J2-420-R17 | 1166 | 1144 | 1120 | 1194 |
| Ua | KM1024 D18-R01 | 1148 | 1127 | 1136 | 1191 |
| Tolu | KM1024 D20-R01 | 1134 | 1101 | 1113 | 1182 |
| Fa | KM1024 D21-R02 | 1166 | | 1151 | 1186 |
| Ono | KM1024 D22-R01 D | 1187 | | | |
| Ono | KM1024 D22-R01 L | 1187 | | | |
| Ono | KM1024 D22-R02 | 1186 | 1166 | | |
| Fitu | KM1024 D23-R01 | 1173 | 1147 | 1154 | 1162 |
| Fitu | KM1024 D23-R04 | 1181 | | | |

Temperatures are calculated for Mata samples using an olivine-liquid thermometer (Ol-Liquid, Equation 5.4), a orthopyroxene-liquid thermometer (Opx-liquid, Equation 5.5), a clinopyroxene-liquid thermometer (Cpx-liquid, Equation 5.6), and a clinopyroxene only thermometer (Cpx only, Equation 5.7). Calculations assumed a pressure of 500 bars and 2.0 wt% water in the melt. Samples from the older eruption(s) of West Mata are J2-418-R01 and J2-420-R02. The olivine-liquid thermometer uses an average of measured olivine rims. The orthopyroxene-liquid thermometer uses an average of measured orthopyroxene rims. The clinopyroxene-liquid thermometer and the clinopyroxene thermometer uses an average of measured clinopyroxene rims.

**Orthopyroxene-Liquid Thermometer (Equation 5.5)**

The orthopyroxene-liquid thermometer yields similar temperatures to the liquid thermometers and the olivine-liquid thermometer (Table 5.5). The data suggest the following findings:

- There is no overall temperature gradient associated with the location of the Mata Volcanoes, within error of the thermometers. However, there is a slight temperature increase to the north.
- The high titanium sample from Mata Fa does not have a significantly higher or lower temperature than the samples from the other Mata Volcanoes.
- Samples from the older eruption or eruptions at West Mata (samples J2-418-R01 and J2-420-R02) were lower in temperature by 30-50 ºC. These samples are from the higher $SiO_2$, lower MgO group.

**Clinopyroxene-Liquid Thermometer (Equation 5.6)**

The clinopyroxene-liquid thermometer yields similar temperatures to the liquid thermometers and the other mineral-melt thermometers (Table 5.5). The data suggest the following findings:

- There is no overall temperature gradient associated with the location of the Mata Volcanoes, within error of the thermometers. However, there is a slight temperature increase to the north.
- The high titanium sample from Mata Fa does not have a significantly higher or lower temperature than the samples from the other Mata Volcanoes.
- Samples from the older eruption or eruptions at West Mata (samples J2-418-R01 and J2-420-R02) were lower in temperature by 20-40 ºC. These samples are from the higher $SiO_2$, lower MgO group.

**Clinopyroxene-Only Thermometer (Equation 5.7)**

Temperatures were calculated with the clinopyroxene-only thermometer two ways: 1.) using an average of clinopyroxene rims for each sample (Table 5.5) and 2.) calculating a temperature for each clinopyroxene point measured (Table 5.6 and Appendix D).

The first method yields values that should be the temperature at or just before eruption, similar to the liquid and mineral-liquid thermometers. When calculated this way, the clinopyroxene-only thermometer yields similar temperatures to the liquid thermometers and the mineral-melt thermometers and suggests the following findings:

- There is no overall temperature gradient associated with the location of the Mata Volcanoes. However, more samples would be required to confirm this.
- The high titanium sample from Mata Fa does not have a significantly higher or lower temperature than the samples from the other Mata Volcanoes.
- Samples from the older eruption or eruptions at West Mata (samples J2-418-R01 and J2-420-R02) were lower in temperature by 20 ºC. These samples are from the higher $SiO_2$, lower MgO group.

An advantage to the clinopyroxene-only thermometer over the liquid and mineral-liquid thermometers is that clinopyroxene cores can be used to examine the temperatures of the melts earlier in their crystallization history. The temperature for each clinopyroxene point measured was calculated. Table 5.5 presents the range in values calculated by the clinopyroxene only thermometer for each volcano and Figure 5.12, 5.13 and 5.14 presents the individual points measured.

Most volcanoes show a range of temperatures. Many volcanoes have clinopyroxene that record temperatures of 1200 ºC or higher. There does not appear to be significant differences between the maximum temperatures of formation of the clinopyroxene from the different volcanoes. Figures 5.13 and 5.3 examine the relationship between the $TiO_2$ content of the clinopyroxene points and their calculated temperatures.

All samples appear to show similar temperature ranges except for Mata Fitu. Only rim measurements corresponding to lower calculated temperatures are available for Mata Fitu. However, a closer inspection of individual samples shows trends. Interestingly, the sample from Mata Fa, which has a higher $TiO_2$ content, has a similar range of temperatures to samples from the other volcanoes but with a different T-$TiO_2$ slope. When looking more closely at West Mata samples, measured samples from the older eruption or eruptions and new eruptions form two separate, but partially overlapping clusters with different T-$TiO_2$ trends. Samples from the older eruption(s) (J2-418-R01 and J2-420-R02) are from the higher $SiO_2$, lower MgO group.

Table 5.6 Range of temperatures determined by the clinopyroxene-only thermometer (in $^{o}$C)

| **Volcano** | **Temperature Range in $^{o}$C from Clinopyroxene Only Thermometer** |
|---|---|
| **East Mata** | 1169-1192 |
| **West Mata** | 1151-1199 |
| **Taha** | 1158-1192 |
| **Ua** | 1150-1200 |
| **Tolu** | 1136-1192 |
| **Fa** | 1165-1195 |
| **Fitu** | 1156-1158 |

For more data see Appendix D.

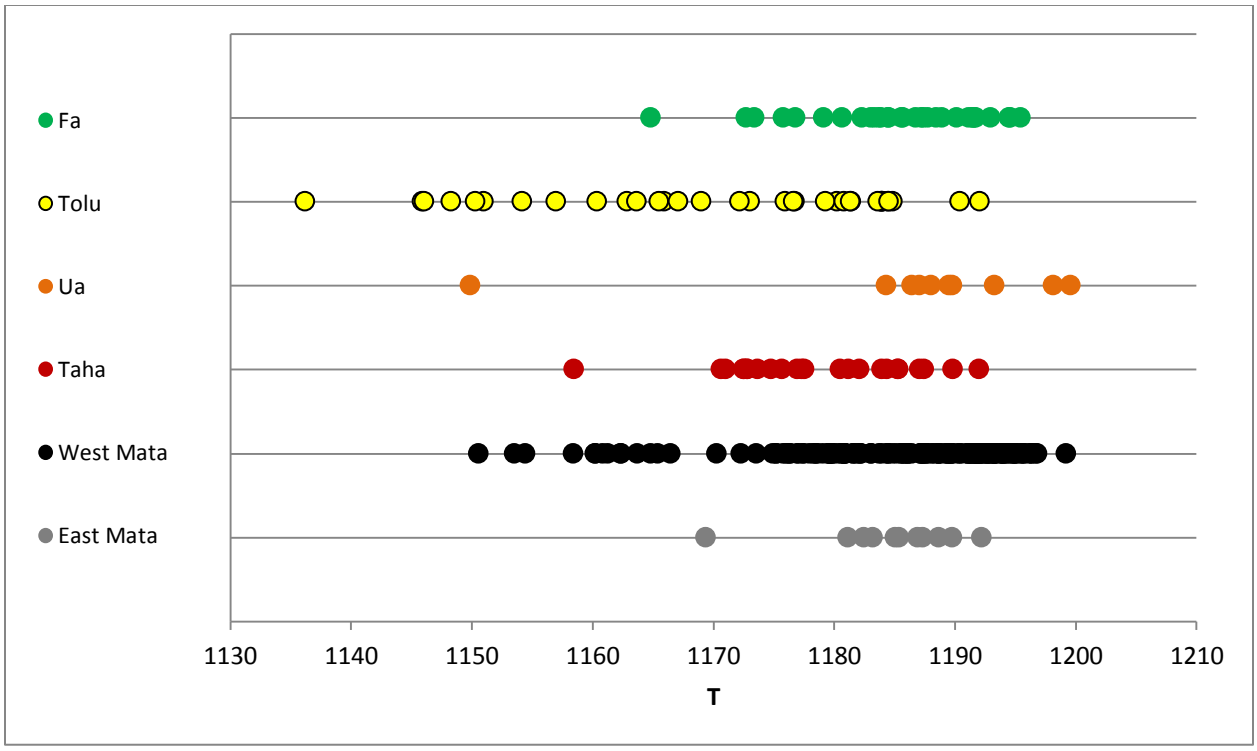


Figure 5.12. Temperature of samples using clinopyroxene-only thermometer (Equation 5.7). Samples are plotted on the same line with others from the same volcano.

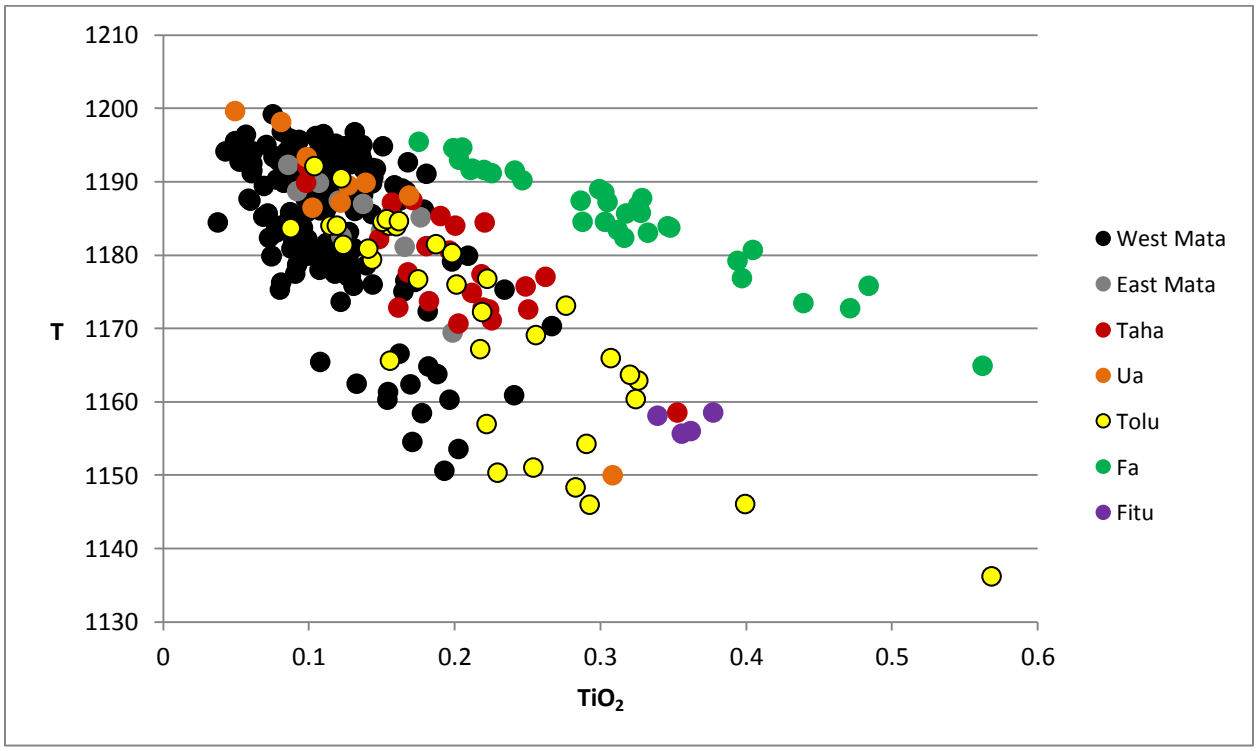


Figure 5.13. Calculated temperature of formation for clinopyroxene points calculated using the clinopyroxene-only thermometer compared to the $TiO_2$ content of the clinopyroxene points. Interestingly, while the clinopyroxene from Mata Fa, the high $TiO_2$ sample, have a similar temperature range to the other samples, the slope of their T-$TiO_2$ trend is slightly different.

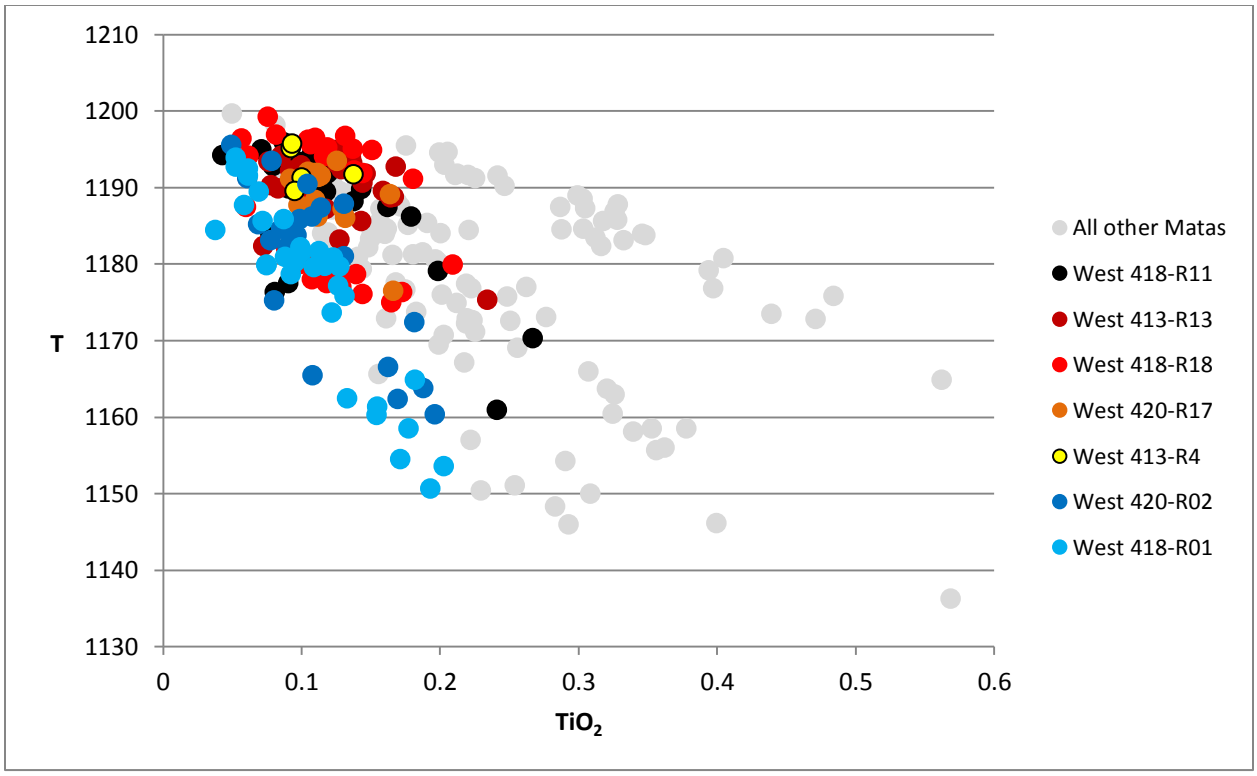


Figure 5.14. Calculated temperature of formation for clinopyroxene points calculated using the clinopyroxene-only thermometer compared to the $TiO_2$ content of the clinopyroxene points looking in detail at West Mata samples. Samples from the other Mata volcanoes are displayed as light grey circles for comparison. West Mata samples from the new eruption are displayed as warm colored circles and samples from the older eruption(s) are displayed as cooler colored circles. J2-418-R01 and J2-420-R02 are from the higher $SiO_2$, lower MgO group from the older eruption(s). Interestingly, samples from the old and new eruptions define two separate, but partially overlapping clusters with different T-$TiO_2$ trends. Pressure is 500 bars.

**Two Pyroxene Thermometer (Equations 5.9-5.10)**

I calculated the temperatures using the preferred pressures of crystallization from MELTS modeling (See Chapter 6), 500 bars and 1000 bars, and obtained very similar temperature ranges. Using a pressure of 500 bars, the temperature range was 999 to 1194 ° C when the regression based on all pyroxenes was used (Equation 5.9) and a temperature range of 985 to 1148 ° C when the thermometer based only on pyroxenes where the Mg# of clinopyroxene was >.75 was used (Equation 5.10). Using a pressure of 1000 bars, the temperature range was 1002 to 1197 ° C when the regression based on all pyroxenes was used (Equation 5.9) and a temperature range of 987 to 1151 ° C when the thermometer based only on pyroxenes where the Mg# of clinopyroxene was >.75 was used (Equation 5.10; Putirka, 2008). Table 5.7 summarizes two pyroxene thermometry results at a pressure of 1000 bars.

Calculated temperatures span a range of approximately 200 °C suggesting that pyroxene crystals from the Mata volcanoes could have formed over a range of temperatures. Temperatures derived from the two pyroxene thermometer appear to be lower than those derived from other thermometers; however, as no uncertainty was reported for the two pyroxene thermometers, it is difficult to compare conclusively.

Table 5.7. Calculated temperatures based on two pyroxene thermometry (in °C)

| Location | Sample | Equation 5.9 | Equation 5.10 |
|---|---|---|---|
| West Mata | J2-413-R13a Pyroxene 1 | 1134 | 1111 |
| West Mata | J2-413-R13a Pyroxene 1 | 1126 | 1109 |
| West Mata | J2-418-R01 pyroxene 11-b | 1057 | 1025 |
| West Mata | J2-418-R11 pyroxene 1 | 1110 | 1089 |
| West Mata | J2-420-R02 pyroxene 4 | 1066 | 1030 |
| West Mata | J2-420-R17 pyroxene 5 | 1107 | 1087 |
| Ua | KM1024 D18-R01 test | 1130 | 1105 |
| Ua | KM1024 D18-R01 test | 1156 | 1144 |
| Ua | KM1024 D18-R01 pyx-3 | 1056 | 1024 |
| Ua | KM1024 D18-R01 pyx-4 | 1106 | 1097 |
| Tolu | KM1024 D20-R01 pyx 12 zone a | 1044 | 1018 |
| Tolu | KM1024-D20-R01 Pyx-12 zone b | 999 | 985 |
| Tolu | KM1024-D20-R01 Pyx-13 | 1102 | 1098 |
| Tolu | KM1024-D20-R01 Pyx-13 | 1115 | 1108 |
| Tolu | KM1024-D20-R01 Pyx-14 | 1115 | 1120 |
| East Mata | KM1024 D14-R02 pyx 3 | 1194 | 1141 |

This table reports data for all pyroxene pairs that were in equilibrium with each other. In a few cases, two measurements are reported from an individual pyroxene pair. These are highlighted in light grey.

## Summary

Overall the thermometers are consistent with each other, within the uncertainty of the thermometers. The two pyroxene thermometer calculates slightly lower temperatures. Using XRF data, temperatures calculated for 5-10 samples reached the range reported by Falloon and Danyushevsky (2000), who found that temperatures as high as 1480 °C may be required during mantle melting to form boninites. However, these calculations must be considered with caution as the XRF whole rock data may not represent true liquid compositions. All other values were lower, with few exceeding 1200 °C. This suggests that crystallization did not occur at unusually high temperatures. The temperatures determined in this study are within the range of temperatures determined for boninitic melts (Acland, 1996; Danyushevsky and Sobolev, 1996; Umino and Kushiro, 1989; Van der Laan et al., 1989). The calculated temperatures from this study do not rule out a higher temperature early history for these lavas.

There are no major temperature variations between the volcanoes, with the exception of the more evolved samples at East Mata which record lower temperatures. Within the uncertainty of the thermometers, temperature does not appear to be correlated with the location of the volcanoes. However, the lowest temperatures recorded for each Mata Volcano tend to increase to the north. Analysis of additional samples would help confirm if there is a geographical temperature gradient. Overall, the higher $TiO_2$ samples record very similar temperatures to typical boninites samples. Interestingly, samples from the older eruption or eruptions at West Mata started at a higher calculated temperature, similar to those recorded in newly erupted clinopyroxene. However, these lavas evolved to a lower temperature by approximately 50 °C. Some samples from the older eruption or eruptions are consistently associated with lower temperature estimates in all of the liquid thermometers and mineral-liquid thermometer. These samples are the higher $SiO_2$, lower MgO group from the older eruption or eruptions. However, the amount of offset in temperatures between some of the older samples and the newer eruption varies between the thermometers and is within the uncertainty of the thermometers. The lower $SiO_2$, higher MgO group of older samples yields similar temperatures to samples from the newer eruption.

# CHAPTER 6: MODELING OF CRYSTALLIZATION

## Introduction

From the onset of melting to eruption on the seafloor, the melts can undergo a variety of complex processes including initial melting of the mantle wedge possibly fluxed by fluids from the subduction zone, migration of the melts to shallower depths, crystallization and differentiation, assimilation of wall rock, and magma mixing. These processes can be studied though geochemical and petrological investigations of erupted samples. For example, trace element concentrations and ratios in the melts can provide clues about the initial composition of the mantle wedge and melting dynamics, such as the degree of melting or the presence of certain residual phases. The presence of different residual phases can in turn provide insight into the temperature and pressure regime of the melting region. The major element concentrations of samples and mineral textures can be used to study crustal processes, such as differentiation by crystallization and magma mixing. The glass concentrations of major elements in a sample suite formed simply by differentiation by crystallization without magma mixing will fall along a liquid line of descent (LLD). A liquid line of descent is the path of compositional evolution of the magma as crystallization occurs. For example, as crystals of olivine and pyroxene are extracted, the MgO content of the melt will decrease. Samples with higher MgO contents are said to be more primitive and samples with lower MgO contents are said to be more evolved or more differentiated. Plots of various oxides vs. MgO can be used to study the differentiation of the sample suite. Crystallization of different types of minerals will affect the composition of the melt as various elements are removed from the melt. For example, crystallization of clinopyroxene will remove CaO from the melt, causing the CaO content of the melt to decrease with decreasing MgO content. Observations of major element trends in glass data and whole rock data for the Mata data, shown in the Chapter Four, suggest that these samples could fall along a liquid line of descent or several subparallel liquid lines of descent. However, the variety of complex textures observed in erupted crystal phases, as presented in the Chapter Three, could be better explained by extensive magma mixing. Forward modeling of crystallization can be used to further investigate the crustal history of these magmas and to inquire if these samples could have formed from differentiation from a single parent magma or if multiple parent melts or significant magma mixing is required to explain the compositions observed.

Therefore, as part of this project, MELTS was used to model crystallization. MELTS is a series of models that can be used to model igneous processes such as melting or crystallization. MELTS uses experimental data and thermodynamic models to predict phase relations and compositions at a range of conditions provided by the user. For example, crystallization can be modeled at a constant pressure as the magma is cooling by providing a temperature range, pressure, oxygen fugacity and major element composition of the starting melt. The user can specify an increment of change in temperature and the program will calculate the phase proportions and compositions of the system after every incremental change in temperature. The output lists mineral phases that are formed and their compositions. It also includes the compositions of the residual melt and the phases that crystallize.

MELTS can be downloaded for free from http://melts.ofm-research.org/ and additional information on the MELTS program is provided online. There are several versions of MELTS available and each version is optimized for different systems. MELTS is primarily calibrated for MORB-like systems, mafic systems with low water contents. It can be extrapolated to other systems. The accuracy to which it can be applied to boninites is not well known. Other versions are available for mantle compositions and rhyolitic systems. None of these models are well calibrated for the bulk compositions studied in this project. Given its possible limitations, I tested MELTS (adiabat_1ph_2-0) to model crystallization of Mata melts (Asimow and Ghiorso, 1998; Ghiorso and Sack, 1995; Smith and Asimow, 2005). This study is the first to apply MELTS to model crystallization of these boninites and boninite-like samples. Within the limits of this thesis, the MELTS modeling was not exhaustive, but primarily aimed at answering several questions:

1. Can MELTS be used to model crystallization of these boninites and boninite-like samples?
2. Under what conditions did the melts from the Mata volcanoes crystallize?
3. Could the samples have formed from simple fractional crystallization along a single LLD starting from a single parent melt?

## MELTS in the Literature

MELTS has been used previously to model crystallization and to answer similar questions to those this study hopes to answer. MELTS can be used to determine if it is possible that a group of samples could have formed by simple fractionation. It can be used to see if it is possible that two groups of samples could be related or if multiple parent melts are required. MELTS can be used to constrain the conditions of crystallization of samples or the initial water content in the parent melt. This section will provide examples of uses of MELTS from literature.

Eason and Sinton (2006) use pMELTS to model melting of a mantle source region below the Galapagos Spreading Center and MELTS to model crystallization. They try to determine the nature of the mantle wedge that melted to form these samples. They divided their samples into two groups: normal MORB (N-MORB) and High-Al MORB, samples with >16.0 wt% $Al_2O_3$ and > 8.5 wt% MgO in the glass. They also try to determine what process or processes can explain the compositional differences between these groups. To do so, they melt different mantle compositions using pMELTS. They model crystallization of parent melts using MELTS. This discussion will focus on their MELTS crystallization modeling. They use fractional crystallization runs at constant pressure of 1000 bars and at a constant oxygen fugacity of QFM - 2. The following figure taken directly from their paper shows their MELTS modeling results (Figure 6.1).

Using these parent melts, they investigated why the high-Al MORB were compositionally different. They investigated two possibilities: 1. Low degrees of melting, and 2. High pressure crystallization. They used several methods to lower the degree of melting using pMELTS. As pMELTS is not used in this thesis, details will not be discussed here and the reader is referred to the original paper. Parent melts obtained from the low degree of melting pMELTS runs were used as starting compositions for the MELTS runs. They found that the low degree of melting runs did not match the data well (Figure 6.1).

Eason and Sinton (2006) then try to model formation of the high-Al samples using high pressure crystallization. Because crystallization occurs deeper in the mantle, melting was stopped at a lower depth. Therefore these models do have a slightly lower percentage of mantle melting than the models for the N-MORB samples. They find that pressures of up to 0.3 to 0.4

GPa are required to produce high-Al MORB. Clinopyroxene forms earlier at these pressures, causing Al values to increase in the residual melt while Si values remain low. A comparison between modeled LLDs and high-Al MORB data is used to determine what pressures of crystallization are a best fit. The figure below, taken from their paper, shows their modeling work (Figure 6.2).

There is some scatter in the data. There are fewer data points for the high-Al MORB than the N-MORB. The N-MORB data also display a wider range in MgO values (approximately 3 wt%) compared to the high-Al MORB (approximately 1.5 wt%). Thus, the range over which the data can be compared to modeled LLDs is reduced. Because changes in pressure greatly impact the modeled LLDs, their assertion that fractionation at pressures of up to 0.3 to 0.4 is necessary for the formation of the high-Al MORB seems robust (Figure 6.2).

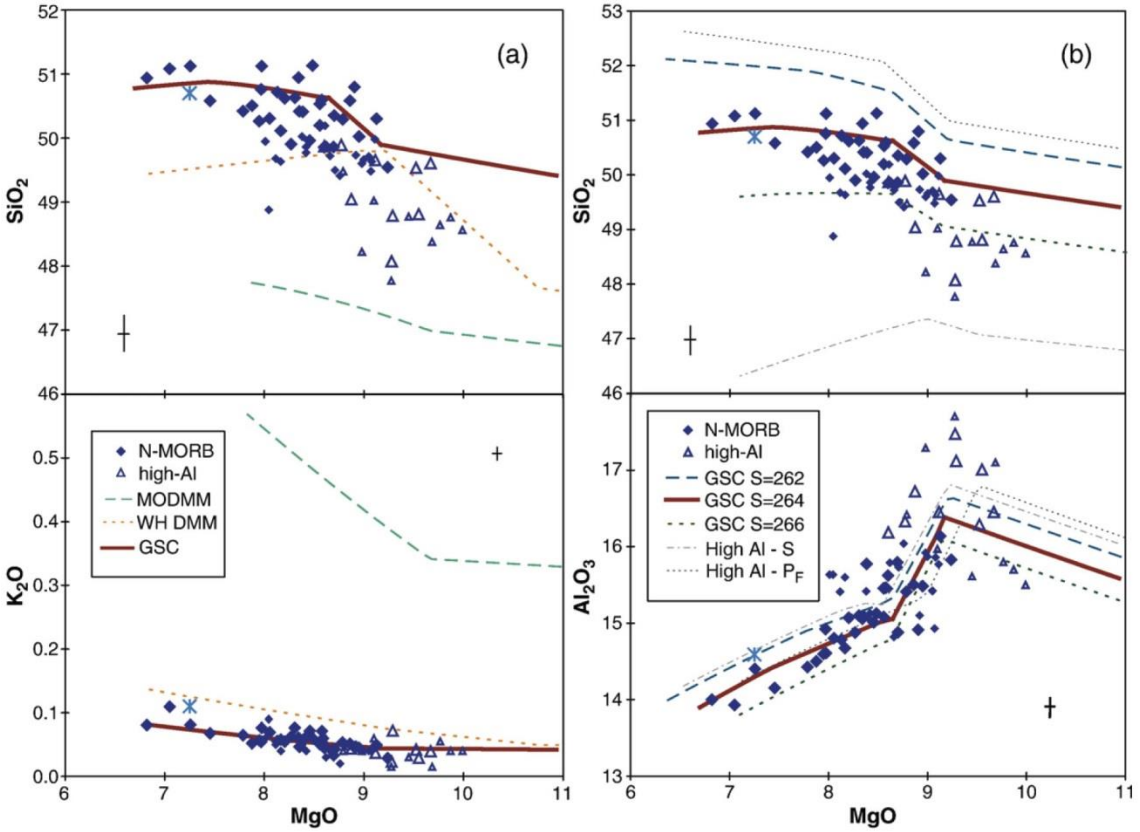


Figure 6.1. MELTS Model used for Galapagos Spreading Center data. The first panel (a) looks at crystallization of different parent melts resulting from melting of different mantle compositions. They found that Galapagos Spreading Center dry and wet sources that they modeled yield a better fit than depleted MORB mantle from other sources. They compare modeled LLDs from these different parent melts to measured glass and whole rock data. For their preferred parent melts, they compared predicted crystallizing phases to observed mineral phases. Plagioclase and clinopyroxene, two of the predicted crystallizing phases are present in samples. B. shows attempts to model high Al liquids using low degrees of partial melting by using a low S or a high $P_F$ value. Figure from Eason and Sinton (2006).

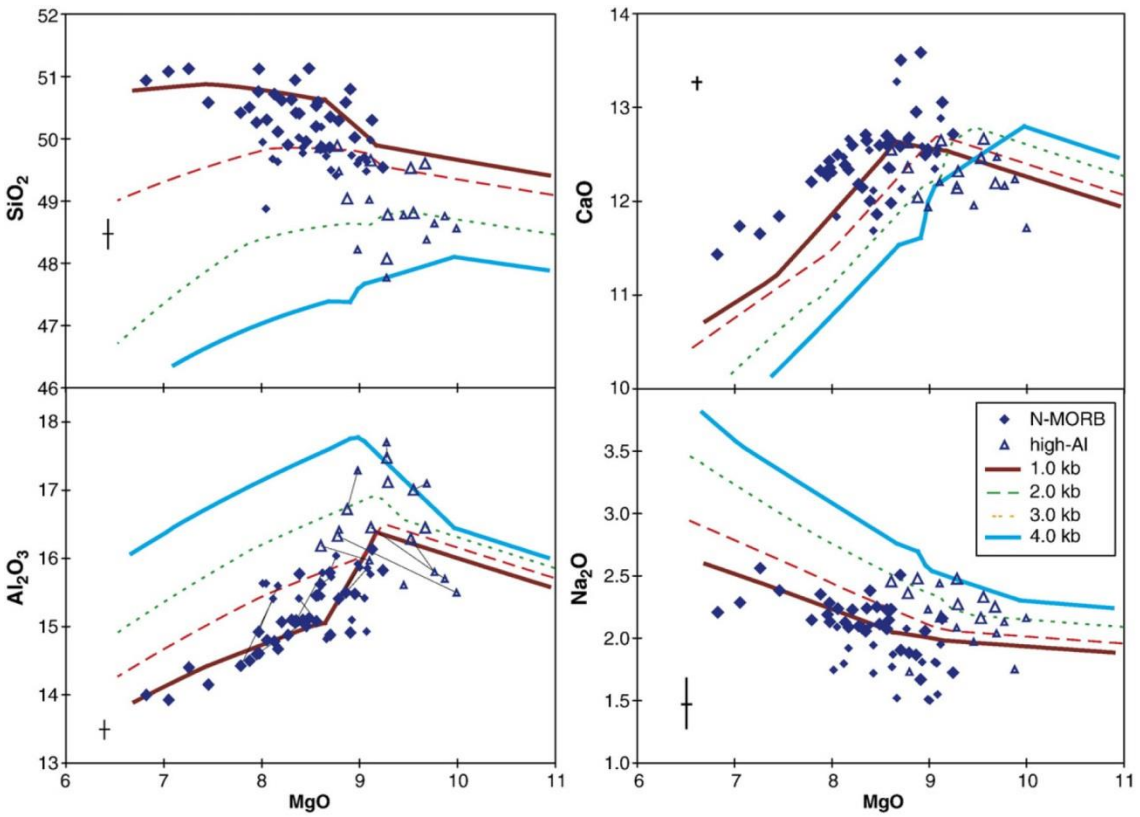


Figure 6.2. Various crystallization models for high-Al MORB samples. All models use the same source and fractional crystallization at QFM -2. Pressure is varied to find the best approximation to measured samples. The tie lines connect glass and whole rock measurements for the same sample. Figure from Eason and Sinton (2006).

Colman *et al*. (2012) apply MELTS modeling of fractional crystallization to individual flow units at the Galapagos Spreading Center. For each portion of the study area, they use field relationships, apparent relative age of the flows, and chemistry to map the units. They use MELTS to determine if samples in individual flow units are related to each other by simple fractional crystallization and to test if the different flow units share parent melts or fall along LLDs. Their methods are similar for the different flow areas, so one was selected as an example (Figure 6.3).

In this case, although it may appear that the samples from the two flows fall along a LLD for CaO and FeO, MELTS modeling shows that their K/Ti ratios cannot be connected by a simple LLD. The two different units probably formed from two different parent melts.

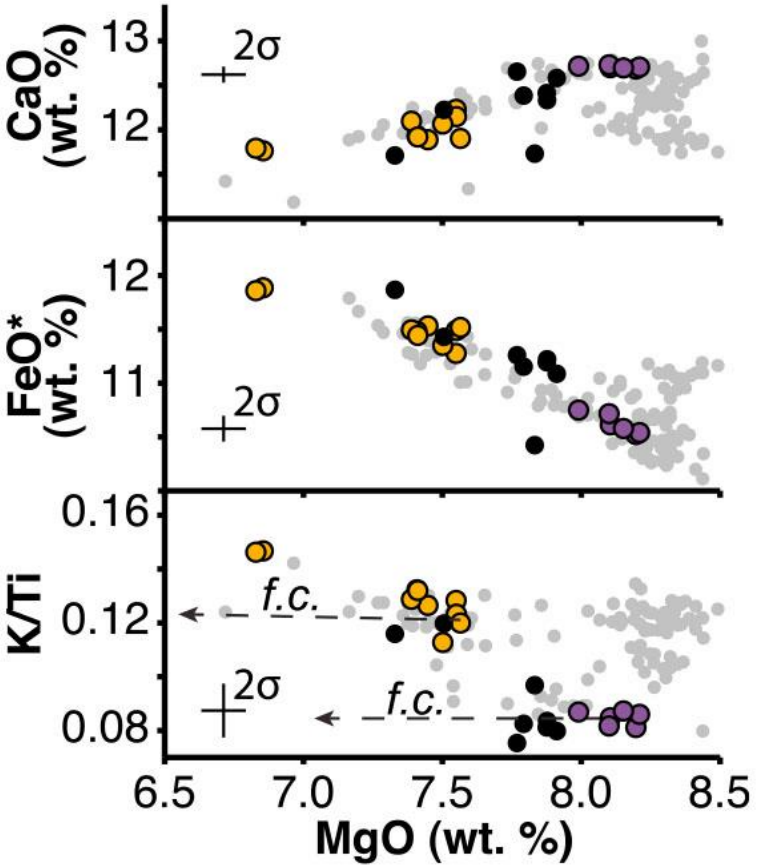


Figure 6.3. MELTS models of two different units from the Galapagos Spreading Center. Purple and yellow symbols show the two different units. The black circles represent a nearby unit. The grey symbols represent nearby units. The dashed line labeled "f.c" shows a MELTS fractional crystallization run at 500 bars and QFM -2. Figure from Colman *et al*. (2012).

Eason and Sinton (2009) use MELTS to study crystallization of samples from Thjófahraun and Lambahraun in Iceland and to determine if the samples can possibly fall along a LLD. Their research suggests that MELTS can successfully model fractionation of the Thjófahraun samples. They investigate several different sets of conditions and determine best fit conditions that correspond with conditions predicted or observed in literature. They only show the best fit run (Figure 6.4).

Eason and Sinton (2009) find that Lambahraun samples from Iceland require crystal accumulation and other processes such as concurrent wall rock assimilation with crystallization and cannot be modeled by simple fractionation with MELTS. The following figure from their paper shows how MELTS runs do not match measured data for CaO, Nb or Nb/Zr. Models of other processes fit better (Figure 6.5). These models will not be discussed here as they are not used in this MS thesis. Their work, however, shows that MELTS can be a useful tool in determining if it is possible for samples to form through simple fractionation alone. Misfit between the data and the model can indicate that other processes may be involved (Figure 6.5).

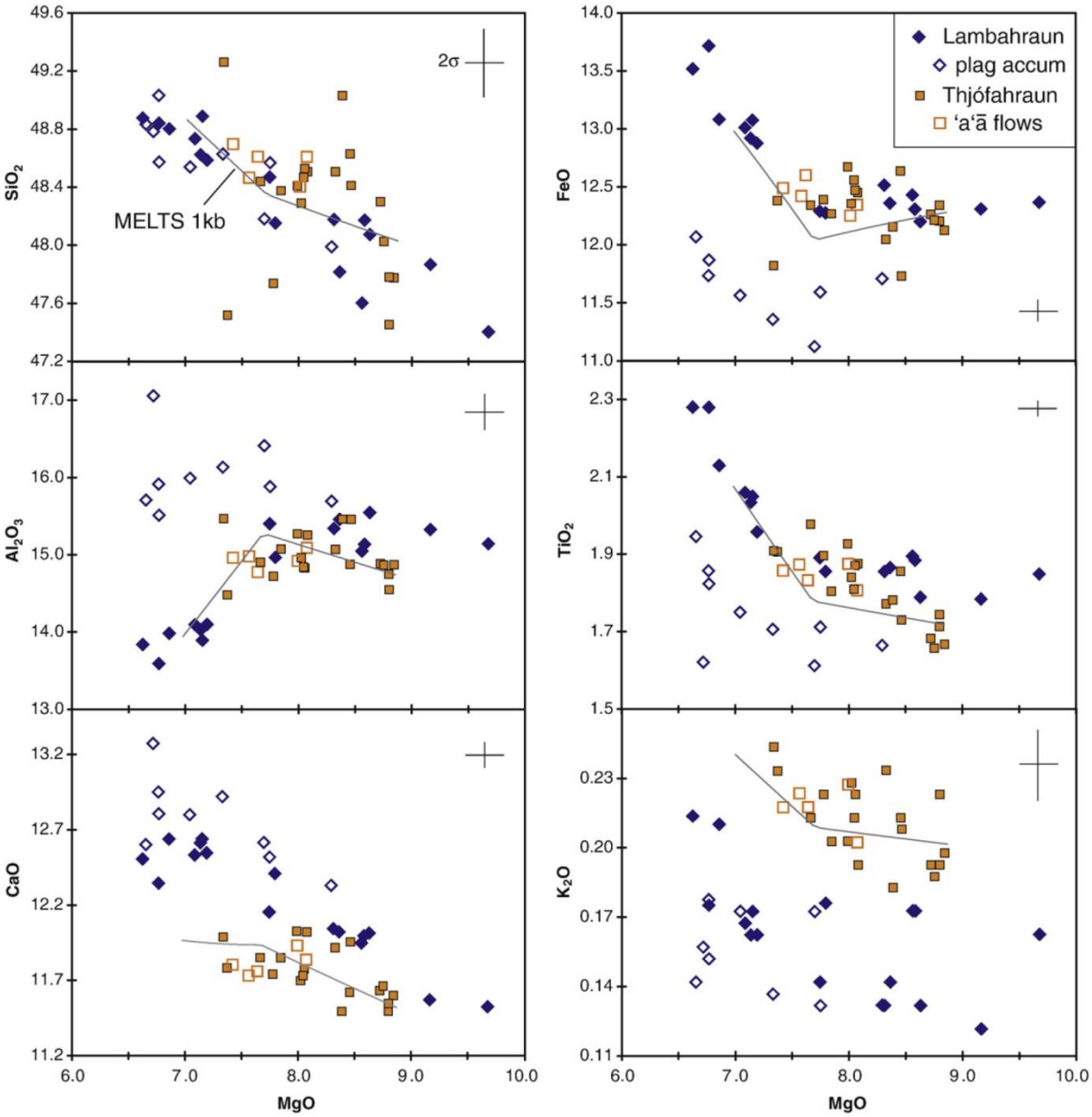


Figure 6.4 MELTS modeling of Thjófahraun lavas (orange squares). Open squares are 'a'ā flows from Thjófahraun. Diamonds are samples from Lambahraun. The line shows a MELTS run at 1 kb, 0.4 wt% $H_2O$, and QFM -2. Figure from Eason and Sinton (2009).

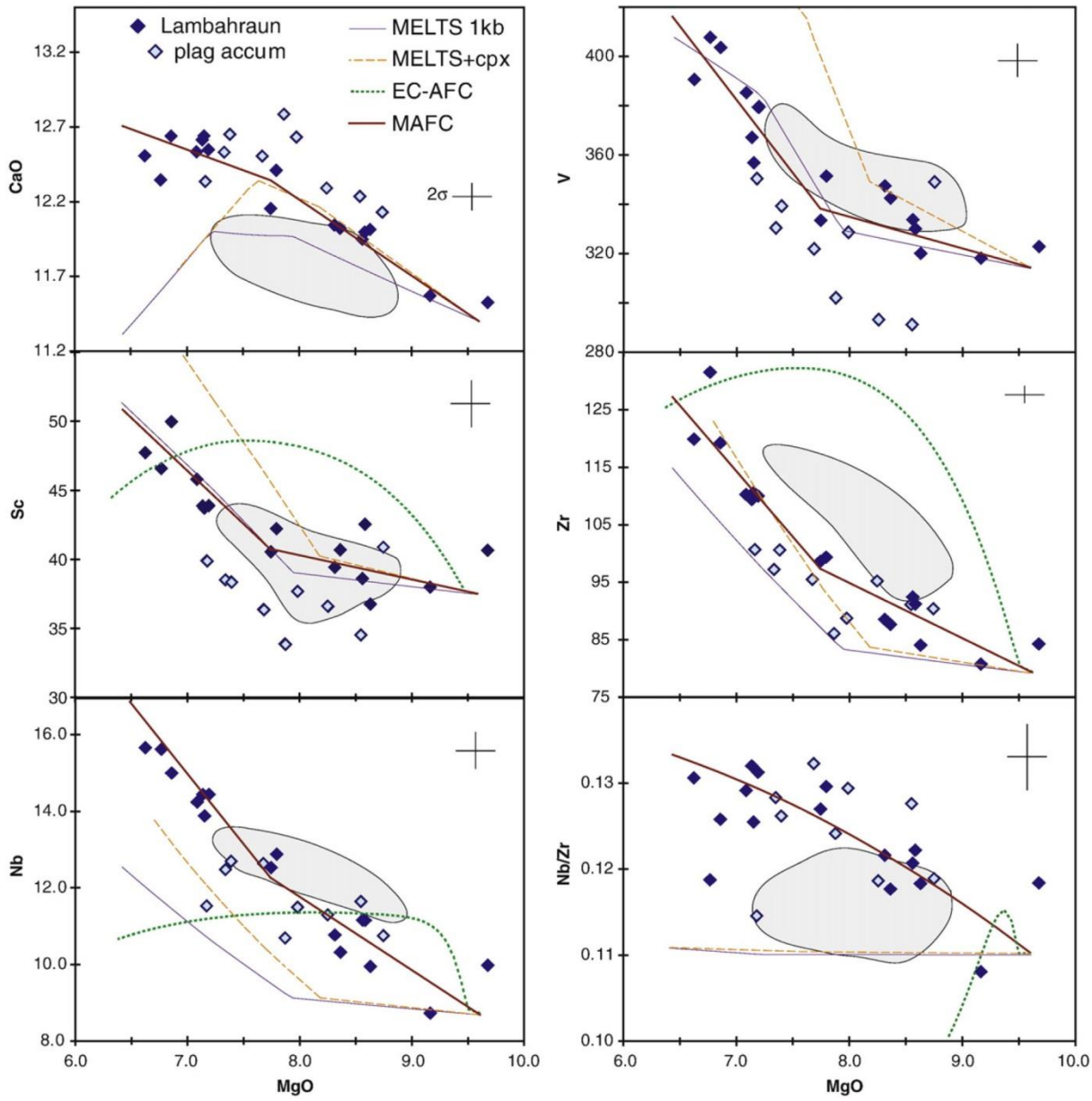


Figure 6.5. Various models compared to samples from Lambahraun. Data from Thjófahraun is shown as gray areas. The solid purple and dashed orange lines are MELTS models. The green line represents an energy constrained assimilation and fractional crystallization model (AFC). The red line shows a migrating assimilation and fractional crystallization model (MAFC) (See Eason and Sinton, 2009 for more information). They conclude that MELTS models do not match the data as well as other scenarios. Figure from Eason and Sinton (2009).

The previously discussed studies apply MELTS to systems that are much less oxidizing, less water rich, and closer in composition to MORB than the samples in this study. Papers that apply MELTS to the conditions or bulk compositions at or near arcs are less numerous. Zellmer et al. (2005) apply MELTS to an arc system in Santorini. Their goal was to see if magmatic evolution at Santorini could be modeled by closed system fractional crystallization. They used one of the less evolved samples as a starting composition. Based on literature values, they set the pressure (1-3 kbar), initial temperature (1160 $^0$C), and oxygen fugacity (QFM +1). They constrain water contents to ~0.7 wt%) at these conditions. They found that MELTS could model closed system fractional crystallization to andesitic compositions (up to 58-60 wt%). Increasing the pressure to 3 kbar did not significantly improve the model for the higher $SiO_2$ range. Further differentiation probably involved different processes, such as magma mixing or assimilation. They evaluated the fit of the model by comparing the predicted results to whole rock data (Figure 6.6).

Zellmer *et al*. (2005)'s success at modeling one portion of the fractionation history of their magmas suggests that MELTS can be applied to the more water rich and oxidized systems found at and near arcs.

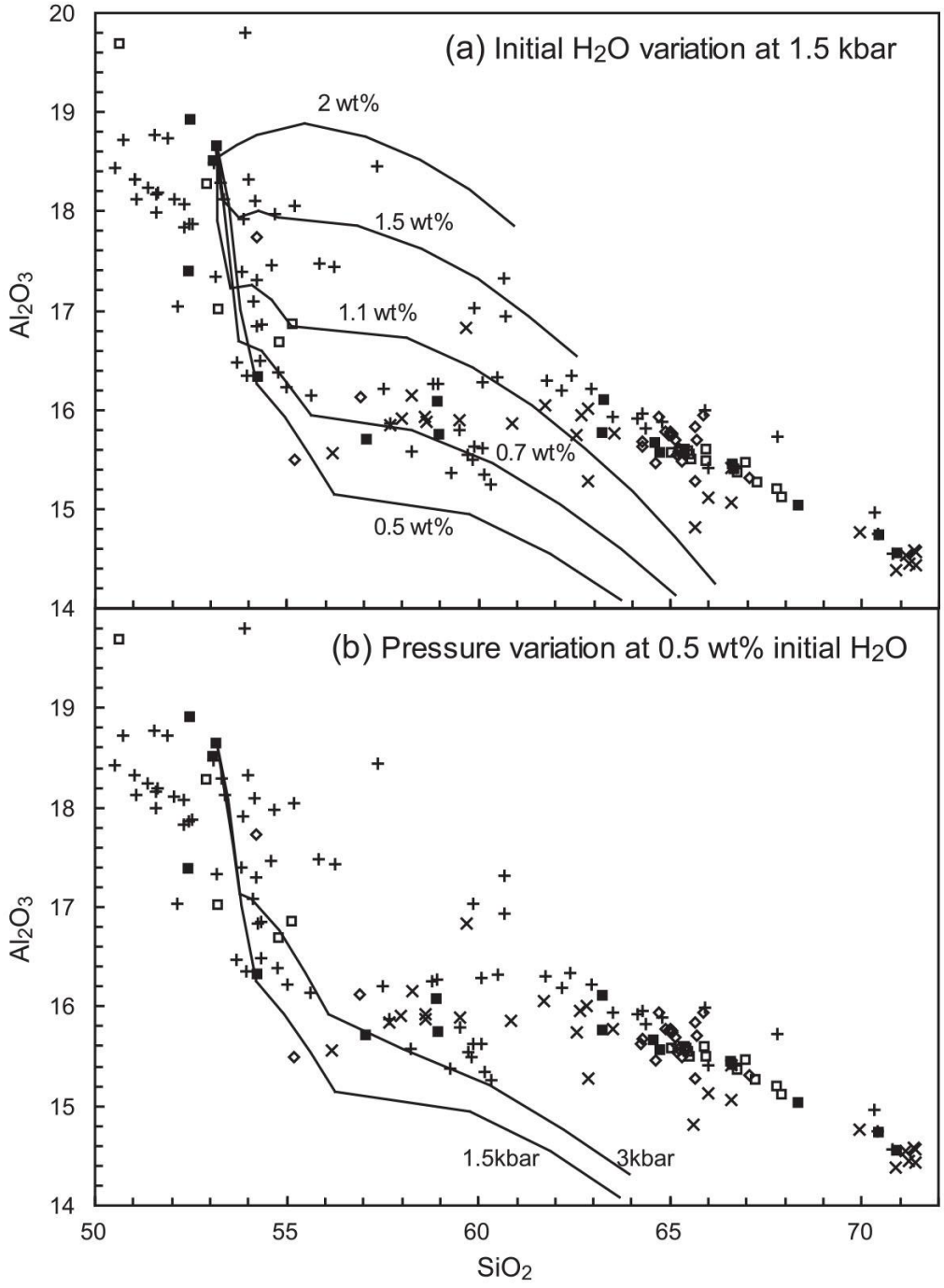


Figure 6.6. Whole rock samples from Santorini compared to MELTS models. Different symbols represent different eruptive cycles. Each MELTS run is labeled with the set pressure value used (See Zellmer *et al.*, 2005 for more details on conditions used and data sources). Figure from Zellmer *et al*. (2005).

## Methods and Additional Information about using MELTS

### Using and Interpreting Data from MELTS

MELTS uses experimental data and thermodynamic models to model crystallization of a melt, using an initial composition and water content with constant pressure and oxygen fugacity conditions provided by the user. The run starts with an initial temperature provided by the user and all components in the system are calculated for increments of change in temperature. After each increment, MELTS calculates the mineral phases formed, their proportions, and compositions, as well as the composition and proportion of residual melt. This section overviews the types of modeled data that is provided for MELTS and how this data can be interpreted. For this section, a best fit modeled run at a pressure of 500 bars, at QFM, at a temperature range of 1300-900°C, and with a starting composition similar to the most magnesium-rich west Mata samples and a water content of 2.0 wt% is used as an example. Oxygen fugacity can be thought of as a measure of how oxidizing or reducing the system is. It can be measured to several buffers, one of which is the QFM system. Discussion of how 'good fit' is determined is provided in the following sections.

The following plot of $SiO_2$ vs. MgO in the residual melt shows how the composition of the residual melt changes as crystallization occurs (Figure 6.7). This run begins with a composition between 6 and 7 wt% MgO and between 55 and 56 wt% $SiO_2$. As crystallization continues, the MgO content of the residual melt decreases while the $SiO_2$ of the residual melt content increases. The decrease in MgO represents the fact that Mg is incorporated into the crystals that are forming. While Si is also incorporated into the crystals, it is not being taken into the crystals as quickly as some other elements, so the overall concentration of $SiO_2$ relative to the other elements in the melt increases. Modeled compositions are provided for all elements from the user selected starting values.

MELTS also calculates the order of formation of minerals and their proportions. For the same run, Table 6.1 provides the range of temperatures over which the various crystal phases form. The first phase to form is olivine. In this example, olivine forms alone for a temperature range of 1137-1127 ºC, then at 1125 ºC, clinopyroxene begins to form along with olivine. At 1101 ºC, olivine stops forming and orthopyroxene begins forming along with clinopyroxene. At

1065 ºC, plagioclase feldspar starts forming along with clinopyroxene and orthopyroxene. These phases form together until the end of the run.

The following plots (Figures 6.8-6.10) show the effect that the crystallization of these phases has on the melt composition for several elements. Different elements are more strongly affected by different minerals. For example, the concentration of CaO in the melt is strongly affected by formation of clinopyroxene, which contains Ca. When clinopyroxene starts to form, the CaO content of the residual melt starts to decrease. The concentration of $Al_2O_3$ in the melt is affected by the formation of plagioclase feldspar, which contains Al. When plagioclase feldspar starts to form, the concentration of $Al_2O_3$ in the melt starts to decrease.

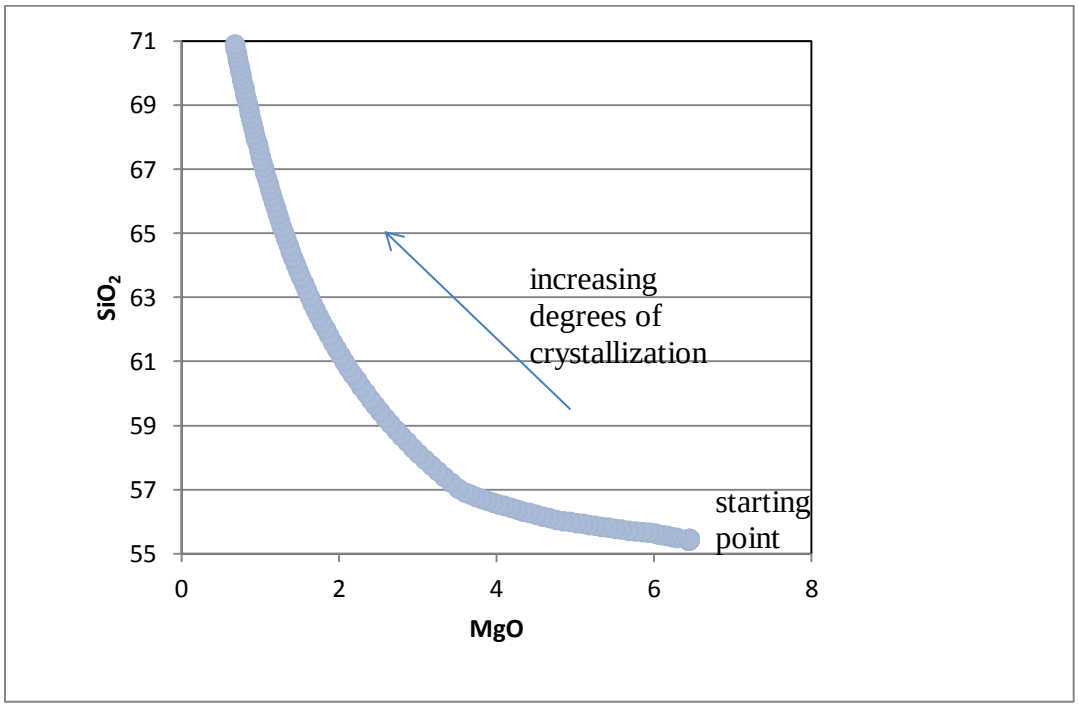


Figure 6.7. $SiO_2$ vs. MgO content in a modeled residual melt. The line represents a LLD formed by crystallization of a parent melt with a starting composition between 6 and 7 wt% MgO and between 55 and 56 wt% $SiO_2$. With increasing degrees of crystallization, the MgO content of the residual melt decreases and the $SiO_2$ content of the residual melt increases. This MELTS model is run at a pressure of 500 bars, at QFM, at a temperature range of 1300-900ºC, and with a starting composition similar to the most magnesium-rich west Mata samples and a water content of 2.0 wt%.

Table 6.1. Temperature range (in °C) in which various crystal phases form in the example MELTS run

| Temperature Range (°C) | Crystals Formed |
|---|---|
| 1301-1139 | None |
| 1137-1127 | Ol |
| 1125-1101 | Ol + CPX |
| 1099-1067 | CPX + OPX |
| 1065-901 | CPX + OPX + Plag |

During the first temperature range (1301-1139°) no crystals form and only melt is present. Crystal phases are: Ol (olivine), CPX (clinopyroxene), OPX (orthopyroxene), and Plag (plagioclase feldspar)

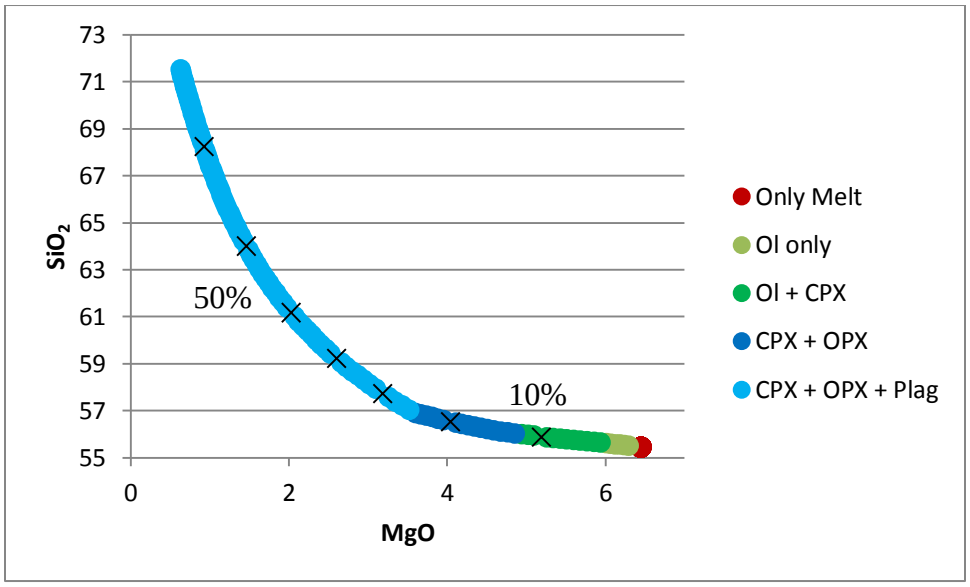


Figure 6.8. $SiO_2$ vs. MgO content of the residual melt in a model MELTS run. The line represents a LLD formed by crystallization of a parent melt with a starting composition between 6 and 7 wt% MgO and between 55 and 56 wt% $SiO_2$. Crystal phases are: Ol (olivine), CPX (clinopyroxene), OPX (orthopyroxene), and Plag (plagioclase feldspar). The slope of the line is relatively constant until plagioclase feldspar starts to form. The black X marks indicate degrees of crystallization in increments of 10% crystallization. This MELTS model is run at a pressure of 500 bars, at QFM, at a temperature range of 1300-900°C, and with a starting composition similar to the most magnesium-rich west Mata samples and a water content of 2.0 wt%.

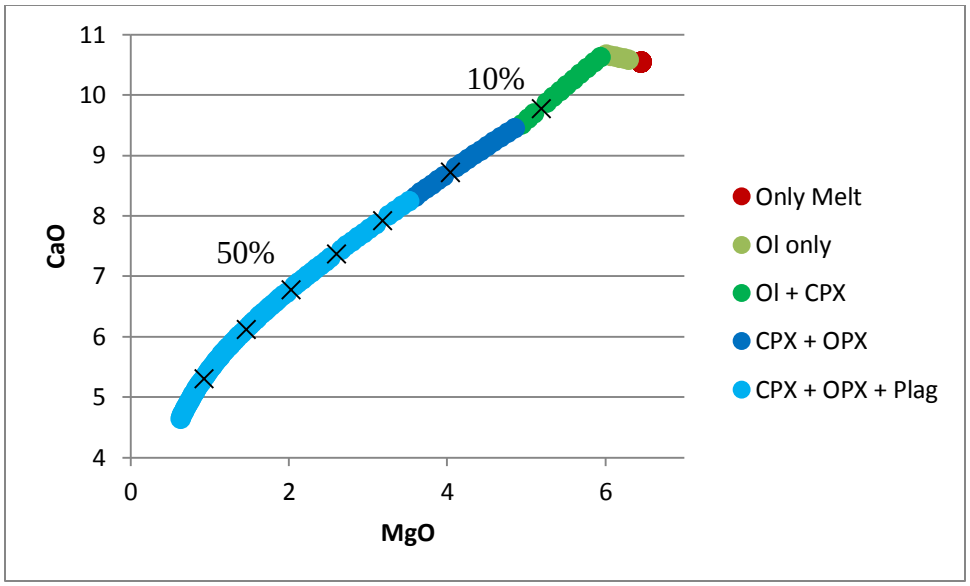


Figure 6.9. CaO vs. MgO content of the residual melt in a model MELTS run. Crystal phases are: Ol (olivine), CPX (clinopyroxene), OPX (orthopyroxene), and Plag (plagioclase feldspar). The CaO content of the melt increases slightly while only olivine forms. When clinopyroxene, which contains Ca, starts to form, the CaO content of the melt begins to decrease. It continues to do so throughout the rest of the modeled run. Clinopyroxene forms for the remainder of the run. The black X marks indicate degrees of crystallization in increments of 10% crystallization. This MELTS model is run at a pressure of 500 bars, at QFM, at a temperature range of 1300-900°C, and with a starting composition similar to the most magnesium-rich west Mata samples and a water content of 2.0 wt%.

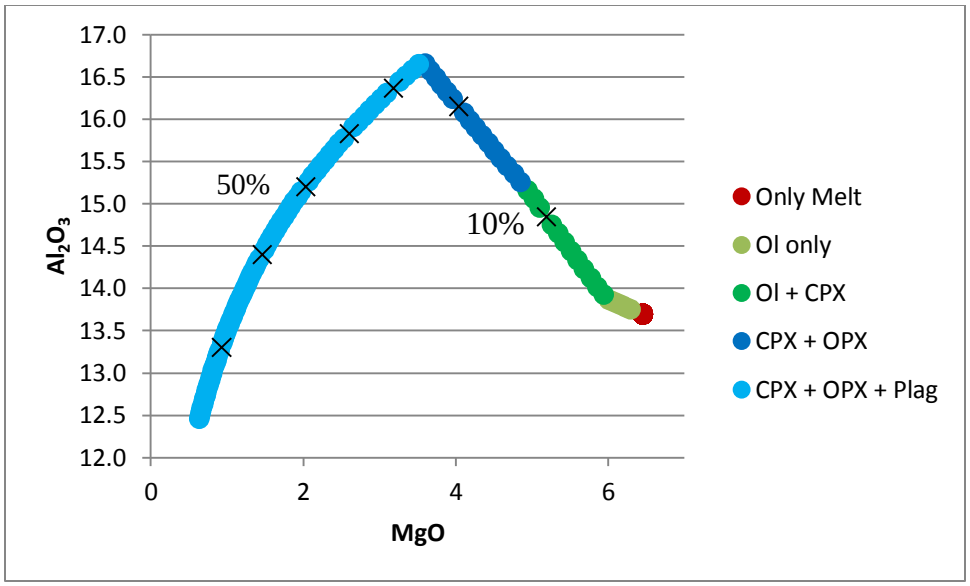


Figure 6.10. $Al_2O_3$ vs. MgO content of the residual melt in a model MELTS run. Crystal phases are: Ol (olivine), CPX (clinopyroxene), OPX (orthopyroxene), and Plag (plagioclase feldspar). The $Al_2O_3$ content of the residual melt increases until plagioclase feldspar starts to form. This is because the other minerals do not contain significant amounts of Al and plagioclase feldspar does. The black X marks indicate degrees of crystallization in increments of 10% crystallization. This MELTS model is run at a pressure of 500 bars, at QFM, at a temperature range of 1300-900°C, and with a starting composition similar to the most magnesium-rich west Mata samples and a water content of 2.0 wt%.

**MELTS Modeling Methods for this Project**

In this project, MELTS is used to model the final stages of crystallization of phenocrysts in melts from the Mata Volcanoes. To do so, a modeled melt is allowed to cool under a constant pressure and oxygen fugacity. The melt starts at a temperature of 1300 $^0$C and cools to 900$^0$C at increments of 2 $^0$C. The results from this modeling are compared to observations of the types of minerals present in the samples and the composition of volcanic glass in the samples. A summary of observations relevant to MELTS modeling is provided in the following section.

The starting composition used for most runs is similar to the more magnesium-rich West Mata samples. Theoretically, these samples would be the least evolved and the most similar to the original parent melt. These are similar to the most magnesium-rich samples from the most of the other Mata volcanoes. An exception is Mata Fa, which has a distinctly higher $TiO_2$ content. A few samples from the other Mata volcanoes have slightly higher MgO contents, such as some samples from Mata Ua. For more detail, see Chapter Four. Initial compositions similar to the more magnesium-rich samples from the other Mata Volcanoes were also tested at the best fit conditions for the West Mata runs to determine if these conditions work for the compositions at the other volcanoes.

I used melts templates, a MELTS file, command file, and a batch file, written by Deborah Eason to facilitate running these models. Most runs were done as batch crystallization runs. A few runs were conducted as fractional crystallization runs for comparison. Both yield similar results. In batch crystallization, newly formed crystals remain in the melt, while in fractional crystallization, newly formed crystals are instantly removed, preventing them from reacting with the melt.

**A Summary of Observed Data for the Mata Volcanoes**

A detailed description of data collected on the Mata Volcanoes is included in Chapters Three and Four. This section summarizes findings presented in more detail in those chapters.

Collected samples consist primarily of vesicular volcanic glass. The main phenocryst phases are olivine, orthopyroxene, and clinopyroxene. These three main phenocryst phases are observed in almost all of the samples. Olivine is not present in some of the most evolved

samples. Clinopyroxene and orthopyroxene are also common as groundmass phases. In contrast, plagioclase is only found in minor amounts as a groundmass phase in some samples. Careful petrographic study under the microscope and by backscattered electron imaging indicates that many samples do not have any plagioclase present (See Chapter Three for more details). This suggests that the three main mineral phases (olivine, clinopyroxene, and orthopyroxene) were present on the liquidus before the onset of plagioclase crystallization. While formation of the final groundmass crystals may have coincided with the beginning of plagioclase crystallization in some lavas, crystallization of the three main phases must have started before the beginning of plagioclase crystallization. Visual analysis of glass and matrix from Mata samples determined which samples contained minor amounts of plagioclase. EPMA analysis of samples provided the MgO contents of these melts. By comparing the MgO contents of samples that contain minor amounts of plagioclase and those that do not, it was determined that plagioclase starts to form at approximately a MgO content of 4.5 wt%. It should be noted that this observation has limitations. The samples are from a variety of volcanoes. Additionally, samples from West Mata are known to be from at least two eruptions. Thus, the samples are not from the same parent melt. However, as will be discussed further below, the different parent melts probably had similar major element compositions. Furthermore, the conditions of their crystallization were probably similar. So it is not unreasonable for plagioclase to start forming at a similar MgO in various melts.

A variety of phenocryst textures were observed in olivine, clinopyroxene, and orthopyroxene phenocrysts. These range from euhedral crystals to anhedral inclusions that may be resorbed. Some crystals occur as individuals while others are intergrown or included in other crystals. Some crystals show evidence of rapid growth. Unzoned, normally zoned, reversely zoned, and oscillatory zoned crystals are present. A range in crystal textures can be found at a single volcano and within an individual thin section. This range in crystal textures suggests that magma mixing may have been a significant process during the period of crystallization of these melts.

The composition of volcanic glass and whole rock were also determined as part of this study. The volcanic glass composition represents the composition of the residual liquid which had not crystallized at the time of eruption. Since this study only focuses on the last stages of

crystallization, only the volcanic glass analysis will be discussed here. Various oxide vs. MgO plots are presented in Chapter Four to study the volcanic glass compositions. Interestingly, some of these plots, such as CaO vs. MgO show a distinct trend for all of the samples from the various Mata Volcanoes which resembles a LLD or several subparallel LLDs (Figure 6.11). However, investigation of other plots, such as $TiO_2$ vs. MgO, show deviation of some samples from a single trend (Figure 6.12). This suggests that the samples may not be related to each other by simple fractionation from a single parent melt.

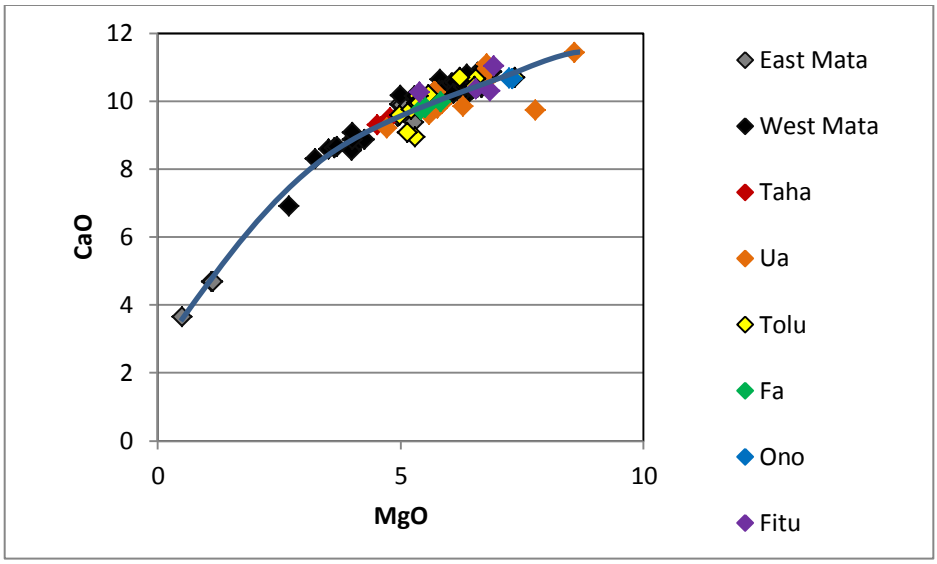


Figure 6.11. CaO vs. MgO for the Mata Volcanoes. Most of the samples from the Mata Volcanoes seem to fall along a single LLD or along several subparallel LLDs. The blue trend line is not a quantitative model but drawn to represent the apparent LLD of the samples.

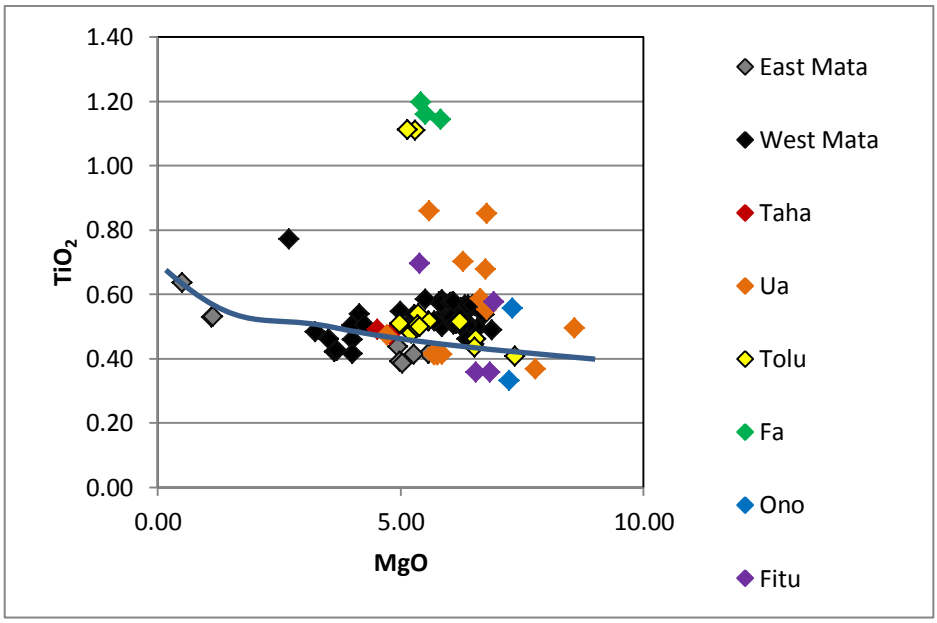


Figure 6.12. $TiO_2$ vs. MgO for the Mata Volcanoes. Some of the samples from the Mata Volcanoes seem to fall along a single LLD or along several subparallel LLDs. However, other samples deviate very dramatically from the main trend. For example, note the three samples from Mata Fa, which have a much higher $TiO_2$ content than other samples with a similar MgO content. The blue trend line is not a quantitative model but drawn to represent the apparent LLD of some of the lower $TiO_2$ samples. It is possible that the sample suite could fall along multiple LLDs. Mixing of magmas is also possible.

**Evaluating the Fit of the Model Using Observed Data**

In batch crystallization MELTS runs, oxygen fugacity, water content and pressure were varied systematically over more than 40 individual runs and modeled liquid compositions and crystal phases were compared to observed glass data. Several key constraints were used to evaluate the model runs.

Given a specific pressure (pressure will be discussed in more detail in the pressure section of this chapter), three primary constraints were used to evaluate if the model was a good fit for the data. The first constraint used to evaluate the model was the crystal phases that the model produced. The major mineral phases in most Mata samples are olivine, clinopyroxene, and orthopyroxene. Only modeled runs in which these three phases formed were then further evaluated based on other constraints. A second constraint was the order of crystal formation, particularly if plagioclase started to form before one of the main crystal phases. Model runs were only accepted if the beginning of plagioclase crystallization occurred after the three main mineral phases had started to form. A third constraint was the melt MgO content at which modeled plagioclase started to form. Plagioclase forming at lower MgO content, approximately 4.5 wt% MgO or lower, was used as a guide for modeling.

The advantage of using these three main constraints based on the crystal phases formed over focusing on the composition of the residual melt is that that these same crystal phases are present in most of the samples collected at the Mata Volcanoes. Thus, this constraint is not dependent on all of the Mata Volcanoes sharing the same parent melt. In order to use liquid compositions to determine the conditions of formation, it would first be necessary to determine if the samples were related to the same parent melt or parent melts.

A comparison of modeled residual melt contents to measured glass data was used after determining water content and oxygen fugacity to study crystallization of the samples and to determine if they could have formed from crystallization of a single parent melt. Modeled trends, for example $SiO_2$ vs MgO, were graphed with observed data and visually evaluated for fit and to see if samples could have crystallized from a single parent melt. Modeled liquid compositions are compared to Mata glass data to try to determine the pressure of crystallization of these samples, which will be discussed in more detail later in this chapter.

## Results

### Evaluating conditions of crystallization

To constrain conditions of crystallization, the conditions were varied and resulting model runs were compared to observations about the Mata Volcanoes. The two primary constraints were: 1. The model produced all of the observed phenocryst phases (olivine, clinopyroxene, and orthopyroxene), 2. The three observed phenocryst phases formed before plagioclase started to form. Formation of plagioclase at low MgO contents (less than 4.5 wt%) was used as an additional check. The samples from the various Mata Volcanoes are treated as a group during this analysis because, despite the fact that they likely have different parent melts, most sample contain the same main phenocryst phases. This suggests that the same crystal phases are forming at the Mata Volcanoes. By focusing on the crystal phases, the whole group can be studied despite potential differences in parental melt compositions. Two conditions were systematically varied: oxygen fugacity and initial water content. These conditions were run at two pressures, 500 and 1000 bars. Pressure will be discussed in the following section. The starting composition was similar to the most magnesium-rich West Mata samples.

Figures 6.13 summarizes conditions tested at these two given pressures. The red dots represent sets of conditions that are not good models because all three of the main mineral phases did not form. Yellow dots represent runs that are a better, but not ideal approximation. This includes runs where plagioclase formed too early or where olivine only formed for less than a 5 °C range. Runs that are the best approximations are colored green. These are the runs in which all of the constraints discussed above were met.

The best fit conditions at a pressure of 500 bars are water contents of 1.7 wt% or higher in the starting composition and an oxygen fugacity of QFM. At an initial water content of 2.0 wt%, MELTS predicts that water is saturated in the system, which does not match actual arc magma data, so the upper limit of water content cannot be determined by MELTS. Magmas from subduction zones are known to be more water rich than those from mid ocean ridges or backarc settings. For example Kelly and Cottrell (2009) measure water contents in melt inclusions from all three settings, finding ranges of 0.14 to 0.49 wt% in MORB, 0.57 to 1.89 in backarc basin basalts, and 2.23 to 5.39 wt% in arc samples. This entire range is greater than the

saturation point of water predicted by MELTS in this study. If the Mata magmas had a similar starting water content to the arc magmas measured by Kelley and Cottrell (2009), this would suggest that MELTS is not accurately predicting the range of water contents in Mata parent magmas. However, the work in this thesis is only investigating the last stages of crystallization using glass data rather than whole rock data and thus is probably representing a later stage of the melt than that investigated by previous studies. For comparison, Danyushevsky and Sobolev (1995) measured the water content of homogenized melt inclusions in olivine in boninites from the Lau Basin and obtained water contents of approximately 2 wt%. To better constrain a range or possible maximum water content in parent magmas, additional work could be done. The water contents of melt inclusions in olivine or pyroxene crystals could be analyzed. This work could compliment the MELTS work in this thesis, but is beyond the scope of this thesis.

The best fit conditions at a pressure of 1000 bars are water contents of 2.5 or higher in the starting composition and an oxygen fugacity of QFM +1. Water is saturated in the system at an initial water content of 3.0 wt%. This is within the range measured by Kelley and Cottrell (2009) in arc magmas.

As an additional test to verify that these conditions worked for the other Mata Volcanoes, a test run using one of the best fit conditions of 2.0 wt% water and at QFM was conducted with a starting composition close to the composition of a more magnesium-rich sample or samples similar to the compositions of the other volcanos. If one sample had a much lower MgO content, this sample value was used. If two samples were very similar, an average was used. The predicted mineral data was compared to samples and predicted residual melt compositions were compared to measured glass for the volcano of interest.

For Matas Ua, Tolu, Ono, and Fitu, the best fit conditions work very well. The main phenocryst phases all formed before the onset of plagioclase crystallization. For the other volcanoes, some differences were noted. For both East Mata and Mata Taha, no olivine forms in the model. This is because the most magnesium-rich sample from these two volcanoes has a lower MgO content than Matas Ua, Tolu, Ono, and Fitu. This is past the range of MgO content over which olivine forms in the model. Despite this, the best fit conditions appear to be a reasonable approximation for these volcanoes. Interestingly, for the East Mata starting

composition, orthopyroxene starts to form before clinopyroxene. This is the opposite of the order observed in the best fit runs for the other volcanoes' starting compositions. For the Mata Taha run, orthopyroxene forms late, just after plagioclase starts to form. There are only two samples from Mata Taha and they are very similar in composition. Additional sampling would be required to determine if these samples are representative of this volcano as a whole and then if the apparent difference in the runs is real and is present if other, more magnesium-rich samples are found and used as starting compositions. Using the Mata Fa starting composition, orthopyroxene does not form. There are only three glass samples from Mata Fa, which are very similar in composition. Again, additional sampling would be required to determine if the differences in the models are significant. For the best sampled volcanoes, West Mata, Mata Ua, and Mata Tolu, these conditions appear to be a good fit. Additional samples would be required at the other volcanoes to tell with more certainty if the best fit conditions work at those volcanoes. However, this preliminary investigation does not indicate significantly different conditions of crystallization at the different Mata Volcanoes.

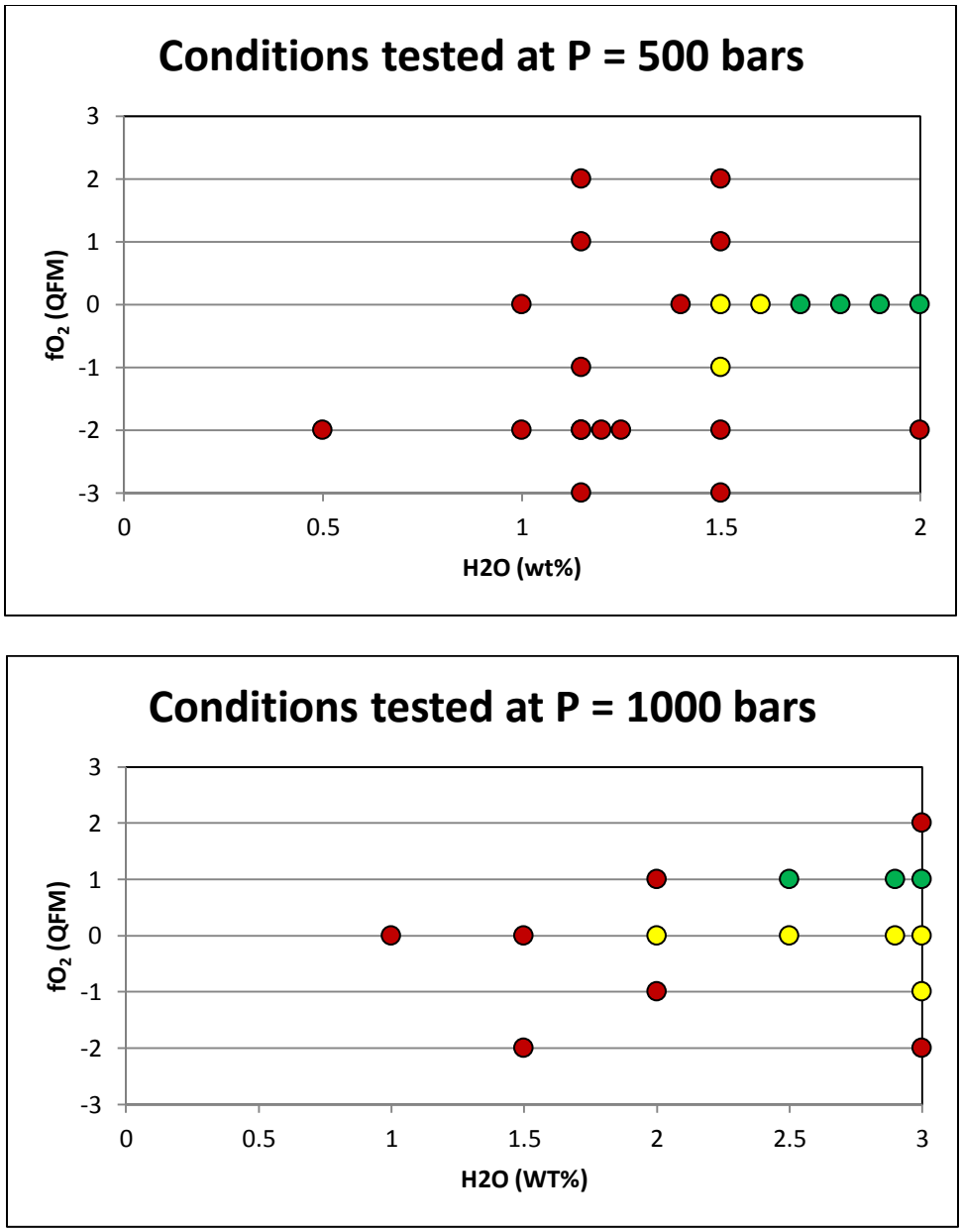


Figure 6.13. Conditions tested at 500 and 1000 bars. Red dots indicate runs that do not approximate the observed data because the three main mineral phases observed in samples did not form. Yellow dots represent runs that are a better, but not ideal approximation. Runs that are the best approximations are colored green. See text for more details. At higher water contents, MELTS is saturated in water, so graphs cut off at the saturation point of water, 2.0 wt% at 500 bars and 3.0 wt% H2O at a pressure of 1000 bars.

**Constraining the Pressure of Crystallization**

To constrain the best fit pressure of formation, runs were conducted at varying pressures while the other conditions were held constant; these runs were compared to each other. Changes in pressure affected the LLD of the models, particularly for $SiO_2$. At higher pressures, more pyroxene forms than olivine. Pyroxene incorporates more $SiO_2$ than olivine, so the higher percentage of pyroxene crystallizing at higher pressures causes the $SiO_2$ content of the higher pressure melt to be lower than that of a lower pressure melt. This can be seen in experimental work, such as that of Presnall *et al*. (1978), where the stability field of olivine is smaller at lower pressures. However, most of this effect was strongest at lower MgO (below MgO of 2 or 3 wt%). The modeled liquid line of descent is most affected at lower MgO (below MgO of 2 or 3 wt%, Figure 6.14).

Based on the data available, the best fits are at lower pressures of 500 or 1000 bars. At higher pressures, the liquid line of descent does not match the few lower MgO samples well, suggesting that the magmas at the Mata Volcanoes possibly crystallized under lower pressures. However, this is based on only a limited data set. There are only very few samples in this range (only three samples have less than 2.0 wt% MgO) and all of these samples are from East Mata. Using these samples to constrain pressure would require the assumption that they have the same or similar parent melt as the more boninitic, less evolved samples. In the future, it is possible that if low MgO samples are recovered from other volcanoes, MELTS models can be run for higher pressures and compared to runs at 500 or 1000 bars to refine the model. Additional data would be required to better constrain the pressure of crystallization using MELTS. Alternate methods for determining pressures of crystallization that are beyond the scope of this thesis include measurements of volatiles in melt inclusions, which could be used to determine pressures of entrapment and thus pressures of crystallization.

Despite the limited amount of data available to constrain the pressures of crystallization using MELTS, for the purposes of this master's thesis, a pressure range of 500 to 1000 bars was used in the MELTS models to constrain water content and oxygen fugacity. Additional work could assume higher pressures and try to constrain best fit conditions at those pressures, but this work is beyond the scope of this thesis. Additionally, the inferred pressure range of 500 to 1000

bars is used for thermometric calculations (Chapter Five). Variation in pressure had a very minor effect on the thermometry results, within the uncertainty of the thermometers, and thus uncertainties in the best fit pressures of crystallization are not expected to greatly impact the results of thermometry work in this master's thesis (see Chapter Five for more detail).

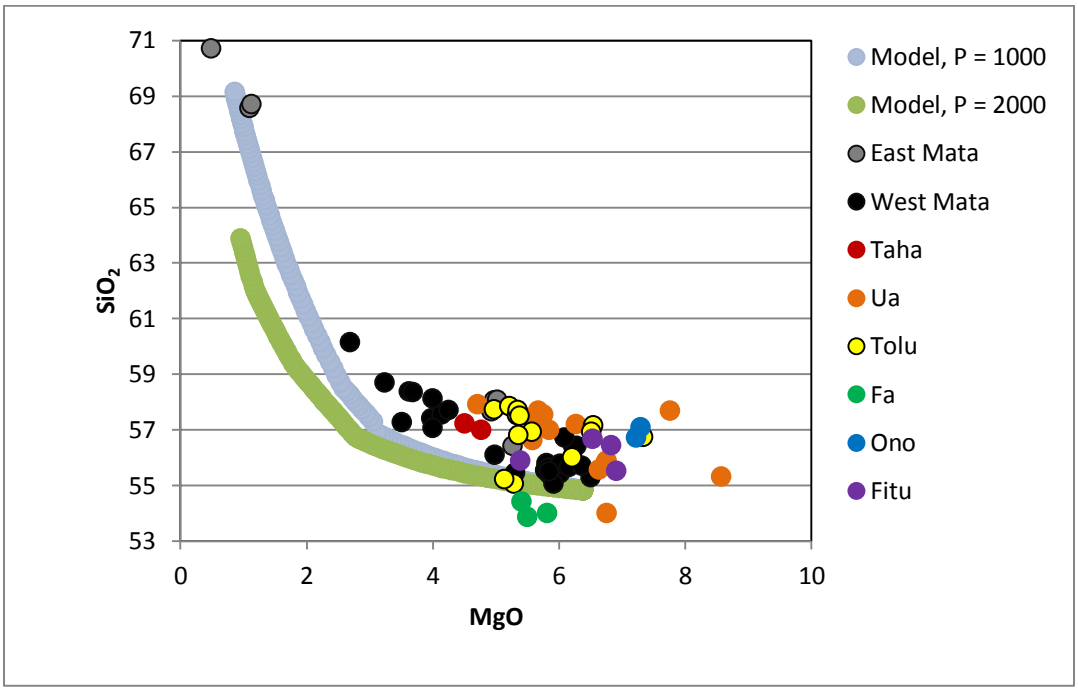


Figure 6.14. Comparison of $SiO_2$ vs MgO to measured glass data for two models run at different pressures, 1000 and 2000 bars. At higher pressures, the modeled liquid line of descent moves further away from the few data points available at low MgO contents.

**Evaluating a "Good" MELTS Run in more Detail**

One of the best fit MELTS models will now be discussed in more detail through a comparison of predicted residual melt composition to measured volcanic glass contents from the Mata samples. This model is run at 500 bars, at QFM, and with a water content of 2.0 wt%. The starting composition for this run is based on the most magnesium-rich West Mata samples. This section will discuss data for five oxides: $SiO_2$, CaO, $TiO_2$, $Al_2O_3$, and MgO. These oxides are presented in oxide vs. MgO plots below (Figures 6.15-6.18). Note that when water is added into the starting composition, MELTS recalculates the bulk composition to 100%. If the provided bulk composition of oxides plus water is more than 100%, the effect is that the percentage of the oxides are slightly lowered. $SiO_2$ is particularly affected. $SiO_2$ continually increases along the modeled LLD as other elements are removed by crystallization, increasing the relative concentration of $SiO_2$ to other elements in the residual melt. CaO consistently decreases in the modeled LLD, representing its removal by the formation of clinopyroxene. Clinopyroxene forms from almost the beginning of the run and continues to form until the run ends (Figure 6.15). $Al_2O_3$ increases in concentration in the residual melt until plagioclase feldspar starts to form (Figure 6.16). $Al_2O_3$ does not readily partition into the earlier forming phases of olivine, clinopyroxene, and orthopyroxene and thus, its relative concentration in the residual melt increases as other elements are removed from the melt by crystallization

For CaO vs. MgO, all samples fall on or near the modeled LLD. However, for other elements, such as $Al_2O_3$ and $TiO_2$, many of the samples do not fall on the modeled LLD. The following section will discuss this further and will discuss the possibility that some of the samples may have different parent melts.

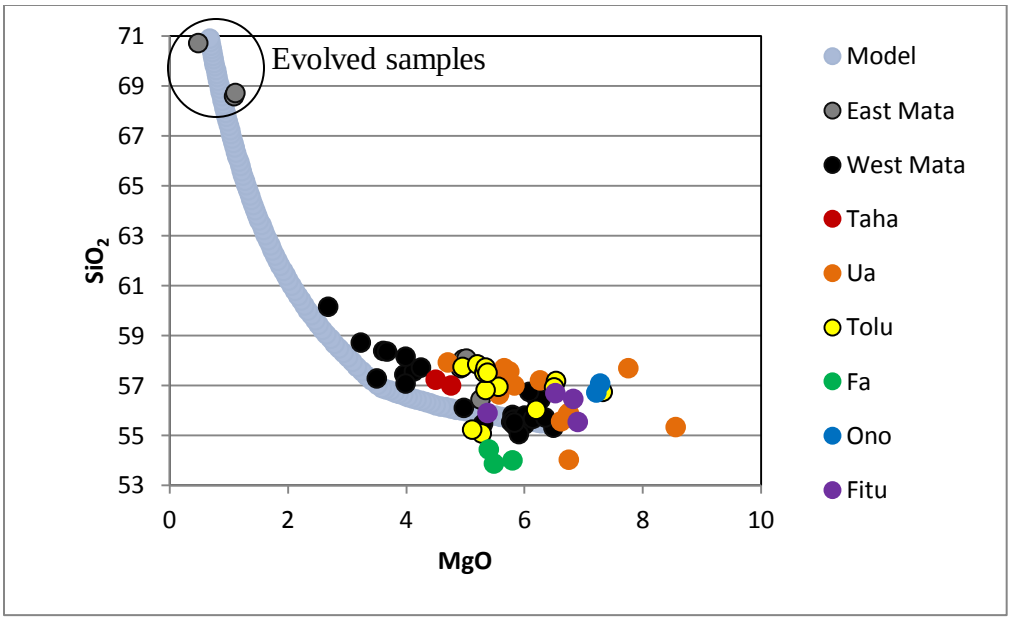


Figure 6.15. Comparison of $SiO_2$ vs MgO for a best fit MELTS model and measured glass data. Most data plot very close to the modeled LLD. This MELTS model is run at a pressure of 500 bars, at QFM, and with a starting composition similar to the most magnesium-rich west Mata samples and a water content of 2.0 wt%. The more evolved samples are indicated. The error on $SiO_2$ measurements based on repeated measurements of standard VG-2 is ±0.27, approximately the size of symbols in this diagram.

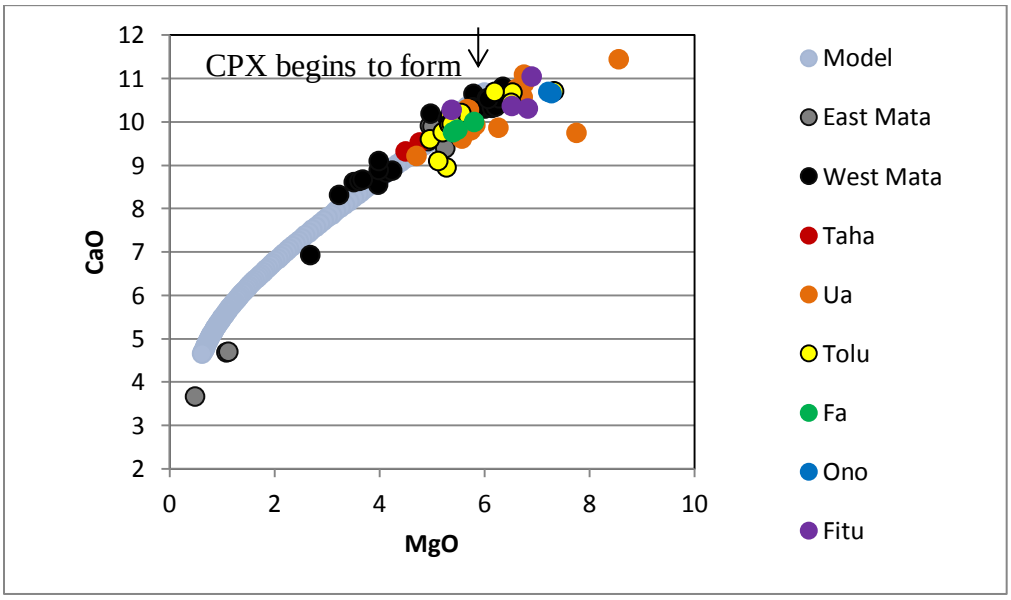


Figure 6.16. Comparison of CaO vs MgO for a best fit MELTS model and measured glass data. Most data plot very close to the modeled LLD. This MELTS model is run at a pressure of 500 bars, at QFM, and with a starting composition similar to the most magnesium-rich west Mata samples and a water content of 2.0 wt%.

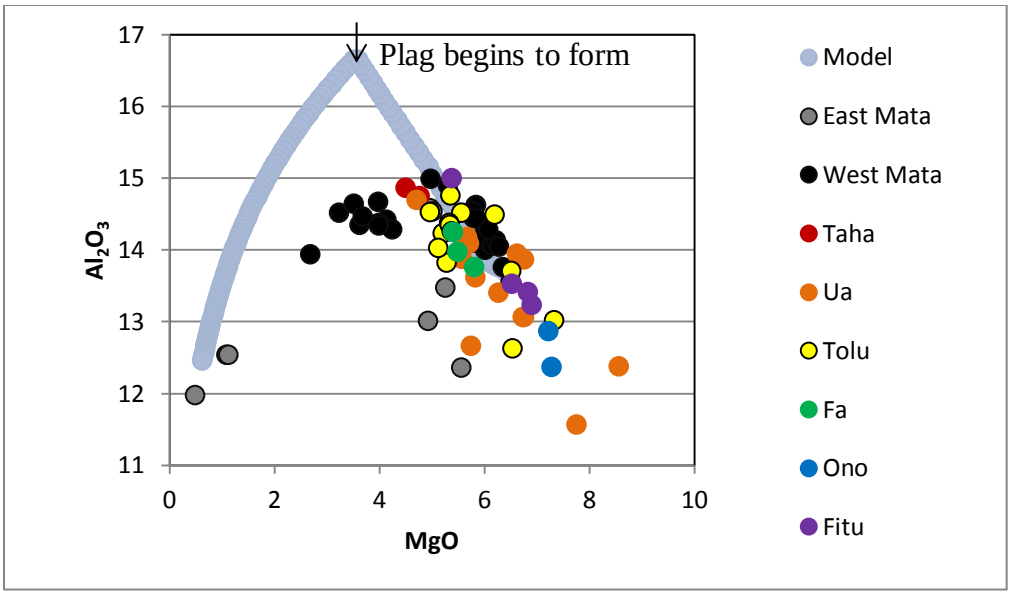


Figure 6.17. Comparison of $Al_2O_3$ vs MgO for a best fit MELTS model and measured glass data. Some of the data plot very close to the modeled LLD, while others deviate. Most notably, the lower MgO samples from West Mata do not fall along the modeled LLD. This MELTS model is run at a pressure of 500 bars, at QFM, and with a starting composition similar to the most magnesium-rich west Mata samples and a water content of 2.0 wt%.

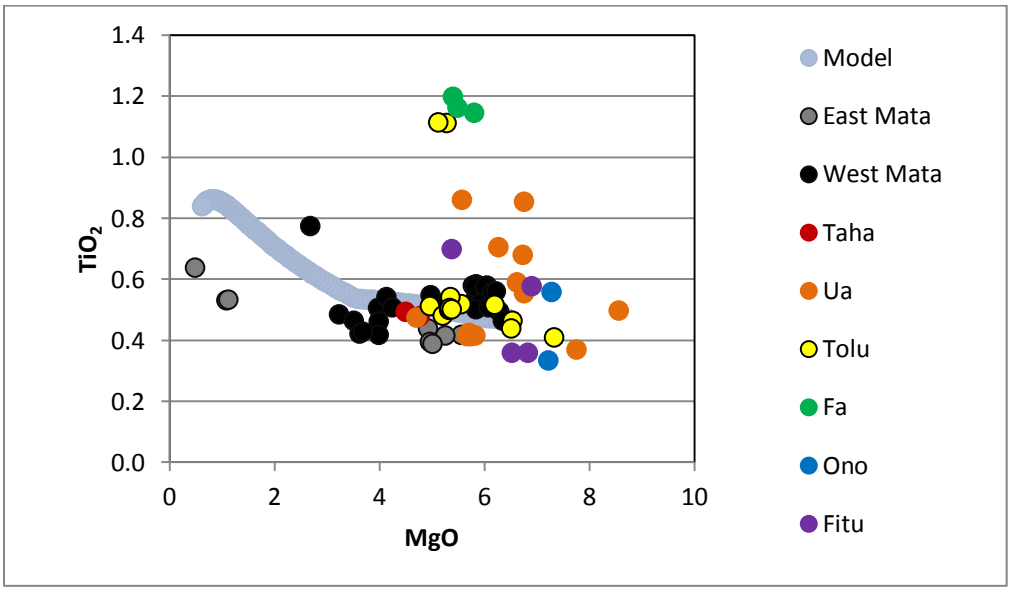


Figure 6.18. Comparison of $TiO_2$ vs MgO for a best fit MELTS model and measured glass data. Some of the data plot very close to the modeled LLD, while others deviate. Most notably, the lower samples from Mata Fa have much higher $TiO_2$ contents that most other samples and then the modeled line. This MELTS model is run at a pressure of 500 bars, at QFM, and with a starting composition similar to the most magnesium-rich west Mata samples and a water content of 2.0 wt%.

**Multiple Parent Melts**

Some samples do not fit modeled trends for certain elements, suggesting possible different parent melts. Specific examples will be explored below. However, when considering the Mata data, it is important to remember that the data comes from eight volcanoes and covers at least two eruptions at West Mata. Thus, it would not be expected that all of the samples evolved from the same parent magma.

This section will continue to base discussion on a model run at 500 bars and at QFM. The starting composition for these runs is based on the most magnesium-rich West Mata samples and a water content of 2.0 wt%. Models based on the other best fit conditions discussed above have similar trends and this discussion is relevant to those models as well.

Figure 6.14 plots $SiO_2$ vs MgO for the model run compared to all Mata data. The Mata data has a range in $SiO_2$ content of up to ~4 wt% at a set MgO content. This variation is not likely to be due to crystallization from a single parent melt. A more likely explanation is that lavas from several parent magma compositions have been sampled at some of these volcanoes. The cluster of samples slightly above and below the modeled LLD for $SiO_2$ could represent subparallel LLDs from these different parent magmas. The modeled line fits much of the higher MgO West Mata data as well as the Mata Fitu data. A subparallel modeled line starting with slightly higher $SiO_2$ and MgO contents would better fit data from Mata Ono and some of the data from Matas Ua and Tolu. However, the model line shown, or even a model that starts with slightly lower $SiO_2$ would better fit other samples from Matas Ua and Tolu. This suggests that lavas from several parent melts with slightly different compositions were erupted and sampled at these volcanoes.

Differences in compositions between some of the samples can be observed in other plots as well. For example, samples at West Mata can be divided into at least two groups, a higher MgO group which falls along the modeled LLD for $Al_2O_3$ and a lower MgO, higher $SiO_2$ group that distinctly falls off the modeled LLD for $Al_2O_3$ (Figure 6.17). Thus, these two groups are probably from two parent melts or two groups of parent melts with different compositions.

Multiple parent melts are required at some of the volcanoes to explain the differences in the observed trends for many elements between the data and the model. For example, the model shows only a slight increase in $TiO_2$ over the range of MgO contents studied. Ti is incompatible and is not incorporated in olivine and is only incorporated in minor quantities in pyroxenes. However, the data show significant variation in $TiO_2$ content, often over constant MgO content. For example, for Mata Ua and Mata Tolu, large variations in $TiO_2$ content at constant MgO suggest multiple parent melts for these samples (Figure 6.18). Similarly, samples from Mata Fa originate from a parent melt with a higher $TiO_2$ content than most of the Mata samples. It is possible that some of the spread in the $TiO_2$ concentrations result from mixing. For example, it is possible that especially for Mata Ua and Mata Tolu there were several different parent melts present with varying concentrations of $TiO_2$. These melts could have mixed together to varying degrees to produce the range in sample concentration in $TiO_2$. It is also possible that several distinct parent melts with varying concentrations of $TiO_2$ evolved to form these samples. It is known that samples represent at least two eruptions at West Mata, but it is unknown for the other volcanoes if samples are representative of one or multiple eruptions. It is difficult to determine if the range in $TiO_2$ data for these two volcanoes is the result of mixing of two end member parent melts, one with low $TiO_2$ and one with higher $TiO_2$ or if multiple parent melts with varying $TiO_2$ contents were present.

**Evolved Samples**

Most of the samples in this sample suite have a MgO concentration of greater than 2.0 wt%. However, three more evolved samples are very low in MgO content, with a MgO content of less than 2.0 wt%. These samples are circled and labeled on Figure 6.14. All of these samples are from East Mata, and are thus geographically close to the arc. These evolved samples are possibly related to the boninites by simple liquid lines of descent (Figures 6.15-6.18). This suggests that these samples may be differentiated from the boninites. Their petrography is also similar to the boninites. They contain both clinopyroxene and orthopyroxene in a glassy matrix. Unlike the boninites, olivine is not a major phase. However, this portion of the model is not well constrained due to a lack of samples. Very few evolved samples have been collected. This could be due to a sampling bias, as little sampling has been done on East Mata. Or it could

indicate that these more evolved rocks are less common than boninites. Additional sampling would be required to confirm if these samples are differentiated from boninites.

## Discussion

### Limitations of MELTS Modeling of Mata Samples

MELTS is primarily calibrated for MORB melts, not boninitic melts. The compositions of these two melts are very different. Importantly, MORB melts do not contain as much water as the Mata liquids probably do. The conditions under which they form also appear to be different, as the Mata boninites appear to crystallize at more oxidizing conditions than MORB liquids. Thus, one could anticipate potential problems with modeling the crystallization of the primarily boninitic Mata melts using the MELTS model.

Nevertheless, the MELTS program can be used to learn about crystallization of the Mata magmas. The phenocryst phases predicted by the model match those observed. Furthermore, the order in which they occur in the best fit models are consistent with interpretations of the order of crystal formation from observations of minerals present in the samples at various MgO contents. However, one limitation of the model is that the modeled mineral compositions do not closely match observed mineral compositions. For example, the Mg# of modeled olivine is lower than that of measured olivine. Finally, glass compositions predicted by the best fit models closely resemble measured volcanic glass compositions.

### Possible Roles of Fractionation and/or Magma Mixing

There are multiple interpretations that could potentially be used to explain observed trends in measured Mata glass data. To discuss these processes, a subset of the data will be discussed. First, $TiO_2$ will be compared to MgO for Ua and Tolu (Figure 6.19). These two volcanoes are chosen for this discussion as a range in melt $TiO_2$ contents are observed at both volcanoes. The model is shown for reference. MELTS does not predict a very rapid change in $TiO_2$ content until low melt MgO values, around 3.0 wt%, are reached. This is lower than the range of melt MgO concentrations observed for Matas Ua and Tolu. Over the range of the measured data, the $TiO_2$ content in the melt predicted by the model only slightly increases, compared to the MgO content in the melt. However, the data shows a wide range in $TiO_2$

contents, from 0.37 to 0.86 at Mata Ua and from 0.41 to 1.11 at Mata Tolu over this MgO range. Each volcano will now be discussed individually.

A few of the samples from Mata Ua plot just below, but roughly parallel to the modeled $TiO_2$ vs MgO trend (Figure 6.19). This may represent fractionation from a single parent melt that had a slightly lower starting $TiO_2$ content than the composition used for the model. The other samples do not plot along this trend and cannot be related genetically to the lower $TiO_2$ samples. There are several possible explanations of the Mata Ua data. It is possible that the data represents fractionation of samples from multiple parent melts with different starting $TiO_2$ contents and that these melts fractionated in isolation from each other. If each trend were modeled, we would expect to see a series of subparallel to parallel LLDs with varying starting concentrations of $TiO_2$. Another possibility is that the intermediate samples were formed by mixing between high and low $TiO_2$ melts.

The bulk of the Mata Tolu data plots along the modeled melt $TiO_2$ vs MgO trend, suggesting that these samples may be explained by fractionation of a single parent melt or multiple parent melts with very similar compositions (Figure 6.19). However, two samples have much higher $TiO_2$ contents. These two can be explained by a parent melt with a different composition. While this data does not require more than two parent melts, it is possible that lavas from additional parent melts are present at Mata Tolu, but have not yet been sampled. Mixing between multiple parent melts cannot be ruled out either.

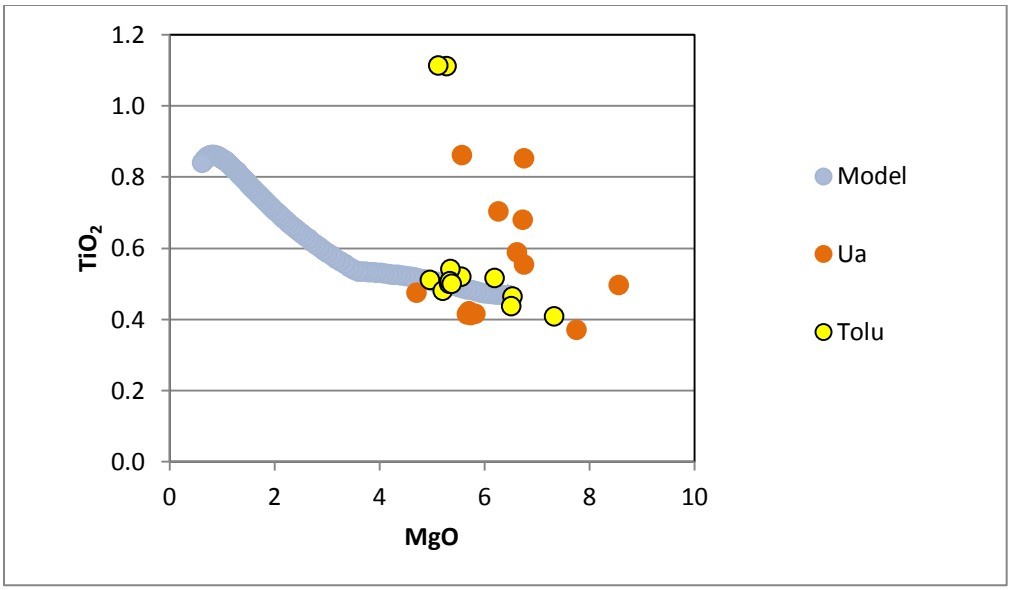


Figure 6.19 $TiO_2$ vs MgO of measured volcanic glass from Mata Ua and Mata Tolu compared to modeled residual melt concentrations.

To further explore the role of mixing in boninite petrogenesis, petrographic data can be utilized. Samples from all of the Mata Volcanoes contain complex mineral textures, supporting the hypothesis that mixing plays a role in boninite petrogenesis from these Mata Volcanoes (Chapter 3).

The possibility that mixing was an important process during the crystallization of these samples can be examined by comparing the $TiO_2$ contents of clinopyroxene crystals. The concentration of $TiO_2$ in growing clinopyroxene crystals is dependent on the concentration of $TiO_2$ in the melt along with other factors. A melt with a higher $TiO_2$ content in the melt would be expected to crystallize clinopyroxene with a higher $TiO_2$ content. Thus, by looking at the concentration of $TiO_2$ in clinopyroxene in a sample, one can determine if part of a clinopyroxene crystal crystalized in a higher or lower $TiO_2$ environment. Significant variation in $TiO_2$ content in the clinopyroxene can suggest that the different crystals or parts of crystals formed in different environments. This variation would suggest that magma mixing was an important process in their formation.

This analysis can also be applied to orthopyroxene crystals. However, as orthopyroxene crystals measured in this study have very low concentrations of $TiO_2$, near the detection limit of the microprobe, this discussion will focus solely on the clinopyroxene crystals.

This section solely examines clinopyroxene data from Mata Ua and Mata Tolu, as these two volcanoes have a range of $TiO_2$ concentrations in their volcanic glass, which may suggest mixing between melts with different $TiO_2$ contents. Clinopyroxene was only measured in one sample at each of these volcanoes. For Mata Ua, KM1024 D18-R01 was used, which has a $TiO_2$ content of 0.41 and a MgO content of 5.68. For Mata Tolu, KM1024 D20-R01 was used, which has a $TiO_2$ content of 0.51 and a MgO content of 4.97. Both of these samples are from the lower $TiO_2$ group (Chapter 4). Table 6.2 below lists the $TiO_2$ contents of every point measured on clinopyroxene for these two samples. The measurements are listed in order of increasing $TiO_2$ content.

A wide range in $TiO_2$ content is preserved in these clinopyroxene crystals, suggesting a range in $TiO_2$ content in their melts. This suggests that magma mixing was a significant process in the formation of these samples.

The distribution coefficient of $TiO_2$ between the melt and clinopyroxene crystals and the $TiO_2$ content in the clinopyroxene crystals can be used to calculate the concentration of $TiO_2$ that would be expected in the corresponding melt. The measured concentrations of $TiO_2$ in clinopyroxene from Mata Ua and Mata Tolu and calculations of coexisting melts are provided in Table 6.2.

A distribution coefficient determined between basaltic liquid and clinopyroxene is chosen as it is more similar in concentration to the boninites studied here than other liquid compositions available. In literature, there is a wide variety of distribution coefficients for $TiO_2$ between a basaltic liquid and clinopyroxene. The Geochemical Earth Reference Model Database (http://earthref.org/) provides a list of possible distribution coefficients. One of the lower values is 0.1 from McKenzie and O'Nions (1991). One of the higher values is 0.786 by Matsui et al. (1977). Most values range from 0.3 to 0.5. These four values (0.1, 0.3, 0.5, 0.786) are used for calculations to provide a range of possible predicted $TiO_2$ contents in corresponding melts. Each analyzed point is used in calculations.

The $TiO_2$ concentrations of each clinopyroxene point analyzed for Mata Ua and Mata Tolu along with the four corresponding melts are provided in Table 6.2. The value of the distribution coefficient greatly affects the concentration in the corresponding melt. The higher distribution coefficients of 0.5 to 0.786 better fit this system. The distribution coefficient of 0.1 yields melt $TiO_2$ concentrations that are much higher than the highest observed $TiO_2$ contents. The higher distribution coefficients of 0.5 to 0.786 yield more realistic values so discussion will focus on these values. For a distribution coefficient, a wide range in melt $TiO_2$ contents is present. For example, using a distribution coefficient of 0.5, calculated melt $TiO_2$ contents range from 0.10 to 0.62 for Mata Ua and from 0.18 to 1.14 for Mata Tolu. Although the measured volcanic glass for these samples is a low $TiO_2$ glass, melts with higher $TiO_2$ concentrations may have been mixed in. Some of the calculated melts have a much lower $TiO_2$ content that those observed in the glass samples with the lowest $TiO_2$ contents. This also suggests that mixing was an important process in the formation of these two samples. To determine if this is representative of most melts at Mata Ua and Mata Tolu, analysis of additional samples would be required.

While studying the $TiO_2$ content in clinopyroxene and calculating the corresponding melt $TiO_2$ composition can provide an idea of how much variation there was in $TiO_2$ content in the melt while clinopyroxene was forming, there are limitations to this interpretation. While the $TiO_2$ content in a growing clinopyroxene does depend on the $TiO_2$ content in the melt, other factors such as growth related effects and sector zoning can affect the $TiO_2$ content in a crystal. Sometimes disequilibrium effects can also impact the $TiO_2$ content in the clinopyroxene crystal. These factors are not explored here and future work can take them into consideration. Additionally, there is significant uncertainty in the optimum distribution coefficient for this system.

Other trace or minor elements in minerals can also be examined. For example, in this study, NiO, MnO, and CaO were measured in olivine in addition to the major elements (Table 6.3). The concentration of these elements in olivine is dependent on the concentration in the melt among other factors. However, the wide range in values observed suggests the possibility of mixing of melts with varying concentrations of NiO, MnO, and CaO.

While this research should be considered as preliminary, results from the MELTS model, theoretical modeling, observed complex mineral textures, $TiO_2$ content in clinopyroxenes, and minor elements in olivine, suggest that mixing of different melts played a significant role while these crystals were forming.

Table 6.2. $TiO_2$ concentrations (in wt%) measured in clinopyroxene from Mata Ua and Mata Tolu and calculations of $TiO_2$ concentrations in corresponding melts using four different distribution coefficients

| Volcano | $TiO_2$ in CPX | Calculated $TiO_2$ in Coexisting Melt Based on Four Distribution Coefficients | | | |
|---|---|---|---|---|---|
| | | D = 0.1 | D = 0.3 | D = 0.5 | D = 0.768 |
| Ua | 0.05 | 0.50 | 0.17 | 0.10 | 0.06 |
| Ua | 0.08 | 0.81 | 0.27 | 0.16 | 0.10 |
| Ua | 0.10 | 0.99 | 0.33 | 0.20 | 0.13 |
| Ua | 0.10 | 1.03 | 0.34 | 0.21 | 0.13 |
| Ua | 0.12 | 1.22 | 0.41 | 0.24 | 0.16 |
| Ua | 0.13 | 1.28 | 0.43 | 0.26 | 0.16 |
| Ua | 0.14 | 1.39 | 0.46 | 0.28 | 0.18 |
| Ua | 0.16 | 1.56 | 0.52 | 0.31 | 0.20 |
| Ua | 0.17 | 1.69 | 0.56 | 0.34 | 0.22 |
| Ua | 0.31 | 3.09 | 1.03 | 0.62 | 0.39 |
| Tolu | 0.09 | 0.88 | 0.29 | 0.18 | 0.11 |
| Tolu | 0.10 | 1.04 | 0.35 | 0.21 | 0.13 |
| Tolu | 0.12 | 1.15 | 0.38 | 0.23 | 0.15 |
| Tolu | 0.12 | 1.19 | 0.40 | 0.24 | 0.15 |
| Tolu | 0.12 | 1.23 | 0.41 | 0.25 | 0.16 |
| Tolu | 0.12 | 1.24 | 0.41 | 0.25 | 0.16 |
| Tolu | 0.14 | 1.41 | 0.47 | 0.28 | 0.18 |
| Tolu | 0.14 | 1.44 | 0.48 | 0.29 | 0.18 |
| Tolu | 0.15 | 1.51 | 0.50 | 0.30 | 0.19 |
| Tolu | 0.15 | 1.54 | 0.51 | 0.31 | 0.20 |
| Tolu | 0.16 | 1.56 | 0.52 | 0.31 | 0.20 |
| Tolu | 0.16 | 1.56 | 0.52 | 0.31 | 0.20 |
| Tolu | 0.16 | 1.61 | 0.54 | 0.32 | 0.20 |
| Tolu | 0.16 | 1.62 | 0.54 | 0.32 | 0.21 |

Each line in the table presents an individual measurement of a point on a clinopyroxene crystal for $TiO_2$. Four calculations of corresponding melt contents are presented based on different distribution coefficients. A range of distribution coefficients between clinopyroxene and a coexisting melt for $TiO_2$ can be found on the Geochemical Earth Reference Model Database (http://earthref.org/). One of the lower values is 0.1 from McKenzie and O'Nions (1991). One of the highest values is 0.786 by Matsui et al. (1977). Most values range from 0.3 to 0.5, so both of these values are used for calculations. Mata Ua clinopyroxene are measured from sample KM1024 D18-R01 and Mata Tolu clinopyroxene are measured from sample KM1024 D20-R01.

Table 6.2 (continued). $TiO_2$ Concentrations (in wt%) Measured in Clinopyroxene from Mata Ua and Mata Tolu and Calculations of $TiO_2$ Concentrations in Corresponding Melts.

| Volcano | $TiO_2$ in CPX | Calculated $TiO_2$ in Coexisting Melt Based on Four Distribution Coefficients | | | |
|---|---|---|---|---|---|
| | | D = 0.1 | D = 0.3 | D = 0.5 | D = 0.786 |
| Tolu | 0.18 | 1.75 | 0.58 | 0.35 | 0.22 |
| Tolu | 0.19 | 1.88 | 0.63 | 0.38 | 0.24 |
| Tolu | 0.20 | 1.99 | 0.66 | 0.40 | 0.25 |
| Tolu | 0.20 | 2.02 | 0.67 | 0.40 | 0.26 |
| Tolu | 0.22 | 2.18 | 0.73 | 0.44 | 0.28 |
| Tolu | 0.22 | 2.19 | 0.73 | 0.44 | 0.28 |
| Tolu | 0.22 | 2.22 | 0.74 | 0.44 | 0.28 |
| Tolu | 0.22 | 2.23 | 0.74 | 0.45 | 0.28 |
| Tolu | 0.23 | 2.30 | 0.77 | 0.46 | 0.29 |
| Tolu | 0.25 | 2.54 | 0.85 | 0.51 | 0.32 |
| Tolu | 0.26 | 2.56 | 0.85 | 0.51 | 0.33 |
| Tolu | 0.28 | 2.77 | 0.92 | 0.55 | 0.35 |
| Tolu | 0.28 | 2.83 | 0.94 | 0.57 | 0.36 |
| Tolu | 0.29 | 2.91 | 0.97 | 0.58 | 0.37 |
| Tolu | 0.29 | 2.93 | 0.98 | 0.59 | 0.37 |
| Tolu | 0.31 | 3.08 | 1.03 | 0.62 | 0.39 |
| Tolu | 0.32 | 3.21 | 1.07 | 0.64 | 0.41 |
| Tolu | 0.32 | 3.25 | 1.08 | 0.65 | 0.41 |
| Tolu | 0.33 | 3.26 | 1.09 | 0.65 | 0.42 |
| Tolu | 0.40 | 4.00 | 1.33 | 0.80 | 0.51 |
| Tolu | 0.57 | 5.69 | 1.90 | 1.14 | 0.72 |

Each line in the table presents an individual measurement of a point on a clinopyroxene crystal for $TiO_2$. Four calculations of corresponding melt contents are presented based on different distribution coefficients. A range of distribution coefficients between clinopyroxene and a coexisting melt for $TiO_2$ can be found on the Geochemical Earth Reference Model Database (http://earthref.org/). One of the lower values is 0.1 from McKenzie and O'Nions (1991). One of the highest values is 0.786 by Matsui et al. (1977). Most values range from 0.3 to 0.5, so both of these values are used for calculations. Mata Ua clinopyroxene are measured from sample KM1024 D18-R01 and Mata Tolu clinopyroxene are measured from sample KM1024 D20-R01.

Table. 6.3 Range in measured NiO, MnO, and CaO content in olivine (in wt%).

| Volcano | Sample | | NiO | MnO | CaO |
|---|---|---|---|---|---|
| West Mata | J2-413-R04 | Minimum | 0.16 | 0.19 | 0.15 |
| | | Maximum | 0.21 | 0.22 | 0.23 |
| | J2-413-R13 | Minimum | 0.13 | 0.13 | 0.15 |
| | | Maximum | 0.26 | 0.23 | 0.29 |
| | J2-418-R01 | Minimum | 0.11 | 0.18 | 0.12 |
| | | Maximum | 0.15 | 0.28 | 0.17 |
| | J2-418-R11 | Minimum | 0.13 | 0.15 | 0.10 |
| | | Maximum | 0.27 | 0.22 | 0.22 |
| | J2-418-R18 | Minimum | 0.14 | 0.18 | 0.16 |
| | | Maximum | 0.23 | 0.22 | 0.24 |
| | J2-420-R02 | Minimum | 0.09 | 0.17 | 0.13 |
| | | Maximum | 0.20 | 0.27 | 0.20 |
| | J2-420-R17 | Minimum | 0.09 | 0.12 | 0.12 |
| | | Maximum | 0.28 | 0.27 | 0.26 |
| Taha | KM1024 D16-R04 | Minimum | 0.07 | 0.15 | 0.00 |
| | | Maximum | 0.24 | 0.22 | 0.19 |
| Ua | KM1024 D18-R01 | Minimum | 0.14 | 0.14 | 0.12 |
| | | Maximum | 0.32 | 0.21 | 0.19 |
| | KM1024 D18-R02 | Minimum | 0.15 | 0.13 | 0.10 |
| | | Maximum | 0.30 | 0.21 | 0.17 |
| Tolu | KM1024 D20-R01 | Minimum | 0.10 | 0.14 | 0.07 |
| | | Maximum | 0.22 | 0.40 | 0.17 |
| Fa | KM1024 D21-R02 | Minimum | 0.12 | 0.12 | 0.12 |
| | | Maximum | 0.40 | 0.21 | 0.23 |
| Ono | KM1024 D22-R01 D | Minimum | 0.08 | 0.14 | 0.12 |
| | | Maximum | 0.22 | 0.22 | 0.23 |
| | KM1024 D22-R01 L | Minimum | 0.08 | 0.14 | 0.12 |
| | | Maximum | 0.24 | 0.20 | 0.19 |
| | KM1024 D22-R02 | Minimum | 0.15 | 0.12 | 0.10 |
| | | Maximum | 0.33 | 0.21 | 0.20 |
| Fitu | KM1024 D23-R01 | Minimum | 0.13 | 0.12 | 0.09 |
| | | Maximum | 0.34 | 0.19 | 0.17 |
| | KM1024 D23-R04 | Minimum | 0.18 | 0.14 | 0.10 |
| | | Maximum | 0.29 | 0.19 | 0.19 |

## Summary and Conclusions

Crystallization of boninitic and boninite-like melts from the Mata Volcanoes were successfully modeled using MELTS. Best fit conditions of crystallization were constrained by systematically varying the conditions and comparing data from the resulting runs to observations from samples. Initial water contents of at least 1.7 to 2.5 wt% and a range in oxygen fugacity of QFM to QFM +1 best approximate the data when pressures of 500 to 1000 bars are used. More data would be required to further constrain the pressure of crystallization. However, with the data available, pressures of 500 to 1000 bars represent the best match. These conditions approximate observations at multiple Mata Volcanoes. For some volcanoes, such as Mata Taha, more data is required to verify optimal conditions. Magma mixing probably occurred during the crystallization of these magmas, as suggested by mineral textures and compositions.

# CHAPTER 7: DISCUSSION

## Mantle Source Composition

This section overviews preliminary findings about petrogenesis of the Mata samples, including mantle depletion and subduction input and discusses implications and avenues for future work. This discussion includes trace element analysis of whole rock samples (Chapter 4). While preliminary LA-ICPMS analysis of glass samples by Frances Jenner is not documented within this thesis, it shows similar trends to XRF whole rock trace element analysis and aids discussion. Therefore, it will occasionally be mentioned here.

Low concentrations of Y in whole rock XRF analysis and glass LA-ICPMS analysis low concentrations of HREE in glass LA-ICPMS analysis imply that the samples formed from partial melting of a depleted mantle source. The concentrations of Y and HREE in these samples are lower than MORB. The whole rock concentration of Y is similar to published data of other boninites found in the Lau Basin and elsewhere.

At some point, the mantle that melted to form the Mata volcanoes was influenced by the nearby subduction zone. The samples have higher concentrations of Ba and other fluid mobile elements in whole rock and glass analysis than MORB. The high concentration of water in samples required by MELTS also suggests input from the subduction zone.

Further analysis of trace elements in whole rock or glass and analysis of isotopes could provide more information about this component or components. Careful study of a range in trace element and isotope compositions and ratios can be used to study addition of various subduction components, such as dehydrated fluids from the subducting slab and sediments and sediment melts. For example, high Ba/Th ratios are associated with addition of components from altered mafic oceanic crust (Elliott, 2003). An altered mafic crust has a high concentration of 2+ cations, such as Ba, Sr, and Pb, and secondarily of 1+ cations, such as K and Rb. This can be seen in elevated ratios such as Sr/Nd (Elliott, 2003). $^{87}Sr/^{86}Sr$ can be used as a tracer of contribution from an altered mafic source (Elliott, 2003 and reference therein). Lead isotopes and Pb/Ce can also be used to investigate this component (Elliott, 2003 and references therein). High La/Sm ratios are associated with addition of components from subducted sediment (Elliott, 2003). $^{10}Be$ abundances are also thought to come from subducted sediment (Elliott, 2003). Lead isotope ratios are affected by subducted sediment composition. For example the concentration of

pelagic sediment vs volcaniclastics from the Louisville Ridge can cause differences in lead isotopic ratios in Tonga (Elliott, 2003; Turner and Hawkesworth, 1997; Wendt *et al.*, 1997).

Variations in other non-fluid mobile trace element concentrations (such as Nb and Zr) and ratios (such as Nb/Zr) suggest input of additional component(s) and/or variations in the mantle wedge. These elements are not normally mobilized in a subduction zone by dehydration or sediment melting. The Mata boninites and higher $TiO_2$ samples are more enriched in Nb and Zr than other boninites in literature despite the fact that they have similar concentrations of Y. Thus, despite similar amounts of mantle depletion, these boninites and related rocks are more enriched in Nb and Zr. Furthermore, there is variation in Nb and Zr concentrations and Nb/Zr ratios between the Mata Volcanoes. Although more studies are needed, I tentatively attribute this to minor local-scale compositional heterogeneities in the mantle wedge. Future work could investigate these possibilities or suggest other scenarios.

Some authors have called on Samoan material to explain observed geochemical signatures in lavas found in the Lau Basin (Ewart *et al.*, 1998; Graham, 2002; Lupton *et al.*, 2009; Lytle *et al.*, 2012; Turner and Hawkesworth, 1997; e.g. Wendt *et al.*, 1997). Helium isotopes can be used to investigate possible involvement of Samoan plume material. Mid ocean ridge basalts have a relatively uniform $^{3}He/^{4}He$ ratio while lavas from Samoa have a higher $^{3}He/^{4}He$ ratio than MORB (Graham, 2002; Lupton *et al.*, 2009). Lupton *et al.* (2009) combined new data with previous studies to map the presence of the Samoan mantle in the Lau Basin, finding evidence of Samoan material in the northwestern part of the basin, but not near the Mata Volcanoes (Lupton *et al.*, 2009 and references therein). Some preliminary analysis of helium isotopes in lavas from the Mata Volcanoes has not found evidence of involvement of Samoan material ( Lupton *et al.* 2013). Additional analysis could further evaluate the presence of the Samoan mantle in the northern Lau Basin at the Mata Volcanoes.

## Crystallization

### Parent Melt/Starting Composition

*Multiple parent melts*

Major element concentrations and trace element concentrations in Mata lavas suggest multiple parent melts were present with distinct starting compositions. Multiple parent melts

would be expected as the samples are from eight volcanoes with at least two eruptions at West Mata. However, the large number of distinct compositions in a small spatial area cannot be explained by crystallization from a single or similar parent magmas (Chapter Five). More sampling, especially from the Northern Matas, and analysis from XRF, microprobe, and ICPMS are necessary to more fully delineate the number of parent melts, their compositional differences, and the causes for those differences.

*Higher $TiO_2$ samples (non-boninites)*

Over a small range in MgO, the measured $TiO_2$ concentration in whole rock samples ranges from boninitic values of less than 0.5 wt% to almost 1 wt%. Most of these higher TiO2 samples also have higher concentrations of $Na_2O$, $K_2O$, and $P_2O_5$ in microprobe glass data. There are also distinctions in trace element concentrations, as observed in XRF whole rock data. The higher $TiO_2$ samples have higher concentrations of fluid mobile trace elements, such as Ba, and non-fluid mobile trace elements, such as Nb and Zr. They have similar concentrations of Y to Mata boninites. These variations cannot be explained by crystallization from a single parent melt. Multiple parent melts with varying concentrations may better explain the compositional variations.

*High $SiO_2$ West Mata samples from the older eruption(s)*

At least two eruptions have been sampled at West Mata. However, there are at least two distinct groups within the older West Mata samples (Chapter 4). One group is compositionally similar to samples from the newer eruption. Another group has higher $SiO_2$ and lower MgO compositions. These samples do not plot along a liquid line of descent using best fit conditions and a starting composition similar to the newly erupted West Mata samples for $Al_2O_3$ vs MgO. Preliminary analyses of highly incompatible trace elements, such as Ba, also suggest that they did not differentiate from samples with a concentration similar to the newly erupted West Mata samples.

The temperature of formation of these older samples is distinct from that of other older samples and from the newly erupted samples. For example, the simple liquid thermometer (Equation 5.1) records lower temperatures of formation due to their lower MgO content. Differences between these samples and samples from the new eruption can be seen in some of the mineral-liquid thermometers as well.

*Water Contents*

In this study, water contents of parent melts are estimated to be at least 1.7 to 2.0 wt% using best fit MELTS models. The estimated parent MELT water content is just for the last stages of crystallization, from a magma with approximately 7 wt% MgO, corresponding to the ranges in MgO contents in sampled volcanic glass. Initial water contents from a mantle melt or earlier stages of crystallization would usually be higher.

To further study the water contents of Mata magmas, the water content of melt inclusions in olivine or pyroxene crystals could be measured. Melt inclusions are common in phenocrysts from the Mata volcanoes. Although, melt inclusions can be affected by post-entrapment processes, by studying a large number of melt inclusions and correcting for these processes, it is possible to obtain estimates of water contents in more primitive stages in the evolution of the Mata magmas.

**Conditions of crystallization**

*Oxygen fugacity.*

All of my work so far suggests that crystallization occurred under relatively oxidizing conditions. However, exactly how oxidizing the conditions are is unclear. There is a discrepancy between the range in oxygen fugacity predicted by MELTS modeling and the range in oxygen fugacity calculated from volcanic glass compositions using assumptions of olivine rim-liquid equilibria to calculate the iron species present in the liquid. Significant concentrations of $Fe^{3+}$ in the melt are indicated by olivine-liquid equilibria (30 to 60%), corresponding to a range in oxygen fugacity of QFM + 1.8 to 4.8 (Chapter 5). Excluding the two very oxidized samples from an older eruption or eruptions of West Mata, the range is QFM + 1.8 to 3.9. MELTS modeling indicated a range in oxygen fugacity of QFM +0 to +1.

The cause of this discrepancy is unclear. Nikolaev *et al.* (1996) reviews published studies relating volcanic glass composition to oxygen fugacity, including the study of Kilinc *et al.* (1983) used to calculate oxygen fugacity in this thesis. Nikolaev *et al.* (1996) conclude that these studies, including the study of Kilinc *et al.* (1983), work best for basalt-like samples and do not work well for samples with andesitic to rhyolitic compositions. Nikolaev *et al.* (1996) conclude that further experimental work is required to understand the relationship between

oxygen fugacity and volcanic glass composition for these rocks and to develop more accurate equations for calculating oxygen fugacity for these compositions. Since the Mata samples differ in many ways from basalts, it is possible that Kilinc *et al.* (1983)'s equation does not work well for these samples. Similarly, MELTS is also ideal for basalts. Because the Mata samples differ compositionally from basalts, it is possible that the MELTS model does not precisely predict the range in oxygen fugacity.

Additional work would be required to better constrain how oxidizing the system was when these melts crystallized. There are many possible avenues for future work. One possible source of uncertainty in this study and possible cause in the discrepancy is that the $Fe^{2+}$ and $Fe^{3+}$ concentration in the melt is not directly measured. Measurements of $Fe^{2+}/Fe^{3+}$ in the melt by traditional wet chemical methods or XANES could be compared to this study's calculations of the $Fe^{2+}$ and $Fe^{3+}$ concentration in the melt from olivine rim-liquid equilibrium.

Furthermore, there are multiple equations in various published studies that relate composition of volcanic glass to the oxygen fugacity of the system (See Nikolaev *et al.,* 1996 for a review of some of these papers). Comparisons of calculations made using these additional equations could determine if the various equations yield consistent or differing results for calculated oxygen fugacity and if the range in oxygen fugacity is consistently different than the range predicted by MELTS.

Additional MELTS models could be run at higher pressures to determine if more oxidizing conditions could have been present if the system was under higher pressure. This could potentially resolve the discrepancy between the MELTS prediction of the oxygen fugacity of the system and calculated range in oxygen fugacity from olivine-liquid equilibrium.

Spinel oxybarometers could also be used to calculate the oxygen fugacity of magmas from the Mata volcanoes. This method would require additional analysis of spinel that was not conducted as part of this thesis. However, because only a limited number of spinel crystals are in contact with the melt, this method would provide direct information about the melt from just a few crystals. Looking into the history of the system by studying spinels included in olivine would also be useful.

*Pressure*

The pressure of crystallization for the Mata magmas could not be well constrained by MELTS modeling (Chapter 5). Although the $SiO_2$ content of the residual melt is sensitive to pressure, the effects are only seen at lower MgO contents. There are very few samples in this range (MgO < 3.0 wt% in measured glass samples) from East Mata. Because this study's MELTS modeling work predicts the formation of a significant amount of plagioclase phenocrysts that is not observed in analyzed samples, this study's MELTS model may not be reliable for modeling crystallization of the Mata magmas at low MgO contents.

Higher pressures could be modeled. For each pressure input, the researcher could systematically change $fO_2$ and the $H_2O$ content of the starting melt to determine best fit conditions at higher pressures, similar to my work for pressures of 500 and 1000 bars (Chapter 5). Additionally, the researcher could test runs starting with lower initial MgO. To increase the data base, the researcher could also utilize whole rock data. However, the measured whole rock compositions may not represent actual liquid concentrations as it could have been affected by crystal loss or accumulation.

Pressure of entrapment of melt inclusions can be calculated by measuring the volatiles in melt inclusions. These measurements could be useful in constraining pressures of crystallization of the Mata magmas. By studying a large number of melt inclusions and looking at the distribution in calculated pressures, it is possible to study the depth of magma chambers. For example, it is possible to determine if many melt inclusions formed at the same pressure, suggesting a magma chamber or chambers at a specific depth; little clustering of pressures would not show a major magma chamber system at a specific depth.

Mineral barometers could also be used to study pressure of crystallization. For example, Putirka (2008) includes a two pyroxene barometer. This thesis does not include this barometer as there are very few measured pyroxene pairs that are in equilibrium with each other and could be used to calculate pressure. However, further work could identify and analyze more clinopyroxene-orthopyroxene pairs so that this barometer could be used.

*Temperature*

Temperatures over which crystallization occurred were calculated using liquid, olivine-liquid, orthopyroxene-liquid, clinopyroxene-liquid, clinopyroxene-only, and two pyroxene thermometers. Temperatures calculated were relatively consistent between the thermometers. Most calculated temperatures are within the range of 1000-1200ºC. Boninites and the higher $TiO_2$ samples crystallized over a similar temperature range. Melt incompatible trace element composition does not correlate with temperature. This suggests that all the magmas crystallized over roughly the same temperature ranges despite variations in composition. Higher temperatures are possible earlier in the history of evolution of these lavas; however, this work was unable to directly observe such potentially higher temperatures.

There is some complexity to the calculated temperatures that is within the error of the thermometers; but because of its consistency and possible implications on petrogenesis, these ideas will be discussed here. The lowest temperatures recorded in the simple liquid thermometer using glass data (Equation 5.1) increased to the north (Figure 5.9). A similar trend is observed when whole rock data is used (Figure 5.10). A similar trend can be seen for the olivine-liquid, orthopyroxene-liquid, and clinopyroxene-liquid thermometers (Chapter 5). However, there are very few temperatures measured by these thermometers (with a minimum of nine points). Not enough measurements were made to determine if the clinopyroxene only thermometer shows the same trend. Consistent with their lower MgO content, the higher $SiO_2$ low MgO group of older samples from West Mata have lower calculated temperatures than other older samples and samples from the new eruption of West Mata.

While good agreement is present between the thermometers and I do not predict that changing the Mg# of the melt, pressure of crystallization, or the water content of the melt will significantly change the results, it would be interesting to recalculate this work if more information about the water content, pressure of crystallization, or the Mg# of these melts becomes available. This additional information could further evaluate the intricacies discussed above.

**Processes occurring during crystallization**

Magma mixing appears to have played a key role during differentiation of these samples, as suggested by complicated mineral textures and highly variable mineral compositions.

Additional analysis of minerals in the thin sections analyzed in this project and in additional thin sections would contribute to a better understanding of this process.

Data supports the hypothesis by Rubin *et al.* (2014) that there does not appear to be a well-developed magma chamber where melts homogenize. This is suggested by significant amount of variation in major and trace elements in an individual volcano and even within the new eruption of West Mata

This study's analysis suggests that magmas did not reside in their magma chamber(s) for a long time, supporting conclusions by Rubin *et al.* (2014). Significant mineral textural and compositional variation within one sample as well as major and trace element variation in whole rock and glass samples for an individual volcano is preserved. Prolonged residence in long-lived magma chambers might lead to more equilibrated minerals.

# CHAPTER 8: CONCLUSION

The important conclusions of this project are:

1. Lavas from the Mata Volcanoes consist primarily of fresh volcanic glass, often with abundant microlites. Lavas tend to be vesicular and crystal-rich. The main crystal phases are olivine, clinopyroxene, and orthopyroxene. Crystals in the Mata samples are usually compositionally and texturally complex. Plagioclase is a very minor crystal phase and is found only as a minor groundmass phase in lower MgO samples (samples with approximately 4.5 wt% MgO or lower).
2. These volcanoes primarily erupt boninite. Higher $TiO_2$ lavas that are largely compositionally similar to boninite also erupt at Matas Ua, Tolu, Fa, and Fitu. (Note that all samples in this study have low $TiO_2$ concentrations relative to MORB). More evolved compositions were found at East Mata.
3. The mantle source or sources feeding the Mata Volcanoes is very depleted, causing the low concentrations of $TiO_2$, Y, Zr, and Nb in Mata samples compared to MORB.
4. The mantle source feeding the Mata Volcanoes was modified by or interacted with material from the subduction zone. Fluids from the dehydrating slab and/or sediments contributed water and fluid-mobile elements such as Ba. Elevated concentrations of fluid mobile elements relative to most MORB compositions are found in Mata samples. MELTS modeling suggests that the magmas feeding the Mata Volcanoes contained at least 1.7 to 2.5 wt% water.
5. Higher TiO2 samples are broadly compositionally similar to the Mata boninites. However, they also tend to be more enriched in $Na_2O$, $K_2O$, $P_2O_5$, fluid mobile trace elements, such as Ba, and non-fluid mobile trace elements, such as Zr and Nb. They have similar concentrations of Y to the Mata boninites.
6. Significant variation in trace element composition within an individual volcano and within a single eruption suggests significant heterogeneity in the mantle source and in enriching components from the subduction zone and/or variations in influx from the subduction zone.
7. The samples formed under oxidizing conditions. MELTS modeling suggest that crystallization occurred at QFM or QFM +1. Olivine liquid equilibria suggest a

significant amount of $Fe^{3+}$ in the melt (30-60%), corresponding with an oxygen fugacity range of QFM + 1.8 to 4.8.

8. Crystallization occurred at a temperature range of approximately 1000-1200 °C. The boninitic and higher $TiO_2$ samples formed over similar temperature ranges.
9. Crystallization can be modeled by simple fractionation from multiple parent melts. However, complicated mineral compositions and textures suggest that magma mixing may have played an important role.
10. The small size of the volcanoes, the range in trace element concentrations and ratios in the whole rock, the range in compositions and textures in the minerals suggest that while mixing is common, there is not a well-developed magma storage system where significant homogenization occurs.

# APPENDIX A:

## Additional Information about EPMA Methods used for Glass Analysis

### Analytical conditions

This section is a supplement to the discussion of EPMA methods used for measuring volcanic glass (Chapter Two). Table A.1 reports analytical the date each sample was analyzed, the number of points included in each average, and the beam diameter used to measure the samples.

Table A.1. Analytical conditions for each sample.

| Sample Name | Date Analyzed | Number of Points Included in Average | Beam Diameter |
|---|---|---|---|
| J2-413-R02 | 3/1/2013 | 9 | 10 |
| J2-413-R13 | 3/1/2013 | 9 | 10 |
| J2-415-R02 | 9/12/2013 | 9 | 10 |
| J2-415-R08 | 9/13/2013 | 9 | 10 |
| J2-418-C02 | 3/1/2013 | 9 | 10 |
| J2-418-R01 | 3/1/2013 | 9 | 10 |
| J2-418-R04 | 3/1/2013 | 9 | 10 |
| J2-418-R05 | 3/1/2013 | 9 | 10 |
| J2-418-R11 | 3/1/2013 | 9 | 10 |
| J2-418-R18 | 3/1/2013 | 9 | 10 |
| J2-420-R01 | 3/1/2013 | 9 | 10 |
| J2-420-R02 | 3/1/2013 | 9 | 10 |
| J2-420-R08 | 3/1/2013 | 9 | 10 |
| J2-420-R10 | 3/1/2013 | 9 | 10 |
| J2-420-R13 | 3/1/2013 | 9 | 10 |
| J2-420-R16 | 3/1/2013 | 9 | 10 |
| J2-420-R23 | 3/1/2013 | 9 | 10 |
| KM1008 CT07-1A | 9/12/2013 | 9 | 10 |
| KM1008 CT07-1B | 9/13/2013 | 9 | 10 |
| KM1024 D01-R01 | 9/13/2013 | 9 | 10 |
| KM1024 D02-R05 | 9/12/2013 | 9 | 10 |
| KM1024 D03-R01 | 9/5/2013 | 9 | 10 |
| KM1024 D04-R01 | 9/5/2013 | 9 | 10 |
| KM1024 D04-R04 | 9/6/2013 | 9 | 10 |
| KM1024 D04-R09 | 9/5/2013 | 9 | 10 |
| KM1024 D05-R01 | 9/5/2013 | 9 | 10 |
| KM1024 D05-R02 | 9/5/2013 | 9 | 10 |
| KM1024 D05-R03 | 9/6/2013 | 9 | 10 |
| KM1024 D06-R01 | 9/4/2013 | 9 | 10 |
| KM1024 D06-R06 | 9/4/2013 | 9 | 10 |
| KM1024 D07-R01 | 9/4/2013 and 9/13/2013 | 20 | 10 |
| KM1024 D08-R02 | 9/4/2013 | 9 | 10 |
| KM1024 D08-R08 | 9/4/2013 | 9 | 10 |
| KM1024 D08-R10 | 9/4/2013 | 9 | 10 |

Table A.1 (continued). Analytical conditions for each sample.

| Sample Name | Date Analyzed | Number of Points Included in Average | Beam Diameter |
|---|---|---|---|
| KM1024 D09-R01 | 9/4/2013 | 9 | 10 |
| KM1024 D09-R03 | 9/4/2013 | 9 | 10 |
| KM1024 D09-R05 | 9/4/2013 | 9 | 10 |
| KM1024 D09-R06 | 9/5/2013 | 9 | 10 |
| KM1024 D10-R01 | 9/5/2013 | 9 | 10 |
| KM1024 D10-R03 | 9/5/2013 | 9 | 10 |
| KM1024 D10-R06 | 9/5/2013 | 9 | 10 |
| KM1024 D11-R03 | 9/5/2013 | 15 | 10 |
| KM1024 D11-R03 | 9/13/2013 | 9 | 10 |
| KM1024 D11-R04 | 9/4/2013 and 9/13/2013 | 18 | 10 |
| KM1024 D12-R01 | 7/1/2012 | 9 | 10 |
| KM1024 D12-R06 | 7/1/2012 | 9 | 10 |
| KM1024 D12-R08 | 7/1/2012 | 8 | 10 |
| KM1024 D13-R01 | 3/1/2013 | 9 | 10 |
| KM1024 D14-R02 | 7/1/2012 | 9 | 10 |
| KM1024 D14-R02 | 9/6/2013 | 9 | 10 |
| KM1024 D14-R05 | 7/1/2012 | 16 | 10 |
| KM1024 D14-R09 | 7/1/2012 | 9 | 10 |
| KM1024 D15-R01 | 7/1/2012 | 9 | 10 |
| KM1024 D15-R03 | 7/1/2012 | 9 | 10 |
| KM1024 D15-R05 | 7/1/2012 | 9 | 10 |
| KM1024 D15-R06 | 9/4/2013 | 9 | 10 |
| KM1024 D16-R01 | 7/1/2012 | 9 | 10 |
| KM1024 D16-R02 | 7/1/2012 | 9 | 10 |
| KM1024 D17-R01 | 7/1/2012 | 9 | 10 |
| KM1024 D18-R01 | 7/1/2012 | 6 | 10 |
| KM1024 D18-R04 | 7/1/2012 | 6 | 10 |
| KM1024 D18-R05 | 7/1/2012 | 6 | 10 |
| KM1024 D20-R01 | 7/1/2012 | 9 | 10 |
| KM1024 D20-R02 | 7/1/2012 | 9 | 10 |
| KM1024 D21-R01 | 7/1/2012 | 9 | 10 |
| KM1024 D21-R02 | 7/1/2012 | 9 | 10 |
| KM1024 D21-R04 | 7/1/2012 | 8 | 10 |

Table A.1 (continued). Analytical conditions for each sample.

| Sample Name | Date Analyzed | Number of Points Included in Average | Beam Diameter |
|---|---|---|---|
| KM1024 D22-R01 | 7/1/2012 | 9 | 10 |
| KM1024 D22-R02 | 7/1/2012 | 9 | 10 |
| KM1024 D23-R01 | 7/1/2012 | 9 | 10 |
| KM1024 D23-R04 | 7/1/2012 | 8 | 10 |
| KM1024 D24-R01 | 9/6/2013 | 9 | 10 |
| KM1024 D24-R03 | 9/5/2013 | 9 | 10 |
| KM1024 D24-R04 | 9/5/2013 | 9 | 10 |
| KM1024 D25-R01 | 7/1/2012 | 9 | 10 |
| KM1024 D25-R04 | 7/1/2012 | 9 | 10 |
| KM1129a D10-R01 | 7/1/2012 | 9 | 10 |
| KM1129a D10-R03 | 7/1/2012 | 9 | 10 |
| KM1129a D10-R06 | 7/1/2012 | 9 | 10 |
| KM1129a D01-R03 | 7/1/2012 | 9 | 10 |
| KM1129a D01-R04 | 7/1/2012 | 9 | 10 |
| KM1129a D02-R01 | 7/1/2012 | 9 | 5 |
| KM1129a D02-R01 | 9/13/2013 | 9 | 10 |
| KM1129a D02-R03 | 7/1/2012 | 9 | 5 |
| KM1129a D02-R03 | 9/13/2013 | 9 | 10 |
| KM1129a D02-R04 | 7/1/2012 | 9 | 5 |
| KM1129a D04-R04 | 7/1/2012 | 9 | 10 |
| KM1129a D07-R01 | 7/1/2012 | 9 | 10 |
| KM1129a D07-R02 | 7/1/2012 | 9 | 10 |
| KM1129a D08-R01 | 7/1/2012 | 9 | 10 |
| KM1129a D08-R04 | 7/1/2012 | 9 | 10 |
| KM1129a D08-R07 | 7/1/2012 | 9 | 10 |
| KM1129a D08-R08 | 7/1/2012 | 9 | 10 |
| KM1129a D09-R01 | 7/1/2012 | 9 | 10 |
| KM1129a D11-R01 | 9/6/2013 | 9 | 5 |
| KM1129a D12-R03 | 9/6/2013 | 9 | 5 |
| KM1129a D13-R02 | 9/6/2013 | 9 | 10 |
| KM1129a D13-R03 | 9/6/2013 | 9 | 10 |
| KM1129a D15-R01 | 9/5/2013 | 9 | 10 |
| KM1129a D23-R01 | 9/12/2013 | 9 | 10 |
| KM1129a D26-R01 | 9/12/2013 | 9 | 10 |

Table A.1 (continued). Analytical conditions for each sample.

| Sample Name | Date Analyzed | Number of Points Included in Average | Beam Diameter |
|---|---|---|---|
| KM1129a D28-R01 | 9/12/2013 | 9 | 10 |
| KM1129a-D09-R02 | 3/1/2013 | 9 | 10 |
| KM1129a-D10-R02 | 3/1/2013 | 9 | 10 |
| RR1211 Q325-R01 | 11/1/2012 | 9 | 10 |
| RR1211-Q325-R03 | 11/1/2012 | 9 | 10 |
| RR1211-Q325-R04 | 11/1/2012 | 9 | 10 |
| RR1211-Q327-BS06 | 11/1/2012 | 9 | 10 |
| RR1211-Q327-R02 | 11/1/2012 | 9 | 10 |
| RR1211-Q328-R03 | 11/1/2012 | 9 | 10 |
| RR1211-Q328-R11 | 11/1/2012 | 9 | 10 |
| RR1211-Q328-R12 | 11/1/2012 | 9 | 10 |
| RR1211-Q329-R01 | 11/1/2012 | 9 | 10 |
| RR1211-Q329-R02 | 11/1/2012 | 9 | 10 |
| RR1211-Q331-R01 | 11/1/2012 | 9 | 10 |
| RR1211-Q331-R02 | 11/1/2012 | 9 | 10 |
| RR1211-Q331-R16 | 11/1/2012 | 9 | 10 |
| RR1211-Q332-R01 | 11/1/2012 | 9 | 10 |
| RR1211-Q332-R02 | 11/1/2012 | 9 | 10 |
| RR1211-Q332-R03 | 11/1/2012 | 9 | 10 |
| RR1211-Q332-R04 | 11/1/2012 | 9 | 10 |
| RR1211-Q332-R05 | 11/1/2012 | 9 | 10 |

**Adjusting standard assignments to achieve consistency between the runs**

In each microprobe session, standards were assigned to try to maximize data quality, as indicated by two standards run periodically as unknowns throughout the run, VG-2 and STG-56. VG-2 is a basaltic glass standard distributed by the Smithsonian Museum of Natural History, and used as a microprobe in many labs worldwide. STG-56 is a synthetic glass standard with 56 wt% SiO2, selected because its composition most closely resembles the boninitic glass analyzed in this study. The standard and its value were provided by Klaus Keil, but further documentation on its origin is not available. Previous analyses have demonstrated its homogeneity.

After completing all of the runs (two runs in July 2012, one run in November 2012, one run in March 2013, and two runs in September 2013), standards run as unknowns in all of the runs were compared. There were a few offsets, most notably offsets in MgO. Figure A.1 shows points measured as unknowns on the standard VG-2 throughout the different runs for MgO and CaO. The points are plotted versus their order in the run excluding samples and other points measured rather than versus the actual time the measurements were taken. The same trends were apparent in plots of measured STG-56 values, so only plots of VG-2 values are included here. Sources for all standard values in the plots are provided in the main text of Chapter Two.

The MgO plot illustrates the effect of using two different standards to reduce MgO data. The July 2012 and November 2012 runs are reduced using VG-2, a more widely used and accepted standard. The March 2013 run and the September 2013 runs are reduced using an in house standard, STG-56, which is not as well characterized (source unknown). To remove this offset, standard assignments were changed for the March 2013 and the September 2013 runs to VG-2. The effect of this change is shown in Figure A.2.

Offsets were also noticeable in CaO, as in Figure A. To eliminate the offset between the November 2012 run and the accepted value, its Ca standard assignment was changed from Sphene glass to VG-2. The standard assignment for the March 2013 run could not be changed, as STG-56 was the only Ca standard in this session. The effects of the standard assignment change for the November 2012 run are shown in the Figure A.4:

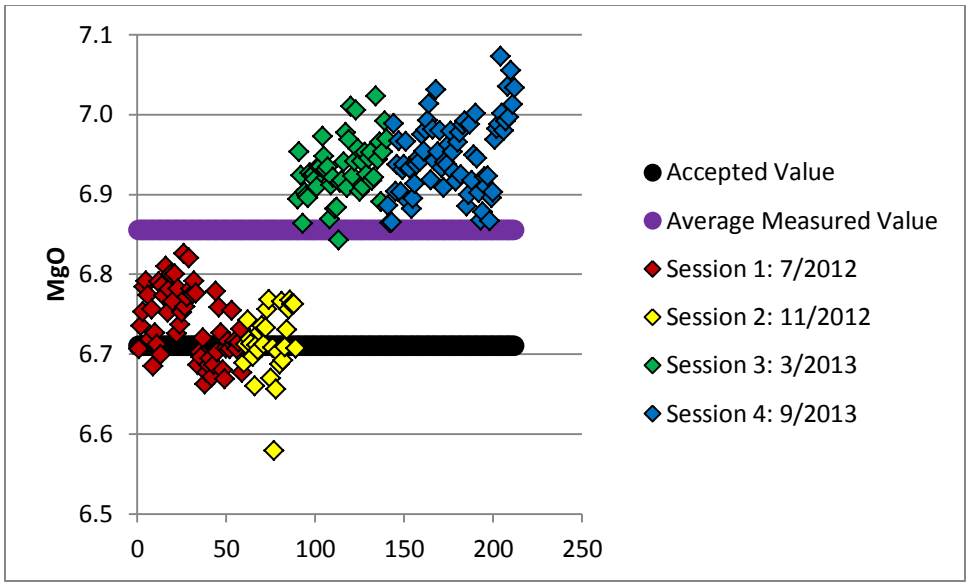


Figure A.1. Abundance of MgO (wt.%) in basalt glass standard VG-2 in illustrating the analytical reproducibility during four different microprobe sessions before changes were made in standard assignments. The two July runs are plotted together, as are the basalt and dacite runs from September. The accepted value of VG-2 for MgO is plotted for comparison. Measured values of the VG-2 standard from the March 2013 run and the September 2013 run are offset from the values measured in the first two runs and from the accepted value. MgO was calculated using STG-56 for the March 2013 run and the September 2013 runs and using VG-2 for the other runs.

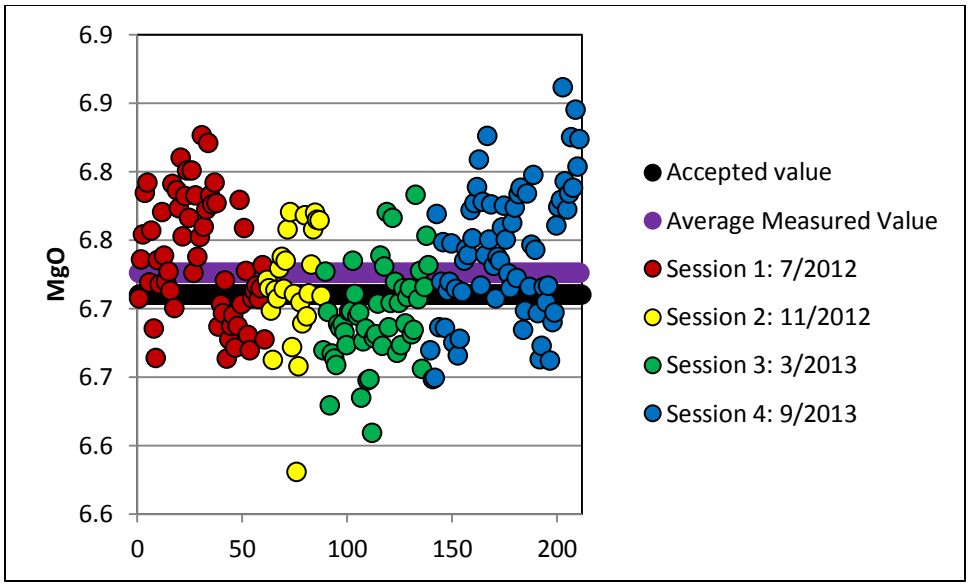


Figure A.2. Abundance of MgO (wt.%) in basalt glass standard VG-2 in illustrating the analytical reproducibility during four different microprobe sessions after changes in standard assignments were made. The two July runs are plotted together, as are the basalt and dacite runs from September. The accepted value of VG-2 for MgO is plotted for comparison. Measured values of the VG-2 standard from the March 2013 run and the September 2013 run are offset from the values measured in the first two runs and from the accepted value. MgO was calculated using VG-2 for all of the runs.

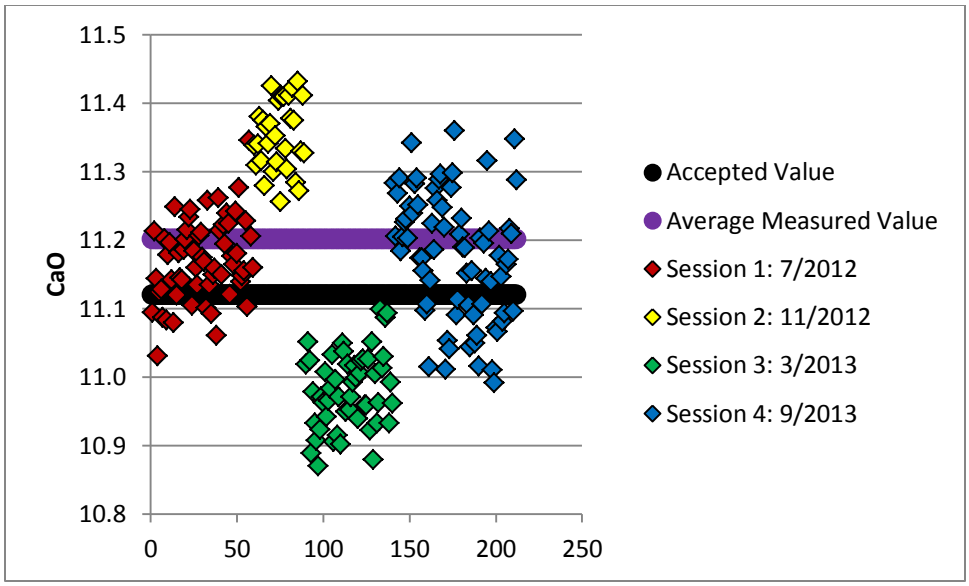


Figure A.3. Abundance of CaO (wt.%) in basalt glass standard VG-2 in illustrating the analytical reproducibility during four different microprobe sessions before changes in standard assignments were made for CaO. The two July runs are plotted together, as are the basalt and dacite runs from September. The accepted value of VG-2 for CaO is plotted for comparison. Measured values of the VG-2 standard from the November 2012 run (reduced using Sphene glass) are offset to higher values of CaO. Measured values of the VG-2 standard from the March 2013 run (reduced using the STG-56 standard) are offset to lower values.

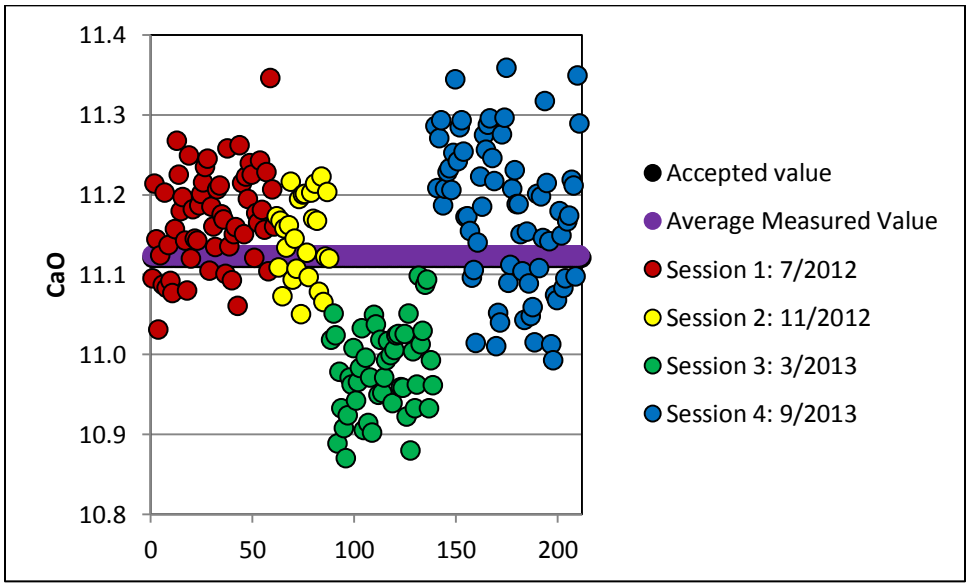


Figure A.4. Abundance of CaO (wt.%) in basalt glass standard VG-2 in illustrating the analytical reproducibility during four different microprobe sessions after changes in standard assignments were made for CaO. The two July runs are plotted together, as are the basalt and dacite runs from September. The accepted value of VG-2 for CaO is plotted for comparison. Measured values of the VG-2 standard from the November 2012 run are no longer offset to higher values of CaO.

While there was no obvious offset in $SiO_2$ between the different runs, the Si standard assignment was changed from VG-2 to STG-56 to match the standard used in all of the other runs (Figures A.5 and A.6)

While compiling the final data set, I noticed that three standard points from the July run are noticeably lower in $Al_2O_3$ than the other points (Figures A.7 and A.8). I re-run the six samples run near this standard in the run. When these samples were re-run, the data results were the same as before, so I determined that there was a problem with the analysis of these three standard points that did not affect the samples. I decided to use the original data and not to report the bad standard analysis, as shown in Figure A.7. None of the other plots in the methods section or this section report values for these bad points.

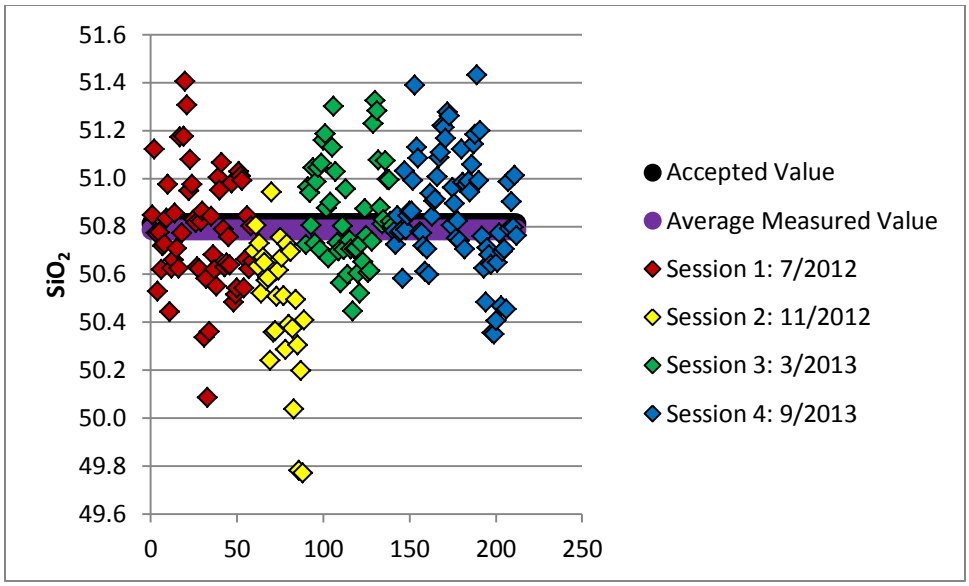


Figure A.5. Abundance of $SiO_2$ (wt.%) in basalt glass standard VG-2 in illustrating the analytical reproducibility during four different microprobe sessions before changes in standard assignments were made for $SiO_2$. The two July runs are plotted together, as are the basalt and dacite runs from September. The accepted value of VG-2 for $SiO_2$ is plotted for comparison.

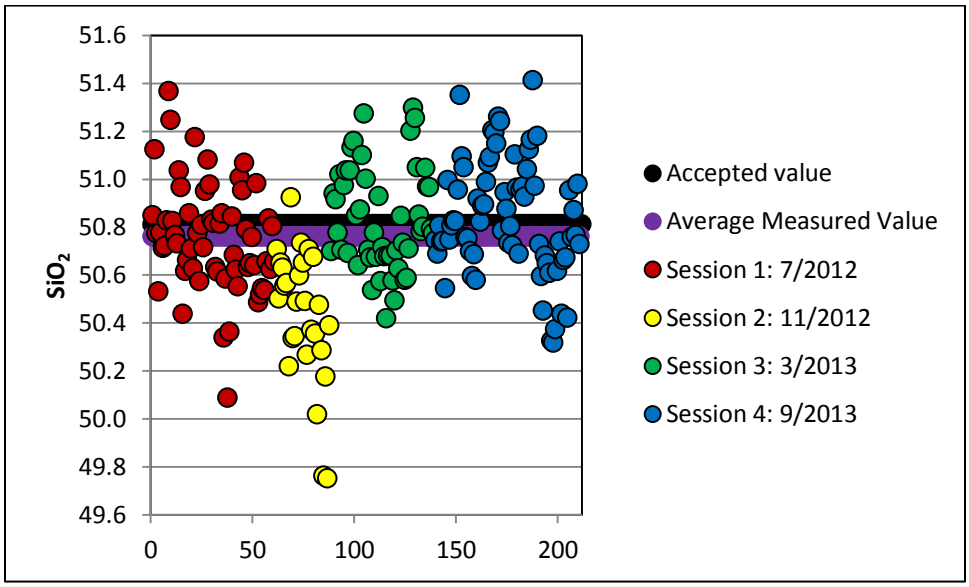


Figure A.6. Abundance of $SiO_2$ (wt.%) in basalt glass standard VG-2 in illustrating the analytical reproducibility during four different microprobe sessions after changes in standard assignments were made for $SiO_2$. The two July runs are plotted together, as are the basalt and dacite run from September. The accepted value of VG-2 for $SiO_2$ is plotted for comparison.

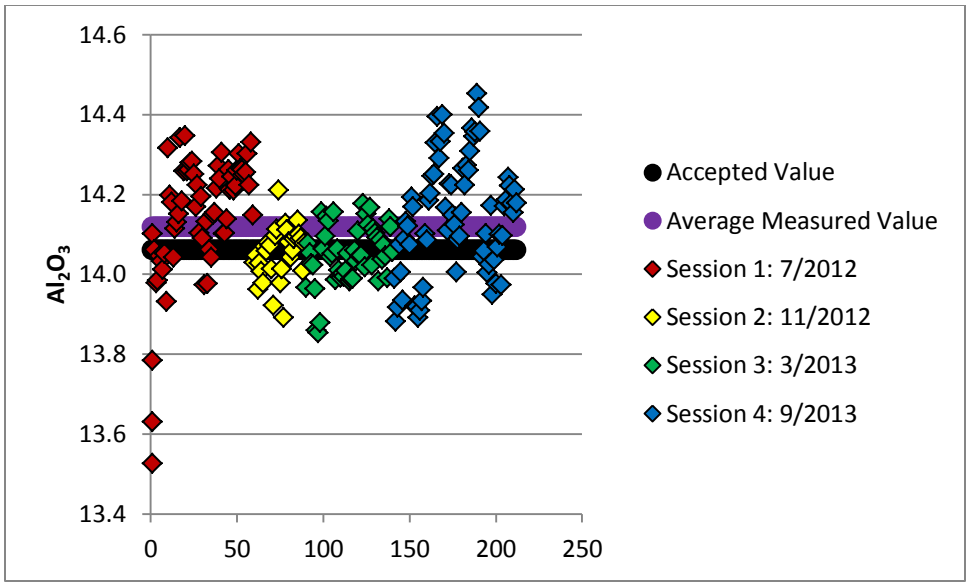


Figure A.7. Abundance of $Al_2O_3$ (wt.%) in basalt glass standard VG-2 in illustrating the analytical reproducibility during four different microprobe sessions before changes in standard assignments were made for $Al_2O_3$. The two July runs are plotted together, as are the basalt and dacite run from September. The accepted value of VG-2 for $Al_2O_3$ is plotted for comparison. Note the three points from the July runs that are much lower in $Al_2O_3$.

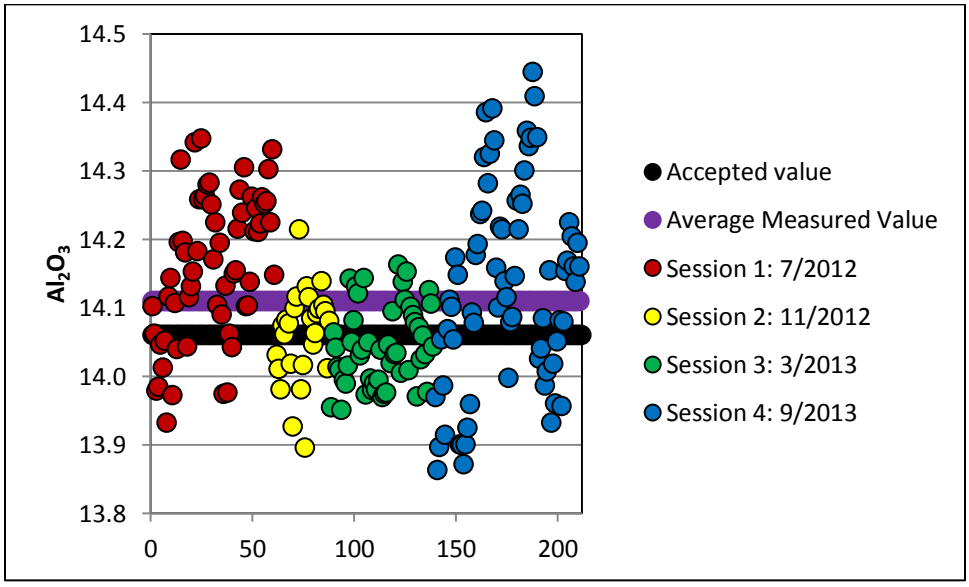


Figure A.8. Abundance of Al2O3 (wt.%) in basalt glass standard VG-2 in illustrating the analytical reproducibility during four different microprobe sessions after changes in standard assignments were made for Al2O3. The two July runs are plotted together, as are the basalt and dacite run from September. The accepted value of VG-2 for Al2O3 is plotted for comparison.

## APPENDIX B: ADDITIONAL FIGURES FOR DISCUSSION OF STANDARD STG-56

As discussed in the Chapter Two, VG-2 and STG-56 were run as an unknowns to monitor for drift in glass runs. Systematic deviations of STG-56 measurements from the accepted value were observed for some elements. The following Figure B.1 shows the accepted and average measured value of STG-56 for all runs and all of the points analyzed for all elements analyzed except for $SiO_2$ and MgO, which are shown in the main text.

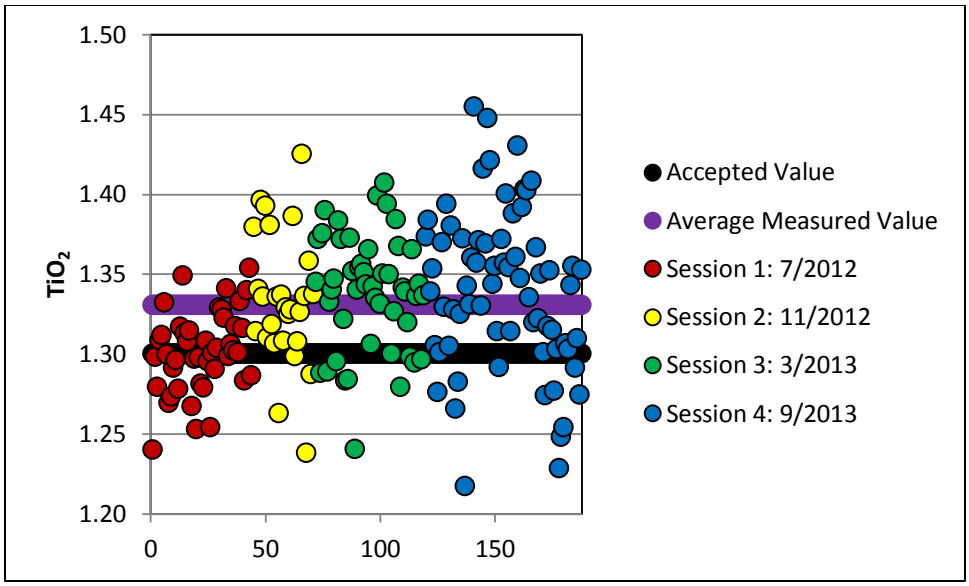
1.50
1.45
1.40
1.35
1.30
1.25
1.20
TiO2
0
50
100
150
Accepted Value
Average Measured Value
Session 1: 7/2012
Session 2: 11/2012
Session 3: 3/2013
Session 4: 9/2013

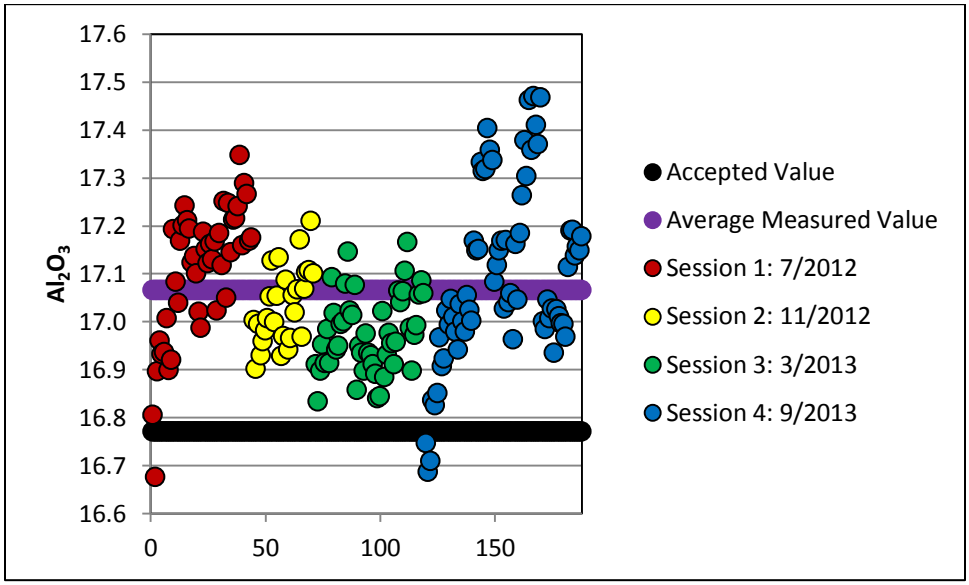
17.6
17.5
17.4
17.3
17.2
17.1
17.0
16.9
16.8
16.7
16.6
Al2O3
0
50
100
150
Accepted Value
Average Measured Value
Session 1: 7/2012
Session 2: 11/2012
Session 3: 3/2013
Session 4: 9/2013

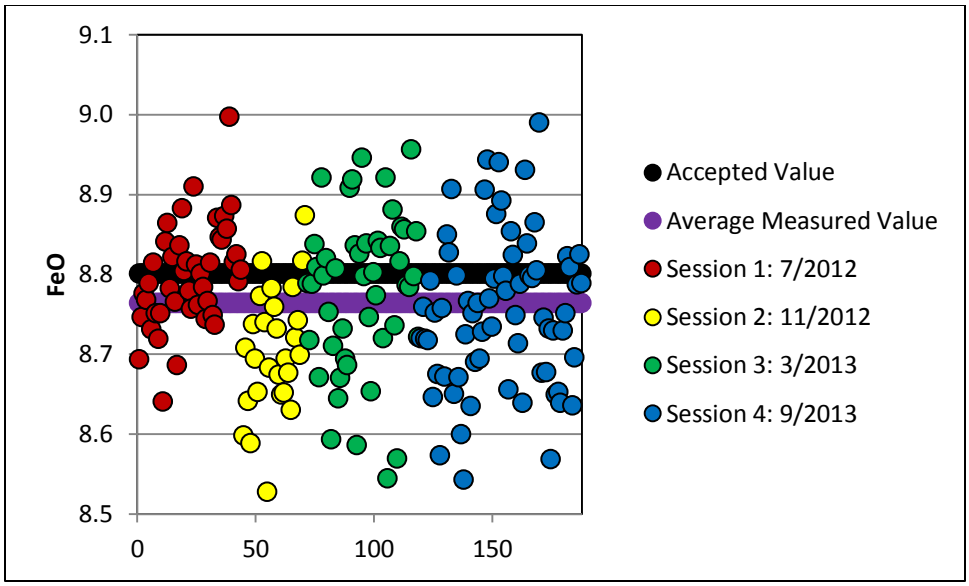
9.1
9.0
8.9
8.8
8.7
8.6
8.5
FeO
0
50
100
150
Accepted Value
Average Measured Value
Session 1: 7/2012
Session 2: 11/2012
Session 3: 3/2013
Session 4: 9/2013

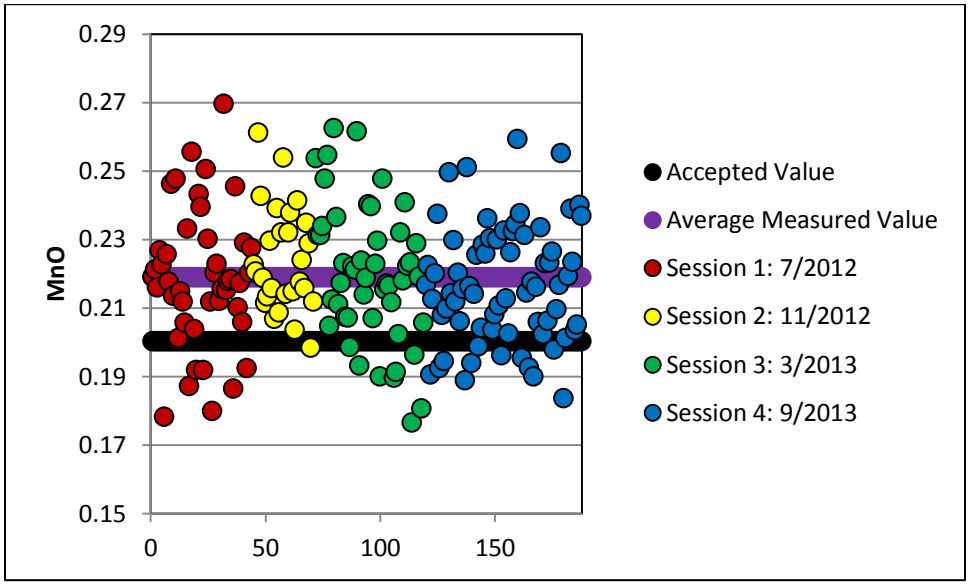
0.29
0.27
0.25
0.23
0.21
0.19
0.17
0.15
MnO
0
50
100
150
Accepted Value
Average Measured Value
Session 1: 7/2012
Session 2: 11/2012
Session 3: 3/2013
Session 4: 9/2013

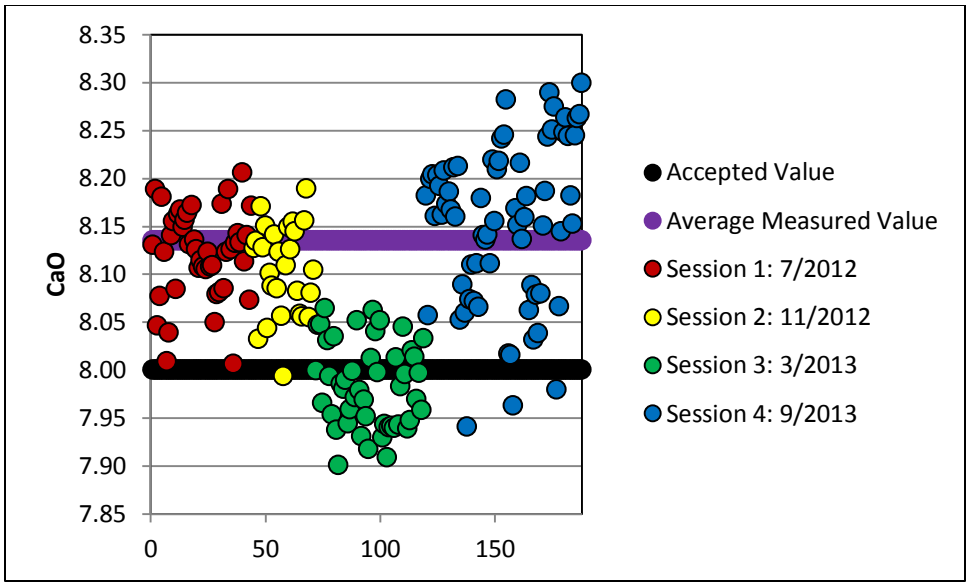
8.35
8.30
8.25
8.20
8.15
8.10
8.05
8.00
7.95
7.90
7.85
CaO
0
50
100
150
Accepted Value
Average Measured Value
Session 1: 7/2012
Session 2: 11/2012
Session 3: 3/2013
Session 4: 9/2013

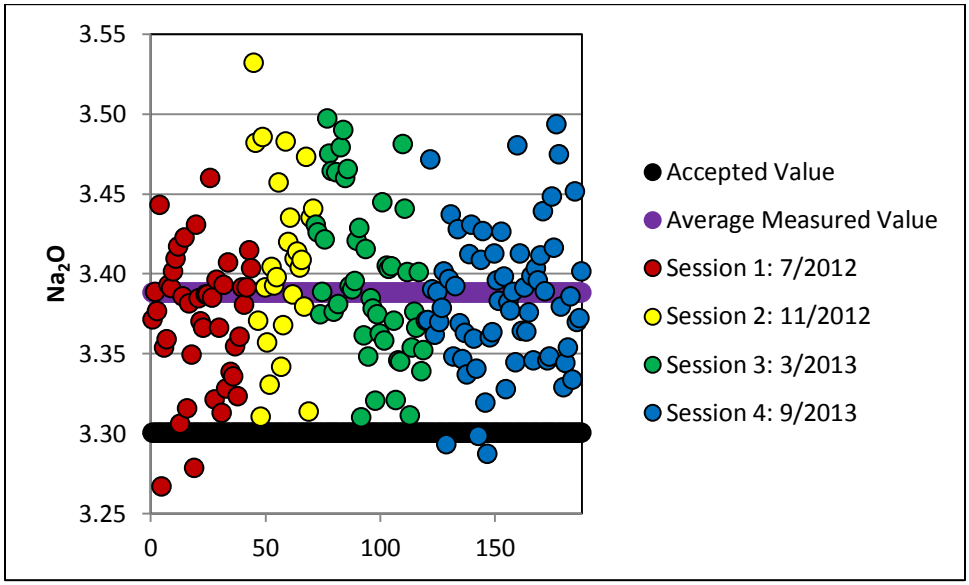
3.55
3.50
3.45
3.40
3.35
3.30
3.25
Na2O
0
50
100
150
Accepted Value
Average Measured Value
Session 1: 7/2012
Session 2: 11/2012
Session 3: 3/2013
Session 4: 9/2013

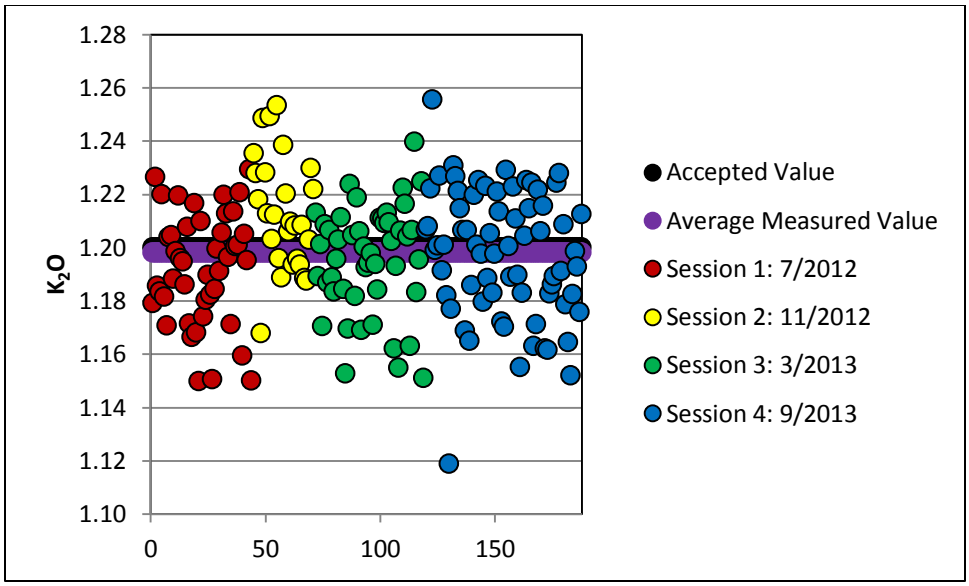
1.28
1.26
1.24
1.22
1.20
1.18
1.16
1.14
1.12
1.10
K2O
0
50
100
150
Accepted Value
Average Measured Value
Session 1: 7/2012
Session 2: 11/2012
Session 3: 3/2013
Session 4: 9/2013

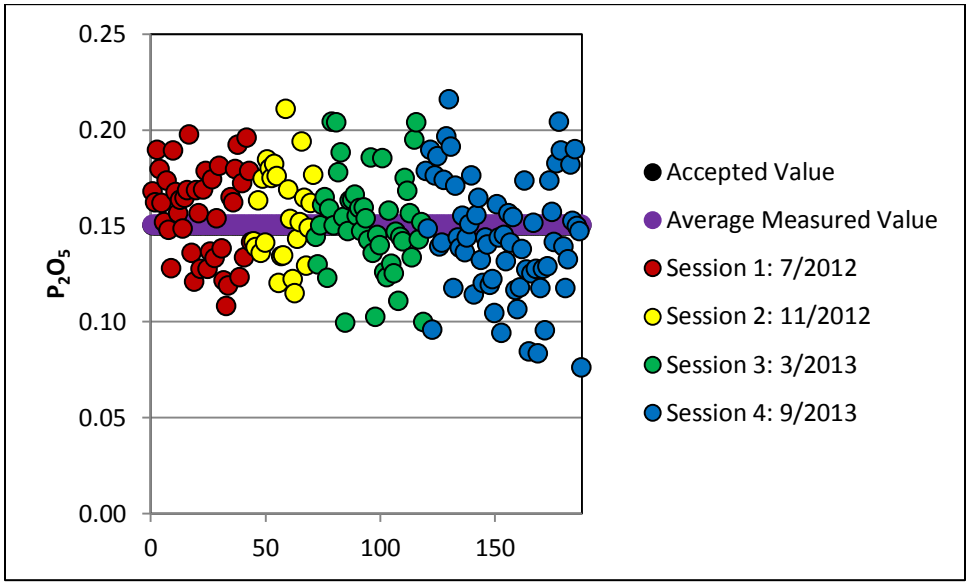
0.25
0.20
0.15
0.10
0.05
0.00
P2O5
0
50
100
150
Accepted Value
Average Measured Value
Session 1: 7/2012
Session 2: 11/2012
Session 3: 3/2013
Session 4: 9/2013

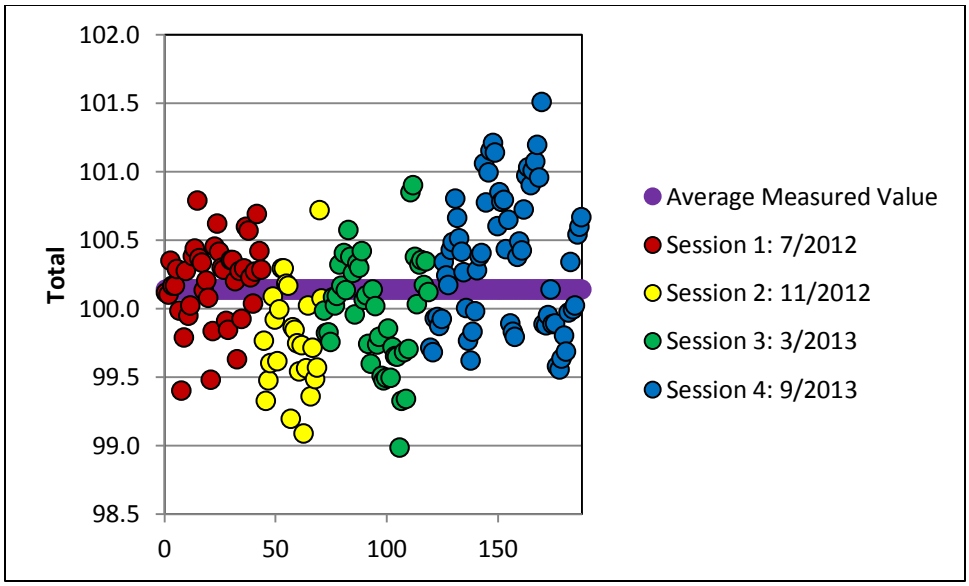


Figure B.1. Measured values for STG-56 comparing the average measured value and the accepted value (where available) for the elements analyzed in this study. Each point is a single spot analysis. $SiO_2$ and MgO are included in the main text of Chapter Two. For further discussion see the Chapter Two. Note offsets for some elements, such as $Al_2O_3$.

## APPENDIX C:

## CONTAMINATION IN PREPARATION OF XRF SAMPLES USING A TUNGSTEN CARBIDE MILL

Some of the samples in this sample suite were affected by cobalt contamination. The affected samples are: KM1024 D16-R01, KM1024 D15-R04, KM1024 D18-R01, KM1024 D21-R02, KM1024 D22-R01, KM1024 D 22-R02, KM1024 D23-R01, and RR121 Q325-R03. This can be seen in the following Co vs. MgO graph (Figure C.1) where these samples plot off of the trend line. Co concentrations off of the Co vs MgO trend are not present in LA-ICPMS glass data as shown in Figure C.2.

The most likely explanation is contamination from tungsten carbide sample preparation equipment. Tungsten carbide can contain Co and others using this equipment have occasionally noticed similar Co contamination (John Sinton, personal communication). I prepared RR1211 Q325-R03 and KM1024 D22-R02, but the other samples were prepared and analyzed before I began working on this project. These were the only two samples I prepared using a tungsten carbide ball mill. All of the other samples were prepared using an aluminum mill. RR1211 Q325-R03 and KM1024 D22-R02 were powdered using the ball mill because there was not enough material to use the aluminum mill. None of the other samples I prepared using the aluminum mill were contaminated.

As tungsten carbide can also contain Nb (John Sinton, personal communication), I checked these samples for possible Nb contamination. Previous lab users who noticed Co contamination did not see any Nb contamination (John Sinton, personal communication). Figures C.3 and C.4 show Nb vs MgO data measured for the whole rock using XRF and for the glass using LA-ICPMS.

By comparison, all of the Co-contaminated samples plot within the normal data range except for RR1211 Q325-R03. Some samples have elevated Nb relative to the average for the Mata Volcanoes, such as KM1024 D16-R01 and KM1024 D21-R02. However these samples are consistent with samples from their respective volcanoes, Taha and Fa, with similar compositions. RR1211 Q325-R03 has the highest Nb concentration in XRF data but has a very similar Nb

concentration to most Mata samples in LA-ICPMS data. Therefore, I conclude that RR1211 Q325-R03 has been contaminated for both Nb and Co due to its preparation in the tungsten carbide ball mill and do not use Nb or Co data for this sample in this project.

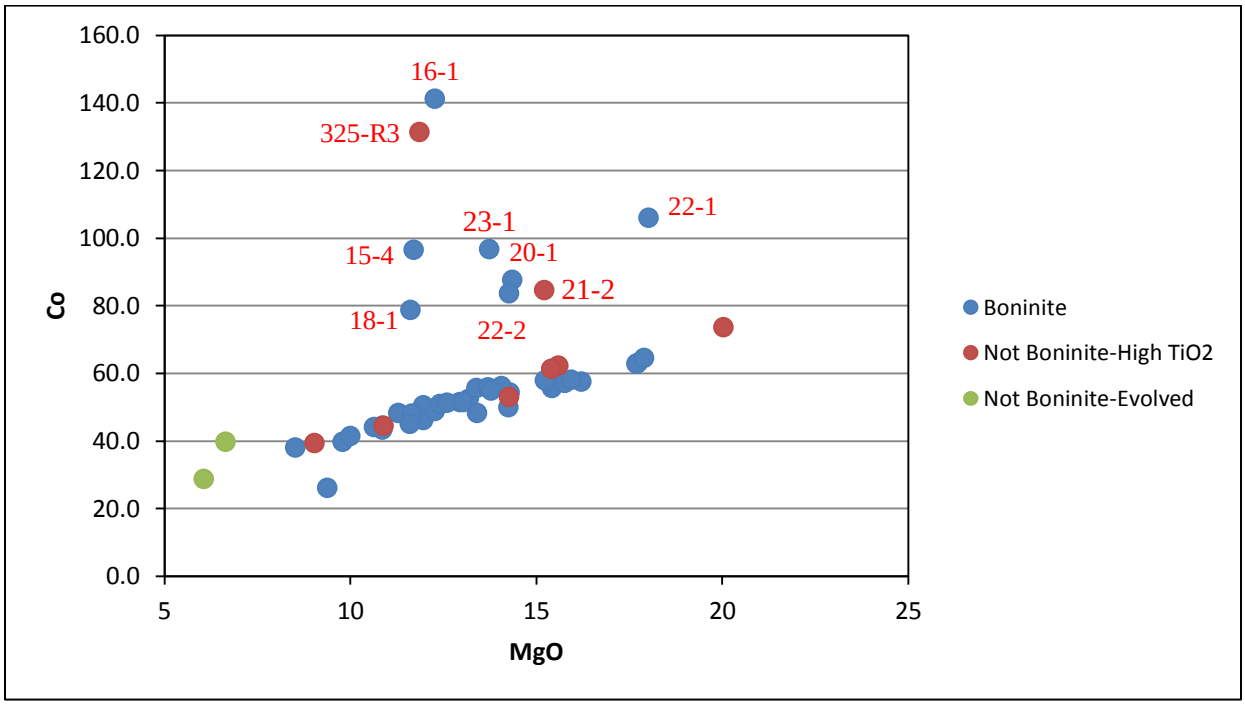


Figure C.1. Co vs. MgO plot of XRF whole rock data showing Co contamination for nine samples. Contaminated samples plot above the trend line and are labeled in short hand in red. Contaminated sample names and abbreviations in parenthesis are: KM1024 D16-R01 (16-1), KM1024 D15-R04 (15-4), KM1024 D18-R01 (18-1), KM1024 D21-R02 (21-2), KM1024 D22-R01 (22-1), KM1024 D22-R02 (22-2), KM1024 D23-R01 (23-1), and RR121 Q325-R03 (325-3).

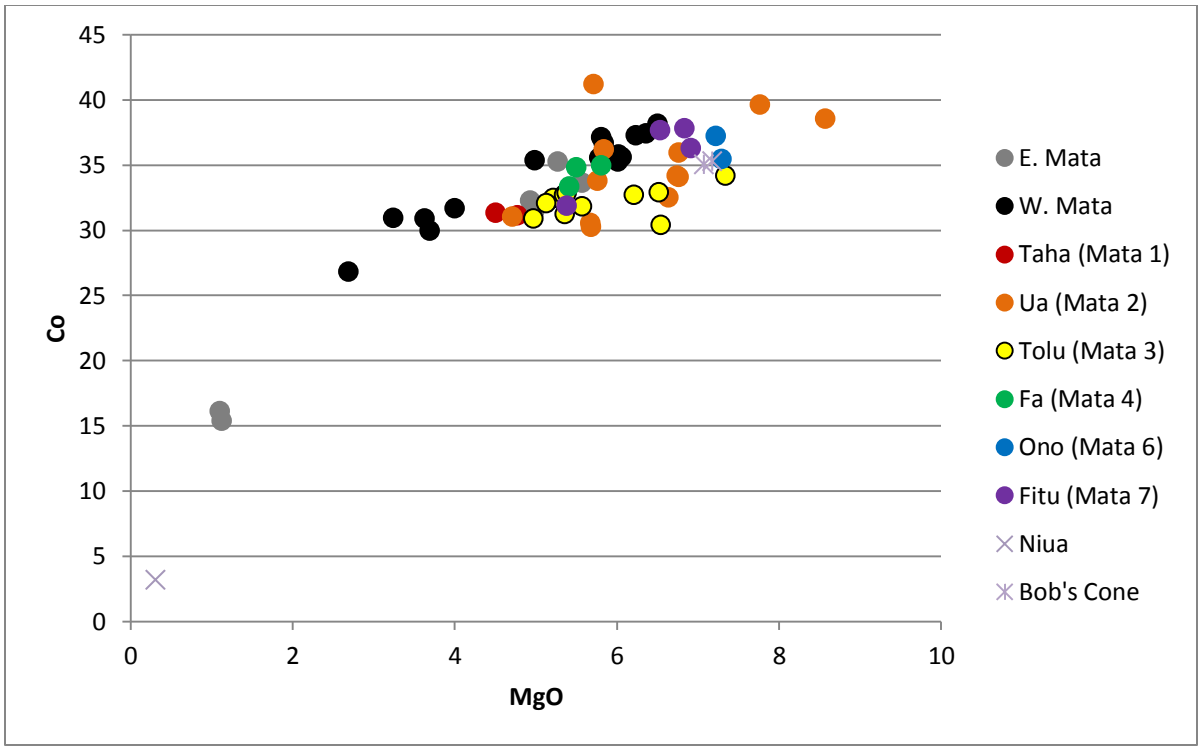


Figure C.2. Co vs. MgO plot of ICPMS glass data. Note that all samples plot along a trend line showing a correlation between Co and MgO contents. Elevated Co concentrations are not observed, suggesting that the elevated Co concentrations observed in the previous plot of XRF data are due to contamination of the XRF samples.

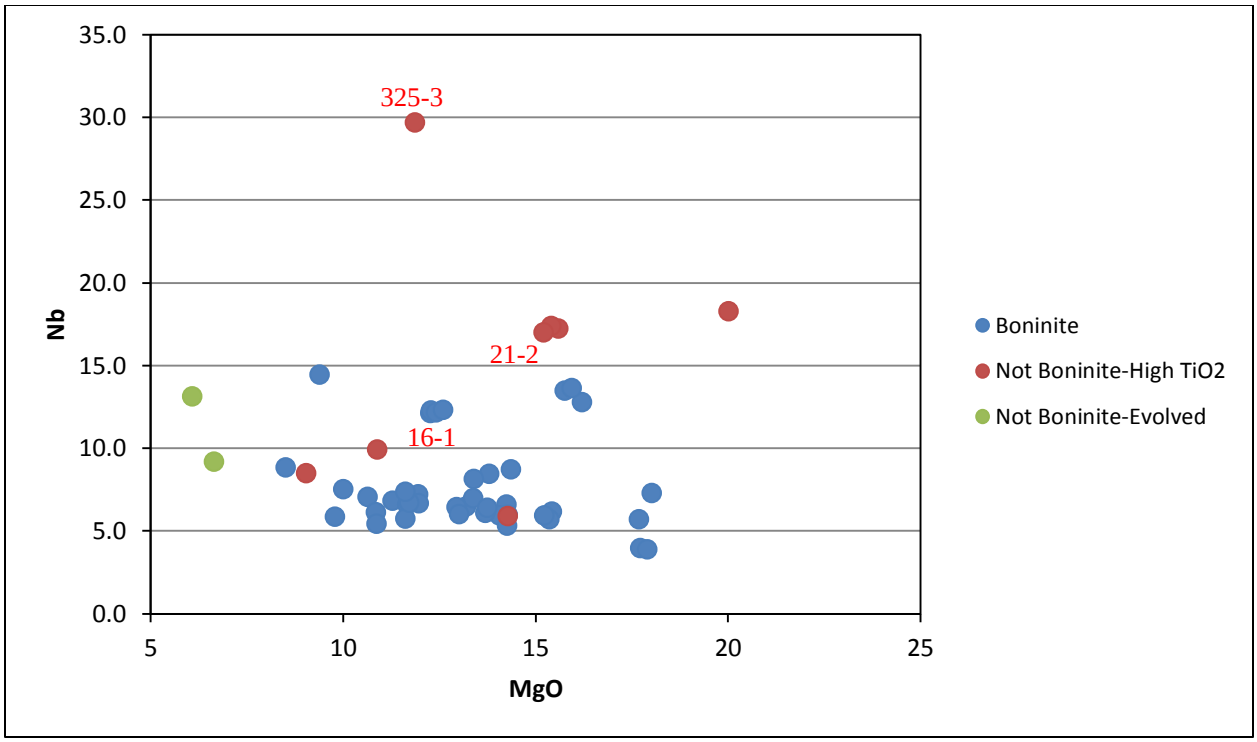


Figure C.3. Nb vs. MgO plot for XRF whole rock data. A few of the Co-contaminated samples are labeled: KM1024 D16-R01 (16-1), KM1024 D21-R02 (21-2), and RR121 Q325-R03 (325-3). RR121 Q325-R03 appears to be the only one that was contaminated with Nb.

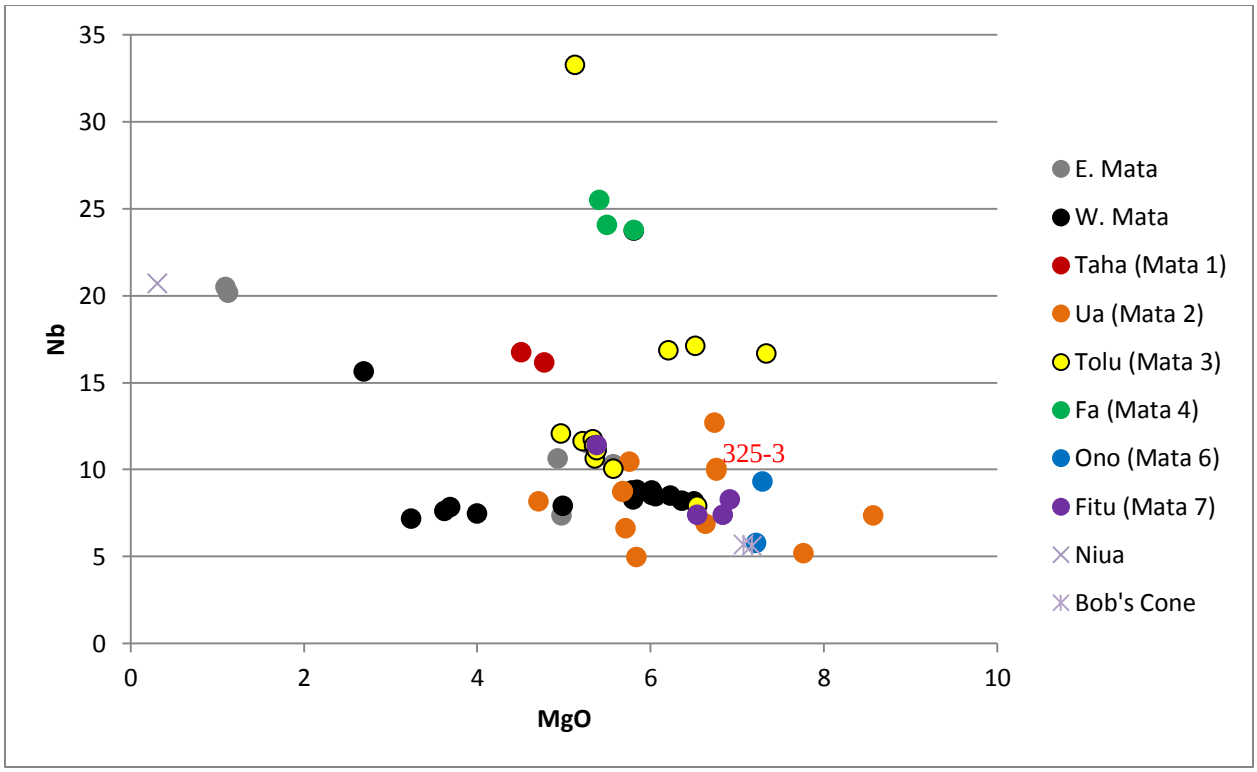


Figure C.4. Nb vs. MgO plot for LA-ICPMS glass data. One of the Co-contaminated samples in XRF is labeled: RR121 Q325-R03 (325-3). RR121 Q325-R03 appears to be the only one that was contaminated with Nb.

## APPENDIX D: ADDITIONAL THERMOMETRY DATA

This appendix presents tables of additional thermometry calculations. The first two tables (Tables D.1 and D.2) show temperatures determined for individual samples using one of the liquid thermometers (Equation 5.1 from Chapter Five). One set of calculations is based on microprobe glass data and the other is based on XRF whole rock data. Note that the XRF compositions may not represent an actual liquid. The third table (Table D.3) is based on clinopyroxene thermometry and reports individual temperature calculations for each measured clinopyroxene point.

Table D.1. Temperature calculations (in °C) from volcanic glass measured by microprobe.

| Location | Eruption | Sample | T |
|---|---|---|---|
| East Mata | | KM1129a D02-R01 | 1007 |
| East Mata | | KM1129a D02-R03 | 1023 |
| East Mata | | KM1129a D02-R04 | 1024 |
| East Mata | | KM1024 D14-R05 | 1124 |
| East Mata | | KM1129a D01-R03 | 1125 |
| East Mata | | KM1129a D01-R04 | 1127 |
| East Mata | | KM1024 D14-R09 | 1133 |
| East Mata | | KM1024 D14-R02 | 1141 |
| West Mata | Maybe New Eruption | J2-417-R28Host | 1139 |
| West Mata | New Eruption | RR1211 Q332-R05 | 1147 |
| West Mata | New Eruption | J2-413-R13 | 1148 |
| West Mata | New Eruption | RR1211 Q332-R02 | 1148 |
| West Mata | New Eruption | RR1211 Q332-R01 | 1148 |
| West Mata | New Eruption | RR1211 Q332-R04 | 1153 |
| West Mata | New Eruption | J2-418-R18 | 1153 |
| West Mata | New Eruption | J2-420-R17 | 1153 |
| West Mata | New Eruption | RR1211 Q332-R03 | 1154 |
| West Mata | New Eruption | J2-413-R04 | 1154 |
| West Mata | Maybe New Eruption | J2-420-R16 | 1155 |
| West Mata | New Eruption | J2-420-R23 | 1157 |
| West Mata | New Eruption | J2-414-R22 | 1160 |
| West Mata | New Eruption | J2-413-R14 | 1161 |
| West Mata | Maybe New Eruption | J2-413-R03 | 1162 |
| West Mata | New Eruption | J2-418-R20 | 1163 |
| West Mata | New Eruption | J2-413-Sed05B | 1168 |
| West Mata | New Eruption | J2-414-R12 | 1168 |
| West Mata | Maybe New Eruption | J2-417-R09 | 1171 |

For West Mata, the table indicates which samples are from the newer eruption vs. older eruption or eruptions. Data is sorted from smallest to largest value for each eruption for West Mata samples. For samples from the other volcanoes, data is sorted from smallest to largest values for each volcano.

Table D.1 (continued). Temperature calculations (in °C) from volcanic glass measured by microprobe.

| Location | Eruption | Sample | T |
|---|---|---|---|
| West Mata | Older Eruption | KM1024 D15-R05 | 1065 |
| West Mata | Older Eruption | J2-418-R01 | 1080 |
| West Mata | Older Eruption | J2-420-R01 | 1087 |
| West Mata | Older Eruption | KM1024 D12-R01 | 1090 |
| West Mata | Older Eruption | KM1024 D12-R08 | 1092 |
| West Mata | Older Eruption | J2-418-C02 | 1099 |
| West Mata | Older Eruption | J2-420-R02 | 1100 |
| West Mata | Older Eruption | KM1024 D12-R06 | 1100 |
| West Mata | Probably Older Eruption | J2-418-R04 | 1103 |
| West Mata | Older Eruption | J2-418-R05 | 1106 |
| West Mata | Older Eruption | J2-420-R05 | 1133 |
| West Mata | Older Eruption | J2-420-R10 | 1134 |
| West Mata | Older Eruption | J2-420-R12 | 1144 |
| West Mata | Older Eruption | J2-420-R13 | 1148 |
| West Mata | Older Eruption | J2-420-R08 | 1150 |
| West Mata | Older Eruption | J2-418-R06 | 1155 |
| West Mata | Older Eruption | J2-420-R09 | 1156 |
| West Mata | Older Eruption | J2-413-R02 | 1158 |
| West Mata | Older Eruption | J2-418-R11 | 1160 |
| West Mata | Older Eruption | J2-420-R07 | 1160 |
| West Mata | Older Eruption | J2-420-R04 | 1162 |
| West Mata | Older Eruption | KM1024 D15-R03 | 1162 |
| West Mata | Older Eruption | J2-414-R27 | 1162 |
| West Mata | Older Eruption | J2-413-R01 | 1165 |
| West Mata | Older Eruption | KM1024 D15-R01 | 1166 |
| West Mata | Older Eruption | J2-417-R02 | 1168 |
| West Mata | Older Eruption | J2-414-R01 | 1170 |
| West Mata | Older Eruption | J2-417-R01 | 1175 |
| West Mata | | RR1211 Q327-BS06 | 1147 |
| West Mata | | RR1211 Q327-R02 | 1126 |
| Lava flow near West Mata | | KM1024 D13-R01a | 1147 |

For West Mata, the table indicates which samples are from the newer eruption vs. older eruption or eruptions. Data is sorted from smallest to largest value for each eruption for West Mata samples. For samples from the other volcanoes, data is sorted from smallest to largest values for each volcano.

Table D.1 (continued). Temperature calculations (in °C) from volcanic glass measured by microprobe.

| Location | Eruption | Sample | T |
|---|---|---|---|
| Taha | | KM1024 D16-R02 | 1113 |
| Taha | | KM1024 D16-R01 | 1120 |
| Ua | | RR1211 Q325-R01 | 1118 |
| Ua | | KM1129a D10-R02 | 1141 |
| Ua | | KM1024 D18-R01 | 1144 |
| Ua | | KM1024 D18-R04 | 1144 |
| Ua | | KM1024 D18-R05 | 1145 |
| Ua | | KM1024 D17-R01 | 1146 |
| Ua | | RR1211 Q325-R04 | 1148 |
| Ua | | KM1129a D010-R01 | 1159 |
| Ua | | RR1211 Q328-R03 | 1169 |
| Ua | | RR1211 Q328-R11 | 1172 |
| Ua | | KM1129a D010-R03 | 1172 |
| Ua | | RR1211 Q325-R03 | 1172 |
| Ua | | KM1129a D010-R06 | 1199 |
| Ua | | RR1211 Q328-R12 | 1220 |
| Tolu | | KM1024 D20-R01 | 1125 |
| Tolu | | KM1129a D09-R01 | 1129 |
| Tolu | | KM1024 D20-R02 | 1132 |
| Tolu | | KM1129a D09-R02 | 1134 |
| Tolu | | KM1129a D08-R01 | 1135 |
| Tolu | | KM1129a D08-R04 | 1135 |
| Tolu | | RR1211 Q331-R16 | 1135 |
| Tolu | | KM1129a D08-R07 | 1136 |
| Tolu | | RR1211 Q331-R02 | 1141 |
| Tolu | | KM1129a D08-R08 | 1158 |
| Tolu | | KM1129a D07-R02 | 1166 |
| Tolu | | RR1211 Q331-R01 | 1167 |
| Tolu | | KM1129a D07-R01 | 1188 |

For West Mata, the table indicates which samples are from the newer eruption vs. older eruption or eruptions. Data is sorted from smallest to largest value for each eruption for West Mata samples. For samples from the other volcanoes, data is sorted from smallest to largest values for each volcano.

Table D.1 (continued). Temperature calculations (in °C) from volcanic glass measured by microprobe.

| Location | Eruption | Sample | T |
|---|---|---|---|
| Fa | | KM1024 D21-R04 | 1137 |
| Fa | | KM1024 D21-R01 | 1139 |
| Fa | | KM1024 D21-R02 | 1147 |
| Ono | | KM1024 D22-R02 | 1184 |
| Ono | | KM1024 D22-R01 | 1186 |
| Ono | | KM1024 D22-R01 | 1186 |
| Fitu | | RR1211 Q329-R02 | 1136 |
| Fitu | | KM1024 D23-R01 | 1166 |
| Fitu | | KM1024 D23-R04 | 1174 |
| Fitu | | RR1211 Q329-R01 | 1176 |

For West Mata, the table indicates which samples are from the newer eruption vs. older eruption or eruptions. Data is sorted from smallest to largest value for each eruption for West Mata samples. For samples from the other volcanoes, data is sorted from smallest to largest values for each volcano.

Table D.2. Temperature calculations (in °C) from whole rock measured by XRF.

| Location | Eruption | Sample | T |
|---|---|---|---|
| East Mata | | KM1024 D14-R02 | 1219 |
| East Mata | | KM1024 D14-R07 | 1242 |
| East Mata | | KM1129a D02-R01 | 1154 |
| East Mata | | KM1129a D02-R04 | 1170 |
| West Mata | New Eruption | RR1211 Q332-R03 | 1347 |
| West Mata | New Eruption | RR1211 Q332-R05 | 1309 |
| West Mata | New Eruption | J2-413-R13 | 1369 |
| West Mata | Older Eruption(s) | J2-418-R01 | 1252 |
| West Mata | Older Eruption(s) | J2-418-R05 | 1309 |
| West Mata | New Eruption | J2-418-R18 | 1342 |
| West Mata | Older Eruption(s) | J2-420-R01 | 1300 |
| West Mata | Older Eruption(s) | J2-420-R02 | 1280 |
| West Mata | Older Eruption(s) | J2-413-R02 | 1400 |
| West Mata | Older Eruption(s) | J2-418-R11 | 1275 |
| West Mata | New Eruption | J2-420-R17 | 1370 |
| West Mata | Maybe New Eruption | J2-420-R16 | 1395 |
| West Mata | Older Eruption(s) | J2-417-R02 | 1335 |
| West Mata | Older Eruption(s) | J2-414-R27 | 1365 |
| West Mata | Older Eruption(s) | J2-420-R05 | 1301 |
| West Mata | New Eruption | J2-414-R12 | 1292 |
| West Mata | Maybe New Eruption | J2-417-R09 | 1399 |
| West Mata | Older Eruption(s) | KM1024 D12-R01 | 1281 |
| West Mata | Older Eruption(s) | KM1024 D15-R01 | 1355 |
| West Mata | Older Eruption(s) | KM1024 D15-R04 | 1303 |
| Taha | | KM1024 D16-R01 | 1318 |
| Taha | | KM1024 D16-R03 | 1318 |
| Taha | | KM1024 D16-R04 | 1321 |
| Taha | | KM1024 D16-R06 | 1326 |

For West Mata, the table indicates which samples are from the newer eruption vs. older eruptions. Data is sorted from smallest to largest value for each eruption for West Mata samples. For samples from the other volcanoes, data is sorted from smallest to largest values for each volcano.

Table D.2. (continued). Temperature calculations (in °C) from whole rock measured by XRF.

| Location | Eruption | Sample | T |
|---|---|---|---|
| Ua | | RR1211 Q325-R01 | 1258 |
| Ua | | RR1211 Q325-R02 | 1281 |
| Ua | | KM1024 D18-R01 | 1300 |
| Ua | | RR1211 Q325-R03 | 1307 |
| Ua | | KM1129a D10-R02 | 1370 |
| Ua | | KM1129a D10-R05 | 1460 |
| Ua | | KM1129a D10-R01 | 1461 |
| Ua | | KM1129a D10-R06 | 1466 |
| Tolu | | RR1211 Q331-R16 | 1347 |
| Tolu | | KM1129a D08-R07 | 1357 |
| Tolu | | KM1024 D20-R01 | 1372 |
| Tolu | | KM1129a D07-R01 | 1409 |
| Tolu | | KM1129a D08-R01 | 1414 |
| Tolu | | KM1129a D07-R02 | 1421 |
| Tolu | | KM1129a D09-R01 | 1521 |
| Fa | | KM1024 D21-R02 | 1395 |
| Fa | | KM1024 D21-R04 | 1400 |
| Fa | | KM1024 D21-R01 | 1405 |
| Ono | | KM1024 D22-R02 | 1370 |
| Ono | | KM1024 D22-R01 | 1469 |
| Ono | | KM1024 D22-R01 | 1469 |
| Fitu | | RR1211 Q329-R01 | 1233 |
| Fitu | | KM1024 D23-R04 | 1337 |
| Fitu | | KM1024 D23-R01 | 1356 |

Table D.2 (continued). Temperature calculations (in °C) from whole rock measured by XRF. For West Mata, the table indicates which samples are from the newer eruption vs. older eruptions. Data is sorted from smallest to largest value for each eruption for West Mata samples. For samples from the other volcanoes, data is sorted from smallest to largest values for each volcano.

Table D.3. Temperatures (in $^{o}$C) calculated for Mata samples based using a clinopyroxene-only thermometer at a pressure of 500 bars (Equation 5.7).

| Volcano | Sample | Temperature in $^{o}$C from Cpx Only Thermometer |
|---|---|---|
| East Mata | KM1024 D14-R02 | 1190 |
| | | 1189 |
| | | 1187 |
| | | 1183 |
| | | 1187 |
| | | 1192 |
| | | 1182 |
| | | 1185 |
| | | 1185 |
| East Mata | KM1024 D14-R07 | 1181 |
| | | 1169 |
| West Mata | J2-413-R04 | 1191 |
| | | 1189 |
| | | 1192 |
| | | 1195 |
| | | 1196 |

Samples from the older eruption or eruptions of West Mata are J2-418-R01 and J2-420-R02. Data are arranged in order from lowest temperature to highest temperature for each sample.

Table D.3 (continued). Temperatures (in $^{o}$C) calculated for Mata samples based using a clinopyroxene-only thermometer at a pressure of 500 bars (Equation 5.7).

| Volcano | Sample | Temperature in $^{o}$C from Cpx Only Thermometer |
|---|---|---|
| West Mata | J2-413-R13 | 1182 |
| | | 1190 |
| | | 1190 |
| | | 1187 |
| | | 1194 |
| | | 1185 |
| | | 1189 |
| | | 1189 |
| | | 1183 |
| | | 1189 |
| | | 1186 |
| | | 1192 |
| | | 1195 |
| | | 1193 |
| | | 1175 |
| | | 1193 |
| | | 1194 |
| | | 1193 |
| | | 1193 |
| | | 1194 |
| | | 1192 |
| | | 1189 |
| | | 1189 |
| | | 1193 |
| | | 1192 |
| | | 1191 |

Samples from the older eruption or eruptions of West Mata are J2-418-R01 and J2-420-R02. Data are arranged in order from lowest temperature to highest temperature for each sample.

Table D.3 (continued). Temperatures (in $^{o}$C) calculated for Mata samples based using a clinopyroxene-only thermometer at a pressure of 500 bars (Equation 5.7).

| Volcano | Sample | Temperature in $^{o}$C from Cpx Only Thermometer |
|---|---|---|
| West Mata | J2-413-R13 | 1176 |
| | | 1177 |
| | | 1181 |
| | | 1180 |
| | | 1180 |
| | | 1181 |
| | | 1180 |
| | | 1179 |
| | | 1154 |
| | | 1158 |
| | | 1161 |
| | | 1160 |
| | | 1182 |
| | | 1174 |
| | | 1182 |
| | | 1180 |
| | | 1184 |
| | | 1188 |
| | | 1186 |
| | | 1186 |
| | | 1151 |
| | | 1154 |
| | | 1182 |
| | | 1162 |
| | | 1165 |
| | | 1189 |
| | | 1180 |
| | | 1192 |
| | | 1180 |
| | | 1191 |
| | | 1181 |
| | | 1193 |
| | | 1194 |

Samples from the older eruption or eruptions of West Mata are J2-418-R01 and J2-420-R02. Data are arranged in order from lowest temperature to highest temperature for each sample.

Table D.3 (continued). Temperatures (in $^{o}$C) calculated for Mata samples based using a clinopyroxene-only thermometer at a pressure of 500 bars (Equation 5.7).

| Volcano | Sample | Temperature in $^{o}$C from Cpx Only Thermometer |
|---|---|---|
| West Mata | J2-418-R11 | 1190 |
| | | 1195 |
| | | 1188 |
| | | 1176 |
| | | 1177 |
| | | 1196 |
| | | 1191 |
| | | 1187 |
| | | 1190 |
| | | 1192 |
| | | 1193 |
| | | 1194 |
| | | 1193 |
| | | 1179 |
| | | 1190 |
| | | 1194 |
| | | 1192 |
| | | 1193 |
| | | 1170 |
| | | 1161 |
| | | 1189 |
| | | 1193 |
| | | 1193 |
| | | 1184 |
| | | 1186 |
| | | 1194 |
| | | 1192 |

Samples from the older eruption or eruptions of West Mata are J2-418-R01 and J2-420-R02. Data are arranged in order from lowest temperature to highest temperature for each sample.

Table D.3 (continued). Temperatures (in $^{o}$C) calculated for Mata samples based using a clinopyroxene-only thermometer at a pressure of 500 bars (Equation 5.7).

| Volcano | Sample | Temperature in $^{o}$C from Cpx Only Thermometer |
|---|---|---|
| West Mata | J2-418-R18 | 1179 |
| | | 1176 |
| | | 1180 |
| | | 1180 |
| | | 1180 |
| | | 1181 |
| | | 1182 |
| | | 1181 |
| | | 1178 |
| | | 1187 |
| | | 1187 |
| | | 1181 |
| | | 1178 |
| | | 1175 |
| | | 1177 |
| | | 1177 |
| | | 1178 |
| | | 1180 |
| | | 1194 |
| | | 1196 |
| | | 1176 |
| | | 1196 |
| | | 1195 |
| | | 1196 |
| | | 1195 |
| | | 1191 |
| | | 1192 |
| | | 1192 |
| | | 1196 |
| | | 1195 |
| | | 1194 |
| | | 1199 |
| | | 1197 |
| | | 1197 |

Samples from the older eruption or eruptions of West Mata are J2-418-R01 and J2-420-R02. Data are arranged in order from lowest temperature to highest temperature for each sample.

Table D.3 (continued). Temperatures (in $^{o}$C) calculated for Mata samples based using a clinopyroxene-only thermometer at a pressure of 500 bars (Equation 5.7).

| Volcano | Sample | Temperature in $^{o}$C from Cpx Only Thermometer |
|---|---|---|
| West Mata | J2-420-R02 | 1191 |
| | | 1183 |
| | | 1185 |
| | | 1184 |
| | | 1186 |
| | | 1184 |
| | | 1190 |
| | | 1193 |
| | | 1185 |
| | | 1182 |
| | | 1162 |
| | | 1172 |
| | | 1181 |
| | | 1160 |
| | | 1175 |
| | | 1165 |
| | | 1188 |
| | | 1187 |
| | | 1196 |
| | | 1186 |
| | | 1164 |
| | | 1166 |
| West Mata | J2-420-R17 | 1191 |
| | | 1186 |
| | | 1191 |
| | | 1192 |
| | | 1193 |
| | | 1187 |
| | | 1191 |
| | | 1192 |
| | | 1188 |
| | | 1189 |
| | | 1176 |
| | | 1188 |
| | | 1192 |
| | | 1186 |
| | | 1186 |

Samples from the older eruption or eruptions of West Mata are J2-418-R01 and J2-420-R02. Data are arranged in order from lowest temperature to highest temperature for each sample.

Table D.3 (continued). Temperatures (in $^{o}$C) calculated for Mata samples based using a clinopyroxene-only thermometer at a pressure of 500 bars (Equation 5.7).

| Volcano | Sample | Temperature in $^{o}$C from Cpx Only Thermometer |
|---|---|---|
| Taha | KM1024 D16-R04 | 1177 |
| | | 1181 |
| | | 1176 |
| | | 1178 |
| | | 1174 |
| | | 1181 |
| | | 1187 |
| | | 1177 |
| | | 1184 |
| | | 1185 |
| | | 1158 |
| | | 1173 |
| | | 1175 |
| | | 1173 |
| | | 1173 |
| | | 1173 |
| | | 1182 |
| | | 1184 |
| | | 1171 |
| | | 1187 |
| | | 1185 |
| | | 1171 |
| | | 1190 |
| | | 1192 |
| Ua | KM1024 D18-R01 | 1150 |
| | | 1193 |
| | | 1190 |
| | | 1188 |
| | | 1186 |
| | | 1200 |
| | | 1198 |
| | | 1190 |
| | | 1184 |
| | | 1187 |

Samples from the older eruption or eruptions of West Mata are J2-418-R01 and J2-420-R02. Data are arranged in order from lowest temperature to highest temperature for each sample.

Table D.3 (continued). Temperatures (in $^{o}$C) calculated for Mata samples based using a clinopyroxene-only thermometer at a pressure of 500 bars (Equation 5.7).

| Volcano | Sample | Temperature in $^{o}$C from Cpx Only Thermometer |
|---|---|---|
| Tolu | KM1024 D20-R01 | 1177 |
| | | 1180 |
| | | 1173 |
| | | 1172 |
| | | 1176 |
| | | 1184 |
| | | 1179 |
| | | 1181 |
| | | 1177 |
| | | 1181 |
| | | 1192 |
| | | 1190 |
| | | 1184 |
| | | 1163 |
| | | 1166 |
| | | 1169 |
| | | 1160 |
| | | 1164 |
| | | 1154 |
| | | 1146 |
| | | 1151 |
| | | 1146 |
| | | 1136 |
| | | 1185 |
| | | 1181 |
| | | 1184 |
| | | 1184 |
| | | 1184 |
| | | 1185 |
| | | 1166 |
| | | 1157 |
| | | 1150 |
| | | 1148 |
| | | 1167 |
| | | 1185 |

Samples from the older eruption or eruptions of West Mata are J2-418-R01 and J2-420-R02. Data are arranged in order from lowest temperature to highest temperature for each sample.

Table D.3 (continued). Temperatures (in $^{o}$C) calculated for Mata samples based using a clinopyroxene-only thermometer at a pressure of 500 bars (Equation 5.7).

| Volcano | Sample | Temperature in $^{o}$C from Cpx Only Thermometer |
|---|---|---|
| Fa | KM1024 D21-R02 | 1195 |
| | | 1176 |
| | | 1192 |
| | | 1188 |
| | | 1191 |
| | | 1185 |
| | | 1173 |
| | | 1191 |
| | | 1188 |
| | | 1192 |
| | | 1190 |
| | | 1189 |
| | | 1183 |
| | | 1182 |
| | | 1184 |
| | | 1184 |
| | | 1184 |
| | | 1183 |
| | | 1195 |
| | | 1195 |
| | | 1186 |
| | | 1181 |
| | | 1186 |
| | | 1187 |
| | | 1177 |
| | | 1173 |
| | | 1187 |
| | | 1192 |
| | | 1193 |
| | | 1187 |
| | | 1165 |
| | | 1179 |
| Fitu | KM1024 D23-R01 | 1156 |
| | | 1156 |
| | | 1158 |
| | | 1158 |

Samples from the older eruption or eruptions of West Mata are J2-418-R01 and J2-420-R02. Data are arranged in order from lowest temperature to highest temperature for each sample.

## REFERENCES


Acland, A. S. (1996). Magma genesis in the northern Lau Basin, SW Pacific. Durham University.

Arculus, R. J. (2013). New insights into arc-backarc systems; the Tonga-Kermadec example. *Abstract V13I-01 presented at 2013 Fall Meeting, AGU, San Francisco, Calif., 9-13 Dec.*

Armstrong, J. T. (1988). Quantitative analysis of silicate and oxide materials: comparison of Monte Carlo, ZAF, and f(rZ) procedures. In: Newbury, D. E. (ed.) , 239–246.

Asimow, P. D. & Ghiorso, M. S. (1998). Algorithmic modifications extending MELTS to calculate subsolidus phase relations. *American Mineralogist* **83**, 1127–1132.

Austin, R. (2012). Early Seafloor Spreading and Variations in Crustal Accretion in the Lau Basin. MS Thesis, University of Hawaii at Manoa.

Barnes, S. J. (1998). Chromite in komatiites, 1. Magmatic controls on crystallization and composition. *Journal of Petrology* **39**, 1689–1720.

Bohnenstiehl, D. R., Dziak, R. P., Matsumoto, H., Lau, T. A., Fowler, M. J., Scheip, C., Cook, K. E., Warren, K. W. & Conder, J. A. (2010). Hydroacoustic monitoring of seismic and volcanic activity within the Lau Basin. *Abstract T11E-02 presented at 2010 Fall Meeting, AGU, San Francisco, Calif., 13-17 Dec.*

Butterfield, D. A., Resing, J. A., Roe, K. K., Christensen, M., Embley, R. W., Lupton, J. E. & Chadwick, W. W. (2009). Chemical properties and hydrothermal processes on the first two directly sampled deep-sea eruptions. *Eos Trans. AGU, 90(52), Fall Meet. Suppl., Abstract V43I-06*.

Cameron, W. E. (1989). Contrasting boninitic-tholeiite associations from New Caledonia. *Boninites and Related Rocks*, 314–339.

Cameron, W. E., McCulloch, M. T. & Walker, D. A. (1983). Boninite petrogenesis: chemical and Nd-Sr isotopic constraints. *Earth and Planetary Science Letters* **65**, 75–89.

Caress, D. W., Thomas, H. J., Conlin, D. & Clague, D. A. (2009). Fine-scale morphology of West Mata Volcano and the Northeast Lau Spreading Center, Lau Basin from AUV multibeam surveys. *Eos Trans. AGU, 90(52), Fall Meet. Suppl., Abstract V51D-1731*.

Caulfield, J., Turner, S., Arculus, R., Dale, C., Jenner, F., Pearce, J., Macpherson, C. & Handley, H. (2012). Mantle flow, volatiles, slab-surface temperatures and melting dynamics in the north Tonga arc–Lau back-arc basin. *Journal of Geophysical Research* **117**.

Clague, D. A., Paduan, J. B., Caress, D. W., Thomas, H., Chadwick, W. W. & Merle, S. G. (2011). Volcanic morphology of West Mata Volcano, NE Lau Basin, based on high-resolution bathymetry and depth changes: MORPHOLOGY OF WEST MATA VOLCANO. *Geochemistry, Geophysics, Geosystems* **12**.

Clague, D. A., Rubin, K. H. & Keller, N. S. (2009). Products of submarine fountains and bubble-burst eruptive activity at 1200 m on West Mata Volcano, Lau Basin. *Eos Trans. AGU, 90(52), Fall Meet. Suppl., Abstract V43I-02*.

Colman, A. *et al.* (2012). Effects of variable magma supply on mid-ocean ridge eruptions: Constraints from mapped lava flow fields along the Galápagos Spreading Center. *Geochemistry, Geophysics, Geosystems* **13**.

Cooper, L. B., Plank, T., Arculus, R. J., Hauri, E. H., Hall, P. S. & Parman, S. W. (2010). High-Ca boninites from the active Tonga Arc. *Journal of Geophysical Research* **115**.

Danyushevsky, L. V. & Sobolev, A. V. (1996). Ferric-ferrous ratio and oxygen fugacity calculations for primitive mantle-derived melts:calibration of an empirical technique. *mineralogy and petrology* **57**, 229–241.

Danyushevsky, L. V., Sobolev, A. V. & Falloon, T. J. (1995). North Tongan High-Ca Boninite Petrogenesis: The Role of Samoan Plume and Subduction Zone-Transform Fault Transition. *Journal of Geodynamics* **20**, 219–241.

Davis, R., Tebo, B. M. & Moyer, C. L. (2009). Community Analysis of Dynamic Microbial Mat Communities from Actively Erupting Seamounts. *Eos Trans. AGU, 90(52), Fall Meet. Suppl., Abstract V44B-05*.

Deer, W. A., Howie, R. A. & Zussman, J. (1966). *An Introduction to the Rock-Forming Minerals*. Longmans.

Dziak, R. P. *et al.* (2013). Acoustic and tephra records of explosive eruptions at West Mata submarine volcano, NE Lau Basin. *Abstract V21C-2733 presented at 2013 Fall Meeting, AGU, San Francisco, Calif., 9-13 Dec.*

Dziak, R. P., Bohnenstiehl, D. R., Baker, E. T., Matsumoto, H., Haxel, J. H., Walker, S. & Fowler, M. J. (2010). Volcanic explosions, seismicity, and debris from the West and North Mata Volcano Complex, NE Lau Basin. .

Dziak, R. P., Embley, R. W., Baker, E. T., Chadwick, W. W., Resing, J., Matsumoto, H., Walker, S. L., Bohnenstiehl, D. R. & Klinck, H. (2009). Long-term explosion records from two erupting submarine volcanoes in the Mariana and Tonga island-arcs. *Eos Trans. AGU, 90(52), Fall Meet. Suppl., Abstract V44B-02*.

Eason, D. E. & Sinton, J. M. (2009). Lava shields and fissure eruptions of the Western Volcanic Zone, Iceland: Evidence for magma chambers and crustal interaction. *Journal of Volcanology and Geothermal Research* **186**, 331–348.

Eason, D. & Sinton, J. (2006). Origin of high-Al N-MORB by fractional crystallization in the upper mantle beneath the Galápagos Spreading Center. *Earth and Planetary Science Letters* **252**, 423–436.

Elliott, T. (2003). Tracers of the slab. In: Eiler, J. (ed.) *Geophysical Monograph Series*. Washington, D. C.: American Geophysical Union, 23–45.

Embley, R. W. *et al.* (2013). Hyperactive hydrothermal activity in the NE Lau basin revealed by ROV dives. *Abstract V21C-2738 presented at 2013 Fall Meeting, AGU, San Francisco, Calif., 9-13 Dec.*

Embley, R. W. *et al.* (2014). Eruptive modes and hiatus of volcanism at West Mata seamount, NE Lau basin: 1996-2012. *Geochemistry, Geophysics, Geosystems*.

Embley, R. W., Merle, S. G., Dziak, R. P., Rubin, K. H., Martinez, F. & Crowhurst, P. (2012). Pit crater formation and mass-wasting on West Mata volcano in 2010-2011 interpreted from repeat bathymetric surveys. *Abstract T51D-2604 presented at 2012 Fall Meeting, AGU, San Francisco, Calif., 3-7 Dec.*

Embley, R. W., Merle, S. G., Lupton, J. E., Resing, J., Baker, E. T., Lilley, M. D., Arculus, R. J. & Crowhurst, P. (2009). Extensive and diverse submarine volcanism and hydrothermal activity in the NE Lau Basin. *Eos Trans. AGU, 90(52), Fall Meet. Suppl., Abstract V51D-1719*.

Escrig, S., Bézos, A., Goldstein, S. L., Langmuir, C. H. & Michael, P. J. (2009). Mantle source variations beneath the Eastern Lau Spreading Center and the nature of subduction components in the Lau basin-Tonga arc system: ISOTOPE GEOCHEMISTRY OF LAU BASIN LAVAS. *Geochemistry, Geophysics, Geosystems* **10**, n/a–n/a.

Escrig, S., Bézos, A., Langmuir, C. H., Michael, P. J. & Arculus, R. (2012). Characterizing the effect of mantle source, subduction input and melting in the Fonualei Spreading Center, Lau Basin: Constraints on the origin of the boninitic signature of the back-arc lavas: GEOCHEMICAL VARIATION ALONG THE FSC. *Geochemistry, Geophysics, Geosystems* **13**.

Falloon, T. J. *et al.* (2007). Multiple mantle plume components involved in the petrogenesis of subduction-related lavas from the northern termination of the Tonga Arc and northern Lau Basin: Evidence from the geochemistry of arc and backarc submarine volcanics. *Geochemistry, Geophysics, Geosystems* **8**.

Falloon, T. J. & Crawford, A. J. (1991). The petrogenesis of high-calcium boninites dredged from the northern Tonga ridge. *Earth and Planetary Science Letters* **102**, 375–394.

Falloon, T. J. & Danyushevsky, L. V. (2000). Melting of refractory mantle and 1.5, 2 and 2.5 GPa under anhydrous and H2O-undersaturated conditions: Implications for the Petrogenesis of high-Ca boninites and the influence of subduction components on mantle melting. *Journal of Petrology* **41**, 257–283.

Falloon, T. J., Danyushevsky, L. V., Crawford, A. J., Meffre, S., Woodhead, J. D. & Bloomer, S. H. (2008). Boninites and Adakites from the Northern Termination of the Tonga Trench: Implications for Adakite Petrogenesis. *Journal of Petrology* **49**, 697–715.

Falloon, T. J., Green, D. H. & McCulloch, M. T. (1989). Petrogenesis of high-Mg and associated lavas from the north Tonga Trench. In: Crawford, A. J. (ed.) *Boninites and Related Rocks*, 358–395.

Frost, R. (1991). Introduction to oxygen fugacity and Its petrologic importance. In: Lindsley, D. H. (ed.) *oxide minerals: Petrologic and magnetic significance*, 1–10.

Ghiorso, M. S. & Sack, R. O. (1995). Chemical mass transfer in magmatic processes IV. A revised and internally consistent thermodynamic model for the interpolation and extrapolation of liquid-solid equilibria in magmatic systems at elevated temperatures and pressures. **119**, 197–212.

Glancy, S., Rubin, K., Hellebrand, E., Jenner, F., Arculus, R. & Embley, R. (2014). Wedge and slab inputs to boninite magmas in the NE Lau Basin. *Goldschmidt 2014 Abstract*.

Glancy, S., Rubin, K. H., Hellebrand, E. & Embley, R. W. (2012). Boninite volcanism in the back-arc: Testing tectonic and magmatic controls at the NE Lau Basin Mata Seamounts. *Abstract T51D-2605 presented at 2012 Fall Meeting, AGU, San Francisco, Calif., 3-7 Dec.*

Goldich, S. S., Ingamells, C. O., Suhr, N. H. & Anderson, D. H. (1967). Analyses of silicate rock and mineral standards. *Canadian Journal of Earth Sciences* **4**, 747–755.

Hanano, D., Weis, D., Scoates, J. S., Aciego, S. M. & DePaolo, D. J. (2010). Horizontal and vertical zoning of heterogeneities in the Hawaiian mantle plume from the geochemistry of consecuctive postshield volcano pairs: Kohala-Mahukona and Mauna Kea-Hualalai. .

Hawkesworth, C. J., Hergt, J. M., Ellam, R. M. & Mc Dermott, F. (1991). Element fluxes associated with subduction related magmatism. *Philosophical Transactions of the Royal Society of London. Series A: Physical and Engineering Sciences* **335**, 393–405.

Hawkins, J. W. (1995). Evolution of the Lau Basin--Insights from ODP Leg 135. In: Taylor, B. & Natland, B. (eds) *Active Margins and Marginal Basins of the Westerm Pacific*, 125–174.

Huber, J. A., Cantin, H., Resing, J. & Butterfield, D. A. (2009). Microbial communities in erupting fluids from West Mata Volcano, Tonga Arc. *Eos Trans. AGU, 90(52), Fall Meet. Suppl., Abstract V43I-07*.

Jarosewich, E., Nelen, J. A. & Norberg, J. A. (1980). Reference Samples for Electron Microprobe Analysis. *Geostandards Newsleter* **4**.

Jenner, F. E. & O'Neill, H. S. C. (2012). Analysis of 60 elements in 616 ocean floor basaltic glasses. *Geochemistry, Geophysics, Geosystems* **13**.

Keller, N. S., Arculus, R. J., Hermann, J. & Richards, S. (2008). Submarine back-arc lava with arc signature: Fonualei Spreading Center, northeast Lau Basin, Tonga. *Journal of Geophysical Research* **113**.

Kelley, K. A. & Cottrell, E. (2009). Water and the Oxidation State of Subduction Zone Magmas. *Science* **325**, 605–607.

Kilinc, A., Carmichael, I. S. E., Rivers, M. L. & Sack, R. O. (1983). The ferric-ferrous ratio of natural silicate liquids equilibrated in air. *Contributions to Mineralogy and Petrology* **83**, 136–140.

Klügel, A., Hansteen, T. H. & Galipp, K. (2005). Magma storage and underplating beneath Cumbre Vieja volcano, La Palma (Canary Islands). *Earth and Planetary Science Letters* **236**, 211–226.

Langmuir, C. H., bezos, A., Escrig, S. & Parman, S. W. (2006). Chemical systematics and hydrous melting of the mantle in back-arc basins. In: Christie, D. M., Fisher, C. R., Lee, S.-M. & Givens, S. (eds) *Back-Arc Spreading Systems: Geological, Biological, Chemical, and Physical Interactions*, 87–146.

Le Bas, M. J. (2000). IUGS Reclassification of the high-Mg and picritic volcanic rocks. *Journal of Petrology* **41**, 1467–1470.

Lupton, J. E., Butterfield, D. A., Lilley, M. D., Resing, J., Embley, R. W., Arculus, R. J., Rubin, K. H., Evans, L. J. & Greene, R. (2009). Helium, carbon, and helium isotopes in the Northern Lau Basin. *Eos Trans. AGU, 90(52), Fall Meet. Suppl., Abstract V51D-1718*.

Lupton, J. E., Lilley, M. D., Butterfield, D. A., Resing, J. A., Arculus, R. J., Rubin, K. H., Embley, R. W. & Evans, L. J. (2013). Gas chemistry of hydrothermal systems of the Northern Lau Basin - New results. *Abstract V21C-2735 presented at 2013 Fall Meeting, AGU, San Francisco, Calif., 9-13 Dec.*

Martinez, F. & Taylor, B. (2006). Modes of crustal accretion in back-arc basins: Inferences from the Lau Basin. In: Christie, D. M., Fisher, C. R., Lee, S.-M. & Givens, S. (eds) *Back-Arc Spreading Systems: Geological, Biological, Chemical, and Physical Interactions*, 5–30.

Matsumoto, H., Embley, R. W., Haxel, J. H., Dziak, R. P., Bohnenstiehl, D. R., Stalin, S. E. & Meinig, C. (2010). First use of an autonomous glider for exploring submarine volcanism in the SW Pacific. *Abstract T13B-2189 presented at 2010 Fall Meeting, AGU, San Francisco, Calif., 13-17 Dec.*

Meffre, S., Falloon, T. J., Crawford, T. J., Hoernle, K., Hauff, F., Duncan, R. A., Bloomer, S. H. & Wright, D. J. (2012). Basalts erupted along the Tongan fore arc during subduction initiation: Evidence from geochronology of dredged rocks from the Tonga fore arc and trench. *Geochemistry, Geophysics, Geosystems* **13**.

Merle, S. (2008). Northeast Lau Basin R/V Thompson Expedition TN 227. *Cruise Report*.

Merle, S. (2009). Northeast Lau Basin Response Cruise (NELRC). *Cruise Report*.

Michael, P., Escrig, S., Rubin, K. H., Cooper, L. B., Langmuir, C. H., Clague, D. A., Keller, N. S. & Plank, T. A. (2009). Major and trace elements and volatiles in glasses from the 2009

Rapid Response Expedition to West Mata Volcano and Northeast Lau Spreading Center (NELSC). *Title, Eos Trans. AGU, 90(52), Fall Meet. Suppl., Abstract V51D-1720*.

Nikolaev, G. S., Borisov, A. A. & Ariskin, A. A. (1996). Calculation of the ferric-ferrous ratio in magmatic melts: testing and additional calibration of empirical equations for various magmatic series. *Geochemistry International* **34**, 641–649.

Pearce, J. A. & Stern, R. J. (2006). Origin of back-arc basin magmas: Trace element and isotope perspectives. In: Christie, D. M., Fisher, C. R., Lee, S.-M. & Givens, S. (eds) *Back-Arc Spreading Systems: Geological, Biological, Chemical, and Physical Interactions*, 63–86.

Phillips, D. A. (2003). Crustal Motion Studies in the Southwest Pacific Geodetic Measurements of Plate Convergence in Tonga, Vanuatu, and the Solomon Islands. PhD thesis, University of Hawaii at Manoa.

Plank, T. (2005). Constraints from Thorium/Lanthanum on Sediment Recycling at Subduction Zones and the Evolution of the Continents. *Journal of Petrology* **46**, 921–944.

Presnall, D. C., Dixon, S. A., Dixon, J. R., O'donnell, T. H., Brenner, N. L., Schrock, R. L. & Dycus, D. W. (1978). Liquidus phase relations on the join diopside-forsterite-anorthite from 1 atm to 20 kbar: their bearing on the generation and crystallization of basaltic magma. *Contributions to Mineralogy and Petrology* **66**, 203–220.

Resing, J. (2010). NE Lau Basin R/V Kilo Moana Expedition KM1008. *Cruise Report*.

Resing, J. A. *et al.* (2011). Active submarine eruption of boninite in the northeastern Lau Basin. *Nature Geoscience* **4**, 799–806.

Resing, J. A. & Embley, R. W. (2009). Active eruptions in the NE Lau Basin. *Eos Trans. AGU, 90(52), Fall Meet. Suppl., Abstract V43I-01*.

Roeder, P. L. & Emslie, Rf. (1970). Olivine-liquid equilibrium. *Contributions to mineralogy and petrology* **29**, 275–289.

Rogers, N. W., MacLeod, C. J. & Murton, B. J. (1989). Petrogenesis of boninitic lavas from the Limassol Forest Complex, Cyprus. In: Crawford, A. J. (ed.) *Boninites and Related Rocks*, 288–313.

Rubin, K. *et al.* (2012). Volcanic Eruptions in the Deep Sea. *Oceanography* **25**, 142–157.

Rubin, K. *et al.* (2013a). Timescale and petrogenesis of 2009 and older W. Mata boninite magmas. *Mineralogical Magazine* **77**, 2094.

Rubin, K. H. & Embley, R. W. (2012). Identification and implications of a submarine monogenetic field in the NE Lau Basin. *Abstract V44C-08 presented at 2012 Fall Meeting, AGU, San Francisco, Calif., 3-7 Dec.*

Rubin, K. H., Embley, R. W., Arculus, R. J. & Lupton, J. E. (2013b). Magmatically greedy reararc volcanoes of the N. Tofua Segment of the Tonga Arc. *Abstract V13I-04 presented at 2013 Fall Meeting, AGU, San Francisco, Calif., 9-13 Dec.*

Rubin, K. H., Embley, R. W., Arculus, R. J., Pyle, D. & Russo, C. J. (2011). Rapid magmatic rates implied by widespread contemporaneous magmatism in the NE Lau Basin. *Abstract V52C-08 presented at 2011 Fall Meeting, AGU, San Francisco, Calif., 5-9 Dec.*

Rubin, K. H., Embley, R. W., Clague, D. A., Resing, J. A., Michael, P. J., Keller, N. S. & Baker, E. T. (2009). Lavas from active boninite and very recent basalt eruptions at two submarine NE Lau Basin sites. *Eos Trans. AGU, 90(52), Fall Meet. Suppl., Abstract V43I-05*.

Rubin, K., Michael, P., Perfit, M. & Sinton, J. (2014). Magma dynamics from temporal and spatial compositional variations within and between eruptions. *Goldschmidt 2014 Abstract*.

Smith, P. M. & Asimow, P. D. (2005). Adiabat_1ph: A new public front-end to the MELTS, pMELTS, and pHMELTS models. *Geochemistry, Geophysics, Geosystems* **6**.

Sobolev, A. V. & Danyushevsky, L. V. (1994). Petrology and geochemistry of boninites from the north termination of the Tonga Trench: constraints on the generation conditions of primary high-Ca boninite magmas. *Journal of Petrology* **35**, 1183–1211.

Stern, R. J. (2002). Subduction zones. *Reviews of Geophysics* **40**.

Sun, W., Hu, Y., Kamenetsky, V. S., Eggins, S. M., Chen, M. & Arculus, R. J. (2008). Constancy of Nb/U in the mantle revisited. *Geochimica et Cosmochimica Acta* **72**, 3542–3549.

Umino, S. (1986). Magma mixing in boninite sequence of Chichijima, Bonin Islands. *Journal of Volcanology and Geothermal Research* **29**, 125–157.

Umino, S. & Kushiro, I. (1989). Experimental studies on boninite petrogenesis. *Boninites and related Rocks*, 89–111.

Van der Laan, S. R., Flower, M. F. J. & Koster van Groos, A. F. (1989). Experimental evidence for the origin of boninites: near-liquidus phase relations to 7.5 kbar. , 112–147.

Workman, R. K. & Hart, S. R. (2005). Major and trace element composition of the depleted MORB mantle (DMM). *Earth and Planetary Science Letters* **231**, 53–72.

Zellmer, G. F., Annen, C., Charlier, B. L. A., George, R. M. M., Turner, S. P. & Hawkesworth, C. J. (2005). Magma evolution and ascent at volcanic arcs: constraining petrogenetic processes through rates and chronologies. *Journal of Volcanology and Geothermal Research* **140**, 171–191.

Zellmer, G., Rubin, K., Gronvold, K. & Juradochichay, Z. (2008). On the recent bimodal magmatic processes and their rates in the Torfajökull–Veidivötn area, Iceland. *Earth and Planetary Science Letters* **269**, 388–398.

Zellmer, K. E. & Taylor, B. (2001). A three-plate kinematic model for Lau Basin opening. *Geochemistry, Geophysics, Geosystems* **2**.